Title

Yucca Mountain Single Heater Test Final Report: Yucca Mountain Site Characterization Project

Author

Tsang, Y.W.

Publication Date

1999

LBNL-42537

ERNEST ORLANDO LAWRENCE
BERKELEY NATIONAL LABORATORY

Yucca Mountain Single Heater Test Final Report

Yucca Mountain Site Characterization Project

Y.W. Tsang, J. Apps, J.T. Birkholzer,
B. Freifeld, M.Q. Hu, J. Peterson,
E. Sonnenthal, and N. Spycher

Earth Sciences Division

January 1999

DISCLAIMER

Earth Science Division
Lawrence Berkeley National Laboratory
One Cyclotron Road MS 90-1116
Berkeley, CA 94720

LBNL-42537
January 1999

Yucca Mountain Single Heater Test Final Report

Yucca Mountain Site Characterization Project

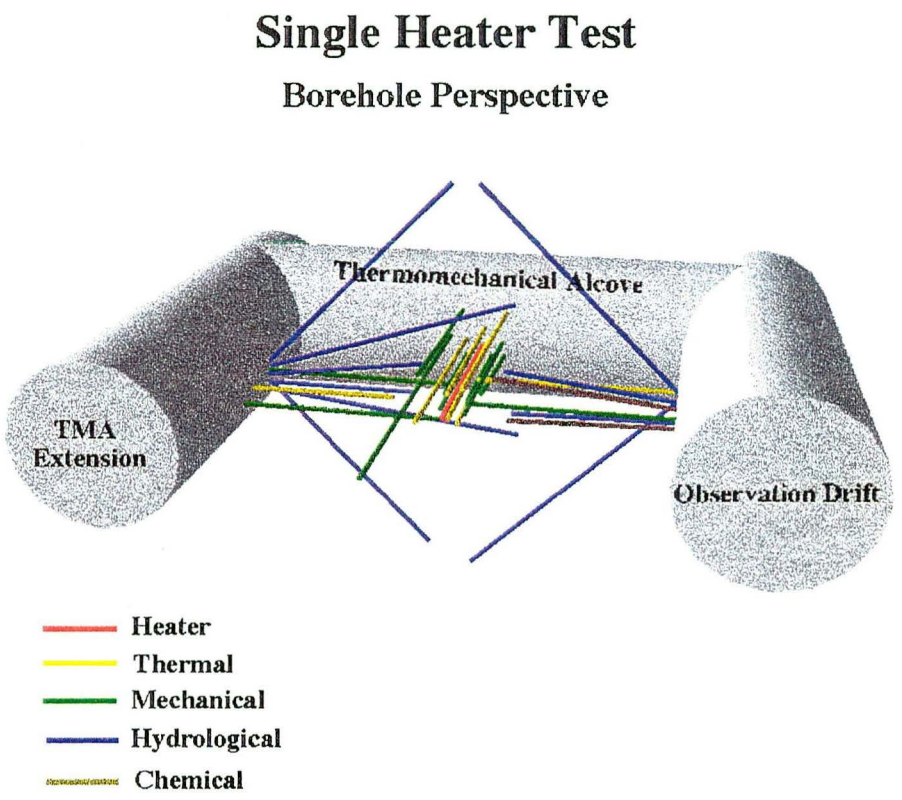

Y.W. Tsang, J. Apps, J.T. Birkholzer, B. Freifeld, M.Q. Hu, J. Peterson, E. Sonnenthal, and N. Spycher

This work was supported by the Director, Office of Civilian Radioactive Waste Management, US Department of Energy, through Memorandum Purchase Order EA9013MC5X between TRW Environmental Safety Systems, Inc. and the Ernest Orlando Lawrence Berkeley National Laboratory, under Contract NO. DE-AC03-76SF00098

Table of Contents

CHAPTER 1 INTRODUCTION **1-1**

Y.W. Tsang

1.1 BACKGROUND 1-1
1.2 STATUS OF THE SHT 1-2
1.3 ORGANIZATION OF THIS REPORT 1-3
1.4 QUALITY ASSURANCE STATUS OF DATA AND SOFTWARE USED IN THIS REPORT 1-3
ACKNOWLEDGMENT 1-4
REFERENCES 1-4
FIGURES 1-6

CHAPTER 2 HYDROLOGICAL MEASUREMENTS **2-1**

Y.W. Tsang, B. Freifeld, M.Q. Hu, and J.Peterson

2.1 ACTIVE PNEUMATIC TESTING 2-1
2.1.1 Pre-Heat Field Characterization by Air-Injection Tests 2-1
2.1.1.1 Local Air Permeability Estimation 2-2
2.1.1.2 Interference Pressure Responses to Air Injection 2-5
2.1.1.3 Summary 2-6
2.1.2 Air-Permeability Measurements During Heating and Cooling Phases of the SHT 2-7
2.1.2.1 Testing Procedure 2-7
2.1.2.2 Test Results 2-8
2.1.3 Post-Cooling Characterization by Air-Permeability and Gas-Tracer Tests 2-9
2.1.3.1 Air Permeability Tests 2-9
2.1.3.2 Gas Tracer Tests 2-13
2.2 PASSIVE MONITORING DATA IN HYDROLOGY HOLES 16 AND 18 2-15
2.2.1 Temperature Measurements 2-15
2.2.2 Relative Humidity Measurements 2-16
2.2.3 Pressure Measurements 2-16
2.2.4 Summary 2-17
2.3 CROSS-HOLE RADAR TOMOGRAPHY 2-17
2.3.1 Overview 2-17
2.3.2 Acquisition 2-18
2.3.3 Processing 2-19
2.3.3.1 Determining the zero time 2-19
2.3.3.2 Well Pair 22-23 2-20
2.3.3.3 Well Pair 15-17 2-20
2.3.4 Interpretation 2-21
2.3.4.1 Saturation Dependence of Dielectric Constant Based on Laboratory Measurements 2-23
2.3.4.2 Comparison to Borehole Neutron Probe Measurements 2-24
2.3.4.2 Discussion of Saturation Estimates 2-25
2.3.5 Conclusion 2-26
2.4 INFRARED IMAGING 2-26
2.4.1 Data and Discussion 2-26
2.4.3 Summary 2-28
2.5 LABORATORY TESTING: HYDROLOGICAL PROPERTIES 2-28
2.5.1 Pre-Heat 2-28
2.5.1.1 Methodology 2-28
2.5.1.2 Results 2-29
2.5.2 Post-Cooling 2-31
ACKNOWLEDGMENT 2-33
REFERENCES 2-33

FIGURES 2-36

CHAPTER 3 INTERPRETIVE ANALYSIS OF THE THERMO-HYDROLOGICAL ASPECTS OF THE SHT 3-1

J.T. Birkholzer and Y.W. Tsang

3.1 INTRODUCTION 3-1
3.2 THERMO-HYDROLOGY IN THE SHT AND MODEL CONCEPTUALIZATION 3-2
3.2.1 Pre-Heat Conditions in the SHT Block 3-2
3.2.2 Potential Thermo-Hydrological Processes in the SHT 3-2
3.2.3 Conceptual Model of the SHT 3-3
3.3 NUMERICAL MODEL OF THE SHT 3-5
3.3.1 Basic Model Assumptions 3-5
3.3.2 Model Domain 3-6
3.3.3 Computational Grid Design 3-6
3.3.4 Boundary and Initial Conditions 3-7
3.3.5 Model Parameters 3-9
3.4 SIMULATION RESULTS AND COMPARISON TO MEASURED DATA 3-11
3.4.1 Qualitative Discussion of Simulation Results 3-12
3.4.2 Quantitative Comparison of Measured and Simulated Temperature 3-16
3.4.2.1 Discussion of Temperature Profiles 3-16
3.4.2.2 Discussion of Temperature Evolution 3-17
3.4.2.3 Discussion of Model Accuracy 3-17
3.4.3 Sensitivity Analysis 3-19
3.4.3.1 Thermo-Hydrological Parameters 3-19
3.4.3.2 Fracture-Matrix Interaction 3-20
3.4.3.3 Discussion on Cooling Phase Results 3-21
3.5 SUMMARY AND CONCLUSIONS 3-22
ACKNOWLEDGMENT 3-23
REFERENCES 3-24
APPENDIX 3-27
TABLES 3-28
FIGURES 3-32

CHAPTER 4 INTERPRETIVE ANALYSIS OF THE THERMO-HYDROLOGICAL-CHEMICAL ASPECTS OF THE SINGLE HEATER TEST 4-1

N. Spycher, E. Sonnenthal, and J. Apps

4.1 INTRODUCTION 4-1
4.1.1 Objective 4-2
4.1.2 Background and Previous Studies 4-2
4.2 QA STATUS OF WORK 4-3
4.2.1 QA Status of Data 4-3
4.2.2 QA Status of Computer Programs 4-4
4.3 GEOCHEMICAL DATA FROM THE SHT 4-4
4.3.1 Mineralogical Data 4-5
4.3.2 Water Analyses 4-5
4.4 CONCEPTUAL MODEL OF THC PROCESSES AFFECTING THE SHT 4-8
4.4.1 The dryout zone 4-8
4.4.2 The boiling zone 4-9
4.4.3 Condensation zone 4-9
4.4.3 Drainage Zone 4-10
4.4.4 CO_2 Halo 4-10
4.4.5 Zoning During Cooling Phase 4-10
4.5 QUANTITATIVE ANALYSIS OF THC PROCESSES 4-11
4.5.1 Numerical Model and Processes Considered 4-11
4.5.2 Grid and Boundary Conditions 4-12
4.5.3 Thermal, Hydrological, and Transport Input Parameters 4-13

4.5.4 Chemical Input Parameters 4-13
4.5.4.1 Initial Water and Gas Compositions 4-14
4.5.4.2 Mineralogy 4-15
4.5.4.4 Thermodynamic Data 4-16
4.5.4.5 Kinetic Data 4-19
4.5.5 Numerical Simulations 4-20
4.5.5.1 Calcite-Silica-Gypsum System 4-20
4.5.5.2 Calcite-Silica-Gypsum-Aluminosilicates System 4-22
4.6 INTERPRETATION AND DISCUSSION 4-28
4.7 CONCLUSIONS 4-30
ACKNOWLEDGMENTS 4-31
REFERENCES 4-31
FIGURES 4-37

CHAPTER 5 SUMMARY AND CONCLUSIONS 5-1

Y.W. Tsang

ACKNOWLEDGMENT 5-4
REFERENCES 5-4

Chapter 1 Introduction

Y.W. Tsang

Earth Sciences Division, LBNL

1.1 Background

The Single Heater Test (SHT) is the first of the two heater tests being carried out in the Yucca Mountain Thermal Test Program in the underground Exploratory Studies Facility (ESF). The ESF Thermal Test is an integral part of the site investigations program to characterize Yucca Mountain, in Nye County, Nevada, for the permanent disposal of spent nuclear fuel and high-level nuclear waste. The primary objective of the ESF Thermal Test is to acquire a more in-depth understanding of the coupled thermal, mechanical, hydrological, and chemical (TMHC) processes likely to exist in the rock mass surrounding the potential geologic repository at Yucca Mountain. These coupled processes are monitored by a multitude of sensors installed in the various instrument boreholes surrounding the nominal 4-kW, 5-m-long single heater, to measure the temperature, mechanical displacement, humidity, and gas pressure of the rock formation in response to the heat generated by the heater. In addition to collecting passive monitoring data, active mechanical, hydrological, and geophysical tests were also conducted periodically in the SHT by the Thermal Test Team. The active tests include borehole jack tests to determine the change in rock mass modulus; air injection tests to monitor the changes of liquid saturation in the fractures; tests involving electric resistivity tomography, neutron logging, and cross-hole, ground-penetrating radar tomography to monitor the moisture redistribution in the matrix. Water samples were also collected for chemical and isotopic analysis.

The SHT test block (Figure 1.1-1) is flanked by 5-m drifts on three sides: the Observation Drift to the north, the Thermomechanical Alcove to the west, and the Thermomechanical Alcove Extension to the south. The +x direction is orientated approximately N-S parallel to the Thermomechanical Alcove drift wall; the origin of the coordinate system is defined to be the collar of the emplacement borehole for the single heater, which is parallel to the +y axis pointing approximately W-E. Figure 1.1-1 shows a 3D perspective of the SHT, with the heater and different boreholes color-coded according to their functions: thermal, mechanical, hydrological, and chemical. The borehole layout in plan view (x-y) and the 2D cross section (x-z) are shown in Figure 1.1-2. Boreholes installed with temperature sensors and multiple point borehole extensometers are drilled both parallel and orthogonal to the single heater. Boreholes labeled "hydrological" in Figure 1.1-1 are all orthogonal to the single heater–they are mainly for monitoring the moisture redistribution by active testing, such as air-permeability, neutron logging,

electrical resistivity tomography, and cross-hole radar tomography. This active testing is conducted periodically for the duration of the SHT. The boreholes labeled "chemistry" are intended for water sampling.

1.2 Status of the SHT

The heater in the SHT was activated on August 26, 1996. The heating phase of the SHT lasted nine months until May 28, 1997. The cooling phase of the SHT continued until January 5, 1998, at which time post-cooling field characterization activities began. All tests and analyses of the SHT have now been concluded.

Four National Laboratories – Lawrence Berkeley National Laboratory (LBNL), Lawrence Livermore National Laboratory (LLNL), Los Alamos National Laboratory (LANL), and Sandia National Laboratories (SNL) – under the coordination of Woodward-Clyde Federal Services (WCFS) share the main responsibility for conducting and analyzing the SHT. All the data from the SHT are shared among the Thermal Test Team members, though the installation of specific instrumentation and the execution of different tests are assigned to respective laboratories.

The approach of the Thermal Test Team to the SHT is as follows: prior to turning on heat, characterization data for the SHT area were collected, consisting of both laboratory and field measurements (CRWMS, 1996). Laboratory measurements encompassed the thermal, mechanical, hydrological, and chemical properties of samples collected at the SHT. Field measurements included fracture mapping, rock mass classification, air permeability testing, infrared imaging and borehole video logging. The Thermal Test Team members also performed predictive modeling of the TMHC coupled processes in the SHT. During the heating and cooling phases of the SHT, the Thermal Test Team members submitted the acquired data to the Technical Data base and prepared brief progress reports on a quarterly basis. At the conclusion of the heating phase, the Thermal Test Team performed interpretive analyses of all the heating phase data of the SHT. At that time, model conceptualizations and input parameters from the predictive models were reviewed and refined to reflect the information obtained from the heating phase data, and insight gained regarding the coupled TMHC processes. The results of these analyses were summarized in a Level 3 milestone report (CRWMS, 1997). With the conclusion of the cooling phase of the SHT in the first week of January, 1998, and the completion of the post-cooling field and laboratory characterization testing, the Thermal Test Team members have analyzed the SHT results using the whole data set: pre-test characterization, heating phase and cooling phase, and post-test characterization.

In this report, we document the results of the study conducted by LBNL, which include comprehensive analyses and modeling of the SHT.

1.3 Organization of this report

In this final report of the SHT, we present a comprehensive analysis of all the test results, including preheat characterization, passive monitoring and active testing data during the heating and cooling phases of the SHT, and post-cooling characterization. All measurements under the responsibility of LBNL are summarized in Chapter 2. Following the discussion of measurements, interpretive analysis of the results by means of numerical modeling are presented in Chapters 3 and 4. Chapter 3 focuses on the thermo-hydrological processes of the SHT. Chapter 4 emphasizes the thermo-hydrological-chemical aspects of the SHT. Chapter 5 summarizes our overall understanding of the SHT based on all measurements and modeling, and includes a discussion of coupled processes and their implications for performance assessment and waste package and repository design.

1.4 Quality Assurance Status of Data and Software Used in This Report

The work described in this report is documented in the following LBNL Scientific Notebooks:

(1) Y. Tsang, 1996, YMP-LBNL-YWT-1B pp. 55-88; (2) B. Freifeld, 1996, YMP-LBNL-YWT-1.2 pp. 74-108; (3) Y. Tsang, 1996, YMP-LBNL-YWT-1.3 pp. 131-148; (4) Q. Hu, 1998, YMP-LBNL-YT-QH-1 pp.1-49; (5) K. Williams, 1998, YMP-LBNL-YT-KHW-1 pp.1-26; (6) J. Birkholzer, 1997, YMP-LBNL-YT-JB-H-1A pp.40-116; and (7) N. Spycher, 1998, YMP-LBNL-YWT-NS-1 pp.116-121. The aforementioned scientific notebooks and data discussed therein have been reviewed according to YMP-LBNL QA Program.

YMP-LBNL-YWT-ELM-1.2 Scientific Notebook pages supporting Section 2.3 of this report have not been reviewed. The review of the Scientific Notebook pages will be completed prior to finishing the NEPO review of this report. If the scientific notebook review generates changes to this report, the report will be resubmitted for NEPO review with the changes indicated.

Most of the SHT data referred to in this report have been submitted previously to the technical data- base and are identified by Data Tracking Numbers (DTN), accession numbers (ACCN), as well as specified Q-status. For this deliverable, post-cooling air injection and gas tracer data (Section 2.1.3) have been submitted through a TDIF with data tracking number LB980901123142.001. These were collected by qualified personnel, with calibrated equipment under the LBNL-QA program. Passive monitoring data of temperature, pressure, and relative humidity in boreholes 16 and 18 (Section 2.2) have been submitted through a TDIF with data tracking number LB980901123142.002. Passive monitoring data of the SHT were transmitted monthly from the ESF Thermal Test data manager to the Thermal Test Team members on compact discs (Homuth, 1996, 1997, 1998). They have been reviewed by qualified personnel at LBNL and are qualified. Cross-hole radar tomography qualified data collected periodically for the SHT, from

pre-heating survey in August, 1996, to post-cooling survey in January 1998, have been submitted through a TDIF with data tracking number LB980901123142.003. Laboratory measurements Section 2.5 of grain density, porosity, water content, and liquid saturation of the post-cooling cores have been submitted through a TDIF with data tracking number LB980901123142.006.

The Q-Status of chemical data used are presented in 4.2 separately.

Modeling data for the thermo-hydrological processes presented in Chapter 3 have been submitted through a TDIF with data tracking number LB980901123142.004. Modeling data for the thermo-hydrological-chemical processes presented in Chapter 4 have been submitted through a TDIF with data tracking number LB980901123142.005. Due to a deficiency on the LBNL QIP related to the software qualification process, the numerical codes such as TOUGH2 used in Chapter 3 and TOUGH-REACT used in Chapter 4 are considered unqualified at this time. Revised software procedures, YMP-LBNL-QIP-SI.0 and YMP-LBNL-QIP-SI.1, which meet the QARD, were issued on June 30, 1998. We are in the process of qualifying all the above software to the new procedures. It is anticipated that TOUGH2 will be qualified before the end of FY98, and TOUGH-REACT before the end of the calendar year.

Standard spreadsheets, as well as visualization and plotting routines, were used to generate graphics. Such programs are not subject to QA requirements under QARD Rev. 8.

Acknowledgment

We are grateful to George Moridis and Sumit Mukhopadhyay for their technical review of this chapter and comments for improvement. We would also like to thank Colleen Haraden and Antoinette Czerwinski for production, and Dan Hawkes for editing all the chapters and Don Mangold for a QA review of this report. This work was supported by the Director, Office of Civilian Radioactive Waste Management, U.S. Department of Energy, through Memorandum Purchase Order EA9013MC5X between TRW Environmental Safety Systems. Inc. and the Ernest Orlando Lawrence Berkeley National Laboratory, under Contract No. DE-AC03-76SF00098.

References

Birkholzer, J. 1997. LBNL Scientific Notebook for *Single Heater Test Final TDIF Submittal and Final Report.* YMP-LBNL-YT-JB-H-1A. Berkeley, California: Lawrence Berkeley National Laboratory. MOL: TBV.

CRWMS M&O. September 1996. *Characterization of the ESF Thermal Test Area.* Report B00000000-01717-5705-00047 Rev. 01. MOL.19970116.0187.

CRWMS M&O 1997. *Single Heater Test Status Report.* BAB000000-01717-5700-00002 Rev. 01. Las Vegas, Nevada. MOL.19980203.0578.

Freifeld, B. 1996. LBNL Scientific Notebook for *Single Heater Test Final TDIF Submittal and Final Report.* YMP-LBNL-YWT-1.2. Berkeley, California: Lawrence Berkeley National Laboratory. MOL: TBV.

Homuth, F. 1996, 1997, 1998. Monthly Memos to Single Heater Test Principal Investigators Regarding Transfer of Data from ESF Data Collection Systems. Memorandum LA-EES-13-LV-11-96-041, LA-EES-13-LV-12-96-008, LA-EES-13-LV-01-97-019, LA-EES-13-LV-02-97-019, LA-EES-13-LV-03-97-004, LA-EES-13-LV-04-97-002, LA-EES-13-LV-05-97-017, LA-EES-13-LV-06-97-001, LA-EES-13-LV-07-97-004, LA-EES-13-LV-08-97-012, LA-EES-13-LV-09-97-003, LA-EES-13-LV-07-10-97-002, LA-EES-7-11-97-011, LA-EES-7-12-97-008, LA-EES-7-01-98-006. MOL. TBV.

Hu, Q. 1998. LBNL Scientific Notebook for *Single Heater Test Final TDIF Submittal and Final Report.* YMP-LBNL-YT-QH-1. Berkeley, California: Lawrence Berkeley National Laboratory. MOL: TBV.

Spycher, N. 1998. LBNL Scientific Notebook for *Single Heater Test Final TDIF Submittal and Final Report.* YMP-LBNL-YWT-NS-1. Berkeley, California: Lawrence Berkeley National Laboratory. MOL: TBV.

Tsang, Y.W. 1996a. LBNL Scientific Notebook for *Single Heater Test Final TDIF Submittal and Final Report.* YMP-LBNL-YWT-1B. Berkeley, California: Lawrence Berkeley National Laboratory. MOL: TBV.

Tsang, Y.W. 1996b. LBNL Scientific Notebook for *Single Heater Test Final TDIF Submittal and Final Report.* YMP-LBNL-YWT-1.3. Berkeley, California: Lawrence Berkeley National Laboratory. MOL: TBV.

Williams, K. 1998. LBNL Scientific Notebook for *Single Heater Test Final TDIF Submittal and Final Report.* YMP-LBNL-YT-KHW-1. Berkeley, California: Lawrence Berkeley National Laboratory. MOL: TBV.

Figures

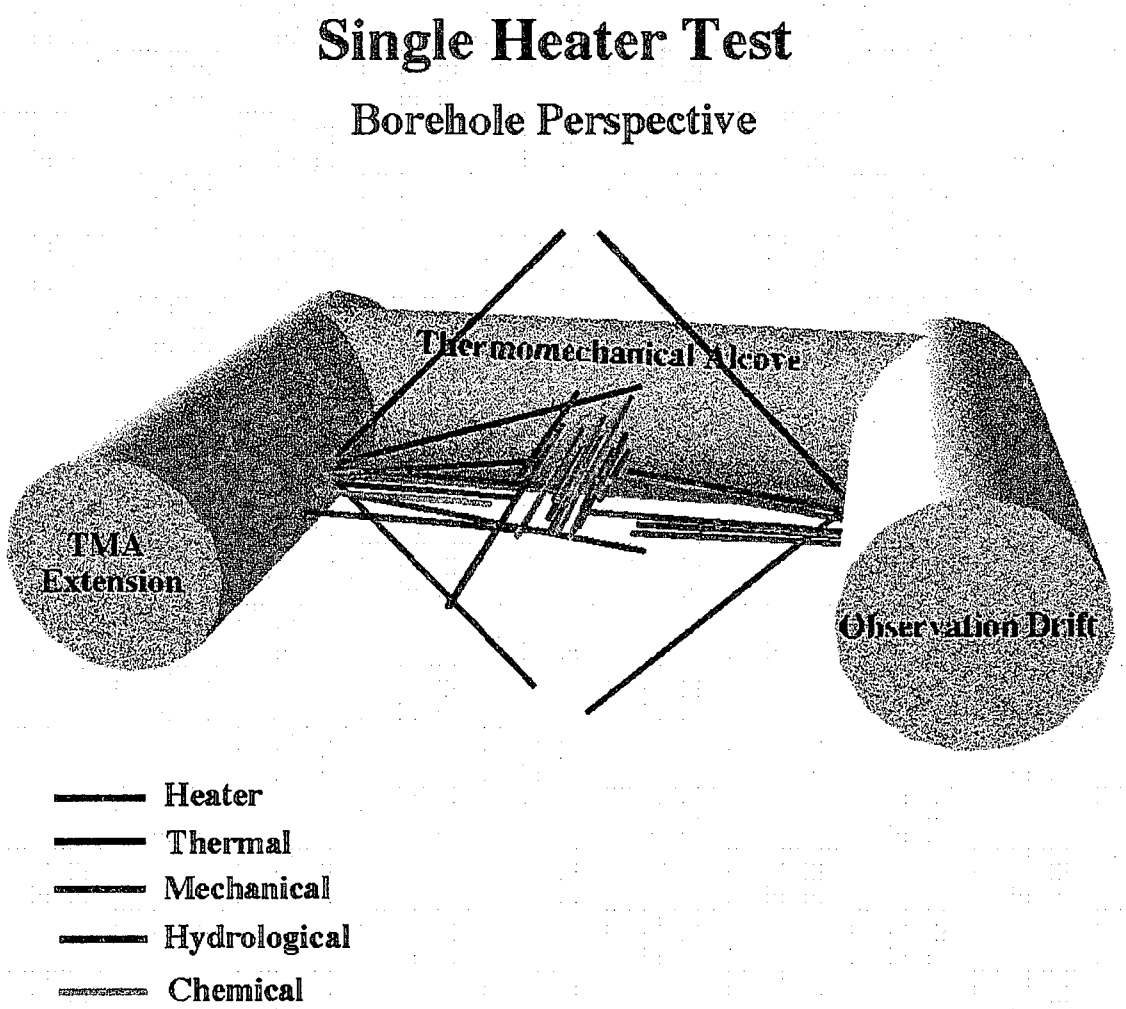

Figure 1.1-1 Schematic of boreholes layout in the SHT (3D perspective)

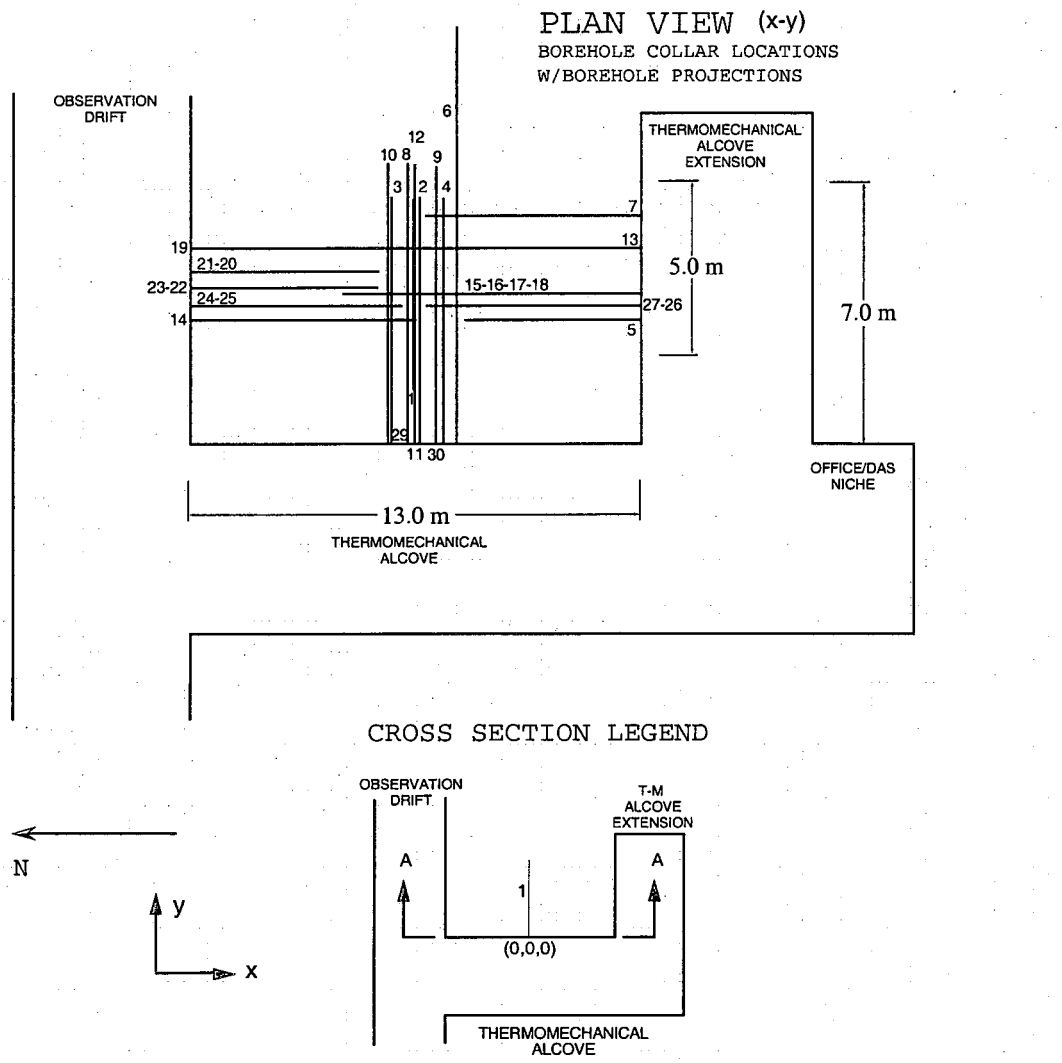

Figure 1.1-2. Borehole layout in the SHT (plan view and cross section).

Chapter 2 Hydrological Measurements

Y.W. Tsang, B. Freifeld, M.Q. Hu, and J. Peterson

Earth Sciences Division, LBNL

While the complete set of Single Heater Test (SHT) data is shared by all members of the Thermal Test Team for interpretation and analysis, the responsibility of conducting specific measurements in the SHT was assigned to respective laboratories. In this chapter, we summarize the SHT measurements obtained by LBNL, which concern the thermohydrological aspects of the test. They include air-permeability measurements and cross-hole radar tomography data obtained (a) before the onset of heating, (b) periodically during the heating and cooling phases, and (c) during the post-cooling phase of the SHT. Passive monitoring data such as temperature, humidity and pressure in boreholes 16 and 18 will also be discussed in this chapter. Infrared imaging of the SHT test block surfaces was conducted prior to heating, and periodically during the heating and cooling phases of the test. The imaging results are summarized in Section 2.4. Finally, the laboratory measurements of the hydrological properties of rock cores from the SHT, both pre-test and post-test, will be presented in Section 2.5.

2.1 Active Pneumatic Testing

2.1.1 Pre-Heat Field Characterization by Air-Injection Tests

A detailed discussion of the pre-heat characterization by means of air permeability tests in the SHT block has been presented in previous milestones reports (Tsang et al., 1996; CRWMS M&O, 1996). A summary of the key findings is presented here.

Characterization by means of air-permeability tests, prior to the onset of heating, provides an understanding of the initial conditions in the SHT block, specifically the potential pathways for gas flow. As the rock mass is heated during testing, water in the rock vaporizes, and the majority of fluid movement presumably occurs in this gas phase. Results of air-permeability tests provide an estimate of the three-dimensional heterogeneous permeability structure and fracture connectivity in the block. This information can provide input to a conceptual model, and allow estimates of liquid, heat, and gas flow in the SHT region. The pre-heat characterization data also serve as a basis for post-cooling comparison by observing where changes in permeability have occurred due to heating and possible thermo-mechanical-hydrologic-chemical coupling.

In May 1996, air injection tests were conducted in the SHT area after all the boreholes had been drilled and logged by video, and prior to the holes being installed with instrumentation for monitoring the heater test proper. To prevent the boreholes from pneumatically communicating with the drifts, inflatable packers were fabricated and installed near the collar in every borehole numbered from 1 through 31 (see Figure 1.1-2 for the borehole layout). A typical test consisted of air injection in one chosen borehole at constant mass flux maintained by mass flow controllers. Pressure responses in this and all other boreholes were monitored continuously for about 20 to 30 minutes after steady state had been reached, which was typically within minutes. Air injection was then terminated. The pressure response in the injection borehole itself was used to calculate the local permeability, averaged over the packed-off zone, L. Interference pressure responses in all other boreholes provided information on the connectivity of pneumatic pathways between the observation and the injection holes.

2.1.1.1 Local Air Permeability Estimation

Local permeability in the injection borehole was estimated from the steady state pressure response to the air injection test. An analytical solution for the steady state pressure response of a constant flow rate injection in a finite line source has been used by both LeCain (1995, p.10) and Guzman et al. (1996, p.10) for the analysis of single hole injection tests in fractured tuff at Apache Leap Research Site, Arizona. It was adapted from the steady state analytical solution for ellipsoidal flow of incompressible fluid from a finite line source (Hvorslev, 1951) in an infinite medium ($L/r_W >> 1$) and is as follows:

$$k = \frac{P_{SC} Q_{SC} \mu \ln \frac{L}{r_w} T_f}{\pi L \left(P_2^2 - P_1^2\right) T_{SC}} \quad . \tag{2.1-1}$$

where

k = permeability, m^2

P_{SC} = Pressure at standard conditions, 1.013×10^5 Pa

Q_{SC} = flowrate at standard conditions, m^3/s

μ = dynamic viscosity of air, Pa-s (1.81×10^{-5} at 20°C)

L = Length of air injection zone, m

r_w = radius of borehole (m)

T_f = temperature of formation, °K

P_2 = steady state pressure, Pa

P_1 = ambient pressure, Pa

T_{SC} = temperature at standard conditions (293.16° K)

The derivation of (2.1-1) requires the assumption that air is the only mobile phase within the rock near the test interval, and that it obeys the ideal gas law so that its compressibility is inversely proportional to pressure. Equation (2.1-1) has its origin in well test analysis for a homogeneous porous medium. The welded tuff of the single heater test block is a fractured medium and is most likely not well represented conceptually by a homogeneous porous medium. Furthermore, the proximity of the drifts implies that the finite line source is not in an infinite medium. Nevertheless, Equation (2.1-1) is valuable as a simple tool of choice to obtain an order-of-magnitude estimate of the average permeability values around each borehole, thus providing an initial idea of the spatial variability of fracture permeability in the test block.

The permeability values estimated from Equation (2.1-1) for injection tests performed in 21 boreholes in the SHT block are tabulated in Table 2.1-1. These values range over three orders of magnitude, from 5.0 x 10^{-15} m^2 to 5.2 x 10^{-12} m^2, and correspond to borehole packed-off zones of lengths L typically from 1.7 to 11 meters. The large range of local permeability values is consistent with the geological formation of the SHT, i.e., the densely fractured Topopah Spring middle non-lithophysal stratigraphic unit. One complete set of estimated permeability values for the 21 boreholes is also shown in 3D in Figure 2.1-1. The logarithm of permeability is color-coded using a rainbow color pallette, with the highest value in red and the lowest value in blue.

Permeability values in Table 2.1-1 are applicable to the entire borehole. However, since borehole videos indicate differing degrees of fracturing in localized zones within each borehole, one would expect the permeability within each borehole to vary from one localized zone to another. This is confirmed by results of air-injection tests performed in consecutive intervals of 0.69 m separated by a movable straddle packer string in borehole 6. The estimated permeability values of the 16 consecutive 0.69-m-sections in the same borehole is tabulated in Table 2.1-2, and ranging from less than 10^{-15} m^2 to 6.2 x 10^{-13} m^2. The first 5 meters of the borehole (measured from the collar) are rather impermeable, having values of 10^{-15} m^2 and less. The two most permeable zones, with permeability values that range from 1.1 to 6.6 x 10^{-13} m^2, are (1) from ~7. to 8.3 m from the borehole collar, and (2) a 0.69-m section centered about 10.36 m from the borehole collar. A comparison of the range of permeability values in Table 2.1-2 for 0.69-m sections to that averaged over the packed length of 11 m for the entire borehole 6, 5.1 x 10^{-14} m^2 (Table 2.1-1) lends support to our belief that fluid flow seeks the least resistive path in a heterogeneous fractured system. Due to a time constraint requiring all characterization effort to be completed within a two-week period before permanent installation of the SHT, the detailed small-scale characterization by

straddle packer was not duplicated for other holes, in which similar level of heterogeneity can be expected.

Table 2.1-1Parameters for the estimation of pre-heat permeability, k, around injection zones for different boreholes based on Equation (2.1-1)[+]

Borehole and datafile ID	Borehole length (m)	Borehole radius (cm)	Packed zone, L (m)	Constant flowrate, Q(SLPM)	P2-P1 (kPa)	Estimated permeability $k(m^2)$
Borehole 1 (5/24-03)	7.00	4.8*	1.73	53.	35.0	1.5E-13
Borehole 1 (5/28-08)	7.00	4.8*	1.73	50.	32.5	1.5E-13**
Borehole 1 (5/30-14)	7.00	4.8*	2.70	22.	9.5	1.8E-13**
Borehole 2 (5/28-06)	6.91	3.79	6.00	22.	13.4	7.2E-14
Borehole 3 (5/28-02)	7.02	3.79	6.11	100.	22.3	1.8E-13
Borehole 4 (5/28-03)	6.89	3.79	5.98	22.	77.0	9.2E-15
Borehole 6 (5/30-07)	11.99	3.79	11.07	40.	20.0	5.1E-14
Borehole 7 (5/31-01)	5.91	3.79	5.00	360.	10.7	1.7E-12
Borehole 7 (5/31-07)	5.91	3.79	2.26	500.	16.0	2.9E-12
Borehole 10 (5/24-02)	8.00	2.4	7.09	3.	10.6	1.2E-14
Borehole 11 (5/28-04)	6.80	2.4	5.89	300.	3.0	5.2E-12
Borehole 12 (5/28-05)	7.67	2.4	6.76	200.	37.0	2.1E-13
Borehole 13 (5/30-08)	5.95	3.79	5.04	22.	16.5	6.6E-14
Borehole 15 (5/29-14)	8.18	3.79	7.09	20.	48.0	1.4E-14
Borehole 16 (5/30-09)	5.18	3.79	3.94	11.	64.0	8.3E-15
Borehole 17 (5/28-07)	8.00	3.79	6.91	100.	1.5	2.8E-12
Borehole 18 (5/30-10)	4.86	3.79	3.59	21.	15.5	8.8E-14
Borehole 19 (5/31-04)	5.79	3.79	4.88	20.	6.6	1.6E-13
Borehole 22 (5/29-02)	5.00	3.79	4.09	1.	6.4	9.9E-15
Borehole 23 (5/29-01)	5.50	3.79	4.59	1.	11.0	5.0E-15
Borehole 24 (5/31-03)	8.71	3.79	7.44	5.	15.7	1.2E-14
Borehole 25 (5/31-02)	8.74	3.79	7.82	100.	7.8	4.6E-13
Borehole 26 (5/31-05)	8.70	3.79	7.73	200.	6.8	1.1E-12
Borehole 27 (5/30-13)	8.70	3.79	7.43	4.5	30.0	5.1E-15

** Revised from values reported in Tsang et al. (1996) due to miscalculation of packed zone length.

* The radius of 4.8 cm is applicable only to the last 5 meters of Heater Hole 1.

+ T_f =24.6°C, P_1=89.1 kPa

Table 2.1-2 Input parameters and estimated pre-heat air permeability, k(m^2) (based on Equation 2.1-1) for consecutive 0.69-meter zones from injection tests between straddle packers in borehole 6.

Borehole 6 data file and straddle zone ID	Mid- zone location from collar (m)	Constant flowrate, Q(SLPM)	P_2-P_1 (kPa)	Permeability k(m^2)
(5/29-03) 3'-5'	1.22	1.03	47.00+	4.0E-15+
(5/29-04) 5'-7'	1.83	0.39	65.00	1.0E-15
(5/29-05) 7'-9'	2.44	0.62	57.20	1.9E-15
(5/29-06) 9'-11'	3.05	0.62	58.00	1.9E-15
(5/29-07) 11'-13'	3.66	0.62	*	*
(5/29-08) 13'-15'	4.27	2.04	*	*
(5/29-09) 15'-17'	4.88	2.01	58.00	6.1E-15
(5/29-10) 17'-19'	5.49	2.01	24.50	1.7E-14
(5/29-11) 19'-21'	6.10	2.01	28.00	1.4E-14
(5/29-12) 21'-23'	6.71	4.00	17.20	5.0E-14
(5/30-06) 23'-25'	7.32	4.02	8.00	1.1E-13
(5/29-13) 25'-27'	7.92	42.00	25.00	3.4E-13
(5/30-01) 25'-27'	7.92	40.50	25.20	3.3E-13
(5/31-06) 25'-27'	7.92	41.00	27.00	3.1E-13
(5/30-02) 27'-29'	8.53	2.00	6.20	7.3E-14
(5/30-03) 29'-31'	9.14	2.03	13.00+	3.4E-14
(5/30-04) 31'-33'	9.75	2.03	14.00+	3.1E-14
(5/30-05) 33'-35'	10.36	2.00	0.75	6.2E-13

* The pressure response to the constant injection flowrate is linear with time, which is that of injection into a nearly closed system, indicating very low permeability.

\+ Modified slightly from previously reported in Tsang et al. (1996) based on data review.

2.1.1.2 Interference Pressure Responses to Air Injection

A typical set of air-injection test data is shown in Figure 2.1-2 for air injection into a 5-m zone in borehole 7. The horizontal axis denotes time, the right vertical axis denotes injection flow rate in standard liters per minute (SLPM = 1.67 x 10^{-5} m^3/s), and the left axis denotes the pressure increase from ambient, ΔP, P_2-P_1, in kPa. The legend on the graph denotes all boreholes in which pressure response is registered. The figure shows that, as expected, the maximum pressure increase occurs in the injection hole. The pressures in the majority of the 31 boreholes in the SHT block rise and fall in response to the constant-flow air injection in borehole 7, though the magnitude of pressure response is smaller in holes other than the injection hole. The behavior displayed in Figure 2.1-2 is typical of that in all the boreholes tested. The almost universal cross-hole pressure response demonstrates that on the scale of one to ten meters, the fractures are well connected, and that the gas flow in the fractures resembles more that of

flow through a heterogeneous continuum than flow through a discrete fracture network, in which case interference pressure response will be limited to very few monitoring zones.

Further study of the cross-hole interference pressure responses of the air injection tests uncovers the presence of a high-permeability direct flow path from borehole 11 to boreholes 7 (Birkholzer and Tsang, 1996, p.7). For the injection test preformed in borehole 1, the magnitudes of pressure rise in the distant monitoring borehole 7 is almost identical to that in the injection borehole 11, while the pressure response in boreholes 28, 29, 30, 31 (which are in close proximity to injection Borehole 11) is much less pronounced. An examination of the borehole video logs show discrete zones of open, unfilled fractures in boreholes 1, 7, 11, 12 lying in a common vertical plane oriented N22°E. Fracture mapping in the thermal alcove (CRWMS M&O, 1996) shows that there is indeed one subvertical joint set with that value of strike azimuth and having a length of three to four meters. The combined data of fracture mapping in the SHT block, borehole video logs, and air-injection interference tests therefore confirm the presence of a high-permeability subvertical fracture zone which is intersected by those horizontal boreholes (boreholes 1, 7, 11, and 12) that give relatively high permeability values. This subvertical fracture lies beyond the mid-plane of the heater, since it apparently is missed by boreholes 28, 29, 30, and 31, all parallel to heater borehole 1 and 5 meters in length from the drift wall.

While a high permeability value can be correlated to a zone of fractures observed in the video log, the air injection data also show that visual observations of densely fractured or rubbled zones (from the video log or mapping data) do not necessarily indicate high permeability in fluid flow. This observation is consistent with common knowledge of fluid flow in saturated fractured formation, where only a very small fraction of the mapped (or visually observed) fractures are hydrologically significant (Tsang and Tsang, 1988).

2.1.1.3 Summary

Pre-heat characterization by air-injection tests on boreholes with isolated zone lengths, L, ranging from 2 to 11 meters show that the permeability values range from 5.0×10^{-15} m^2 to 5.2×10^{-12} m^2. We attribute the three-orders-of-magnitude difference in permeability values to flow through fractures of hierarchical scales, with the microfractures accounting for the lower values, and fracture zones (a few meters in extent) responsible for the highest values. The range of measured permeability values of the boreholes in the SHT is similar to those obtained from surface-based vertical boreholes at the SHT stratigraphic unit over zones 2-3 m long (LeCain, 1997, pp.11-14).

The spatial distribution of the permeability values from steady state pressure response of the injection holes (Figure 2.1-1) indicates that on the scale of the single heater test block (~13m x 8m x 4.5m), there seems to be an overall segregation of the permeability values: lower to the north of the single heater borehole 1 (on the side of the Observation Drift) than to the south (the Thermomechanical Alcove Extension); lower above the single heater borehole 1 horizon than below; and lower permeability toward

the front of the heater borehole 1 (west) than in the back (east). Higher permeability toward the back of the heater borehole 1 may be associated with a discrete, high-permeability fracture zone, whose presence was corroborated by the combined data of fracture mapping in the SHT block, borehole video logs, and air-injection interference tests. The subvertical fracture zone is about 4 m in extent, beyond the mid-plane of the heater, and is intersected by several horizontal boreholes parallel to the heater borehole 1.

Though the interference pressure responses in the SHT test block show that the fractures are well connected and may be conceptualized as a continuum, on a finer scale the estimated permeability can vary by an order of magnitude between adjacent holes; within the same borehole, permeability estimates of different 0.69-m isolated sections can again vary over three orders of magnitude. The data in Table 2.1-2 confirm that in the SHT block, there are fractures of hierarchical scales forming a heterogeneous continuum, and that gas flow does not occur uniformly in the continuum; rather, flow would seek out preferential, least resistive paths (Tsang and Tsang, 1987). Therefore, the pre-heat air-permeability characterization, though providing useful information and valuable insight on the "average" fracture permeability and large-scale connectivity in the SHT block, cannot possibly identify all the preferential gaseous pathways in the SHT block. The presence of these preferential pathways linked to fractures were supported by the thermo-hydrological data during the heating and cooling phases of the SHT, and confirmed by post-cooling hydrological characterization.

2.1.2 Air-Permeability Measurements During Heating and Cooling Phases of the SHT

While pre-heat air-permeability measurements provide a description of the potential flow paths in the test block, periodic air-permeability measurements during the SHT provide information on the changes of flow path during the heating, i.e., on the thermo-hydrological coupled behavior. Constant mass flux air-injection tests, in addition to continuous monitoring of relative humidity, temperature, and pressure, were conducted periodically in the SHT block in the two hydrology boreholes 18. These data have been presented in a series of Level 4 Milestone reports (Freifeld and Tsang, 1997a, 1997b and 1997c; Freifeld 1997, and 1998). Key insight into the hydrologic response of the host rock based on results of the active testing will be reiterated here. A discussion of the passive monitoring data will be presented in Section 2.2.

2.1.2.1 Testing Procedure

Boreholes 16 and 18 are instrumented with relative humidity, temperature, and pressure transducers. Each borehole contains four pneumatically inflated packers, labeled P_1, P_2, P_3, and P_4 on Figure 2.1-3. Instrumented intervals are numbered from the closest to the collar of the borehole, 1, to the deepest zone, behind the last packer in the string, 4. The eight instrumented intervals are referred to by borehole number followed by the instrument interval number, i.e., 18-3 is the third instrument cluster from the collar in borehole 18. The pressure, temperature, and relative humidity sensors are all located just below

the packer (deeper in the borehole) and are assigned the same numeric identifier as the packer just above them.

Each interval between packers and one interval past the end of the last packer are fitted with a 1/4" Teflon injection tube. Dry, clean, compressed air is regulated using mass flow controllers and injected into the designated zone. By selectively deflating different packers, various injection zones for each hydrology hole are formed. Illustrated in Figure 2.1-3 are three possible test configurations: (1) deflate packer P_2, and use air injection line for P_1, (2) deflate packer P_3 and use air injection line for P_2, (3) inflate all four packers and inject behind packer P_4. These three configurations are denoted as injection zones 1, 2, and 3 respectively in Figure 2.1-3. All four packers in the monitoring hole are always inflated so that pressure response can be monitored in each of the four sensors.

2.1.2.2 Test Results

The local permeabilities specific to each of the zones were estimated from Equation (2.1-1), and are shown in Table 2.1-3. Only Sensor 4 in injection Zone 3 in boreholes 16 and 18 shows a significant decrease of permeability values from its pre-heat level during the heating phase. This reduction in the local air permeability is attributed to the fact that a larger portion of the fracture pore space is occupied by water condensed from vapor transported from the boiling zones near the heater. Note that after heating was terminated, during the cooling phase, the permeability returned to the pre-heating values of August 1996 in the same zones. This is clearly seen in Figure 2.1-4. The slight increase in permeability values post-heat may be due to fracture opening during heating and/or the presence of drilling water from wellbore construction. The effect of thermo-mechanical coupling – either opening of existing fractures or generation of new fractures – on air-permeability will be discussed in more detail in the following section. Here, we focus on effects from thermo-hydrological coupling. Based on the permeability values in Table 2.1-3, we conclude that the increase in liquid saturation in the fractures during the heating phase of the SHT was limited only to injection Zone 3 (behind Packer P_4) of boreholes 16 and 18 (which spans a radial distance of about 1.5 m to 3 m from the heater). No apparent change of liquid saturation is noted at radial distance larger than 3 m from the heater.

Table 2.1-3 Comparison of air permeability (in m^2) measured at different phases: pre-heat, during-heat, and post-heating of the SHT in hydrology boreholes 16 and 18.

Location	Measurement Dates						
	Pre-heat	Heating				Cooling	
	7,8-Aug-96	25-Nov-96	4,5-Feb-97	8-Mar-97	22,23-May-97	8-Oct-97	18,19-Nov-97
Inj Behind 16-4	1.10E-14	2.58E-15	2.67E-15	N/A	2.61E-15	2.72E-14	2.67E-14
Inj Behind 18-4	2.30E-13	1.00E-13	1.01E-13	9.86E-14	9.86E-14	2.69 E-13	2.57E-13
Inj Between 16-2, 16-4	5.27E-15	2.83E-15	3.81E-15	4.14E-15	2.76E-15	4.05E-15	4.44E-15
Inj Between 16-1, 16-3	8.85E-14	9.03E-14	9.56E-14	8.76E-14	8.76E-14	8.67E-14	1.34E-13
Inj Between 18-1, 18-3	1.12E-14	1.08E-14	1.12E-14	1.29E-14	9.73E-15	1.27E-14	1.30E-14

The increase of liquid saturation in the fractures surrounding boreholes 16 and 18, behind Packer P_4, during the heating phase of SHT, is also evidenced by the transient air pressure response. Figure 2.1-5

shows a comparison of the before, during, and after heating pressure increases for borehole 18, Zone 3, in response to air injection into this zone. The pressure responses before and after heating show that the pressure remains constant during the test. On the other hand, in the air injection tests during the heating phase of the SHT, the pressure reaches a maximum immediately after the beginning of injection, from which it slowly declines during the test. This indicates that there is a slight increase in air permeability during the two-hour air-injection test. This behavior is attributed to the evaporation of some of the water in the fractures by the dry injected air, and its transport away from the boreholes under the pressure gradient created by injection (Freifeld, 1998, p. 3-4). The different behavior during injection for the pre-heat and post-heat phases of the SHT indicates that increase in the water saturation of the fractures surrounding boreholes 18 (behind P_4) occurs only during heating, while condensation of vapors is continuous. In the absence of vapor transport when the heater is turned off, thermodynamic equilibrium between fractures and matrix resumes, and the disparity of the capillary suction between matrix and fractures ensures that the majority of water is being held in the matrix pores.

The summary above on air-permeability tests in the hydrology holes shows that the pressure response data to air injection can be used to delineate the redistribution of moisture in the fractures in the SHT, and to confirm our understanding of strongly heat-driven two-phase flow and transport processes in fractured rocks.

2.1.3 Post-Cooling Characterization by Air-Permeability and Gas-Tracer Tests

2.1.3.1 Air Permeability Tests

Post-test activities at the SHT began in the first week of January, 1998, with the removal of insulation material from the test block. Most of the 31 boreholes involved in the pre-heat air injection tests in the SHT (see section 2.1.1) had since been grouted for installation of instruments for the heater test, and were therefore not suitable for air permeability tests. The exception are boreholes 1, 3, 6, 7, 19. Therefore instrumentation was removed from these boreholes, immediately following the removal of insulation material, to make them available for post-cooling characterization. Instrumentation in all other boreholes which were grouted were left in place, their removal was scheduled to follow the completion of air permeability tests. Figure 2.1-6 shows the subset of ungrouted boreholes in which post-cooling pneumatic tests were performed. This is in contrast to the pre-heat characterization, where all 31 boreholes of the SHT (as shown in Figure 1.1-2) were involved.

The post-cooling characterization by means of pneumatic field tests took place in the third and fourth weeks of January, 1998. Our post-test characterization strategy is to duplicate the pre-test characterization test conditions when feasible. Therefore, inflatable packers were installed near the collar of boreholes 3, 6, 7, 19, to depths identical to those of their pre-test characterization positions. The hydrology boreholes 16 and 18 were already equipped with packer strings for the duration of the SHT (see previous section 2.1.2 and Figure 2.1-3). They were left "as is" for the post-cooling air permeability

measurements, i.e., pressure response would be monitored in four isolated zones in boreholes 16 and 18. For injection, test was conducted in injection Zone 3, behind the fourth packer P_4, as discussed earlier (Section 2.1.2).

The pneumatic connection between the heater borehole 1 and the two hydrology boreholes 16 and 18 is of particular interest. Pressure response to air-injection tests during the heating phase of the SHT (Section 2.1.2.2) indicated the presence of condensed water in the fractured rock mass surrounding boreholes 16 and 18 behind the fourth packer. On the other hand, accumulation of water in the borehole itself was observed and collected (Section 2.2.3) only in borehole 16 behind P_4. Since a borehole is a capillary barrier, seepage into a borehole occurs only if the capillary barrier is overcome by presence of fully saturated rock mass at the borehole wall. Localized zones of fully saturated rock mass at the borehole wall are more likely if there is a fast path for vapor transport, i.e., if there is a fracture connection between the heater borehole 1 (where vaporization takes place), and borehole 16 (between P_4 and the bottom of hole, where condensation takes place). The fact that water is found in borehole 16, and not in borehole 18 suggests that a fast path for vapor transport exists between heater borehole 1 and the former, but not the latter. Post-cooling pneumatic characterization allows testing of this hypothesis, and the determination of fast pathway(s). With this in mind, air-permeability tests were carried out in a multi-zone configuration for boreholes 1, 16 and 18. Specifically, injection was conducted in six consecutive zones in the heater borehole 1, and the pressure response in Sensors 16-4 and 18-4 were measured to identify plausible fast path connections. Upon conclusion of air permeability tests, gas tracer tests were also performed between the heater borehole 1 and boreholes 16 and 18 to investigate the possible presence of fast paths for vapor transport. The multi-zone configuration for injection in borehole 1 and monitoring in boreholes 16 and 18 is shown in Figure 2.1-7.

Table 2.1-4 Post-cooling air permeability, k (m^2) (based on Equation 2.1-1), for boreholes 1, 3, 6, 7, 16, 18, 19.

Injection zone and datafile ID	Packed zone L (m)	Constant flowrate. Q(SLPM)	P_2-P_1 (kPA)	k(m^2) assuming T_f=24.6° C	k(m^2) assuming T_f=30.6°C
Borehole 1-Zone 1 (Jan21-08)	0.59	1	1.62	1.4E-13	1.5E-13
Borehole 1-Zone 2 (Jan21-09)	0.59	10	3.48	6.7E-13	6.8E-13
Borehole 1-Zone 3 (Jan21-10)	0.59	10	2.3	1.0E-12	1.0E-12
Borehole 1-Zone 4 (Jan21-11)	0.59	10	2.36	9.8E-13	1.0E-12
Borehole 1-Zone 5 (Jan21-13)	0.59	10	0.46	5.1E-12	5.2E-12
Borehole 1-Zone 6 (Jan21-12)	1.34	10	0.972	1.4E-12	1.4E-12
Borehole 3 (21Jan03)	6.11	40	3.22	5.6E-13	5.7E-13
Borehole 6 (21Jan04)	11.07	40	14.8	7.1E-14	7.2E-14
Borehole 7 (21Jan05)	5.00	100	2.17	2.5E-12	2.5E-12
Borehole 7-back zone (22Jan01)	2.43	100	2.15	4.4E-12	4.5E-12
Borehole 16 Zone 3 (Jan2106)	2.10	1	2.71	3.9E-14	3.9E-14
Borehole 18 Zone 3 (Jan2107)	1.55	10	4.9	2.6E-13	2.7E-13
Borehole 19 (21Jan02)	4.88	20	3.37	3.2E-13	3.3E-13

The air-permeability values of the various injection zone were estimated from Equation (2.1-1). Table 2.1-4 includes all the post-cooling results. Table 2.1-5 shows a comparison of permeability estimates from pre-heat and post-cooling measurements using data from injection into boreholes 3, 6, 7, 16, 18, and 19. Direct comparison is possible in these boreholes because of the identical pre-test and post-test packer configurations. The post-cooling and pre-heat permeability values in these boreholes are on the same order of magnitude. Furthermore, a study of the cross-hole steady state pressure response show that they are also comparable under pre-test and post-test conditions, i.e., the data do not reveal that the pneumatic connectivity between the boreholes tested had been significantly altered by the heating and cooling of the SHT. The ratios of post to pre-test permeability values, however, show that there is a consistent upward trend in the permeability values from pre-heat to post-cooling (Table 2.1-5). This increase in the permeability ranges from about 20% to a factor of 3.5. The magnitude of the increase is not as significant as the fact that the change is positive for every zone tested. One may speculate that the consistent increase in post-heat permeability values in the SHT test block arises from the fact that wet-drilling of the boreholes increased the moisture content in the fractures and suppressed the pre-heat air permeability. A more likely scenario, though, is that the overall larger post-test permeabilities in the SHT block may be attributed to microfracturing and expansion of fracture apertures. Heating may cause some fractures to close and others to open. However, since (a) the air-permeability tests are conducted over length scales of meters, and (b) fluid flow always seeks the least resistive path and avoids low permeability zones, air-permeability field tests preferentially register the effect of fracture opening. This is consistent with the interpretation in Section 2.1.2.2 that the reduction of air-permeability in injection Zone 3 of boreholes 16 and 18 (Table 2.1-3, Figure 2.1-4) during heating should be attributed to thermo-hydrological coupling, that is, to water condensation that occupies a large, continuous zone, and thus prevents their being circumvented by the air flow. On the other hand, the post-heat increase in permeability in Zone 3 of

boreholes 16 and 18 is most likely due to thermo-mechanical coupling effects, which may have been present, but masked by the thermo-hydrological effects during heating. These mechanisms are supported by the observation: as soon as the heating ceased, measurements during the cooling phase of the SHT show that air permeability in Zone 3 of boreholes 16 and 18 exceed their pre-heat values (Table 2.1-3 and Figure 2.1-4).

Table 2.1-5 Comparison of pre-heat and post-cooling air permeability measurements for boreholes 3, 6, 7, 16, 18, 19.

Pre-test air permeability (assume T_f=24.6°C)			**Post-test air permeability (assume T_f=30.6°C)**			
Borehole and datafiles ID	**L (m)**	**k(m^2)**	**Borehole and datafiles ID**	**L (m)**	**k(m^2)**	**post/pre-heat**
Borehole 3 (5/28-02)	6.11	1.8E-13	3 (21Jan-03)	6.11	5.7E-13	3.1
Borehole 6 (5/30-07)	11.07	5.1E-14	6 (21Jan-04)	11.07	7.2E-14	1.4
Borehole 7 (5/31-01)	5.00	1.7E-12	7 (21Jan-05)	5.00	2.5E-12	1.5
Borehole 7 (5/31-07)	2.26	2.9E-12	7 (22Jan-01)	2.43	4.5E-12	1.6
16 Zone 3 (Aug 7,8, 1996)	2.10	1.1E-14	16-Zone 3 (Jan21-06)	2.10	3.9E-14	3.5
18 Zone 3 (Aug7,8, 1996)	1.55	2.3E-13	18-Zone 3 (Jan21-07)	1.55	2.7E-13	1.2
Borehole 19 (5/31-04)	4.88	1.6E-13	19 (21Jan-02)	4.88	3.3E-13	2.0

To further investigate the connectivity of flow paths from the heater borehole 1 to the two hydrology boreholes 16 and 18, post-cooling air-injection tests were performed in consecutive zones (intervals isolated by straddle packers) in borehole 1. Table 2.1-6 shows a comparison of the pre-test and post-test air-permeability measurements. Note that the heater occupies the borehole length from 2 m to 7 m from the collar, and for pre-test characterization, two packed-off zones were tested, 1.73 m and 2.70 m from the bottom of the borehole (at ~ 7 m from the collar). In the post-cooling characterization, pressure data from injection into borehole 1 revealed that Zone 5, a 0.59-m section centered at 5.36 m from the collar, was the most permeable. This is consistent with observations from the pre-heat characterization of the SHT test block, which indicated the presence of a high permeability fracture zone intersecting heater hole 1 somewhere beyond y=5.0 m. That conclusion was drawn mainly from the interference pressure responses to injection in borehole 11, which suggest that the fracture zones is intersected by boreholes 1, 7, 11, and 12. It was gratifying that a detailed post-cooling testing of borehole 1 confirmed the location of its intersection with that hypothesized fracture. The post-cooling results also afford an opportunity to investigate further the conclusion from the pre-heat permeability measurements that this fracture zone provides the large-permeability pathway between several boreholes: 1, 7, 11, 12 (Birkholzer and Tsang, 1996 p. 7).

To investigate this connectivity issue, we examined the pressure response in the monitoring zones during air injection in the six consecutive zones in borehole 1. Table 2.1-7 shows the cross-hole steady-state pressure response to the constant flux injection in isolated sections of borehole 1. The steady-state pressure change in the monitoring zones – borehole 7, and Zone 3 of boreholes 16 and 18 – are expressed

as a fraction of the pressure response in the injection zone of borehole 1. The magnitude of the response in borehole 7 clearly identifies the preferred pneumatic connection to be between borehole 1- Zone 5 and borehole 7, thus confirming the pre-test assumption of the presence and location of the large permeability fracture zone.

Table 2.1-6 Comparison of pre-heat and post-cooling air permeability measurements for borehole 1.

Pre-test air permeability (assume T_f=24.6°C)			**Post-test air permeability (assume T_f=30.6°C)**			
Borehole injection zone and datafiles ID	**L (m)**	**Permeability k(m^2)**	**Borehole injection zone and datafiles ID**	**L (m)**	**Permeability k(m^2)**	**Zone center wrt collar (m)**
			1-Zone 1 (Jan21-08)	0.59	1.5E-13	2.92
			1-Zone 2 (Jan21-09)	0.59	6.8E-13	3.53
Borehole 1 (5/24-03)	1.73	1.5E-13	1-Zone 3 (Jan21-10)	0.59	1.0E-12	4.14
Borehole 1 (5/28-08)	1.73	1.5E-13	1-Zone 4 (Jan21-11)	0.59	1.0E-12	4.75
Borehole 1 (5/30-14)	2.70	1.8E-13	1-Zone 5 (Jan21-13)	0.59	5.2E-12	5.36
			1-Zone 6 (Jan21-12)	1.34	1.4E-12	6.33

2.1.3.2 Gas Tracer Tests

Following the cooling phase of the Single Heater Test, gas tracer tests were conducted between borehole 1, the heater hole, and boreholes 16 and 18. The purpose of the tracer tests was to gain a better understanding on the hydrologic conditions that permitted rapid transport from the heated region into borehole 16. The zones behind the 4th packer (referred to as Zone 3 in previous sections) in boreholes 16 and 18 were chosen as the tracer withdrawal interval, and borehole 1 was chosen as the tracer injection borehole. A schematic drawing of the equipment used for conducting the tracer tests is shown in Figure 2.1-8.

Based on the results of the post-cooling air-permeability tests, two intervals in borehole 1 were selected for gas injections. The first interval extended from 3.83 m to 4.42 m (denoted as 1-Zone 3 in Tables 2.1-4, 2.1-6 and 2.1-7) from the collar of the borehole, produced a strong response in Zone 3 of borehole 16, and a much weaker response in Zone 3 of borehole 18. The second interval extended from between 5.05 m to 5.64 m (denoted as 1-Zone 5 in Tables 2.1-4, 2.1-6 and 2.1-7) from the collar of the borehole produced a stronger response in Zone 3 of borehole 18 than in Zone 3 of borehole 16. Four other intervals in borehole 1 were tested (see Table 2.1-7), but because of weaker cross-hole responses were not selected for conducting tracer testing. Figure 2.1-9 shows the pressure response in sensors 16-4 and 18-4 in response to air injection in the six different intervals isolated of borehole 1. It is clear that the strongest cross-hole response is between Zone 3 of borehole 1, and 16-4, and secondly from Zone 5 of borehole 1, to 18-4. Very weak cross-hole responses are obtained from injection in any other zones.

Table 2.1-7 Ratio of pressure increases in monitoring boreholes 7 and Zone 3 of boreholes 16 and 18 to that in the six injection zones in borehole 1.

	1-Zone1*	1-Zone2	1-Zone3	1-Zone4	1-Zone5	1-Zone6
ΔP for injection in Borehole 1	1.62	3.48	2.3	2.36	0.46	0.97
ΔP(Borehole 7)/ΔP(injection in 1)	6.79E-03	8.62E-04	1.74E-02	1.23E-02	3.70E-02	2.16E-02
ΔP(16-Zone 3)/ΔP(injection in 1)	1.54E-03	1.32E-02	3.54E-01	7.63E-02	1.02E-01	1.75E-02
ΔP(18-Zone 3)/ΔP(injection in 1)	1.54E-03	8.19E-03	2.39E-02	2.12E-02	2.35E-01	2.89E-02

* Injection flowrate is 1 SLPM for Zone 1, 10 SLPM for Zones 2 through 6.

Several factors complicate the analysis of the tracer data. First, the perpendicular layout between borehole 1 and boreholes 16 and 18 (Figure 2.1-6), which significantly complicates transport geometry, made the test results less amenable to more detailed analysis. Analyses such as the effective porosity calculations that were performed on Drift Scale Test gas tracer data (Freifeld, 1998, p. 2-8) were not applied to the Single Heater Test tracer data. Second, the use of SF_6 as a gas tracer during air-permeability testing in pre-heat characterization had elevated the background concentration of SF_6 in the SHT area. Due to elevated background SF_6 concentration, a determination of the mean transport time t_{50}, at which 50% of total tracer mass injected was recovered, was problematic, and, therefore, was not attempted. Since the purpose of the tracer testing was to gain an understanding of the rapid flux of water (condensate) into the back of borehole 16, as opposed to borehole 18, which saw no influx of condensate, it was determined that we would focus on the first arrival of tracer and only qualitatively examine the rate at which cumulative mass recovery occurred.

The results of five gas tracer tests are shown in Table 2.1-8. Tracer transport from Zone 3 of borehole 1-to Zone 3 of borehole 16 was extremely rapid, with 100% tracer recovery occurring within 30 minutes from injection. First arrival of tracer to Zone 3 of borehole 18 took more than twice as long and 100% tracer recovery took approximately 15 hours. The differences in the transport times and recovery efficiencies suggests that the path between Zone 3 of borehole 18 and borehole 1 is much more tortuous and indirect than the path between Zone 3 of borehole 16 and borehole 1. The air-permeability tests, which indicate high permeability between the 3.83 m to 4.42 m interval in borehole 1 and Zone 3 of borehole 16 support the hypothesis that there exists a direct fracture connection between borehole 1 and Zone 3 of borehole 16, behind the 4th packer. This high permeability feature does not exist in Zone 3 of borehole 18, even though single-hole permeability analysis (see Tables 2.1-4) shows that Zone 3 of borehole 18 has a higher air-permeability than Zone 3 of borehole 16. The orientation of fractures and the location of the fractures' intersection with the borehole may also lead to a condition in borehole 18, in which any flux of water moving through the packed off interval does not lead to an accumulation of condensate. The complexity of the system precludes the detailed description of the system behavior, and serves to highlight the difficulty in monitoring transport in heterogeneous fractured rock.

Table 2.1-8 Gas tracer test results. Only a qualitative analysis was performed on the cumulative tracer mass recovery data, due to high background concentrations of tracer.

Tracer Injection (borehole 1, location w.r.t collar)	Withdrawal Location borehole # - Zone	First Arrival Time	Mass Recovery (qualitative analysis)
3.93m – 4.42m	16-Zone 3	3 minutes	100% within 30 minutes
3.93m – 4.42m	16-Zone 3	3 minutes	100% within 30 minutes
3.93m – 4.42m	18-Zone 3	7 minutes	100% within 15 hours
5.05m – 5.64m	16-Zone 3	12 minutes	50% within 1 hour
5.05m – 5.64m	18-Zone 3	8 minutes	No analysis made

2.2 Passive Monitoring Data in Hydrology Holes 16 and 18

As discussed earlier in Section 2.1.1.2 and illustrated in Figure 2.1-3, borehole 16 and borehole 18 each contains four pneumatically inflated packers, labeled as P_1, P_2, P_3, and P_4. Relative humidity, temperature, and pressure sensors are located just below (deeper in the borehole) the packer, and are assigned the same numeric identifier as the packer immediately above them The eight instrumented intervals are referred to by borehole number followed by the instrument interval number, i.e., 18-3 is the third instrument cluster from the collar in borehole 18. Temperature, relative humidity, and gauge pressure are monitored continuously, at hourly intervals, for the duration of the SHT. Figures 2.2-1 through 2.2-4 display the temperature, relative humidity, and pressure measurements from August 1996 through December 1997.

2.2.1 Temperature Measurements

Temperature monitoring data are shown in Figure 2.2-1. Because of their relative distance from the heater, temperature rise registered in sensors in boreholes 16 and 18 are modest. The highest temperature attained is about 52°C in sensor 18-4. Temperature data for 16-4 are not represented in Figure 2.2-1 because the sensor failed to function normally after November 8, 1996 (Freifeld and Tsang, 1997b, p.2). As expected, the sensors located closest to the heater Hole 1 show the quickest response to heater turn-on and turn-off. Temperatures began declining in 18-4 within a few days from the heater turn-off (May 28, 1997), but it took several weeks before cooling become apparent in the more distant sensors (16-1 and 18-1). At the termination of the SHT in January 1998, the temperature in the sensors closest to the borehole collar had fallen below 30°C, but were still a few degrees above the pre-test values. The match between temperature data and numerical modeling will be discussed in Chapter 3.

2.2.2 Relative Humidity Measurements

Relative humidity measurements for the duration of the SHT are shown in Figure 2.2-2. These measurements have an accuracy of ± 2% below 90% RH and an accuracy of ± 3% above that point. The relative humidity sensor is effective in monitoring very dry rock mass with strong capillary suction, but is not sensitive to "normal" liquid saturation – that is, unless the rock mass is very dry, the relative humidity sensor is expected to register 100% (Freifeld and Tsang, 1997b, pp. 6-7). Laboratory measurements (Section 2.5 below) show that the pre-test matrix liquid saturation at the SHT is of the order of 90%, it is therefore our expectation that all the sensors in Holes 16 and 18 should register effectively 100 (±3) % before the initiation of heating. Moreover, since even the sensors closest to the heater (16-4 and 18-4) are about 3 meters from the heat source and lie outside the drying zone developed after one year of heating, based on thermo-hydrological predictive simulations (Birkholzer and Tsang, 1996, p. A21, p. A36), the readings of humidity sensors are expected to continue registering 100% during the heating phase of the SHT.

The relative humidity monitoring data in Figure 2.2-2 show that by the first week of September, 1996, the vapor phase in the monitoring zones in boreholes 16 and 18 have come into equilibrium with the liquid in the rock mass, and the readings in 16-4 and 18-4 stabilize to 100% (and for 18-4, remain at 100% for the duration of the test). Sensor 16-4 ceased to function properly beginning November 8, 1997, possibly because of being submerged in condensate in borehole 16 (Freifeld and Tsang, 1997b, p.2). While we anticipated data in all the humidity sensors to be similar to those of 18-4, in fact, the humidity measurements of the three sensors that are closest to the collar for each borehole remain below 96% for the duration of the SHT. These observed low values of relative humidity are attributed to drying from the ventilation in the thermomechanical Alcove Extension. At the locations of the first three humidity sensors, boreholes 16 and 18 appear to be in communication with the drift through the fractures in the rock mass.

The small discontinuities in the humidity readings are due to perturbation from injection of dry air during active air permeability testing, which took place on November 25, 1996; February 4, 5 1997; March 8, 1997; May 22, 23 1997; October 8, 1998; and November 18, 19 1997. The large dip in sensor 18-2 from March through July of 1997 indicate drying of the zone, and subsequent recovery to its former value, the exact cause for the drying is not understood.

2.2.3 Pressure Measurements

Gauge pressure monitoring data are presented in Figure 2.2-3. It is expected that no significant pressure buildup would occur due to heating, because all monitoring zones in boreholes 16 and 18 are too far removed from the boiling zone near the heater, and because the heater borehole is in direct communication with the Thermomechanical Alcove. All pressure transients, except the ones from 16-4, show no significant pressure variation from ambient. The pressure response in 16-4 has been replotted in Figure 2.2-4. The pressure buildup shown in Figure 2.2-4 corresponds to the buildup of condensate in

Zone 3 of borehole 16. The four pressure drop events (prior to the termination of heat) correspond to the four times that water was drained from Zone 3; i.e., on November 25, 1996; February 4, 1997; February 27, 1997; and May 22, 1997. Note that within one week from August 26, 1996 (the heater turn-on date), the pressure of condensate resulted in an increase of the pressure in Zone 3. The very rapid transport of vapor to Zone 3 is confirmed by the post-cooling tracer test results described earlier (Section 2.1.3.2).

An explanation for water accumulation in Zone 3 of borehole 16 is as follows: vapor from the boiling of water near the heater flows outward and condenses around Zone 3 of borehole 16. The liquid saturation in the rock mass reaches unity in some areas adjacent to the borehole, thus overcoming the capillary barrier at the borehole wall and enabling water to drip freely into the borehole. Within days from the heater turn-off date (May 28, 1998), the pressure in Zone 3 of borehole 16 started to decrease. This indicated that the condensate was being imbibed by the rock formation. This imbibition process may very well have occurred during heating, but could have been masked by the continuous supply of vapor transported through fractures from the heater hole to Zone 3.

2.2.4 Summary

Many of the observed responses of the passive monitoring data of temperature, relative humidity, and pressure are understood and predictable. Observations such as the drying of rock formation adjacent to the drifts and the seepage of condensate into borehole 16, all add to our knowledge of the important role of fractures in the performance of the SHT. In the former, drying is caused by communication of the rock formation with ventilated alcoves and drifts through fracture network. In the latter, a discrete fast path for vapor transport accounts for the fact that seepage of condensate occur in borehole 16, and not in borehole 18.

2.3 Cross-Hole Radar Tomography

2.3.1 Overview

This section presents a discussion of the borehole radar tomography experiment conducted within the Thermomechanical Alcove (TMA) centered around the single heater test. The intent of the experiment was to perform high resolution, cross-hole radar data to estimate the spatial distribution of the moisture content within the rock mass. The application of heat over time to the subsurface rock mass was expected to progressively drive moisture away from the heater. The extreme sensitivity of radar measurements to even very slight changes in water saturation suggested the suitability of this data collection methodology. Borehole radar tomography data are useful for delineating the geometry of the condensation front and for studying moisture migration that occurs as a result of the dramatic increase in rock temperature during

the heater test. The effect of temperature on radar measurements and its impact on the estimation of moisture content estimation is included in the processing methodology.

The borehole radar field effort in the ESF for FY96-97 consisted of data collection exclusively within the TMA. The holes available for survey consisted of those neutron log access holes left open during the entire duration of the single heater test. These holes are numbered as follows: boreholes 22 and 23 - holes collared on the Observation Drift and boreholes 15 and 17 – holes collared on the Thermochemical Alcove Extension wall. The holes themselves are drilled several degrees off horizontally into the drift, cased with a Teflon liner and grouted into place. Each pair of holes defines a two-dimensional plane perpendicular to the heater assembly and trending towards this assembly (Figure 2.3-1, where the collar of the heater hole is at (0., 0., and 0)). In the case of boreholes 15 and 17, this plane actually extends across the strike of the heater. This is not the case with boreholes 22 and 23 which stop just short of this boundary. Deviation records specifying azimuth angle and declination for locations along the length of each hole (derived from ESF survey of as-built boreholes in the Thermomechanical Test Block) were used for the data processing.

2.3.2 Acquisition

A pulseEKKO 100 radar system was used for data acquisition at the TMA. A full description of the instrumentation and acquisition is given in Peterson and Williams (1997). The borehole radar technique utilized at the TMA during the single heater experiment was a cross-hole radar profiling method in which the transmitter and receiver antennas were located in separate boreholes and data were collected with the antennas at various vertical offsets. The data collection was performed using two acquisition modes. The first was a Zero Offset Profile (ZOP) in which the transmitter and receiver antennas were positioned within the boreholes at equal depths such that there was no vertical offset. The second was a Multiple Offset Profile (MOP) in which the receiving antenna remained at a fixed depth while the transmitter antenna was moved incrementally in the second borehole. Each multiple offset profile constitutes a "receiver gather", and a series of these gathers are used to construct tomographic images.

Over the course of the heater experiment, the radar system was operated by using identical acquisition parameters for each of the five field surveys; one before the heater was turned on, and four during the heater test. No adjustments, filters or gains are applied to the stored raw data. Therefore, data acquisition and hence data repeatability is the same regardless of who operates the system and when - so long as the antenna configuration is the same. Data repeatability is tantamount to successful tomographic differencing and interpretation. Small deviations in experimental methodology at such close spacing can result in large discrepancies in data processing.

The most important information to be obtained from radar data is the travel times, which are inverted for the velocity structure between boreholes. It is important to know the precise time when the transmitter fires (known as time-zero), to determine accurate travel times between the transmitter and receiver

antennas. Direct air wave measurements (the signal from transmitter antenna to receiver antenna in air) with the antennas held together in air and at the borehole collars in air were taken to help determine the zero-time. After these measurements were taken, the antennas were immediately moved into the boreholes and a ZOP dataset was collected, concluding with another set of measurements in air at the borehole collars and together in air. Following this procedure, the MOP datasets were then collected with the locations determined before the start of the survey. In the case of the TMA surveys, the transmitter and receiver intervals were every 0.25 meters. As in all MOP gathers, the receiver antenna remained at a fixed location (1m, 1.25m, 1.5m, etc.) while the transmitter antenna occupied each of its possible locations down the borehole (e.g., 0-19m at 0.25m spacing). Each of the necessary raypaths was collected and recorded for the subsequent tomographic processing. Following MOP acquisition, a final ZOP dataset is collected as described above. This is done in an attempt to estimate the time-zero drift that unavoidably occurs.

Five separate surveys were performed using the two well pairs 22 to 23 and 15 to 17. The first data set was acquired on August 22, 1996 before the heater was turned on (time = t_0). Three data sets were acquired during the heater test; on January 15, 1997, 5 months after heating began (t_2); on March 12, 1997, 7 months after heating began (t_3); and on May 29, 1997, the day after the heater was turned off (t_4). Another data set was acquired on January 7, 1998, after the termination of the cooling phase of SHT (t_5).

2.3.3 Processing

2.3.3.1 Determining the zero time

The zero time is defined as that instant the source emits a signal. The determination of this time is essential for the inversion of travel times for velocity and any differencing of times between data sets. The determination of the zero time proved far more difficult than we had anticipated. We had hoped that taking a measurement with the source and receiver antennas together before each surveyed well pair would give an adequate value for the zero time. It was not anticipated that the zero time would shift after some time, or when the battery was recharged, or for various other reasons. Therefore, a different methodology had to be found to determine the zero time accurately. The zero time, as measured with the antennae together, was subtracted from the ZOP data to find the absolute time for this data. An equivalent ZOP profile was extracted from the MOP data set that could be compared to the ZOP profile acquired from the field. The zero time was subtracted from this pseudo-ZOP profile and if the travel times match, then this is taken to be the zero time. When the times were offset, the average offset time was calculated and the MOP zero times were corrected for this value. This proved to provide an accurate measure of zero time throughout the surveys.

2.3.3.2 Well Pair 22-23

Boreholes 22 and 23 are 0.656 meters apart at their collars at the alcove wall and deviate to approximately 1.4 meters at their endpoints while remaining in the same plane. Accurate coordinates

must be calculated for each source and receiver point before any processing can begin. This is done using the surveyed borehole coordinates. The source and receiver coordinates, which are at 0.25 meter intervals, must be determined by interpolating between the given coordinates. The casing sticks out of the wall about 0.3 meters for borehole 22 and 0.60 meters for borehole 23. Since boreholes 22 and 23 are virtually in-plane, the x and z coordinates can be used as coordinates for the 2-D tomographic inversions.

Figure 2.3-2 shows three typical receiver gathers for the 22-23 well pair. The time scale along each trace is in nanoseconds, and each gather contains one receiver depth and many source depths. The frequency content of a trace at near zero offset shows the peak energy occurring at 100 MHz with a slow roll-off for higher and lower frequencies (Figure 2.3-3). The travel times were picked for the three surveys; t_0, t_1, and t_2. Since this well pair has only three surveys and the results were consistent with the 15-17 well pair, the results will not be shown.

2.3.3.3 Well Pair 15-17

Boreholes 15 and 17 are separated by 0.785 meters at their collars at the alcove wall and deviate to approximately 4.0 meters at their endpoints while remaining in the same plane. The source and receiver coordinates are determined from the deviation coordinates as in the 22-23 well pair. The casing stick-up was 0.50 meters for both borehole 15 and borehole 17 so the zero point was more easily and accurately determined for this well pair.

Figure 2.3-4 shows a typical receiver gather for the 15-17 well pair. The variation in amplitude as a function of source/receiver antenna separation distances indicates that the threshold distance for using radar in this material is about 4.5 meters. This is more easily observed in the plot of the log of the root mean square of the amplitude as determined by the first 20 samples after the first arrival time (Figure 2.3-5). Given our system and acquisition parameters, the lower limit of detection was a log amplitude of 5.9 which was detected at a source/receiver separation distance of 4.5 meters. The spectrum of a typical trace shows that the peak amplitude remains at about 100 MHz, so no loss in frequency content of the signal is observed (Figure 2.3-6).

Despite the low signal amplitudes a sufficient number of travel times could be picked to perform a velocity inversion for each of the five surveys. An Algebraic Reconstruction Technique (ART), as described in Peterson (1986), was used for the inversion. All travel time inversion techniques invert for the slowness, which is equal to 1/v, where v is velocity. A 4.25 x 8.5 meter field in the plane of boreholes 15 and 17 was divided into a grid of 16x32 pixels producing a pixel dimension of 0.265x0.265 meters, which approximately corresponds to the station spacing of 0.25 meters. The multiplicity of source and receivers resulted in a dense sampling of the interwell area; 400 arrival times were available for each tomographic inversion.

The inverted times produce the velocity fields surveys shown in Figures 2.3-7a-e. The velocity field changes significantly between each survey, with the greatest changes occurring between the t_0 and t_1 surveys (Figures 2.3-7a and 2.3-7b). There are some common features such as a diagonal high velocity zone, a high velocity zone around the heater, and a low velocity zone a meter away from the heater. The differences can be highlighted by subtracting the velocity values between two tomograms. The baseline velocity tomogram is subtracted from the four post-heating velocity tomograms producing four velocity difference tomograms. The difference tomograms are shown in Figures 2.3-8a-d. The average absolute velocity value is about 0.1 m/ns, so a difference value of 0.01 m/ns is about a 10% change in velocity. The tomograms all show significant velocity increases and decreases. The increases in velocity occur in two zones: one around the heater (black dot at (0,0)), the other near the alcove wall (top of figures). There is one decrease in velocity and it occurs near the center of the tomogram, about one meter toward the alcove wall from the heater. Another decrease in velocity may occur one meter on the other side of the heater, but the resolution at this area of the tomogram is quite poor.

2.3.4 Interpretation

For low electrical conductivity environments and at the frequencies used for GPR imaging, the relationship between electromagnetic wave velocity and dielectric constant is $v = c/\sqrt{\kappa}$, where v is velocity, c is the velocity of light and κ is dielectric constant. Temperature and saturation are two parameters which affect the dielectric constant and thus the velocity change in this experiment. The dielectric constant of dry rocks is 3 to 6 and of water is 80; the dielectric constant of a material increases and thus the velocity decreases with increasing saturation. If the temperature dependence of dielectric constant was ignored, then the difference tomograms (Figure 2.3-8) would suggest that saturation decreases near the heater and increases about a meter away, consistent with the thermal hydrological condition of a drying zone around the heater, and a condensation zone commencing at about one meter from the heater. However, temperature dependence of the dielectric constant is not negligible and must be compensated for in the estimation of saturation from dielectric constant estimates.

Saturation estimates can be obtained from ground penetrating radar data using two different methods. The first method involves obtaining relationships between temperature, saturation and dielectric constant under laboratory conditions. These relationships can then be used together with field measurements of dielectric constants from radar and field measurements of temperature to predict the interwellbore saturation. An alternative method of relating the dielectric constant to saturation and temperature is to determine a relationship between dielectric constants obtained at the wellbore from cross-hole radar, borehole measurements of saturation obtained from neutron logs, and borehole temperature measurements. This method will also produce a dielectric constant-saturation-temperature relationship that can be used in a predictive manner to estimate interwellbore saturation. A drawback of this method is that the inverted radar velocities are less reliable near the wellbore and the neutron logs must be of good quality. Both methods require the temperature field between boreholes. The temperature can be interpolated from the values from the temperature probes down the boreholes. A relationship between

temperature and distance from the heater is estimated using regression analysis on all temperature measurements in the plane of the two well pairs (Figure 2.3-9). A fifth order polynomial equation was used to fit these data values and to then estimate the temperature at each pixel as a function of distance to the heater.

Linear regression and neural network methods were used with both the borehole and laboratory data to develop relationships between dielectric constant, temperature, frequency and saturation. Linear regression techniques for relating geophysical and hydrological measurements have been used extensively to aid reservoir studies; these techniques assume a linear relationship between some parameterization of the geophysical and hydrological variables. Neural networks are being used to solve a variety of scientific and engineering problems concerned with unknown and varied functional relationships among measured variables. Neural networks attempt to emulate the brain process by adopting simple rules that govern interactions between input and output information; this technique is particularly advantageous when searching for nonlinear relationships. Typical neural network systems have an input layer, where data are presented to the network, and an output layer, which holds the response of the network to a given input, and at least one hidden layer, which connects the input layer to the output layer (Figure 2.3-10). Each layer is fully connected to the succeeding layer with corresponding weights. The values of the weights represent the current state of knowledge of the network, and the weights are adjusted during training to improve the network performances. The number of hidden layers and nodes in each layer are chosen by the user. Training is complete when convergence has been achieved, or when the mean squared error at the output is less than a designated tolerable error. The recent success of neural networks is in part due to advances in computer technology which have made it possible to bring together a large number of nodes and massive connections of simple neurons. However, developing a proper neural network model that is an accurate representation of the process of interest is still a combination of art, science and technology.

2.3.4.1 Saturation dependence of dielectric constant based on laboratory measurements

Laboratory measurements of dielectric constant as a function of saturation and temperature were obtained from Topopah Springs Tuff cores and made available to us for analysis by Jeff Roberts (Roberts and Lin, 1997). An example of similar laboratory measurements using a 1 MHz signal is shown in Figure 2.3-11 where it is observed that dielectric constant increases with both temperature and saturation. Regression analysis was used to obtain a relationship between the logarithm of saturation and the explanatory variables of temperature and dielectric constant; this relationship was linear and valid for saturations greater than 15%. Our original intent was to use dielectric constant values obtained from radar velocity data together with field temperature measurements, both collected prior to and during the heater experiment, to predict saturation states at different times. The difference in these two saturation states would then delineate the change in saturation due to the influence of the heater. However, upon application, we observed that the range of dielectric constant measurements obtained from the cross-hole radar (using a frequency of 100 MHz) differed dramatically from those collected under laboratory

conditions (with frequency ranging from 400 Hz to 1 MHz). The difference is attributed to the dispersive nature of the dielectric constant, or to the fact that the dielectric constant measurement is a function of measurement frequency.

The effect of frequency on the results can be seen in Figure 2.3-12 where a large variation of the affects of saturation on dielectric constant due to frequency of the signal is observed. The saturation vs. dielectric constant curves level off at dielectric constants above 25 in Figure 2.3-11. The dielectric constants determined from the velocity inversions at the TMA site are between 5 and 12, which are similar in range to dielectric constants estimated by Daily and Ramirez (1989) using cross-hole radar techniques in the Topapah Springs Tuff. This suggests that to adequately determine a relationship between temperature, saturation and dielectric constant using the above methodology, laboratory measurements must be made at a frequency similar to the field measurements (100 MHz). At this time these laboratory measurements have not been made. Therefore, frequency must be used as one of the variables when determining a relationship to estimate saturation. The saturations may be estimated by obtaining a relationship between the logarithm of saturation (S) and the explanatory variables of temperature (T), dielectric constant (κ), and frequency (f). Linear regression was used to obtain the following relationship:

$$\ln(S) = 0.1083\ln(\kappa) - 0.4523\ln(T) + 0.112\ln(\kappa f) \qquad (2.3\text{-}1)$$

with a correlation coefficient of 0.88. The fit is shown in Figure 2.3-13. Using this relationship, the saturation field at each survey time was estimated by using a frequency of 100 MHz in Equation (1) (Figure 2.3-14). The saturation values indicate an increase in drying near the heater with time while the heater was on, with the saturation returning toward baseline after the heater was turned off. There is also a small decrease in saturation near the drift wall (located at bottom of each tomogram) which may be due to effects from ventilation of the drifts. A very small increase in saturation occurs a meter or two away from the heater.

The relationship between the saturation and dielectric constant and temperature can also be obtained using a neural network approach Boadu (1997). The input data to the neural network consisted of laboratory values of dielectric constant and temperature, and the output data consist of laboratory saturation measurements. Hence, for this application, there are only two input variables to the neural net system (Figure 2.3-10). Because no laboratory measurements were made at the frequency of the cross-hole radar data (100 MHz), and because neural networks have a difficult time interpolating outside of the training range, only the highest frequency laboratory data of 1 MHz was used to train the neural network. It is assumed that the change in dielectric constant values due to the difference in frequencies between the field radar and laboratory measurements (1 MHz to 100 MHz) will be a linear shift. The tomographic radar data were scaled prior to saturation estimation so that the dielectric constant values would fall in the range of the 1 MHz laboratory data (see Figure 2.3-11); this was accomplished by multiplying the dielectric constants obtained from the field tomographic radar data by 2.3. Also, the laboratory maximum

temperature value of 95 °C was used when the field temperatures exceeded this value. The observed vs. predicted values obtained from the neural network model are shown in Figure 2.3-15. The change in saturation predicted using the neural network model (Figure 2.3-16) is quite similar to the results from linear regression (Figure 2.3-14). Because of the scaling that was performed to compensate for the frequency discrepancies, the absolute values shown in Figure 2.3-16 may not be precise, but the relative position between areas of drying and wetting should be reasonable.

2.3.4.2 Comparison to Borehole Neutron Probe Measurements

An alternative method to using laboratory data is to compare the change in dielectric constant obtained from cross-hole radar data at the wellbore to the change in moisture content and temperature measurements obtained along the borehole using neutron and temperature probes, respectively. The non-linearity revealed by the neutron borehole measurements (Figure 2.3-17) suggested that these data are good candidates for the neural network, but not the linear regression. However, for this technique to work, it must be assumed that the neutron data is most sensitive to a change in water content. Neutron logs were acquired every two to four weeks at 0.1 meter intervals down each well. The neutron data were calibrated to give the difference in moisture content from the baseline measurement taken before the heat initiation. An average moisture content was calculated using the value plus the two values adjacent in time. This value was again averaged using the value plus the two adjacent values in space. Since the neutron data is in change in water content from one survey time to another, change in dielectric constant and change in temperature values must also be used. The average change in dielectric constant associated with this neutron value was calculated by averaging all dielectric constant values within a radius of 0.4 meters of the neutron log point. Such a large radius was taken since the size of each dielectric pixel is 0.25 x 0.25 and the center of the pixel must be within the chosen radius of the neutron acquisition point to be included. As in the laboratory data neural net analysis, the temperature data are limited by the maximum borehole temperatures; much higher temperatures exist in the interior where there is no neutron log data. Therefore, the results would not be valid in this region of higher temperatures, so a maximum change in temperature value was assigned in this region.

These averaged field dielectric constant differences and change in temperature values were used as input to the neural network model (Figure 2.3-10), and the change in moisture content was used as the desired output. The observed vs. predicted values as calculated by the neural network model is shown in Figure 2.3-18. The model obtained from the neural network was used together with the tomographic dielectric constant field and interwellbore temperature field to predict the change in moisture content for three time intervals (borehole neutron data were not collected at time=t_4) as shown in Figure 2.3-19. The change in water content predicted by this model appear to correlate more with the temperature field than with the models estimated by the laboratory data (Figures 2.3-14 and 2.3-16). This may indicate that the neutron probe may be more sensitive to change in temperature than change in water content.

2.3.4.2 Discussion of Saturation Estimates

Saturation changes were estimated from dielectric constant tomograms as converted from the velocity tomograms using various methods. In order to compare the estimates obtained using linear regression and neural network approaches on both laboratory and borehole data, the correlation between the different estimated change in saturation or moisture content at the time interval t_1-t_0 was obtained:

	Laboratory Data Regression	Laboratory Data Neural Net	Borehole Data Neural Net
Laboratory Data Regression	1.00	0.86	0.54
Laboratory Data Neural Net	0.86	1.00	0.52
Borehole Data Neural Net	0.54	0.52	1.00

This table indicates that the neural network and linear methods produce similar results if the data used to develop the petrophysical relationship are the same (i.e., laboratory data), and that correlation decreases when different data sets (borehole data) are used to develop the petrophysical model. In spite of the differences suggested by the correlation table for the absolute values of the change in saturation or moisture content, the estimated fields shown by Figures 2.3-14, 2.3-16 and 2.3-19 all reveal similar patterns in the condensation front that moves away from the heater upon heat application. Comparison of these estimates with those obtained using petrophysical relationships developed with laboratory data suggests that the borehole data are more influenced by the temperature than the laboratory measurements. Two-dimensional time-lapse high resolution information about the saturation patterns such as that given by these figures is necessary for understanding and predicting the influence of the stored radioactive waste in the Topopah Spring Tuff; this information is unattainable with conventional one-dimensional borehole measurement techniques.

2.3.5 Conclusion

The radar velocity tomograms taken before heating and after heating show significant differences. These tomograms and the differenced tomograms were quite effective in mapping changes in moisture content due to the heating. Saturation changes were estimated from dielectric constant tomograms as converted from the velocity tomograms using various methods (Figures 2.3-14, 2.3-16, and 2.3-19). The saturation changes indicate a region of extreme drying to about a radius of one meter from the heater, where the saturation drops to about 20 to 40 percent. Beyond this region of drying is a region of no saturation change or an increase in wetting. It is difficult to detect small changes in saturation in highly saturated material using radar. This region is about 2 meters thick. It is not symmetric; possibly due to a zone of anomalous velocities (Figure 2.3-7a). There is also another region of drying near the drift walls, most likely due to ventilation in the drift.

2.4 Infrared Imaging

During the single heater test, the noninsulated surfaces of the SHT block were periodically examined using an infrared (IR) camera. The purpose of this study was to assess whether the temperature distribution observed on the block surface can be related to any physical features in the block, and perhaps to discover features, including surface outlets for pathways of fluids or gases that undergo thermally induced changes. The results of the IR mapping study have been discussed in quarterly progress reports (Cook and Wang, 1997a, 1997b, 1997c; Cook, 1997; and Cook, 1998). A sample of the results reported previously (Cook, 1998) shall be presented below.

Because the insulated material on all three exposed surface of the SHT block extends almost to the top of the drift walls, surfaces available for IR imaging were several meters removed from the collar of the heater. That was sufficiently removed from the heat source to limit the maximum temperature rise to only about 10° C above ambient, in the region above the heater collar. Otherwise, the IR data have revealed no discernible discrete thermal features of the rock.

2.4.1 Data and Discussion

The IR camera (Inframetrics PM 200 Thermacam SN 8954) was used to take pictures of the region above the heater collar, along the right side of the heater block and at the end of the extension drift (Figure 2.4-1). The same areas were mapped at approximately three-month intervals, starting in August 1996 before the onset of heating. Frames in a given data set were taken from approximately the same distance and perpendicular to the surface of interest. Each frame covers an area approximately 1 meter square. We present in the following two-dimensional gray scale IR montages and line plots to illustrate the evolution of IR data over time.

Montages from the area above the heater are shown on Figures 2.4-2 through 2.4-4. The image from August 1996 is included in Figure 2.4-2 as baseline data. Figure 2.4-3 shows the montages from February and July of 1997, and the image for December 1997 is shown in Figure 2.4-4. All montages except that of December 1997 have the same temperature scale. The scale for the December 1997 data was adjusted to maintain contrast at the lower temperature levels, which followed the conclusion of heating on May 28, 1997. May 1997 data are not shown on the montages due to partial data file corruption (Cook and Wang, 1997c, pp. 2-3); sufficient data, however, were salvaged for line plots. The main features in the montages of Figures 2.4-2 through 2.4-4 are the presence of two warm regions directly above the heater hole collar, which are discernible in the data of December, 1996 (three months after heating), and which become more prominent in February 1997. The temperature distribution of the warm areas had become spatially diffused in July 1997 mapping, i.e., six weeks after termination of heat.

Figure 2.4-5 shows line plots of August, December, February, May and July temperatures obtained from the montages of the SHT front face just above the insulation. Line plots give better quantitative detail

than montages and are able to highlight actual changes in temperature over time better than a montage. The location of data collection corresponds to the red line overlaid across the February image in Figure 2.4-3. Temperature is plotted against distance. The scale of the bottom of the plot represents the distance between the extensometer pins TMA-WX-2 and TMA-WX-1, left to right. This distance is roughly 4 meters, centered on the single heater itself. The magnitude and variation with position of the temperatures on the face are consistent with the heating and cooling schedule of the SHT. The trough in the values in the center of the line plots corresponds to the image of a cable tray that radiates at ambient temperature. The trough is of different widths because the tray is an item not flush with the wall, and its image is subject to parallax changes in the images. The highest temperature seen is in the May 1997 data set just prior to termination of heat, at about 35°C.

Figure 2.4-6 contains line plots of the December 1996, and February, May, July, and December 1997 temperatures taken immediately above the insulation on the right side of the SHT block (see Figure 2.4-1). Here also, the temperature variation and magnitude increase with time while the heating in SHT is in progress. The left side of the plot, which corresponds to the corner, shows lower temperatures than the rest of the plot due to the higher exposed area of the corner section. It is uncertain why there are two temperature peaks along the top of the insulation in the May data. A possible explanation for the first peak on the left could be a heat leak from the insulating blanket.

The plots from July 1997 in Figures 2.4-5 and 2.4-6 both show a temperature decline after six weeks of heater shutoff. In addition, the peaks in the July 1997 data have flattened as the heat redistributes on the rock surface. The data from December 1997 (i.e., six months after cooling), show that the temperatures have decreased to approximately the February 1997 levels, for both the side and front faces of the single heater block.

2.4.3 Summary

The data from the IR camera show that the heat distribution followed the expected pattern, initially emanating from regions closer to the single heater and then dissipated towards the corners of the single heater block. The maximum temperature recorded on the images was about 35 °C on the front face. No discernible discrete thermal features were detected.

2.5 Laboratory Testing: Hydrological Properties

2.5.1 Pre-Heat

Laboratory measurements of saturation, porosity, bulk density, particle density, and gravimetric water content for cores from the SHT area were conducted. These studies constitute a component of the

hydrological characterization study, and aim to determine the amount of pore water available for evaporation and boiling during the heating phase. Core data from both the Drift Scale Test and the Single Heater Test boreholes in the Thermal Test Facility at the Exploratory Studies Facility were reported in a previous project milestone (Wang and Suarez-Rivera, 1997). The information specific to the SHT area shall be summarized here.

2.5.1.1 Methodology

Core samples previously stored in sealed packets were placed in containers with tight-fitting lids and immediately weighed. The samples were subsequently oven-dried at a temperature between 100°C to 110°C, until they reached a constant weight (from several weighing). They were then placed in a desiccator, cooled, and weighed to determine the gravimetric water content. This procedure ensures that the samples are dried at a specified temperature to a constant weight, and that only water is lost.

The samples were then water-saturated in a vacuum chamber, after which they were weighed following the Archimedes method (i.e., immersed in air and water) to determine the weight under conditions of full saturation and the sample bulk volume. Knowledge of the dry-weight, saturated weight and sample bulk volume were used to calculate bulk density, porosity, and particle density.

Table 2.5-1 Pre-heat laboratory measurement of grab samples from wet excavation of the Observation Drift of the Thermal Test Facility

Observation Drift Grab Samples

Sample location	Saturation	Porosity	Bulk Density	Particle Density	Gravimetric Water Content
(m)	(%)	(%)	(g/cc)	(g/cc)	(g/g)
30.0	99.00	8.60	2.26	2.47	0.038
Sub-sample	94.90	8.30	2.27	2.47	0.035
40.0	95.40	9.30	2.27	2.50	0.039
Sub-sample	93.80	10.10	2.24	2.49	0.042
Sub-sample	80.50	10.40	2.24	2.50	0.037

Observation Drift (OD) Grab Sample Summary

	Saturation	Porosity	Bulk Density	Particle Density	Gravimetric Water Content
	(%)	(%)	(g/cc)	(g/cc)	(g/g)
OD average:	**92.72**	**9.34**	**2.26**	**2.49**	**0.038**
standard	7.10	0.91	0.02	0.02	0.003

2.5.1.2 Results

The data from two grab samples from the wet-excavation of the Observation Drift near the SHT block are shown in Table 2.5-1. Five subsamples were tested. One of the subsamples had an 81% saturation, while

the saturation of the other four subsample exceeded 94%. These measurements provide the only site-specific data for the liquid saturation at the time of the initiation of the SHT, and they form the basis of the choice of parameter value (92%) in modeling of the SHT (Chapter 3). In Wang and Surarez-Rivera (1997), liquid saturation for 39 cores from the Drift Scale Test (12 dry-drilled and 27 wet-drilled), and 17 wet-drilled cores from the SHT were reported. The measurements from the cores from boreholes 1, 5, and 6 of the SHT are shown in Table 2.5-2. We note that the liquid saturation is in the 95% range. Wang and Surarez-Rivera (1997, p.6) also reported that the average liquid saturation for the dry-drilled Drift Scale Test samples was 84%, while that for the wet-drilled samples was 93%. They attributed the 9% discrepancy partly to spatial heterogeneity, and partly to the different drilling methods.

Table 2.5-2 Pre-heat laboratory measurement of wet drilled cores from the SHT

Borehole 1, ESF-TMA-H1

Sample location	Saturation	Porosity	Bulk density	Particle density	Gravimetric water content
(m)	(%)	(%)	(g/cc)	(g/cc)	(g/g)
1.0	89.46	10.66	2.25	2.51	0.043
2.5*	88.04	13.30	2.18	2.52	0.054
3.7	93.60	8.87	2.29	2.52	0.036
4.7	97.27	11.83	2.22	2.51	0.051
5.7	93.97	13.83	2.16	2.51	0.061
6.7	96.03	11.89	2.21	2.51	0.052

* contains small voids

Borehole 6, ESF-TMA-OMPBX-1

Sample location	Saturation	Porosity	Bulk density	Particle density	Gravimetric water content
(m)	(%)	(%)	(g/cc)	(g/cc)	(g/g)
0.2	94.82	11.00	2.24	2.51	0.047
2.4	94.75	10.43	2.25	2.51	0.044
4.4	93.58	10.18	2.26	2.51	0.042
7.5*	96.87	23.62	1.96	2.57	0.104
Subcore		20.44	2.02	2.53	
9.3	96.17	11.55	2.22	2.52	0.050
11.3	93.07	9.74	2.27	2.51	0.040

* split along axis during oven drying

Borehole 5, ESF-TMA-MPBX-4

Sample location	Saturation	Porosity	Bulk density	Particle density	Gravimetric water content
(m)	(%)	(%)	(g/cc)	(g/cc)	(g/g)
0.7*	95.85	17.03	2.05	2.48	0.079
2.1*	101.61	9.69	2.25	2.49	0.044
2.6#	102.17	13.33	2.17	2.50	0.063
3.8#	96.74	10.58	2.24	2.50	0.046
Subcore		10.44	2.24	2.50	
5.4	97.65	9.60	2.27	2.51	0.040

* contains open fractures and large vugs.
# received in fragments

SHT Borehole Summary

	Saturation	Porosity	Bulk density	Particle density	Gravimetric water content
	(%)	(%)	(g/cc)	(g/cc)	(g/g)
SHT average:	95.39	12.53	2.20	2.51	0.053
standard deviation	3.56	3.89	0.09	0.02	0.017

2.5.2 Post-Cooling

A number of boreholes were dry-drilled following the termination of the cooling phase of the SHT for post-test characterization. In particular, protected (wrapped and sealed) cores from three dry-drilled boreholes (boreholes 199, 200, 201) were tested for porosity, density, and water content or liquid saturation. The locations of these protected cores were designed to pass through both the anticipated "dry-out" and "condensing" regions developing in the SHT block as a result of the heating. Figure 2.5-1 shows a x-z view of the boreholes and the locations of the protected core samples. Locations of the cores along the borehole are identified by the last two digits of their Sample Management Facility ID, shown in the legend of Figure 2.5-1. The two dashed circles, with radius of 1 m and 3 m respectively from the heater, delineate the anticipated drying zone (approximately within the inner circle), and the wetting region (between the two circles). The radial symmetry does not account for gravity drainage of the condensate, hence borehole 201 was drilled at a steep angle in order to access rock at depth over 3 m below the heater horizon, with the intention that the importance of drainage of condensate via the fractures may be investigated.

While the quantities measured and the methodology of these post-cooling laboratory measurements remain the same as their pre-heat counterparts described in the previous section (2.5.1), the focus here in the post-cooling effort is substantially different. In the pre-heat results, the intent is to estimate an average initial liquid saturation of the matrix cores; in the post-cooling results, the focus ison the change from their initial value, and more importantly, the spatial location of the cores (with respect to the heater) where changes have occurred.

Table 2.5-3 presents the laboratory-determined saturation, porosity, and particle density. Average porosity and particle density values are given at the end of the table. An average value for liquid saturation is not a meaningful parameter in these post-cooling cores because liquid saturation of the cores reflect the thermo-hydrological processes that have taken place in the SHT, and their importance lies in their spatial variability. Rather, Figure 2.5-1 plots the liquid saturation of all cores tested, in their respective locations. We note (from Table 2.5-3) that the porosity of three core samples (local ID H-1, H-22, H-27) is exceptionally high, and is attributed to visible evidence of fractures. In turn, the liquid saturation of these samples would be less reliable, and this should be kept in mind while studying the saturation results in Figure 2.5-1.

Saturation for cores along borehole 201 is relatively uniform. Excluding the two samples with large porosity, liquid saturation for all cores along borehole 201 is within 2% of their average 86%. For the cores along boreholes 199 and 200, we note the following: (a) drying due to heat has occurred near the heater, as evidenced by the lower liquid saturation of cores within the 1-m radius from the heater; (b) the liquid saturations in the anticipated "condensing" zone between two circles are generally lower than those values in borehole 201; and (c) the liquid saturation seems to be higher below the heater horizon than above the heater horizon. These observations are consistent with a scenario stipulating that condensate is not held in the matrix (thus elevating its liquid saturation) but is drained through fractures

of hierarchical scales. Drainage through the microscopic fractures account for the slightly drier cores above the heater horizon in borehole 199 than below the heater horizon in borehole 200. Drainage through larger fractures extending a few meters account for the overall wetter cores in borehole 201 than those in the "condensing" zones in boreholes 199 and 200.

Table 2.5-3 Laboratory measurement of post-cooling dry drilled cores from the SHT

Sample ID	LBNL ID	Saturation	Porosity	Bulk Density	Particle Density	Gravimetric Water Content
				(g/cc)	(g/cc)	(g/g)
SPC01009880	H-1	0.50	0.169	1.96	2.36	0.043
SPC01009882	H-2	0.79	0.105	2.19	2.44	0.038
SPC01009884	H-3	0.75	0.115	2.16	2.44	0.040
SPC01009885	H-4	0.44	0.099	2.20	2.44	0.020
SPC01009887	H-5	0.19	0.101	2.18	2.42	0.009
SPC01009888	H-6	0.32	0.110	2.17	2.43	0.016
SPC01009889	H-7	0.80	0.104	2.19	2.45	0.038
SPC01009806	H-8	0.80	0.098	2.19	2.43	0.035
SPC01009807	H-9	0.61	0.099	2.19	2.43	0.027
SPC01009808	H-10	0.82	0.090	2.21	2.43	0.033
SPC01009809	H-11	0.78	0.092	2.20	2.42	0.033
SPC01009810	H-12	0.53	0.105	2.16	2.41	0.026
SPC01009811	H-13	0.38	0.097	2.19	2.43	0.017
SPC01009812	H-14	0.41	0.089	2.21	2.43	0.016
SPC01009890	H-15	0.76	0.090	2.21	2.43	0.031
SPC01009891	H-16	0.87	0.102	2.17	2.42	0.041
SPC01009892	H-17	0.89	0.101	2.18	2.42	0.041
SPC01009893	H-18	0.94	0.093	2.20	2.43	0.040
SPC01009894	H-19	0.83	0.106	2.17	2.43	0.041
SPC01009895	H-20	0.85	0.087	2.24	2.45	0.033
SPC01009896	H-21	0.89	0.082	2.22	2.42	0.033
SPC01009897	H-22	0.73	0.131	2.12	2.44	0.044
SPC01009898	H-23	0.86	0.104	2.17	2.42	0.041
SPC01009899	H-24	0.86	0.099	2.20	2.44	0.039
SPC01009900	H-25	0.82	0.117	2.15	2.44	0.045
SPC01009901	H-26	0.86	0.103	2.20	2.45	0.040
SPC01009902	H-27	0.77	0.143	2.09	2.44	0.053
SPC01009903	H-28	0.88	0.087	2.23	2.44	0.034
Average			0.104	2.18	2.43	
standard deviation			0.018	0.05	0.02	

Acknowledgment

We gratefully acknowledge the authors of previous milestone reports on the SHT, the contents of which have been incorporated into the present chapter. In particular, we like to acknowledge Paul Cook, Joe Wang, Roberto Suarez-Rivera, Tetsu Tokunaga, and Ken Williams. We thank Melani Menendez-Barreto for her assistance with graphics. We are grateful to George Moridis, Sumit Mukhopadhyay, Mark Feighner, and Ken Williams for their review of this chapter and comments for improvement.

References

Birkholzer, J.T. and Tsang, Y.W. 1996. *Forecast of Thermal-Hydrological Conditions and Air Injection Test Results of the Single Heater Test at Yucca Mountain.* Yucca Mountain Project Level 4 Milestone SP918M4; Report LBNL-39789, UC-814. Berkeley, California: Lawrence Berkeley National Laboratory. MOL.19971124.0089.

Boadu, F.K. 1997. "Rock Properties and Seismic Attenuation: Neural Network Analysis." *Pure and Applied Geophysics, 149,* 507-524. TIC: Copyright Clearance Pending.

Cook, P. and Wang, J. 1997a. *Infrared Imaging in the Single Heater Test Area.* Yucca Mountain Site Characterization Project Level 4 Milestone SP9230M4. Berkeley, California: Lawrence Berkeley National Laboratory. MOL.19971121.0882.

Cook, P. and Wang, J. 1997b. *Infrared Imaging in the Single Heater Test Area.* Yucca Mountain Site Characterization Project Level 4 Milestone SP9237M4. Berkeley, California: Lawrence Berkeley National Laboratory. MOL.19971201.0842. LB970400123142.001 (Q).

Cook, P. and Wang, J. 1997c. *Third Quarter Results of Infrared Mapping of the Single Heater Test Block.* Yucca Mountain Site Characterization Project Level 4 Milestone SP9291M4. Berkeley, California: Lawrence Berkeley National Laboratory. MOL.19971204.0439.

Cook, P. 1997. *Fourth Quarter FY1997 Results of Infrared Mapping in the Single Heater Test Area.* Yucca Mountain Site Characterization Project Level 4 Milestone SP1080M4. Berkeley, California: Lawrence Berkeley National Laboratory. MOL.19971208.0352.

Cook, P. 1998. *First Quarter FY1998 Results of Infrared Mapping in the Single Heater Test Area.* Yucca Mountain Site Characterization Project Level 4 Milestone SPY1160M4. Berkeley, California: Lawrence Berkeley National Laboratory. MOL.19980508.0044.

CRWMS M&O 1996. *Characterization of the ESF Thermal Test Area.* Report B00000000-01717-5705-00047 Rev. 01. Las Vegas, Nevada: U.S. Department of Energy. MOL.19970116.0187.

Daily, W. and Ramirez, A. 1989. "Evaluation of Electromagnetic Tomography to Map *In Situ* Water in Heated Welded Tuff." *Water Resources Research, 25,* 1083-1096. NNA.19910326.0097.

Freifeld, B. and Tsang, Y.W. 1998. "Active Hydrogeological Testing." *In: Second Quarter TDIF Submission for the Drift Scale Test (Hydrological, Radar, Microseismic),* Chapter 2. Yucca Mountain Project 4 Milestone Report SP2790M4. Berkeley, California: Lawrence Berkeley National Laboratory. MOL.19980812.0240 (TBV).

Freifeld, B. 1997. *Letter Report on Fourth Quarter Results of Measurements in the Hydrology Holes in the Single Heater Test Area in the ESF.* Yucca Mountain Project Level 4 Milestone SP1080M4. Berkeley, California: Lawrence Berkeley National Laboratory. DTN:LB9710000123142.001 (Q). MOL.19971208.0352.

Freifeld, B. and Tsang, Y. 1997a. *Letter Report on First Quarter Results of Measurements in Hydrology Holes in the Single Heater Test Area in the ESF.* Yucca Mountain Project Level 4 Milestone SP9263M4. Berkeley, California: Lawrence Berkeley National Laboratory. MOL.19970711.0192. LB970100123142.001 (Q).

Freifeld, B. and Tsang, Y. 1997b. *Letter Report on Second Quarter Results of Measurements in Hydrology Holes in the Single Heater Test Area in the ESF.* Yucca Mountain Project Level 4 Milestone SP9216M4. Berkeley, California: Lawrence Berkeley National Laboratory. MOL.19980826.0160 (TBV).

Freifeld, B. and Tsang, Y. 1997c. *Letter Report on Third Quarter Results of Measurements in the Hydrology Holes in the Single Heater Test Area in the ESF.* Yucca Mountain Project Level 4 Milestone SP9252M4. Berkeley, California: Lawrence Berkeley National Laboratory. DTN: LB970700123142.001 (Q). MOL.19971204.0428.

Guzman, A.G.; Geddis, A. M.; Henrich, M. J.; Lohrstorfer, C. F. and Neuman, S.P. 1996. Summary of Air Permeability Data from Single-Hole Injection Tests in Unsaturated Fractured Tuffs at the Apache Leap Research Site; Results of Steady-State Interpretation. U.S. Nuclear Regulatory Commission Report NUREG/CR-6360. NRC. Washington, DC. : Nuclear Regulatory Commission. TIC: 234385.

Hvorslev, M.J. 1951. "Time Lag and Soil Permeability in Groundwater Observations." *Bulletin 36.* U.S. Army Corps of Engineers, Water Ways Experimental Station, Vicksburg, Michigan. TIC: Copyright Clearance Pending.

LeCain, G. D. 1995. *Pneumatic Testing in 45-Degree-Inclined Boreholes in Ash-Flow Tuff near Superior, Arizona.* U.S. Geol. Surv. Water Resour. Invest. Rep. 95-4073. Denver, Colorado: U.S. Geological Survey. MOL.19960416.0160.

LeCain, G.D. 1997. *Air-Injection Testing in Vertical Boreholes in Welded and Nonwelded Tuff, Yucca Mountain, Nevada:* U.S. Geol. Surv. Water Resour. Invest. Rep. 96-4262. Denver, Colorado: U.S. Geological Survey. GS960908312232.012 (Non-Q), GS960908312232.013 (Q).

Peterson, J. E. 1986. *The Application of Algebraic Reconstruction Techniques to Geophysical Problems.* Ph.D. Thesis. Berkeley, California: Lawrence Berkeley National Laboratory. LBL-21498. TIC: On Order.

Peterson, J.E. and Williams, K.H. 1997. *To Assess the Effectiveness of the Ground Penetrating Radar Method in Measuring Moisture Content in the Single Heater Test.* Yucca Mountain Project Milestone Level 4 SP9241M4. Berkeley, California: Lawrence Berkeley National Laboratory. MOL.19971119.0542.

Roberts, J.J. and W. Lin. 1997. "Electrical Properties of Partially Saturated Topopah Spring Tuff: Water Distribution as a Function of Saturation." *Water Resources Research, 33* (4), 577-587. MOL.19961014.0060.

Tsang, Y.W. and Tsang, C. F. 1988. "Channel Model of Flow Through Fractured Media" *Water Resources Research, 23*, 467-479. TIC: Copyright Clearance Pending.

Tsang Y. W., Wang, J.; Freifeld, B.; Cook, P.; Suarez-Rivera, R.; and Tokunaga, T. 1996. *Letter Report on Hydrological Characterization of the Single Heater Test Area in the ESF.* Yucca Mountain Project Level 4 Milestone OS327322D1. Berkeley, California: Lawrence Berkeley National Laboratory. MOL.19971119.0549. LB960500834244.001 (Q).

Tsang, Y.W. and Birkholzer, J.T. 1997. *Interpreting the Thermal-Hydrological Response of the ESF Single Heater Test.* Yucca Mountain Project Level 4 Milestone SP9267M4. Berkeley, California: Lawrence Berkeley National Laboratory. MOL.19971204.0759.

Wang, J.S.Y. and Suarez-Rivera, R. 1997. Laboratory Test Results of Hydrological Properties from Dry Drilled and Wet Drilled Cores in the Drift Scale Test Area and in the Single Heater Test Area of the Thermal Test Facility. Yucca Mountain Project Level 4 Milestone SP5130M4. Berkeley, California: Lawrence Berkeley National Laboratory. LB970500123142.003 (Q). MOL.19971224.0056.

Figures

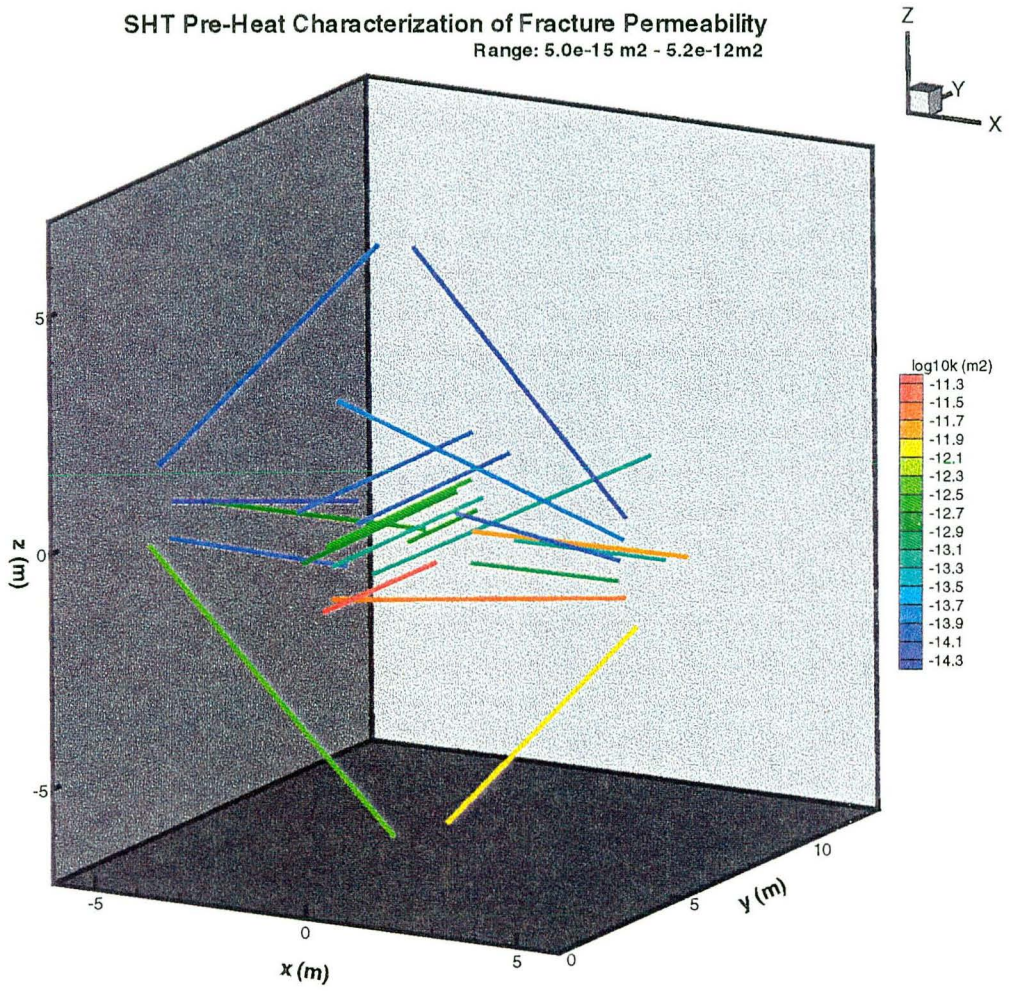

Figure 2.1-1 Pre-test estimated air permeability values associated with 21 boreholes in the SHT.

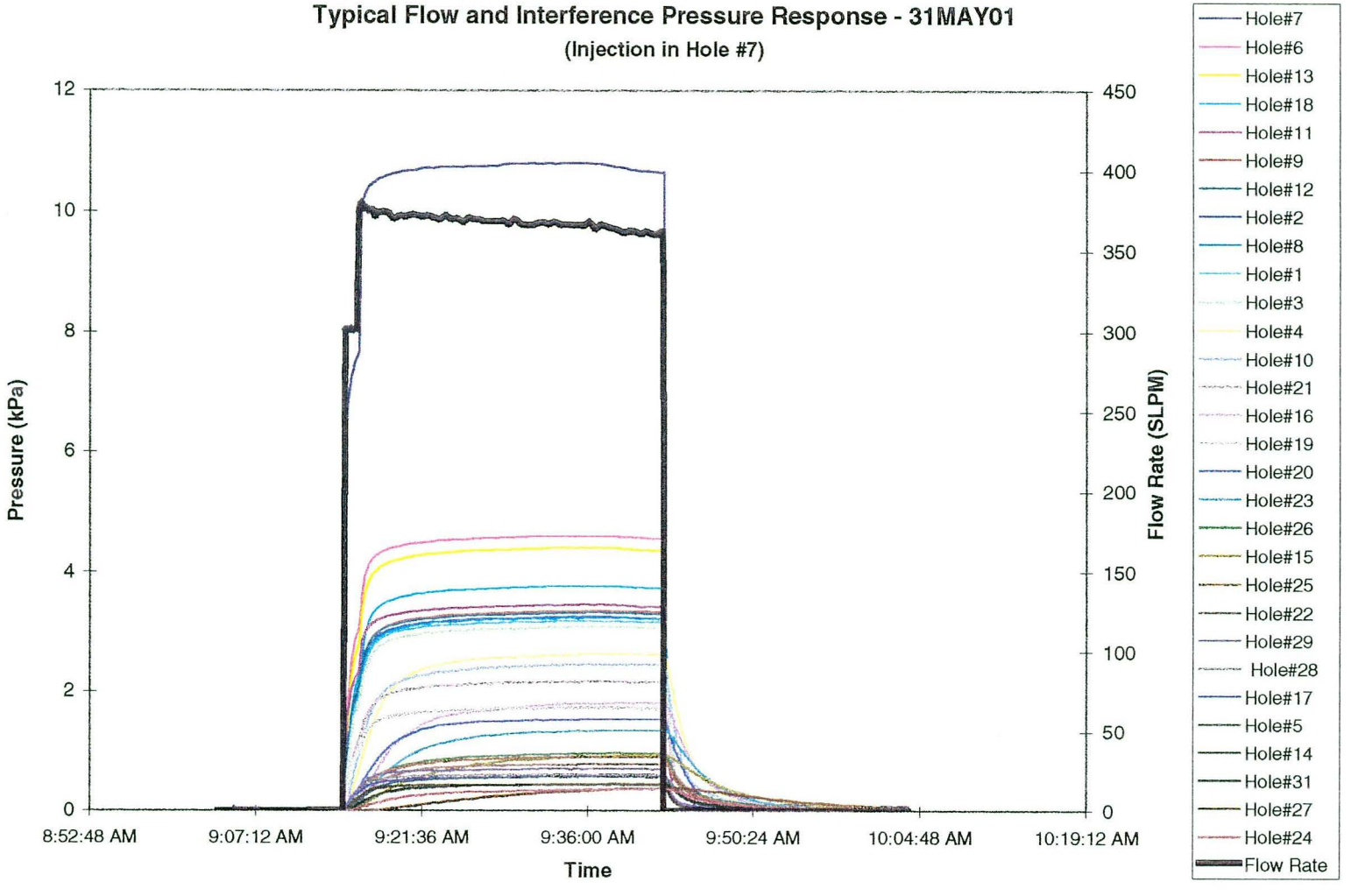

Figure 2.1-2 Flow and interference pressure responses of a typical air injection test performed in the pre-test characterization of the SHT.

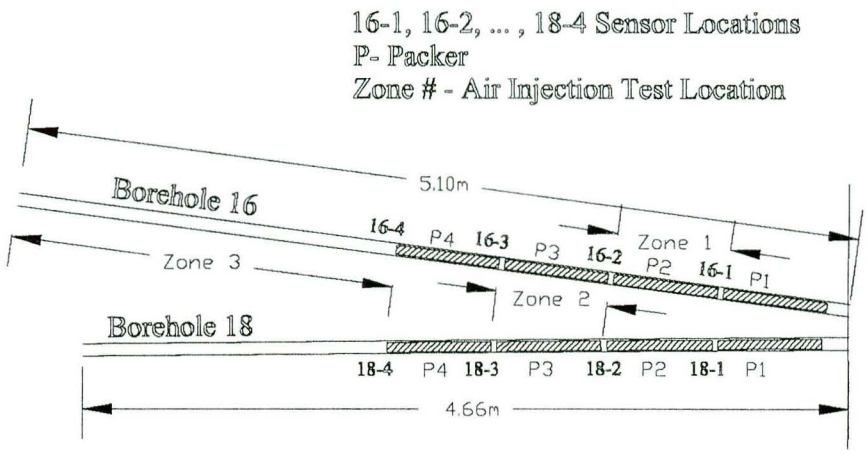

Figure 2.1-3 Geometry of the instrumentation and air injection zones in boreholes 16 and 18.

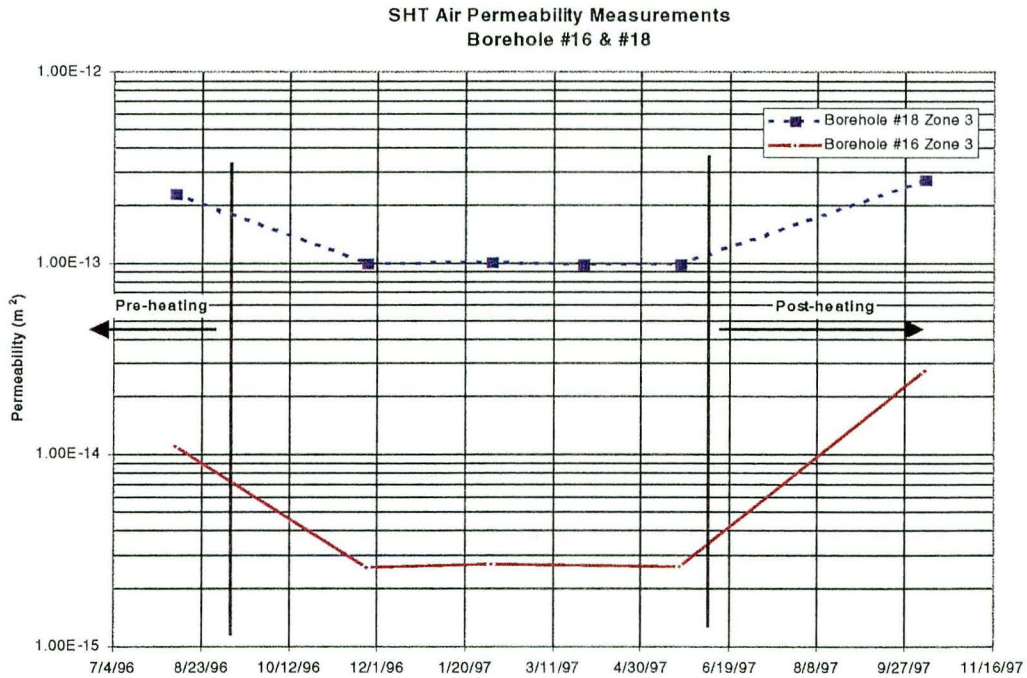

Figure 2.1-4 Changes in air permeability values: (pre-heat, during and post-heat) for Injection Zone 3 in boreholes 16 and 18.

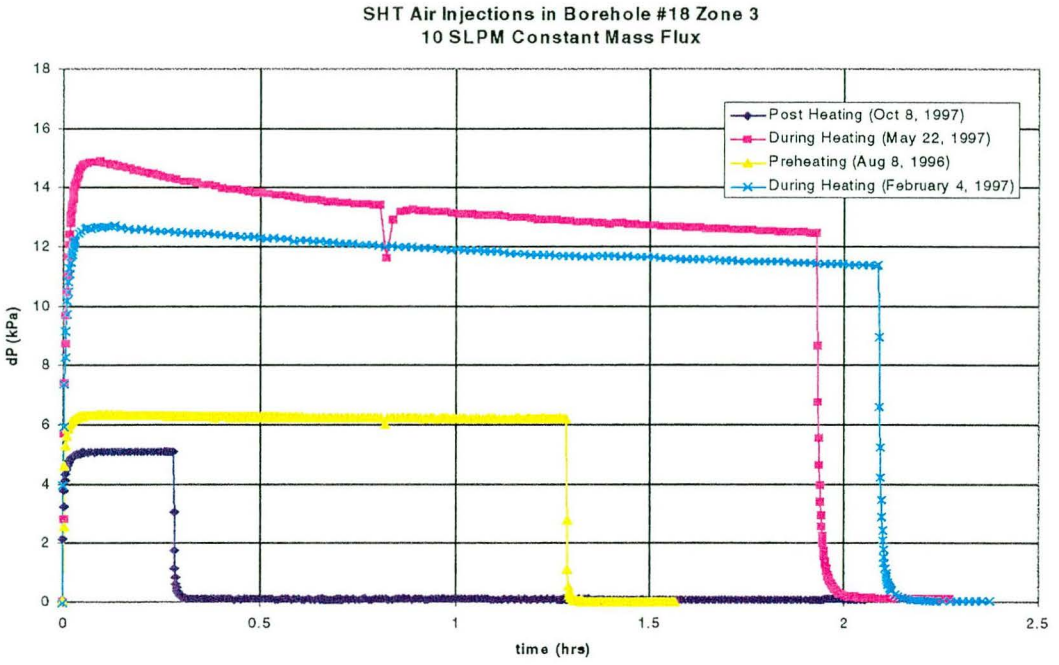

Figure 2.1-5 Pressure transients for the air injection tests conducted in borehole 18, Injection Zone 3. Before and after the heating phase of the SHT, air injection quickly reaches a steady state pressure. During heating, the large amount of condensate present creates a transient, two-phase system which reduces permeability.

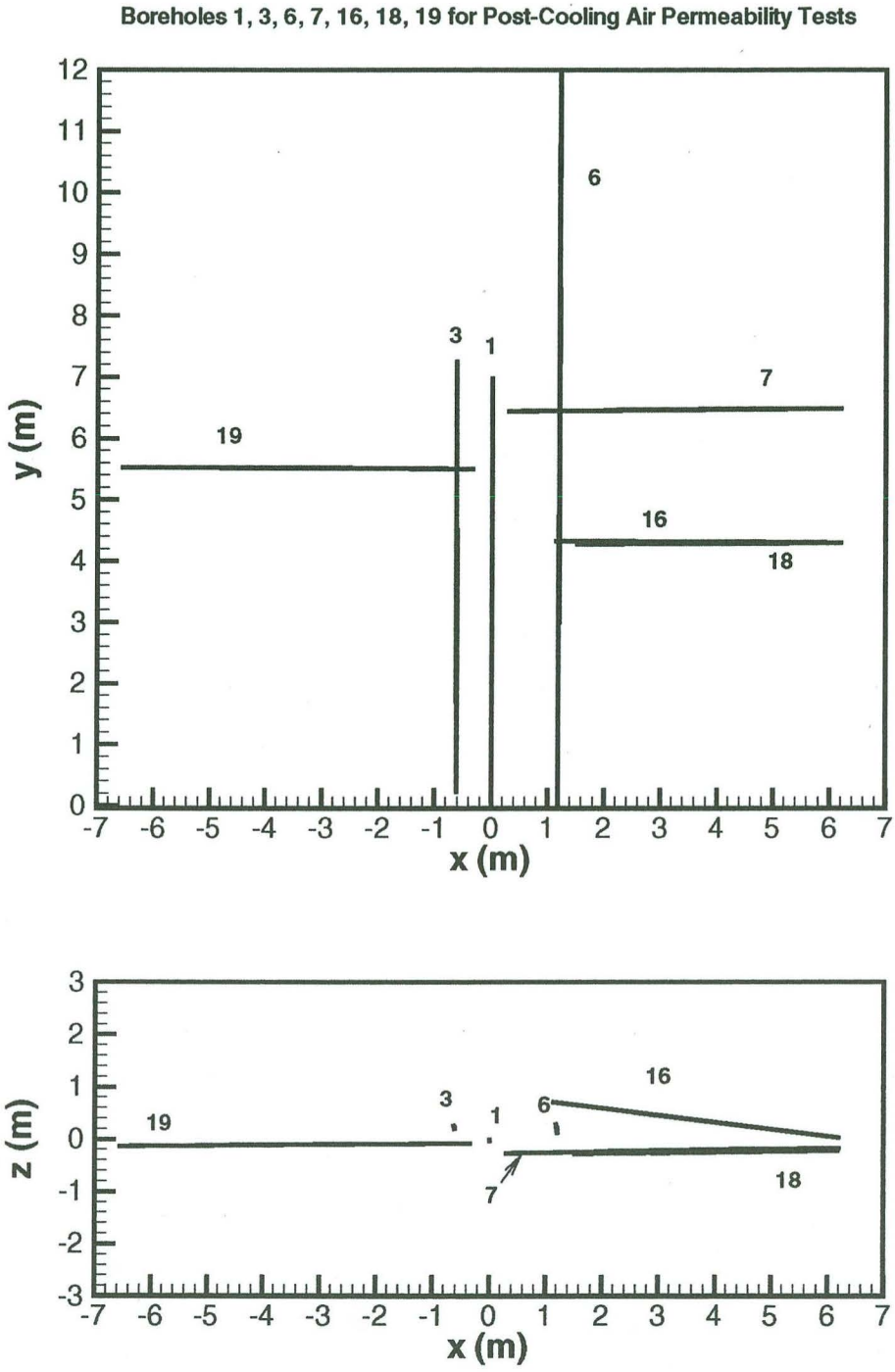

Figure 2.1-6 Subset of SHT boreholes available for post-cooling air permeability measurements.

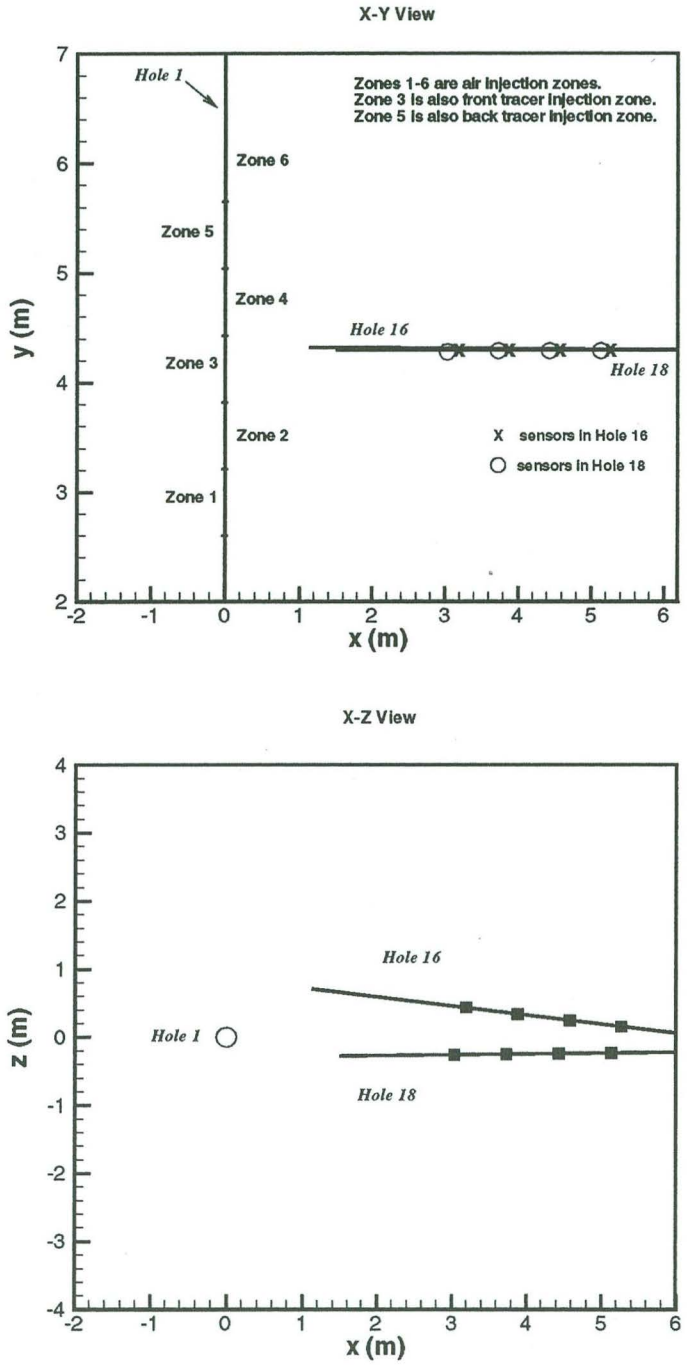

Figure 2.1-7 Multi-zone configuration of borehole 1 and boreholes 16, 18 for post-cooling air injection tests.

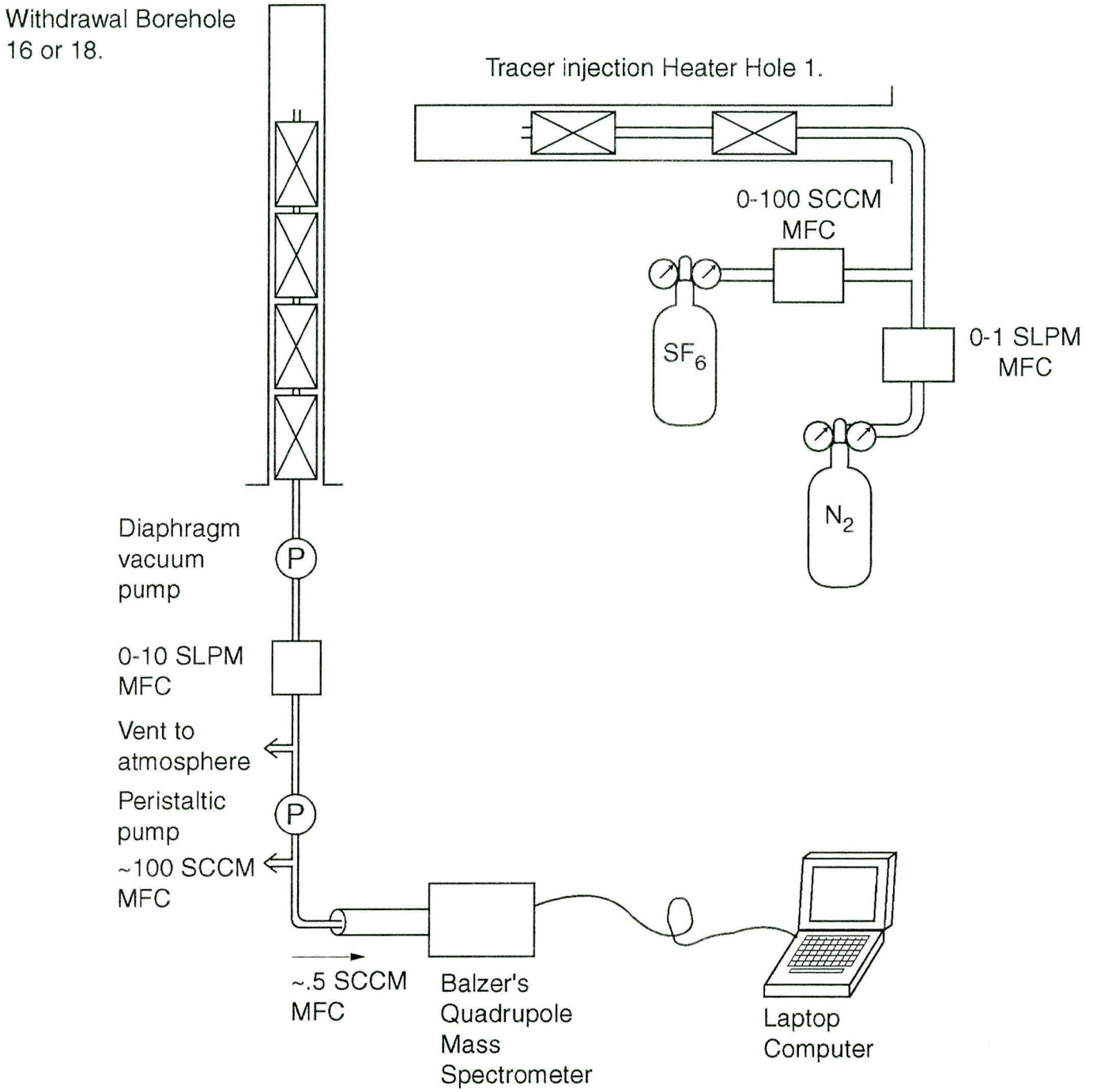

Figure 2.1-8 A schematic drawing of the equipment used for conducting tracer tests in boreholes 1, 16, 18 of the SHT.

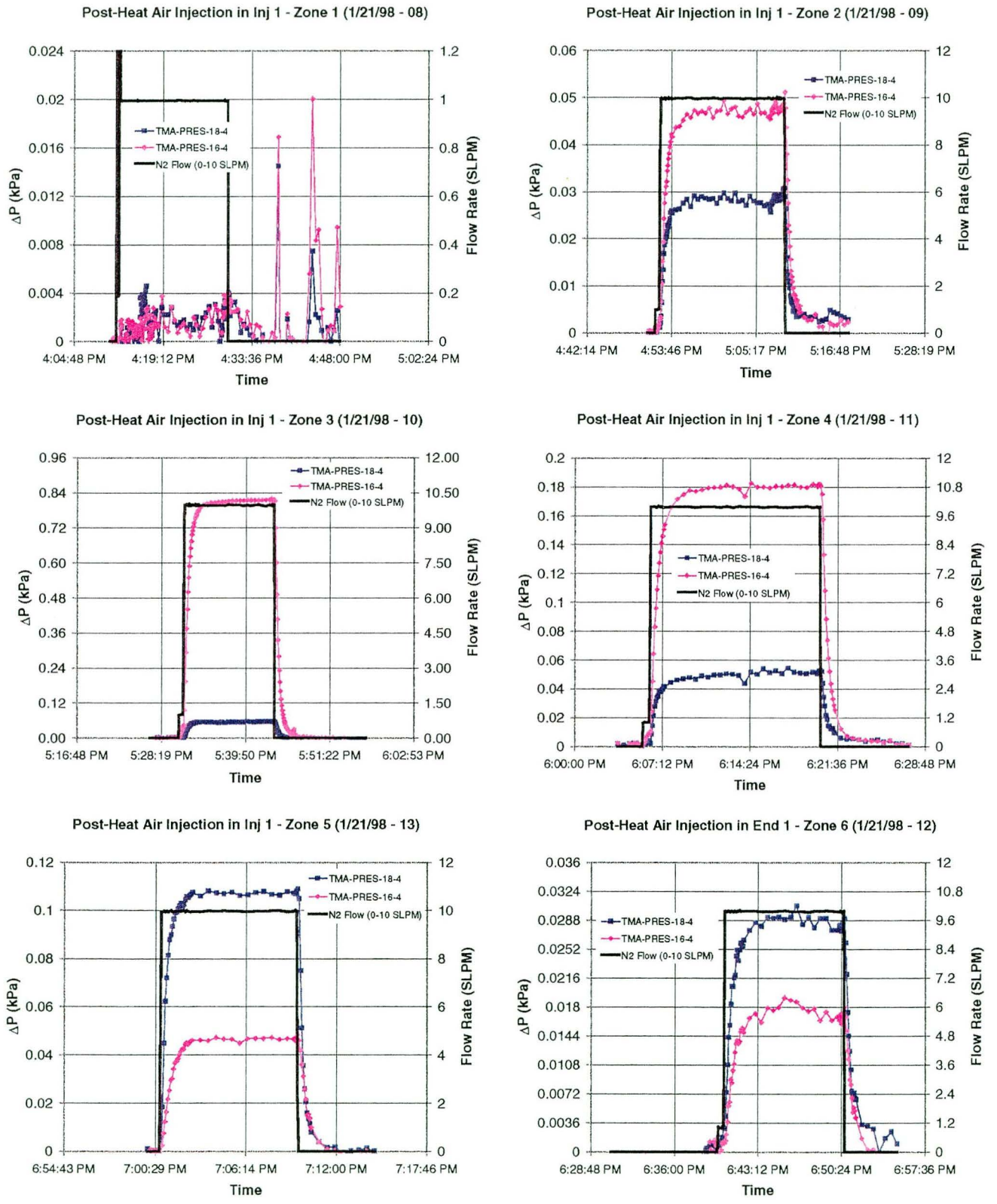

Figure 2.1-9 Response in pressure sensor 4 in Zone 3 of boreholes 16 and 18 to injection in consecutive isolated sections in borehole 1.

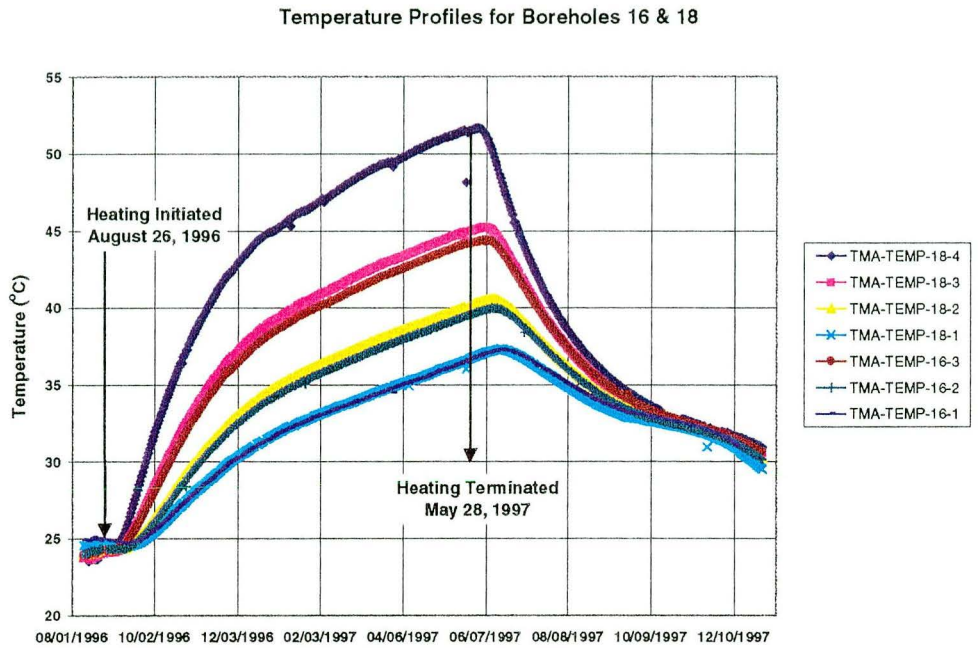

Figure 2.2-1 Passive monitoring temperature data in boreholes 16 and 18 of the SHT from August 1996 through December 1997.

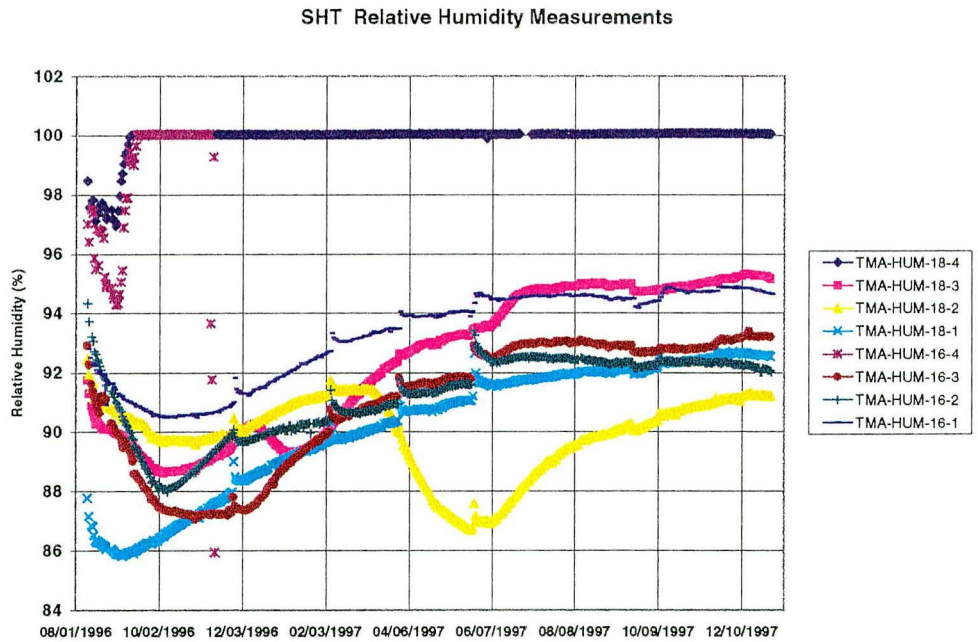

Figure 2.2-2 Passive monitoring relative humidity data in boreholes 16 and 18 of the SHT from August 1996 through December 1997.

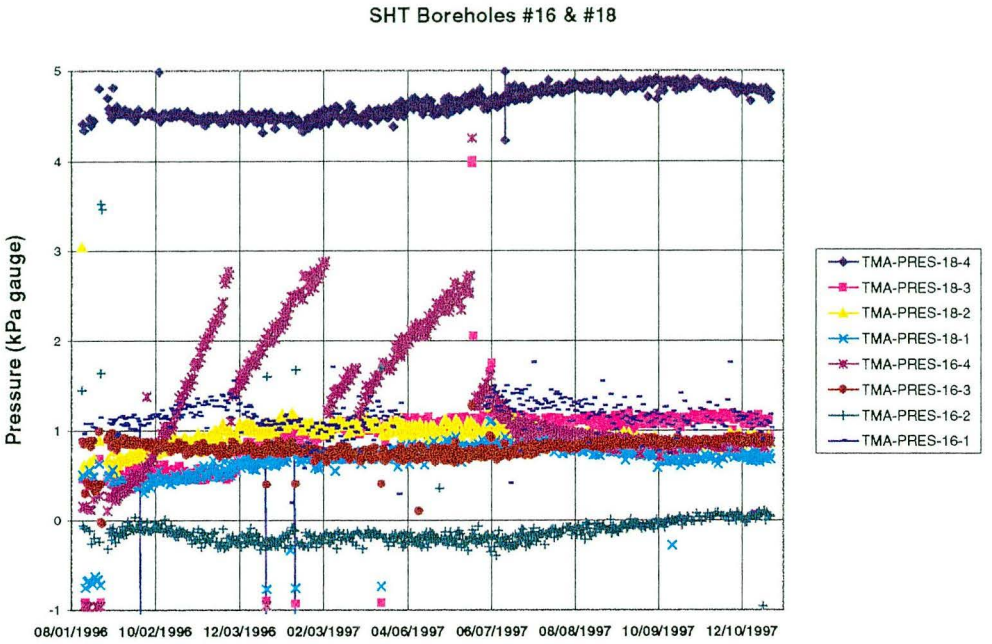

Figure 2.2-3 Passive monitoring pressure data in boreholes 16 and 18 of the SHT from August 1996 through December 1997.

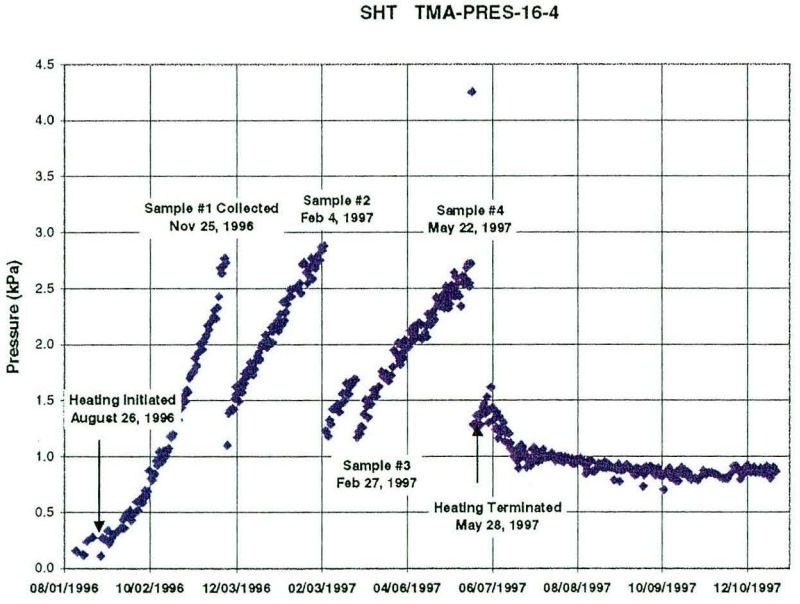

Figure 2.2-4 Passive monitoring pressure data from sensor 16-4 in borehole 16 of the SHT from August through December 1997.

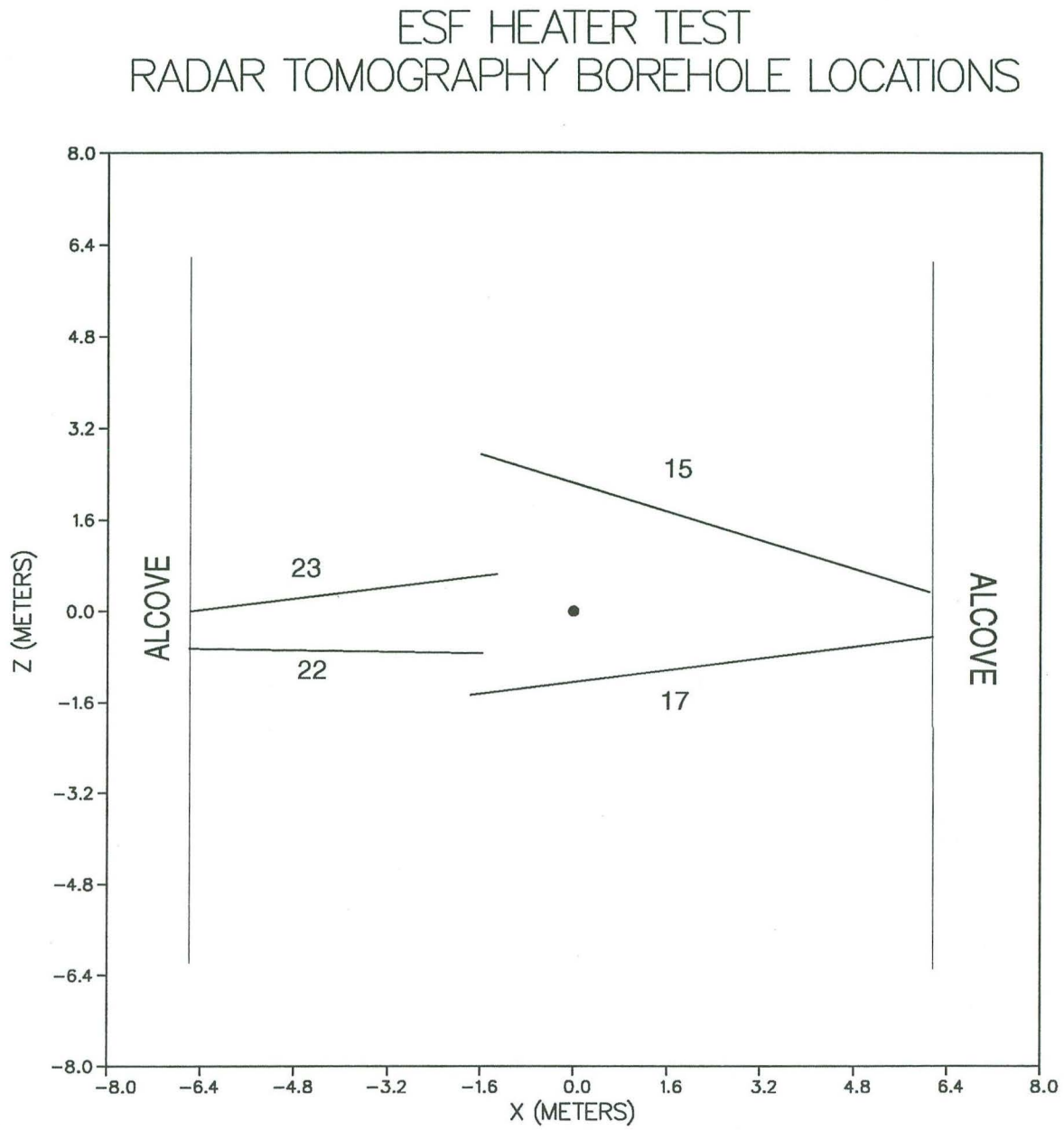

Figure 2.3-1 The Geometry of the boreholes used for crosswell radar. The heater well is located at (0.,0.,0.).

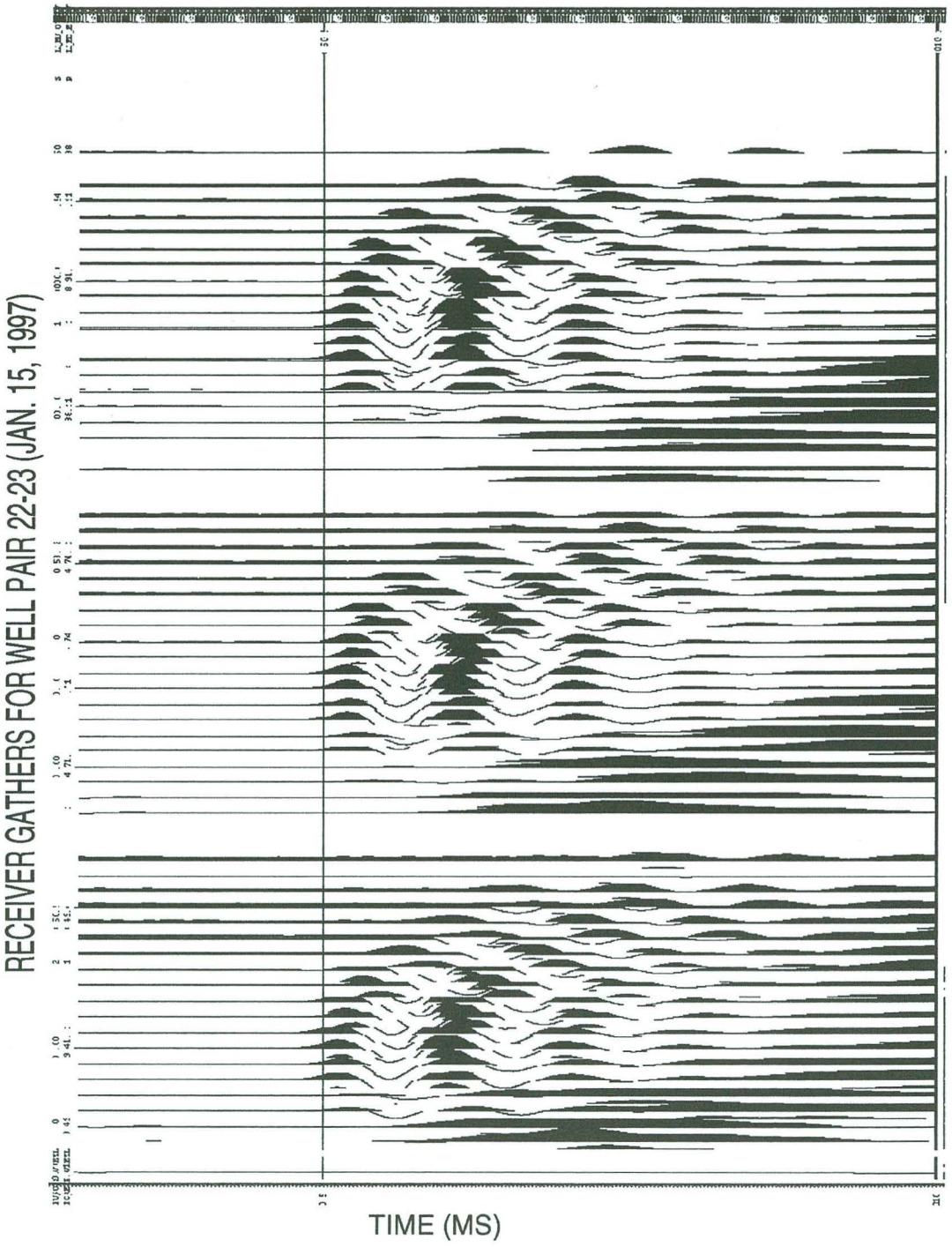

Figure 2.3-2 Three typical receiver gathers for well pair 22-23. Shown are gathers for receivers at 1.49, 1.74, and 1.98 down well 23.

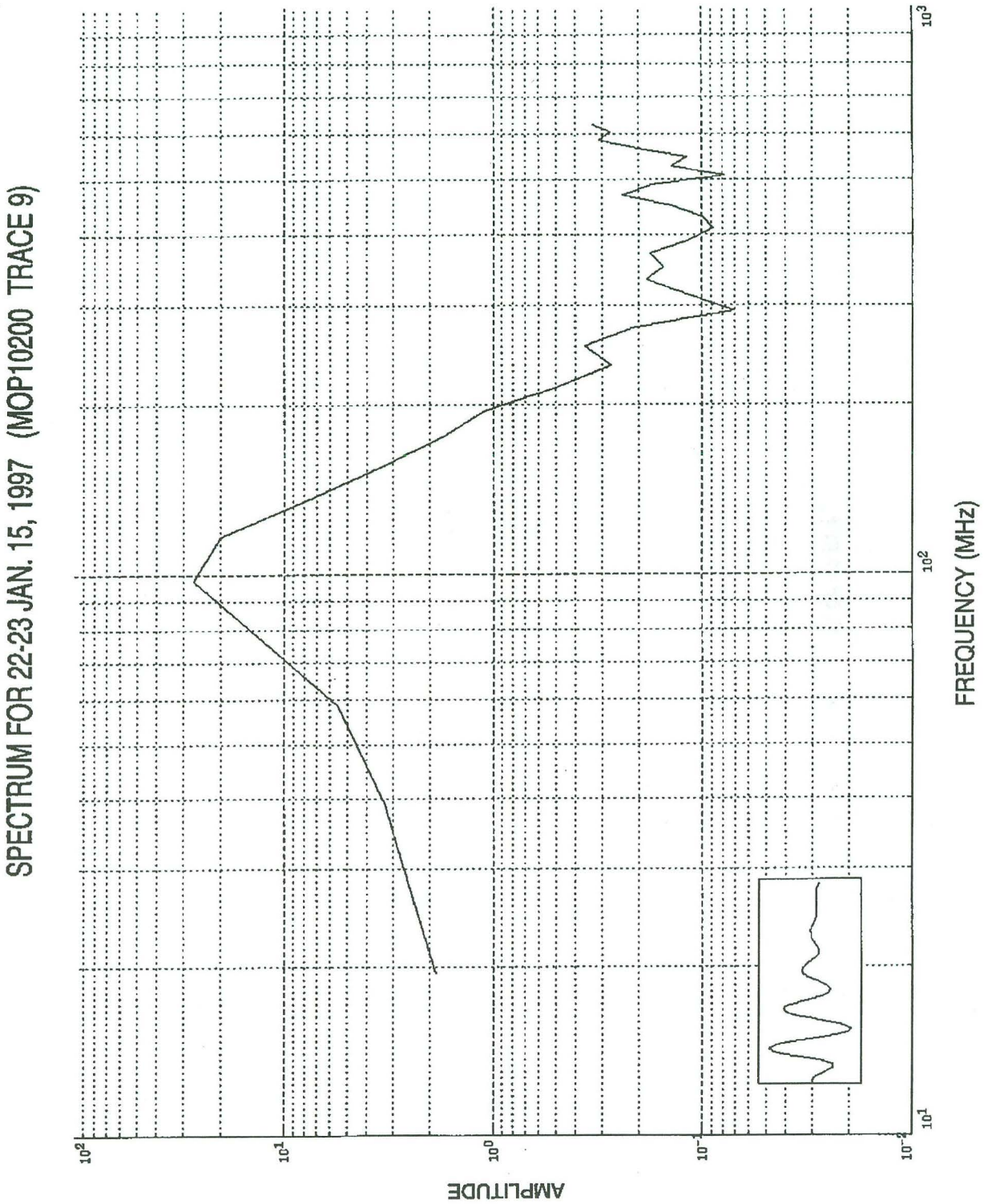

Figure 2.3-3 Frequency spectrum for trace number 9 in MOP10200, when the receiver is 2.0 meters down well 23.

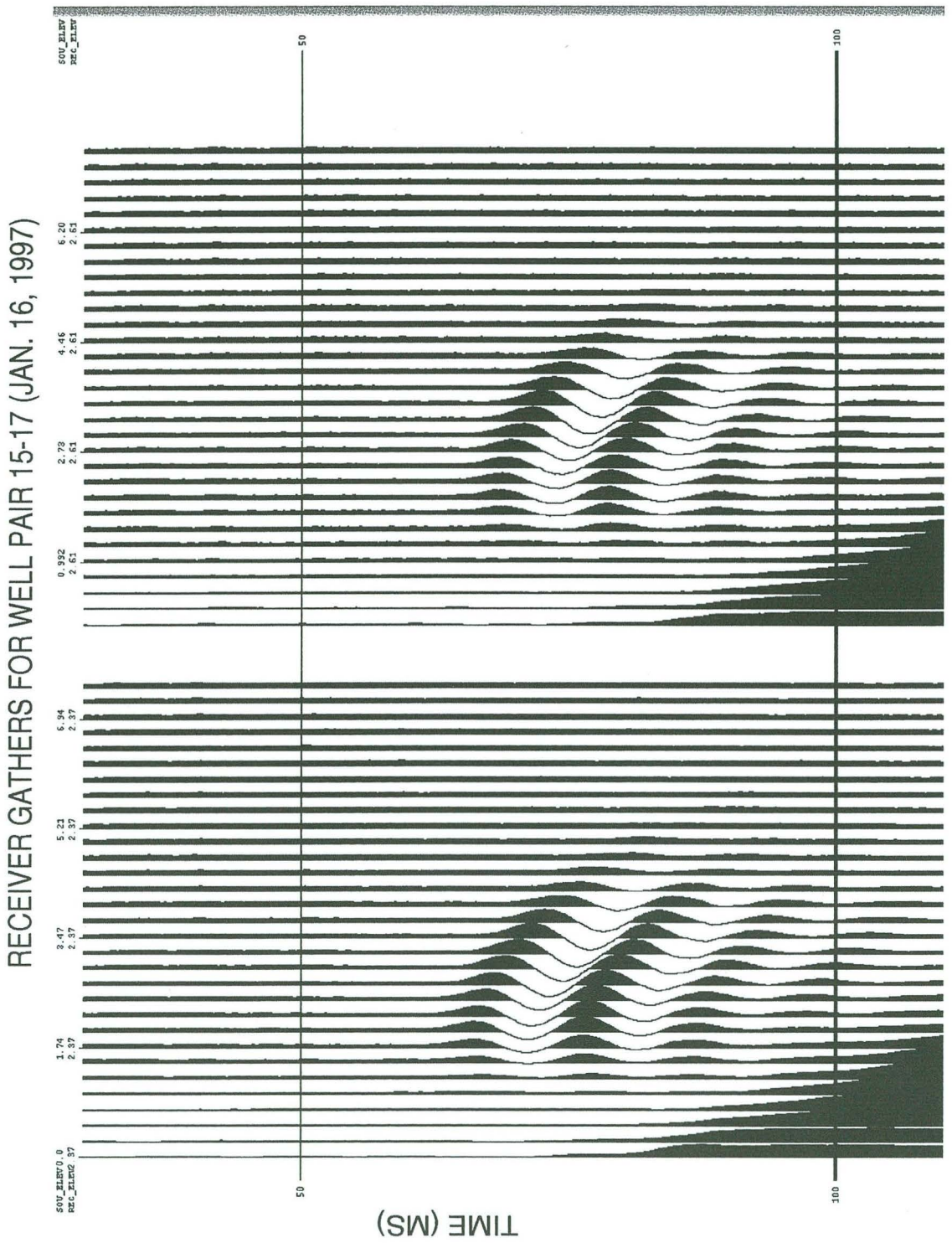

Figure 2.3-4 Two typical receiver gathers for the 17-15 well pair. Shown are gathers for receivers 2.37 and 2.61 meters down well 15.

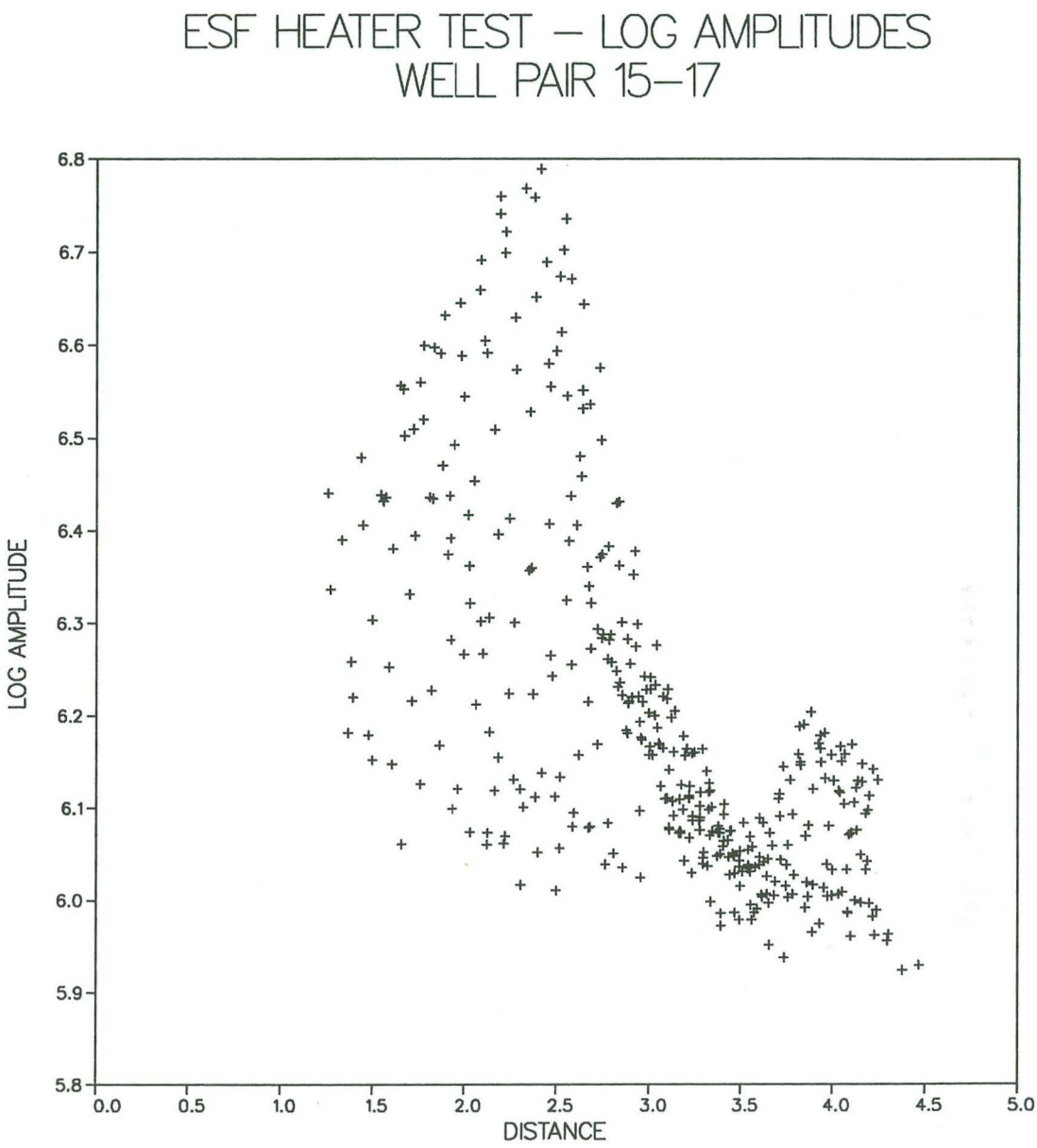

Figure 2.3-5 The log amplitudes of all traces with picked travel times for well pair 17-15. The amplitudes are RMS values of the first 20 samples after the picked sample.

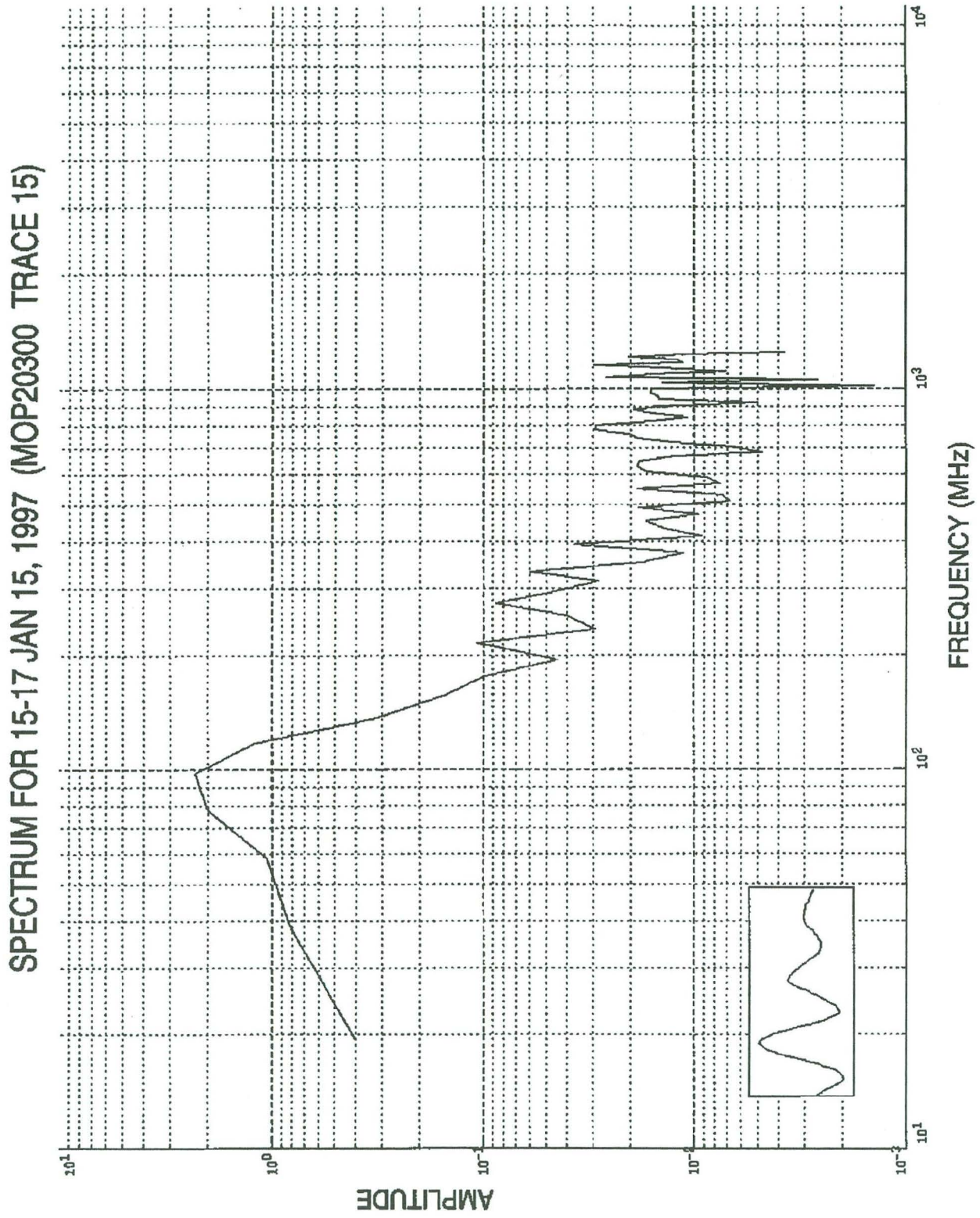

Figure 2.3.6 Frequency spectrum for trace number 15 in MOP20300, when the receiver is 3.0 meters down well 15.

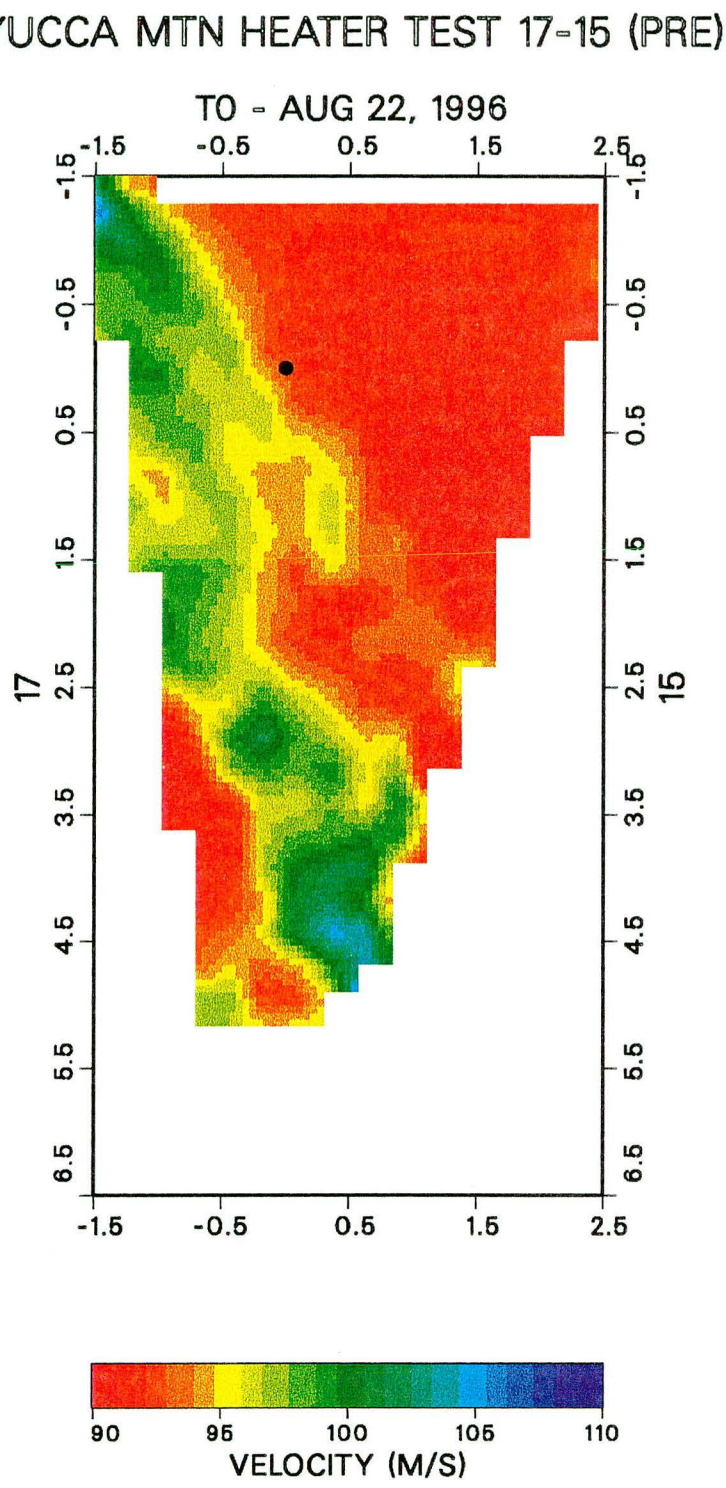

Figure 2.3-7a Baseline radar velocity tomogram.

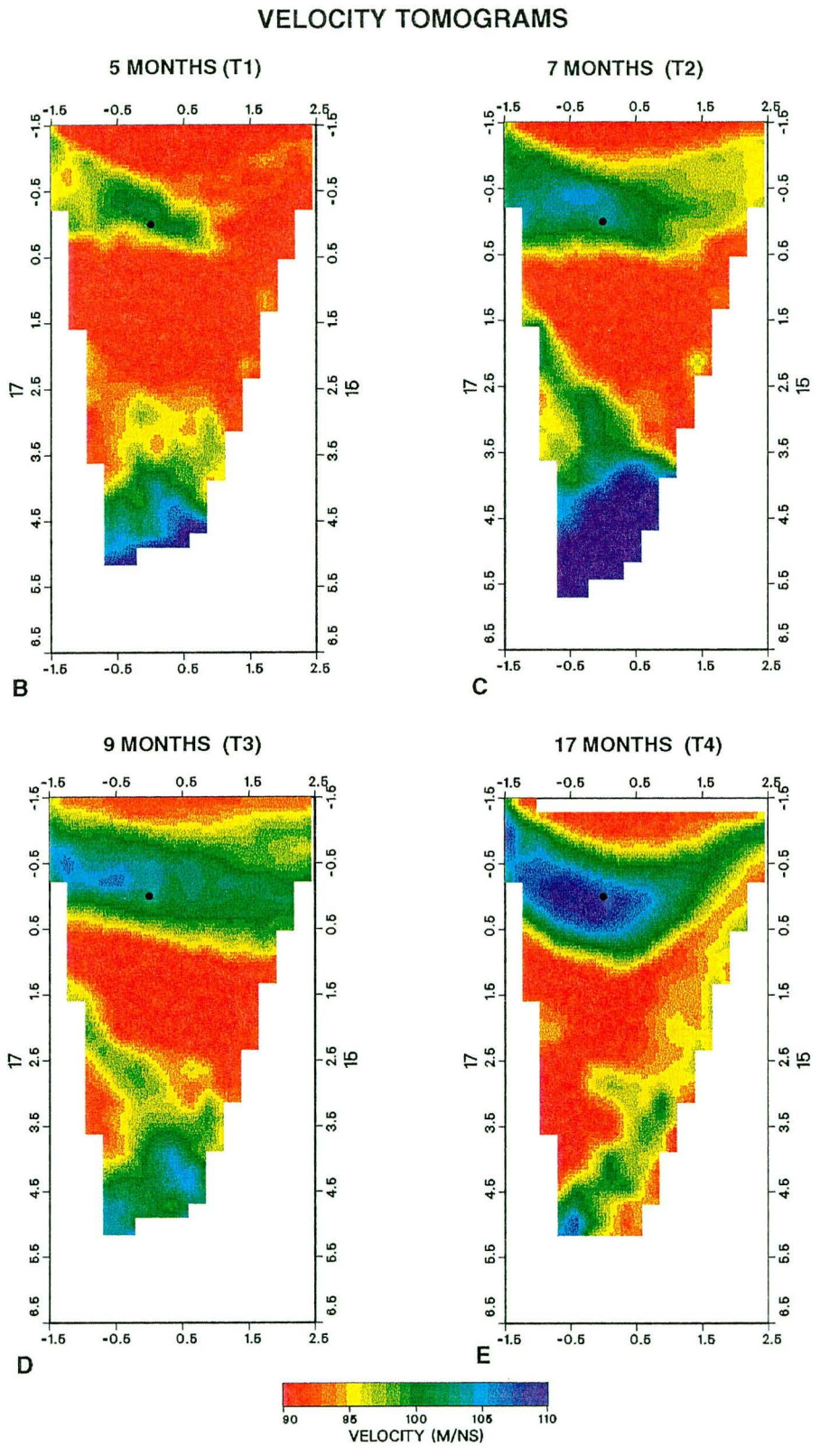

Figure 2.3-7b-e Velocity tomograms for well pair 17-15 during (B-D) and after (E) heating.

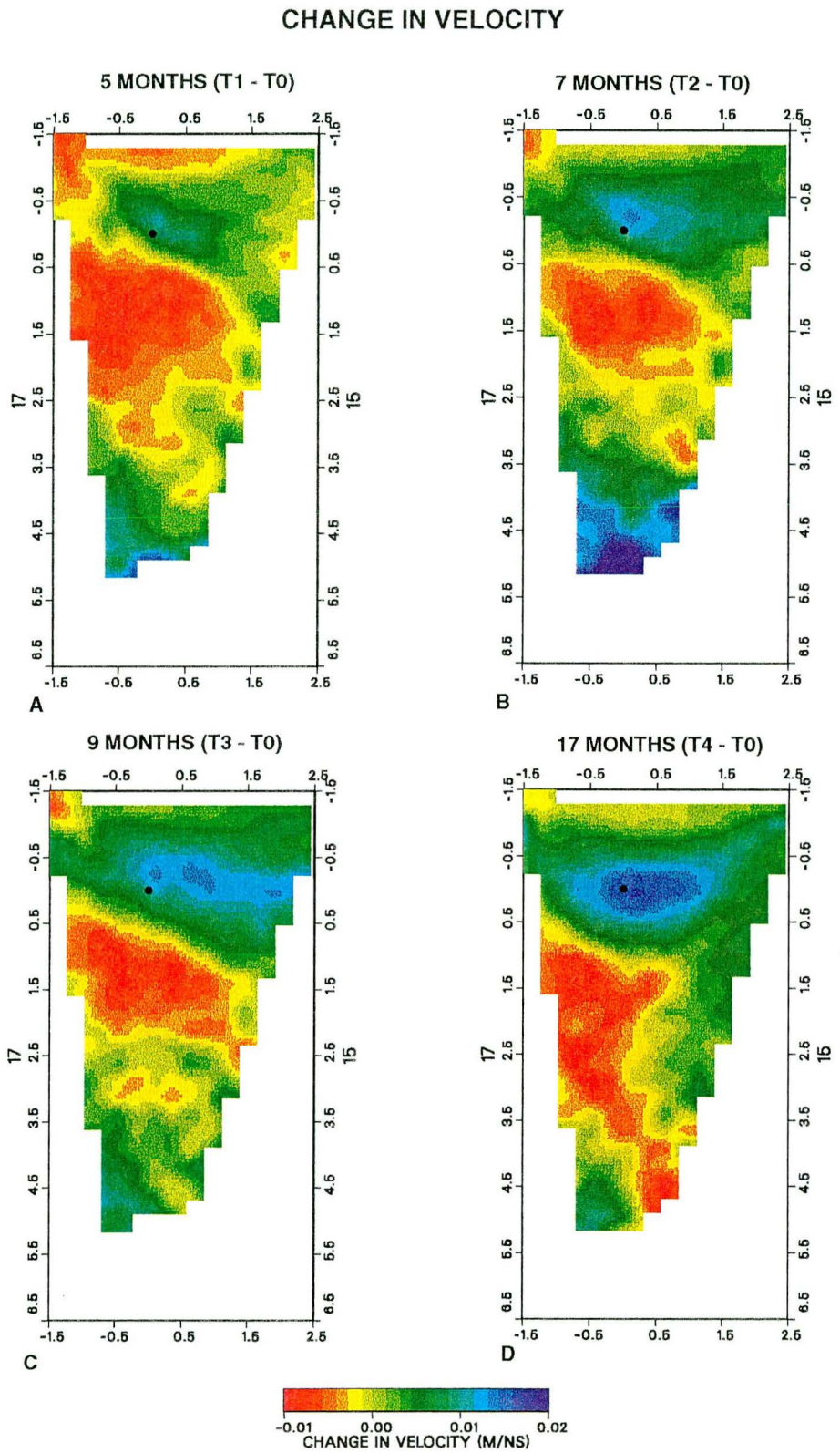

Figure 2.3-8 Change in velocity during the heater test for well pair 17-15.

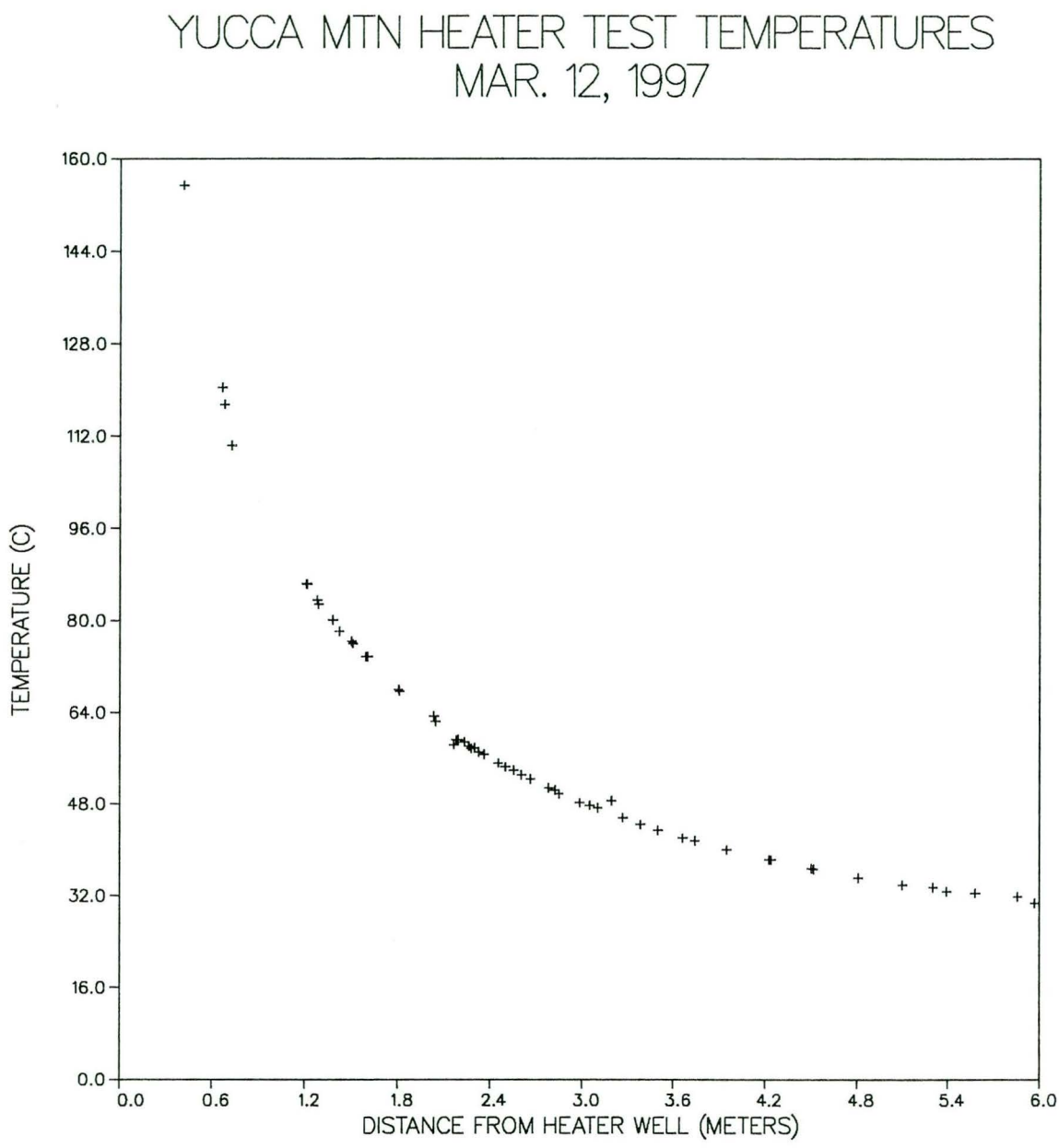

Figure 2.3-9 Temperature measurements with respect to distance from heater in the plane of the tomograms, used to estimate temperature profile.

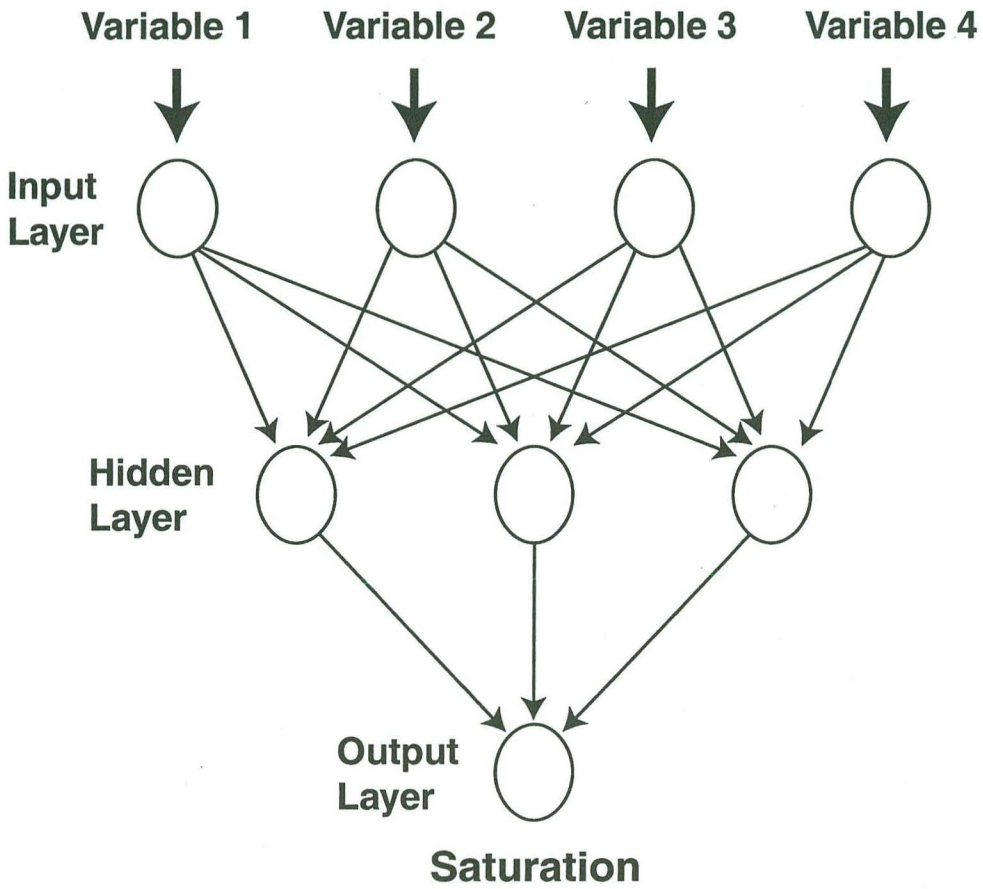

Figure 2.3-10 Neural net methodology flowchart.

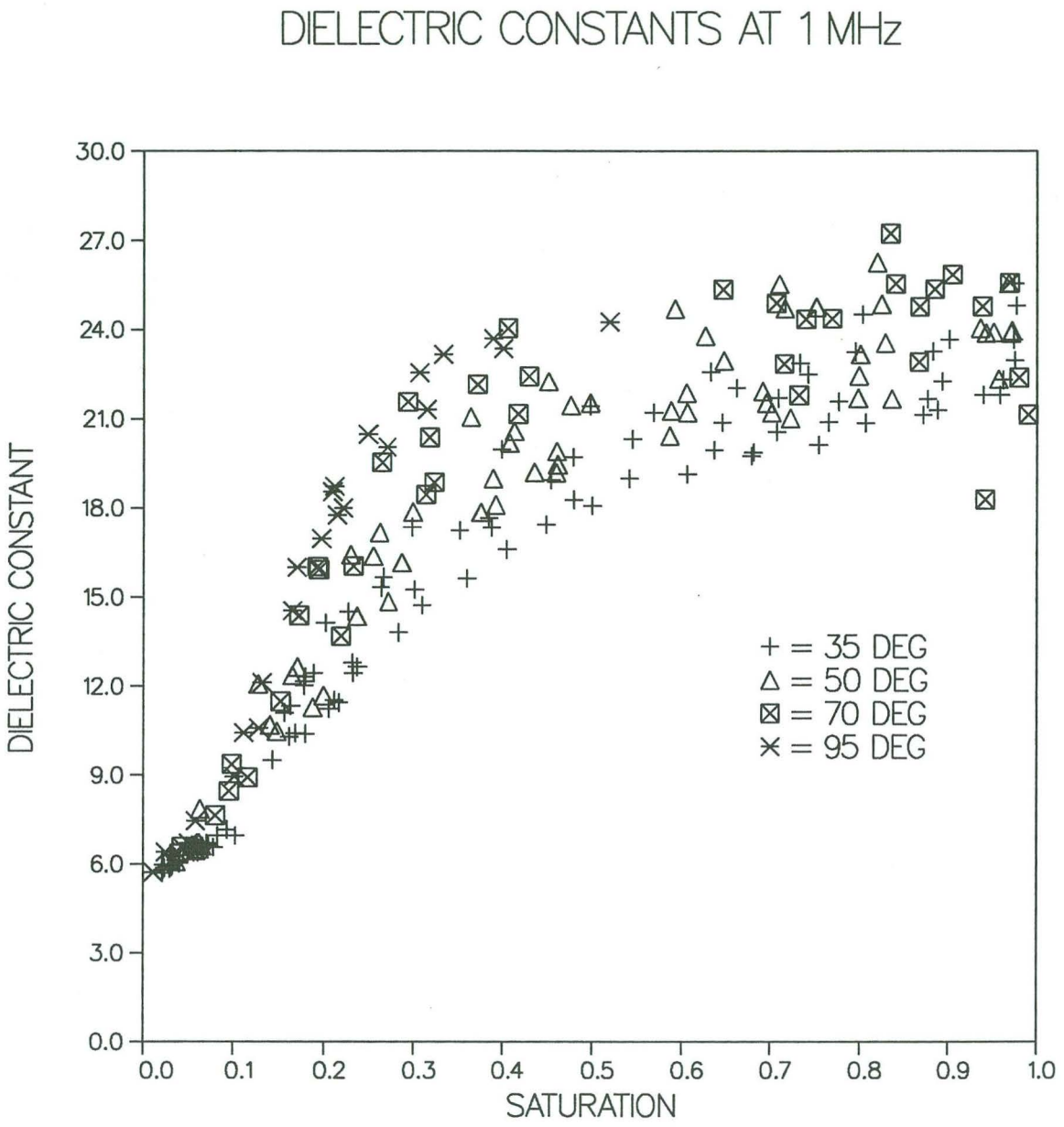

Figure 2.3-11 Laboratory measurements of dielectric constant at various saturations and temperatures at a frequency of 1MHz.

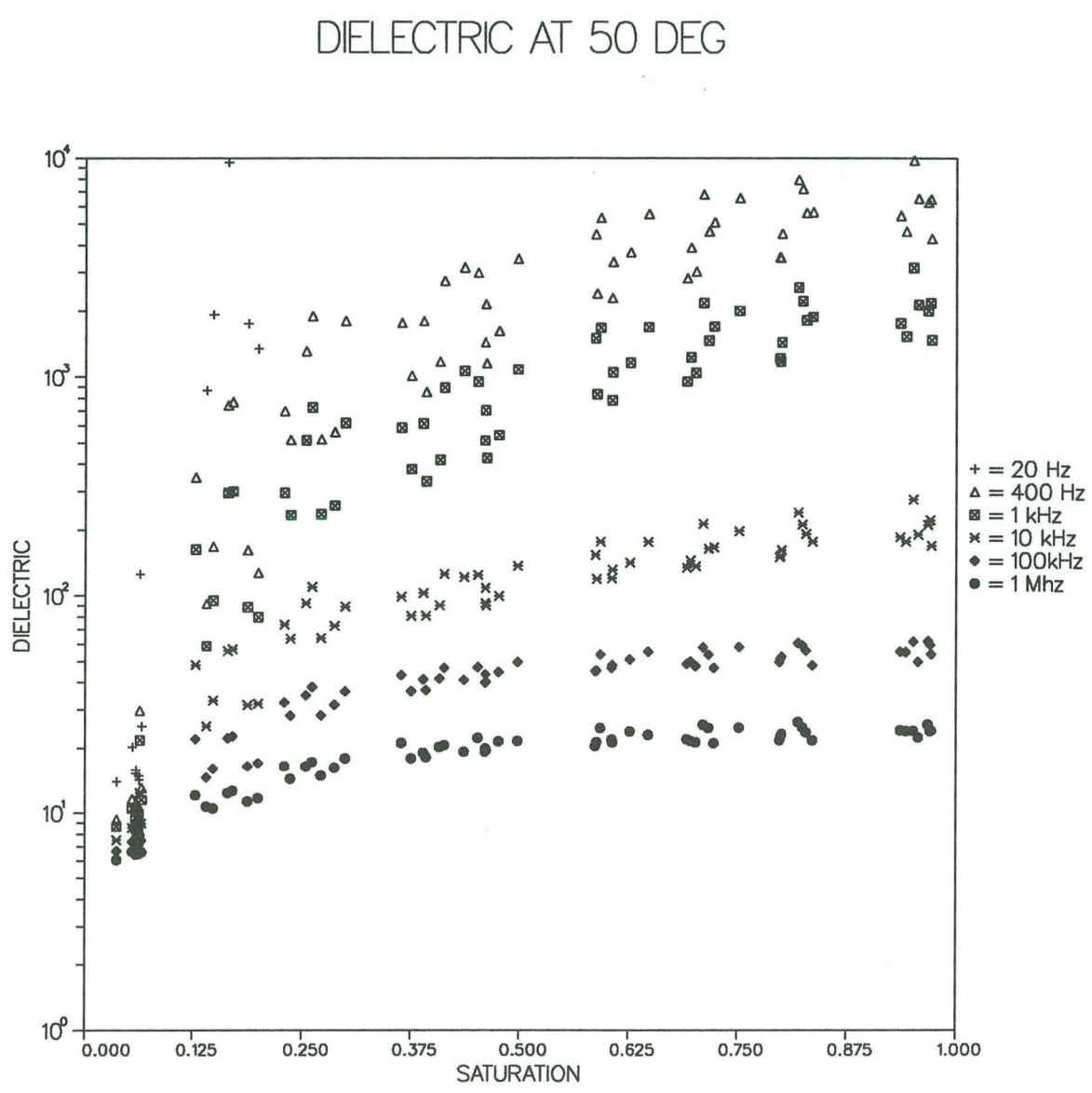

Figure 2.3-12 Laboratory measurements of dielectric constant at various saturations and frequencies and a temperature of 50° C.

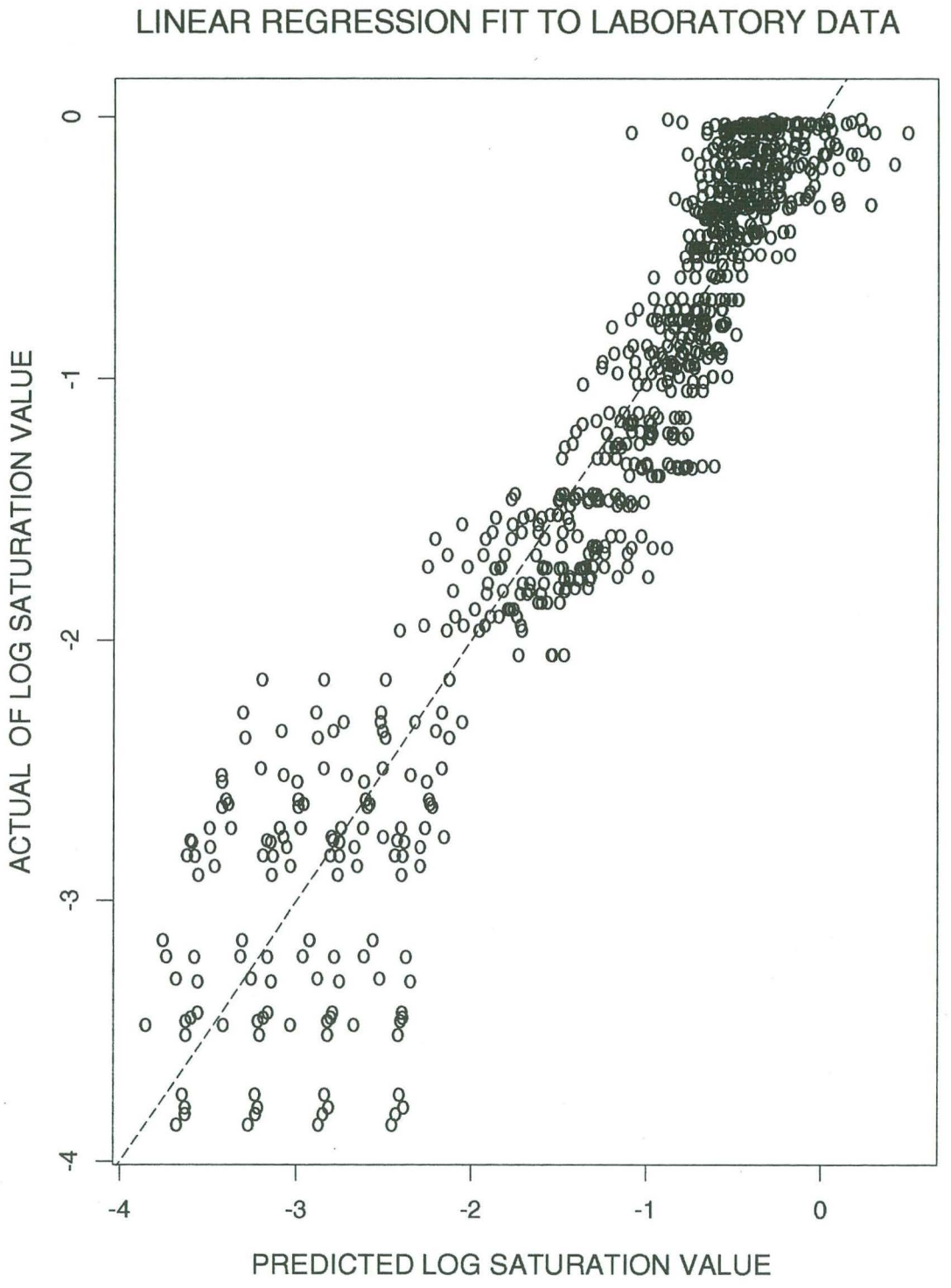

Figure 2.3-13 The estimated fit to the laboratory data using the relationship in Equation 1.

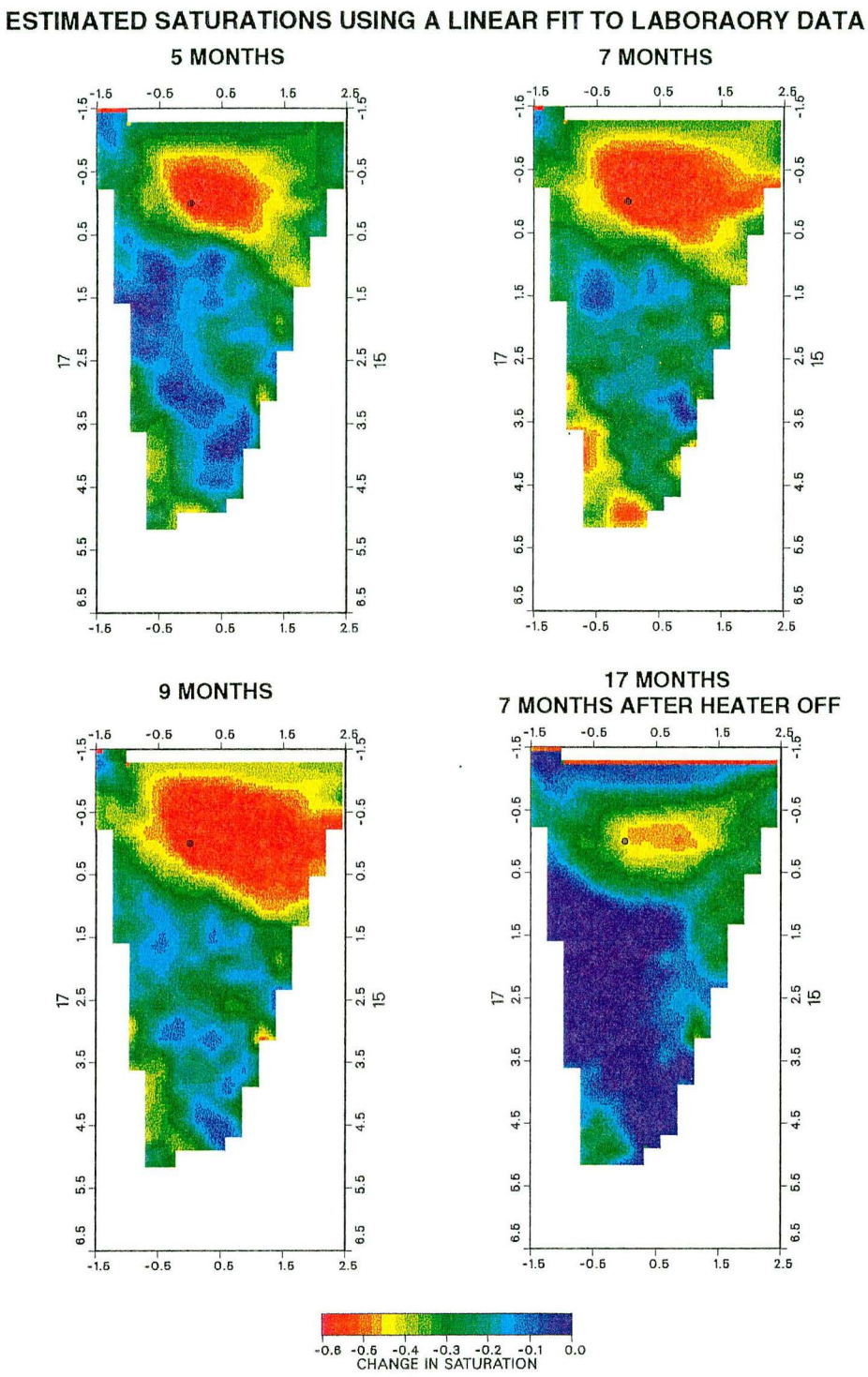

Figure 2.3-14 Saturations estimated from the linear fit to the laboratory data.

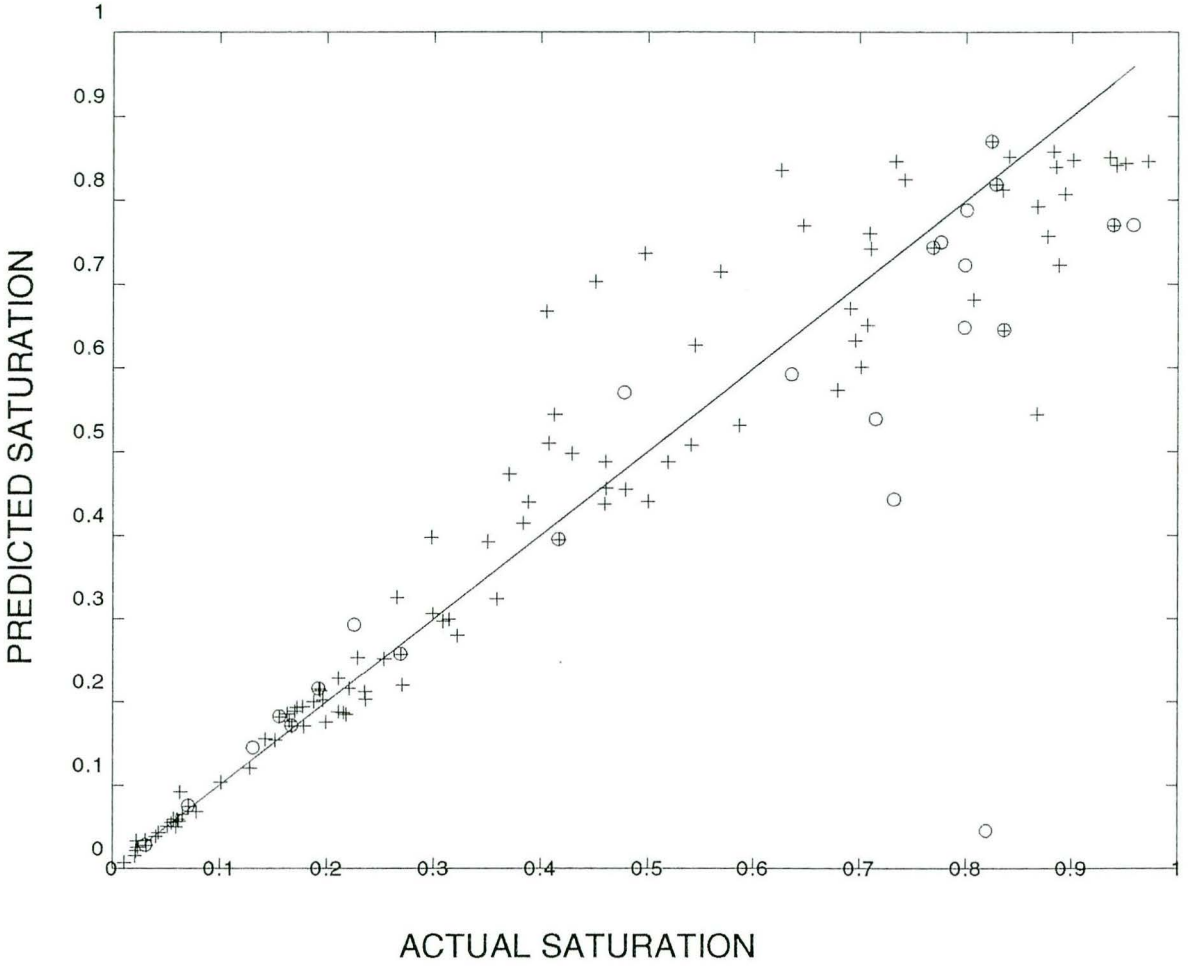

Figure 2.3-15 The observed vs. predicted values obtained from the neutral network fit to the laboratory data.

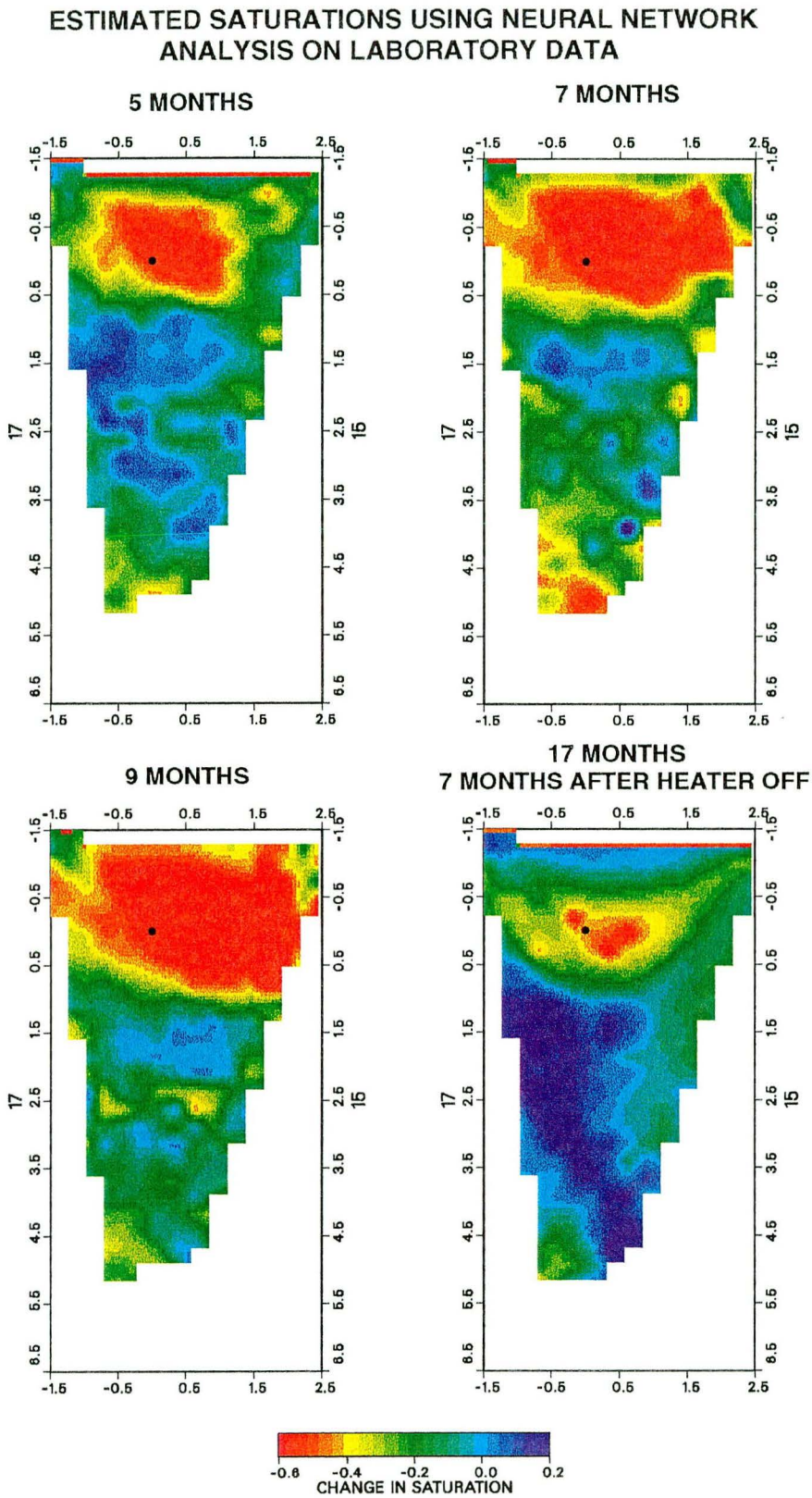

Figure 2.3-16 Estimated saturations from the neural network analysis using laboratory data.

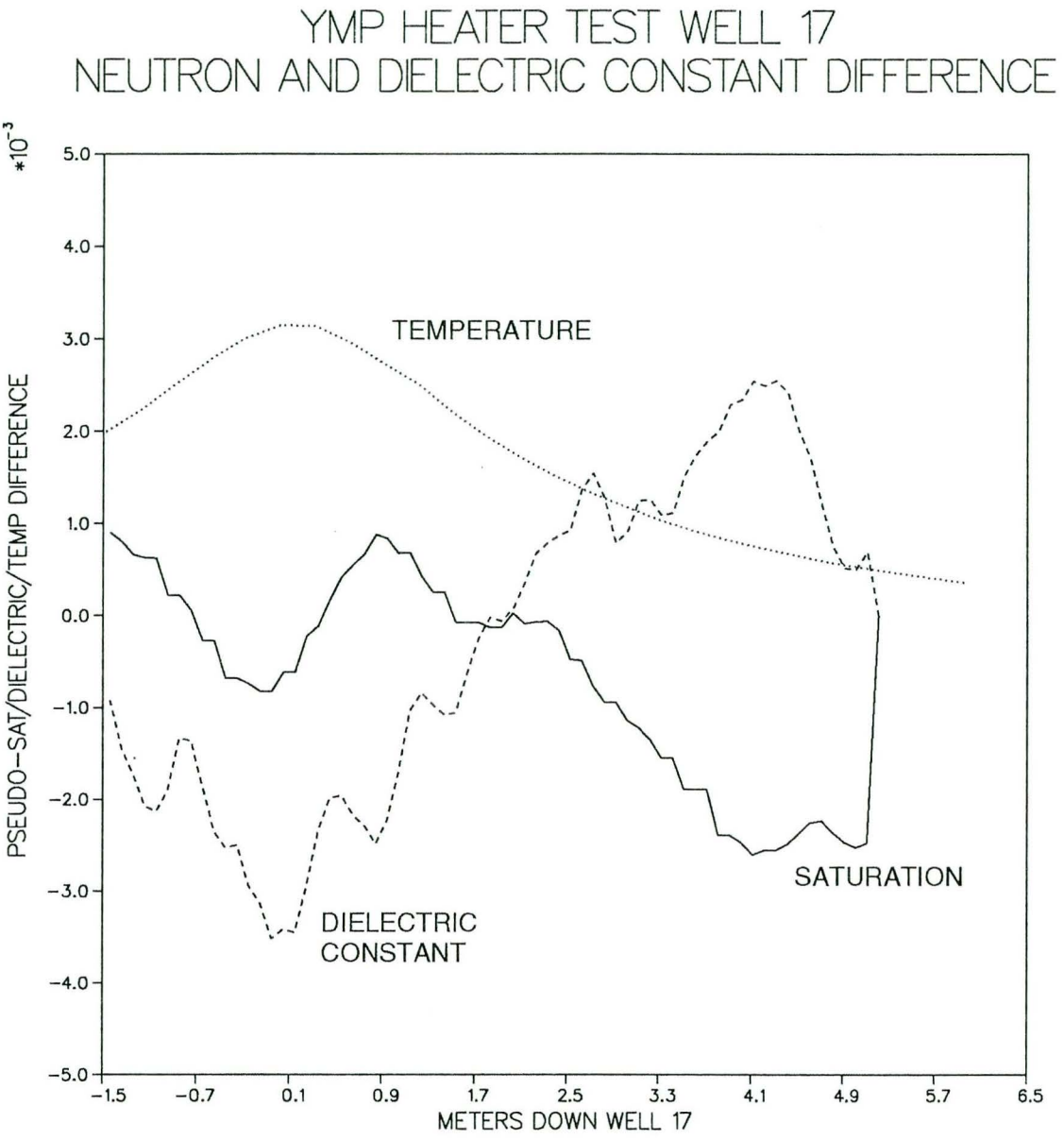

Figure 2.3-17 Normalized change in saturation, temperature, and dielectric constant values down well 17. The values have been normalized to fit on the same plot.

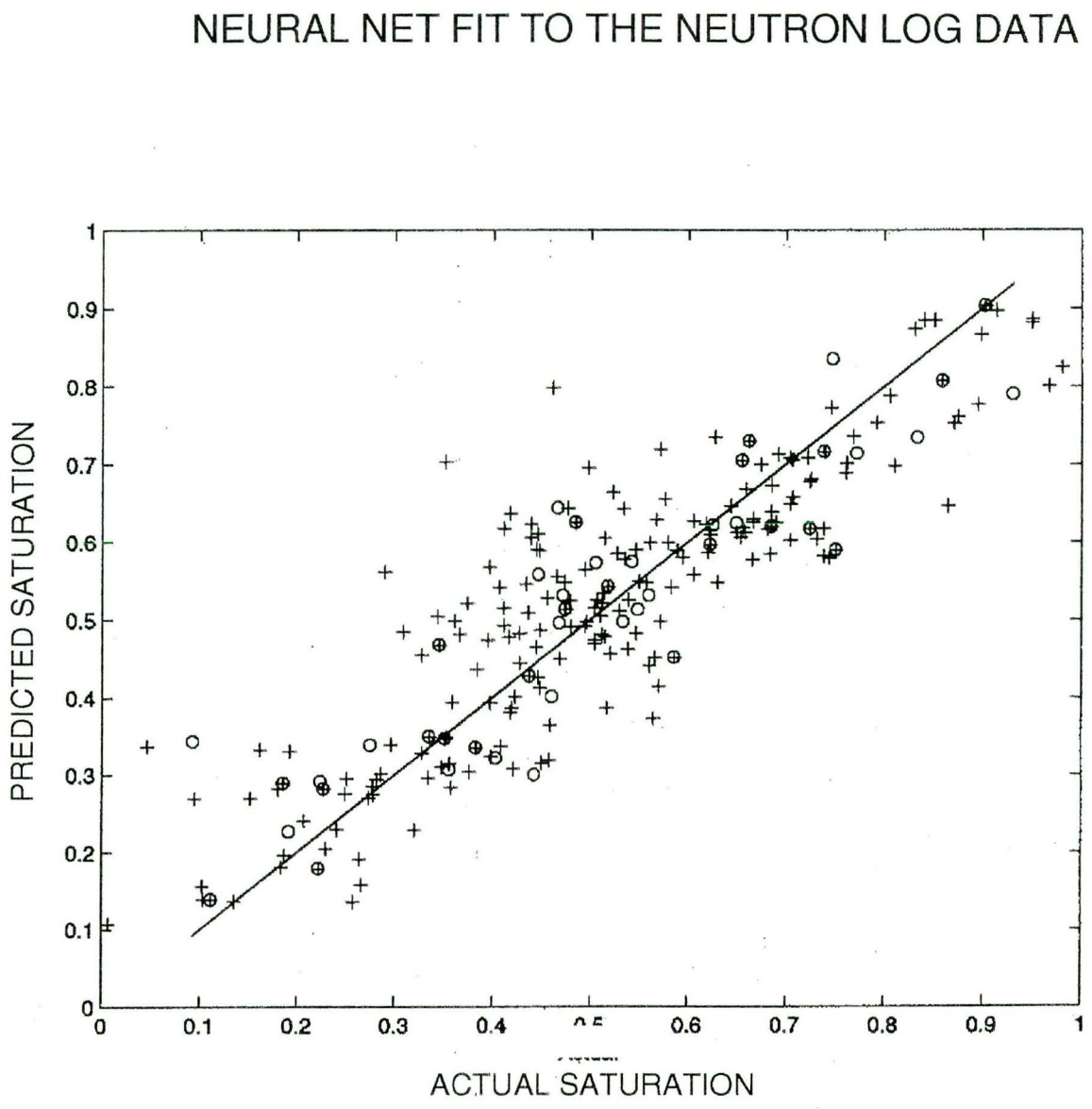

Figure 2.3-18 The observed vs. predicted values obtained from the neural net fit to the neutron log data.

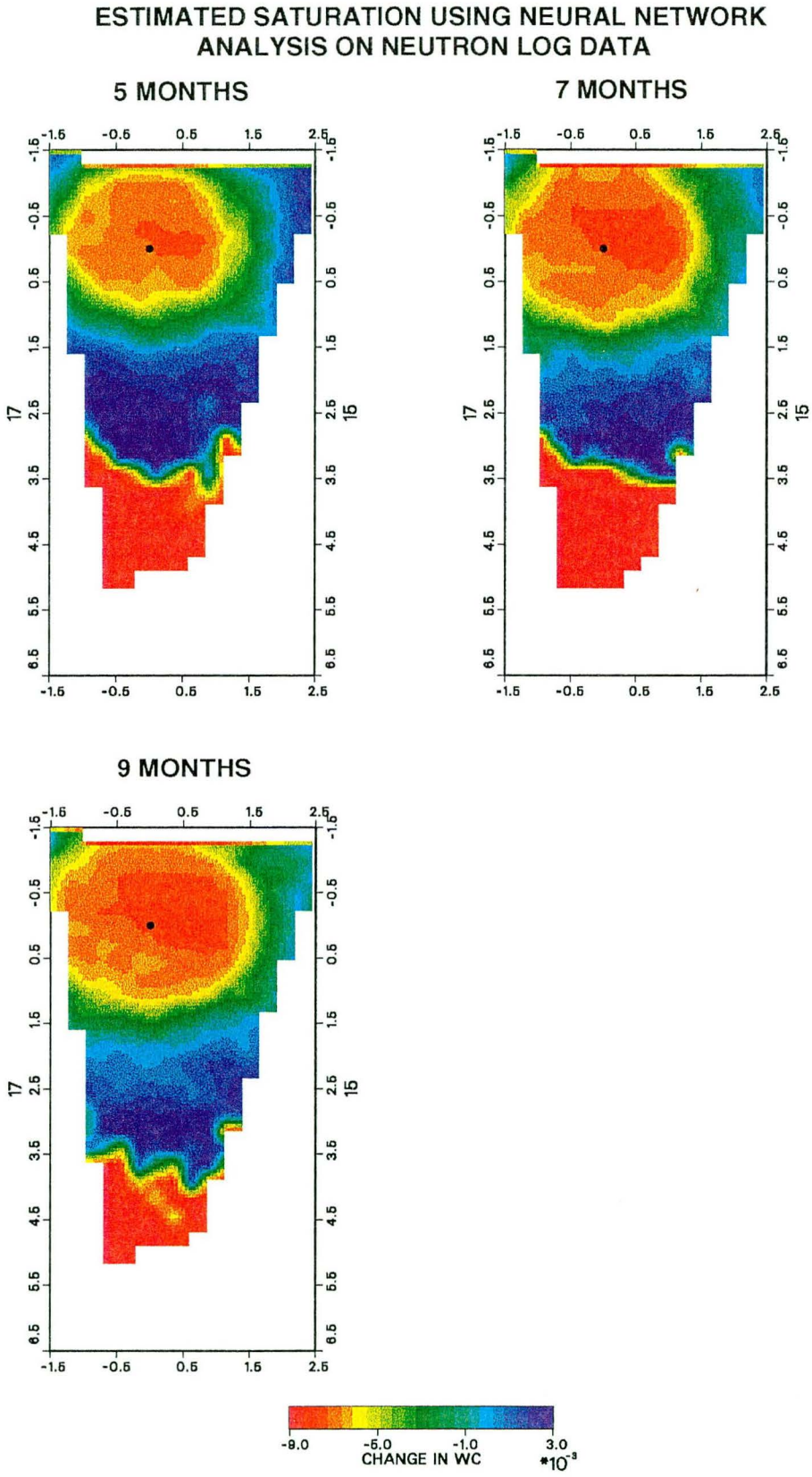

Figure 2.3-19 Estimated saturations from the neural network analysis using neutron log. data.

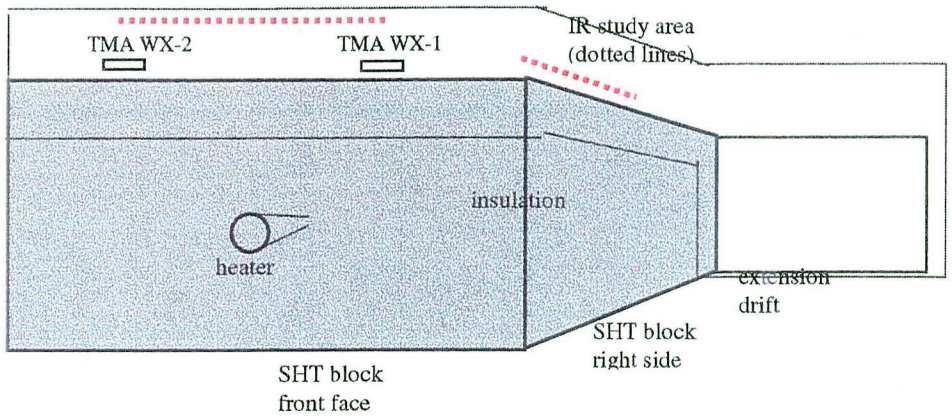

Figure 2.4-1 Diagram of IR study area at the SHT area. Heavy dashed lines show location of temperature plot lines shown in figures 2.4-5 and 2.4-6.

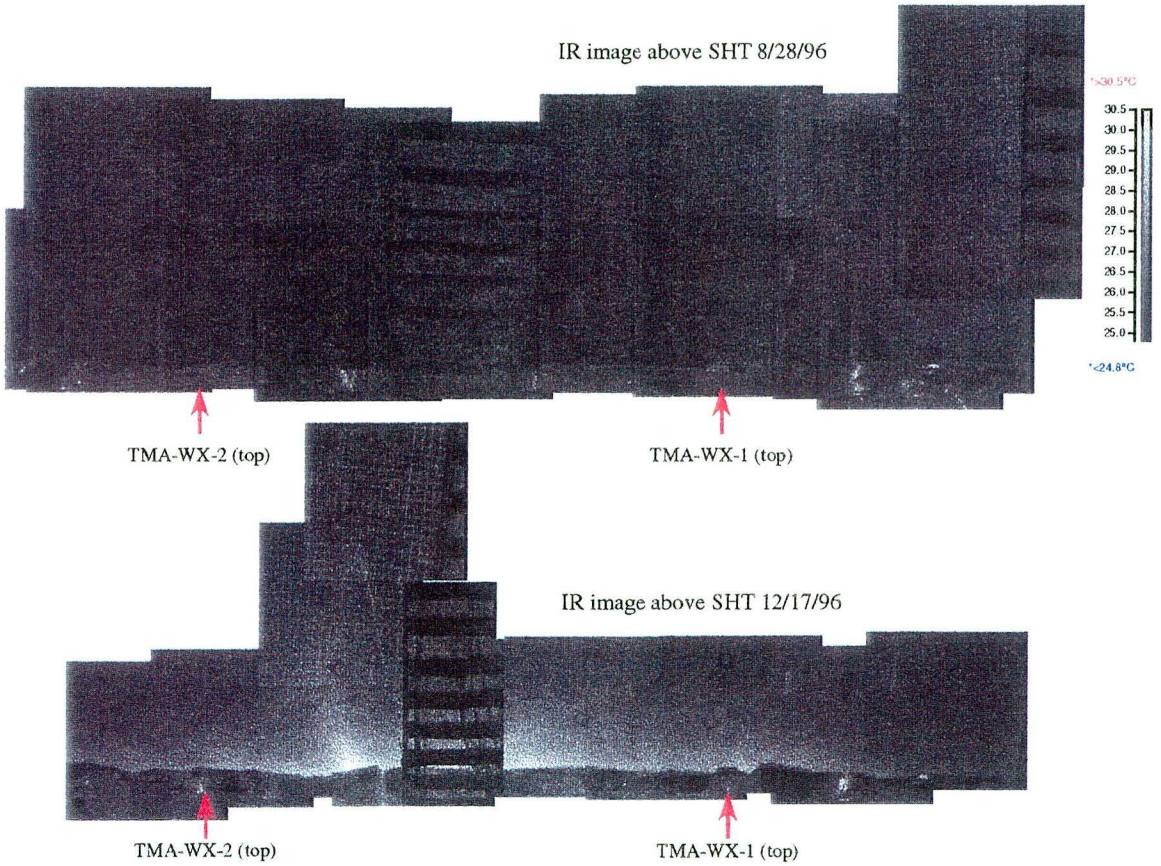

Figure 2.4-2 IR images from the front face of the SHT, August and December 1996.

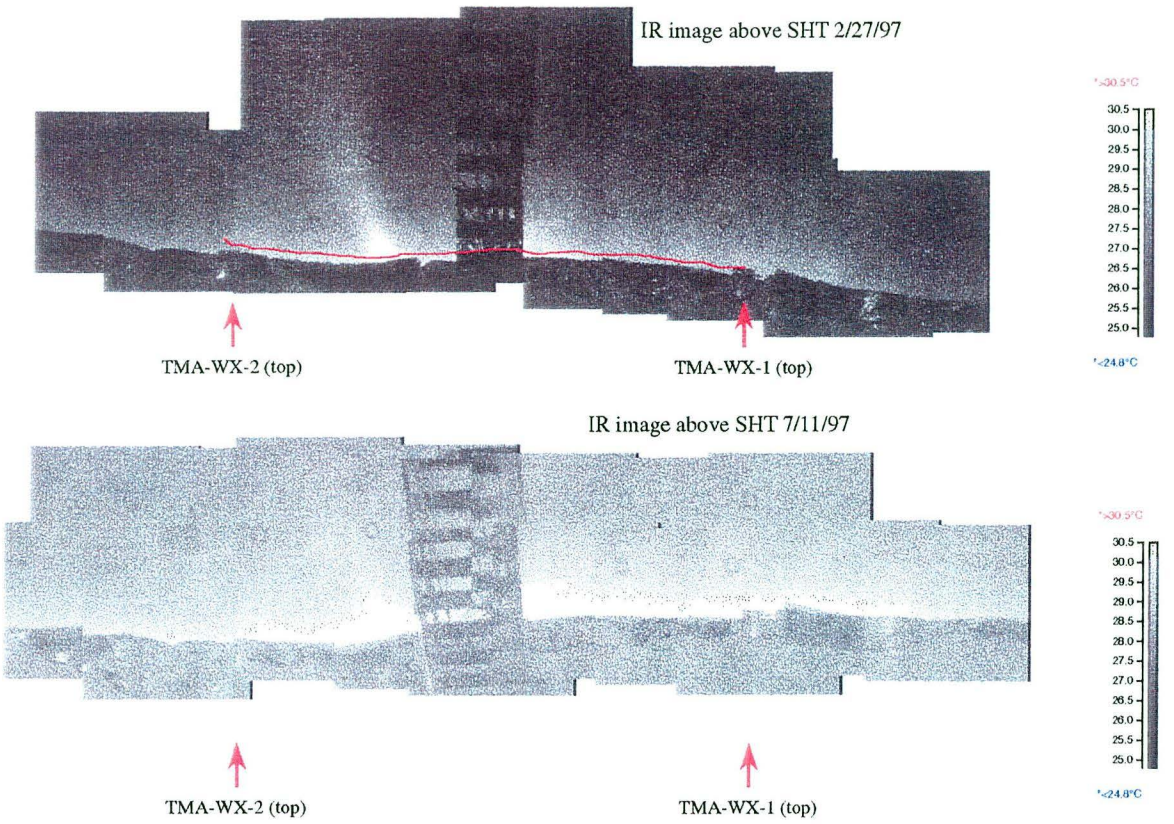

Figure 2.4-3 IR images from the front face of the SHT, February and July 1997.

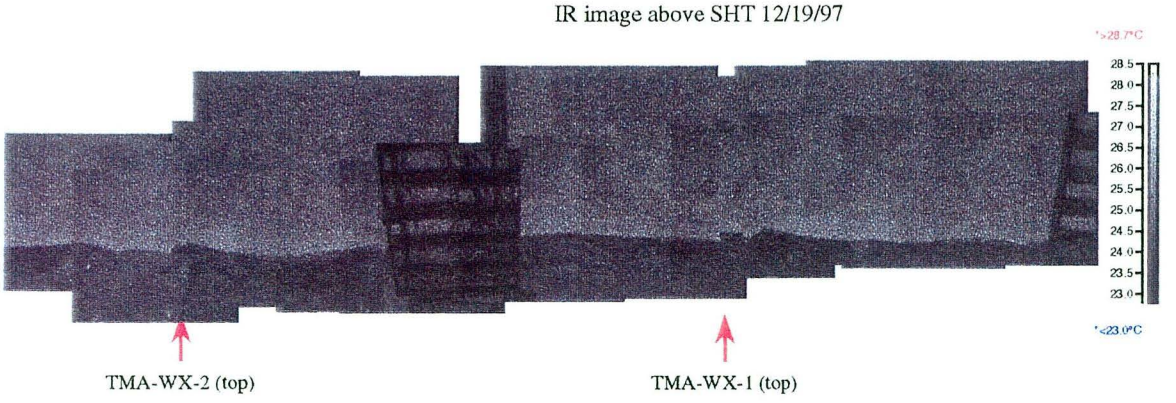

Figure 2.4-4 IR images from the front face of the SHT, December 1997.

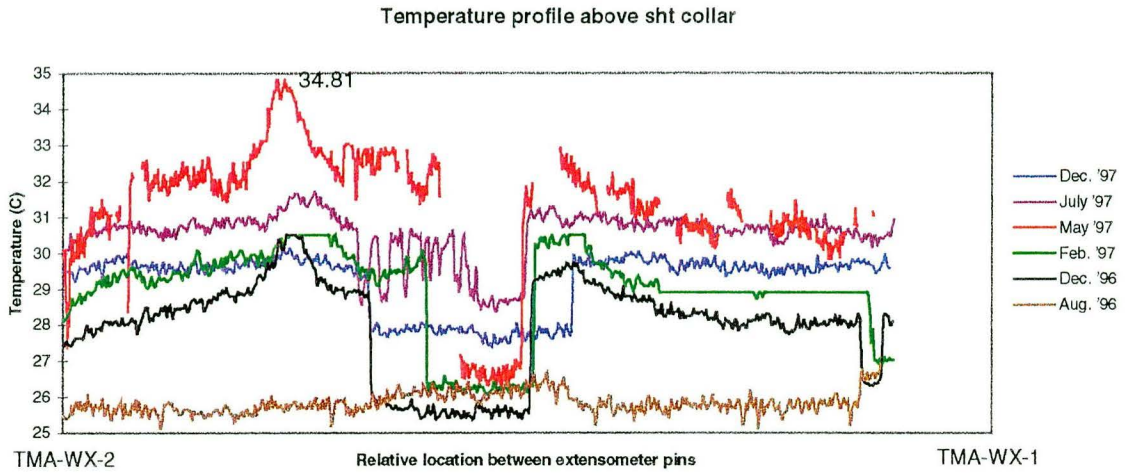

Figure 2.4-5 Line plots of the front face above the insulation. See Figure 2.4-3, February 1997 montage for line location.

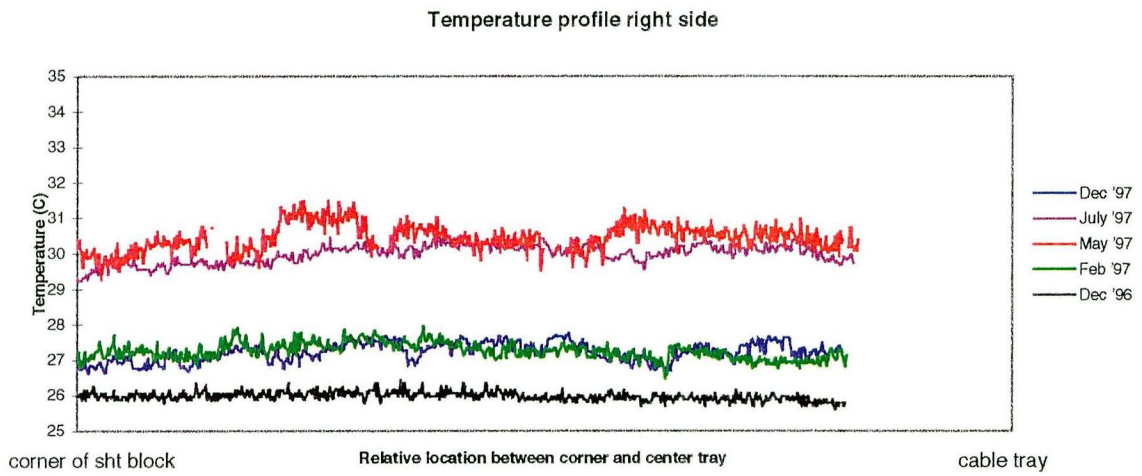

Figure 2.4-6 Line plots on right side above insulation from corner to center of block.

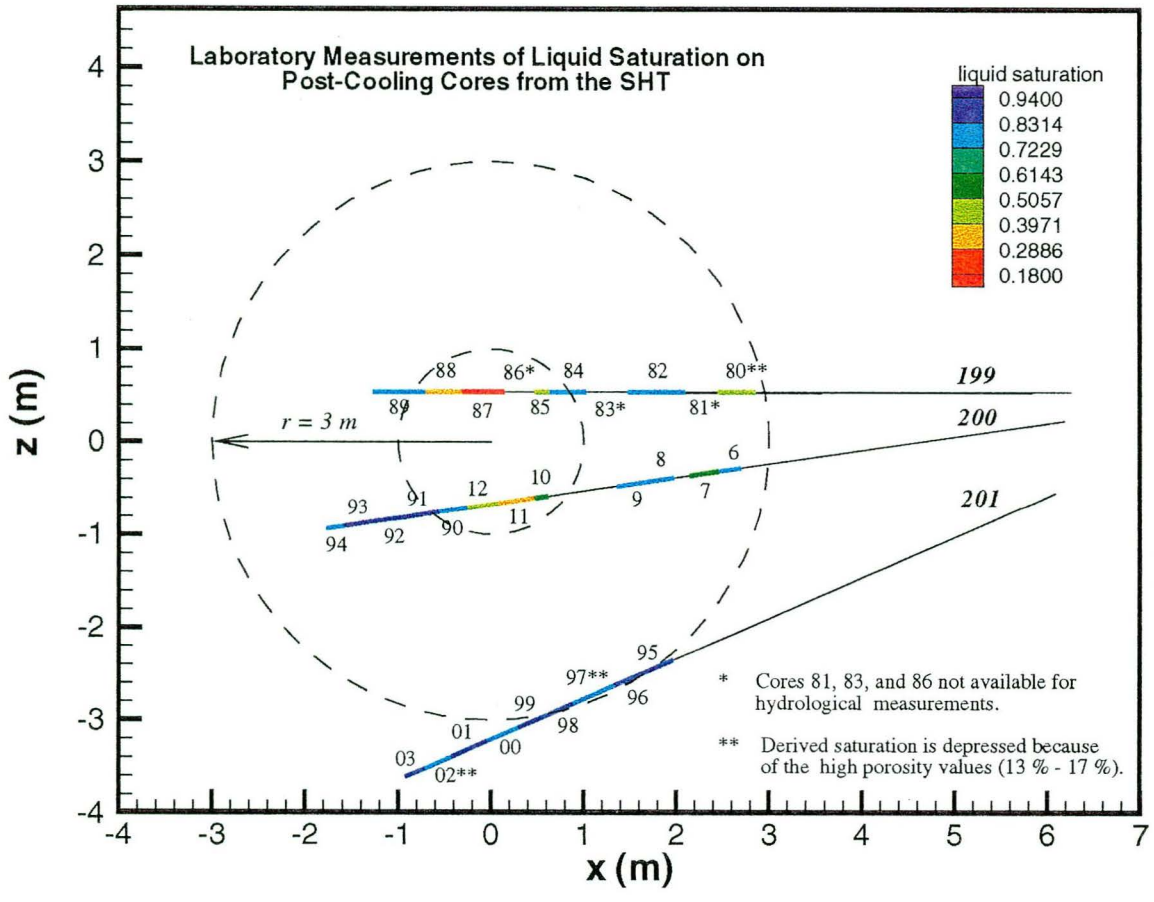

Hole 199 (ESF-TMA-PTC-1):

1009880
1009881
1009882
1009883
1009884
1009885
1009886
1009887
1009888
1009889

Hole 200 (ESF-TMA-PTC-2):

1009806
1009807
1009808
1009809
1009810
1009811
1009812
1009890
1009891
1009892
1009893
1009894

Hole 201 (ESF-TMA-PTC-3):

1009895
1009896
1009897
1009898
1009899
1009900

Figure 2.5-1 Liquid saturation of cores from boreholes 199, 200, 201, dry-drilled after the cooling phase of the SHT.

Chapter 3 Interpretive Analysis of the Thermo-Hydrological Aspects of the SHT

J. T. Birkholzer and Y.W. Tsang

Earth Sciences Division, LBNL

3.1 Introduction

In this chapter, we conduct an interpretive analysis of the thermo-hydrological processes of the SHT during the heating and cooling phases of the test by means of numerical simulations. A three-dimensional numerical model of the SHT was developed to simulate the transient coupled transport of water, vapor, gas, and heat in the rock mass surrounding the heater. The simulated results are compared with the measured data available from extensive active and passive testing (Chapter 2). Special attention is focused on understanding the plausible cause of agreement and discrepancies between data and simulation, with the intent to constrain conceptual model assumptions and input parameter uncertainties in the coupled thermo-hydrological processes. Therefore, in this chapter we include sensitivity studies considering different conceptual models and hydrological properties. These studies provide insight as to how individual processes or parameters affect the thermo-hydrological performance of the SHT.

The numerical model used in this report is based on the three-dimensional predictive model of the SHT developed by Lawrence Berkeley National Laboratory in 1996 (Birkholzer and Tsang, 1996). Since then, some improvements and refinements have been made to the predictive model to better represent the actual test conditions (Tsang and Birkholzer, 1997). Also, a few parameter adjustments were made, based on more recent results from site characterization measurements. The refined numerical model represents our best understanding to date of the SHT; it describes the Single Heater Test realistically with respect to test configuration, rock properties, initial and boundary conditions, etc. The simulated results based on our refined model compare favorably with measured data from the SHT, thus adding confidence in our understanding of the complex processes involved with the heating of unsaturated fractured tuff, and in our ability to predict the performance of the potential waste repository.

3.2 Thermo-Hydrology in the SHT and Model Conceptualization

3.2.1 Pre-Heat Conditions in the SHT Block

The SHT consists of a 5-m long, nominal 5 kW heating element, horizontally placed among 30 instrumented boreholes, which span a block of approximately 13 m x 10 m x 13 m in a side alcove of the underground Exploratory Studies Facility (ESF) at Yucca Mountain (see Figure 1.1-2). Heating commenced on August 26, 1996; heater power was maintained for about 9 months until May 28, 1997. The test block resides in the middle non-lithophysal unit of the Topopah Spring welded tuff (tptpmn) approximately 200 m above the groundwater table. An extensive pre-heating characterization program was carried out to obtain site-specific thermal, mechanical, and hydrological rock properties (see Chapter 2). These site-specific data include laboratory measurements of hydrological properties such as grain density, matrix porosity, and liquid saturation; and thermal parameters such as thermal conductivity, heat capacity, and thermal expansion coefficients. In addition to these site-specific data, numerous laboratory measurements of matrix properties are also available from borehole cores taken from the same geological unit as the SHT. A detailed field characterization by means of air permeability tests was conducted in the SHT block to determine the *in-situ* fracture permeability prior to turning on the heater. Additional fracture information was available from fracture mapping and borehole video logs.

The welded tuff in the SHT block has very low matrix permeability. However, the rock is intensely fractured, with the fracture permeability several orders of magnitude higher than the matrix permeability. The interference pressure data from air-injection tests indicate that the fractures are well connected, because pressure response to injection is obtained in most monitoring boreholes. This is consistent with the borehole videos, showing that all the boreholes are intersected by numerous fractures. A fracture zone with particularly high permeability was identified in the back of the SHT block, connecting the end of the heater hole with some of the monitoring holes.

Due to the low precipitation at Yucca Mountain, the percolation flux in the unsaturated flow regime is very small. At ambient state, the fractures are essentially dry and not very conductive. In contrast, strong capillary forces hold a significant amount of water in the matrix pores, with a liquid saturation of about 80% to 99% at the SHT location (Tsang et al., 1996, page 23, Table 3; Wang and Suárez-Rivera, 1997, pages 17ff, Tables 3 and 4). This water is hardly mobile at ambient state, but can be mobilized when the rock mass is heated above boiling. This can give rise to significant heat-induced moisture redistribution processes in the SHT block (see following subsection).

3.2.2 Potential Thermo-Hydrological Processes in the SHT

Emplacement of a heat source into the unsaturated fractured tuff at Yucca Mountain can initiate very complex thermo-hydrological processes, which depend on the hydrological properties of the fractures and the rock matrix. Most of the key processes potentially involved are reviewed in Figure 3.2-1. As the

formation temperatures rise to 100°C around the heater, matrix pore water boils and vaporizes. Most of the vapor generated moves into the fractures, where it becomes highly mobile, and is driven by the gas pressure gradient away from the heat source. When the vapor encounters cooler rock, it condenses at the fracture walls, and the local fracture saturation builds up. Part of the condensate may then imbibe into the matrix, where it is subject to a very strong capillary gradient towards the heat source, giving rise to a reflux of liquid to the dry-out areas. If matrix imbibition is relatively slow, the condensate may also remain in the fractures and eventually become mobile. Because capillary forces are relatively weak in the fractures, a substantial amount of liquid may drain from the heater by gravity. Occurrence of gravity drainage depends on the strength of vaporization-condensation and fracture-matrix interaction. The stronger the vapor flux away from the heater and the condensate reflux towards the heater, the more obvious will be a "heat pipe" signature in the temperature data, namely, a small temperature gradient at the nominal boiling point. In fact, certain matrix and fracture hydrological properties may give rise to such strong condensate reflux that a stable heat-pipe extends all the way to the heater, preventing the drying of rock and keeping the temperatures near or below 100°C.

The results of vaporization, drying, condensation and rewetting processes in the SHT are reflected in the spatial variation and temporal evolution of the liquid saturation in the rock mass. Changes in the rock mass moisture content have been evaluated by active testing such as neutron logging, electrical resistivity tomography, cross-hole radar tomography, and interference air permeability tests (Chapter 2). In addition, passive monitoring was performed with a multitude of sensors to measure the temperature, humidity, gas pressure, mechanical displacement, and stresses of the rock mass. Both the passive monitoring and active testing data are considered in the analysis and interpretation of SHT (see Section 3.4).

3.2.3 Conceptual Model of the SHT

A model for the SHT must be capable of representing all the important thermo-hydrological processes taking place in the unsaturated fractured rock. Our 3-D modeling study uses the numerical simulator TOUGH2 (Pruess, 1991; Pruess et al., 1996; Wu et al., 1996), which simulates multi-dimensional coupled transport of water, vapor, air, and heat in heterogeneous porous and fractured media. TOUGH2 accounts for the movement of gaseous and liquid phases (under pressure, viscous, and gravity forces according to Darcy's Law, with interference between the phases represented by relative permeability functions); transport of latent and sensible heat; and phase transitions between liquid and vapor. Mass- and energy-balance equations are written in integral form for an irregular flow domain in one-, two-, or three-dimensions. The physical processes of capillary suction and adsorption in the liquid phase, binary diffusion in the gas phase, thermal conduction, and the effect of vapor pressure lowering due to capillary and phase adsorption effects are all accounted for in the model.

A key issue in simulating flow processes in fractured tuffs at Yucca Mountain is the numerical representation of fractures and matrix, and the interaction between them, under multi-phase, non-isothermal conditions. Available concepts representing fracture-matrix systems with numerical models

include (1) an explicit discrete fracture and matrix model, (2) the effective-continuum model (ECM), (3) the dual-permeability method (DKM), and (4) the more general "multiple interacting continue" method (MINC). One question arising from the choice of model concept is whether the fractured system in the SHT block may be considered as a continuum at the scale of interest; a second question deals with the complexity of describing flow of fluid, gas, and heat between fractures and matrix. Because the combined data from fracture mapping, borehole video logs, and air-injection interference tests indicate that the numerous fractures in the SHT block form a well-connected network, it seems appropriate to represent the SHT block with a continuum approach rather than a discrete model. (Furthermore, a discrete-fracture modeling approach would hardly be feasible because of the computational intensity involved and the lack of detailed data describing the discrete fractures.)

The continuum model used for the SHT block must be capable of accurately describing the heat-induced flow processes in fractures and matrix; e.g., the rock must be conceptualized as composed of the matrix continuum with very low permeability, and the fracture continuum with permeability orders of magnitude higher. Also, the model must account for the significant differences in capillarity and storativity in fractures and matrix. All the above-mentioned continuum models—ECM, DKM, and MINC—capture the different characteristics of unsaturated flow in fractures and matrix; however, they differ in the way the fracture-matrix interaction is treated (Figure 3.2-2). The ECM is the most simplified method; it assumes that a local thermodynamic equilibrium is maintained between the fractures and the matrix at all times, thus implying infinitely fast mass and energy exchange between fractures and matrix (Pruess et al., 1990). As a result, gravity-driven liquid flow in the fractures tends to be underestimated, because heat-generated vapor condensing on the fracture walls is readily imbibed into the matrix pores. The DKM conceptualizes the fractured rock as two interacting continua, one representing the matrix, the other representing the fractures, with the fracture-matrix exchange explicitly calculated from the local pressure and temperature difference. Thus, the DKM can account for different transient behavior in fractures and matrix. However, it may sometimes overestimate gravity-driven liquid flow in the fractures, as the rate of condensate imbibing into the matrix can be underestimated for early times when steep gradients occur at the fracture-matrix interfaces. Such steep gradients cannot be appropriately modeled with the DKM, because a linear pressure/temperature distribution is assumed within the matrix blocks. The more rigorous MINC method solves this steep-gradient problem by subdividing the matrix continuum into a number of nested continua defined at different distances from the surface (Pruess and Narasimhan, 1985). This concept allows for representing a non linear distribution of pressure or temperature in the matrix; therefore, the MINC method should be best suited for simulating a localized intense perturbation such as that encountered in the SHT. In terms of computational efficiency, however, the MINC method is less suitable to a complex three-dimensional model, because it requires definition of multiple additional inner grid elements.

As a good compromise between accuracy and feasibility, the DKM is chosen to be the baseline method in our study. We assume that the entire geometric matrix-fracture interface, estimated from fracture mapping along the ESF tunnel walls (Sonnenthal et al., 1997, page 7-9, Table 7.7), participates in the matrix-fracture coupling. A possible reduction of the matrix-fracture interaction—arising from fracture coating,

flow channeling in fractures, and other factors—is not accounted for. For comparison with the DKM simulations, we additionally investigate the ECM concept in a sensitivity analysis (Section 3.4.3).

3.3 Numerical Model of the SHT

3.3.1 Basic Model Assumptions

The thermo-hydrological simulations of the SHT are performed with the Integrated Finite Difference Code TOUGH2 (Pruess, 1991; Pruess et al., 1996; Wu et al., 1996). TOUGH2 is a numerical simulation program for non isothermal flows of multicomponent, multiphase fluids in porous and fractured media. The TOUGH2-EOS4 module is used which simulates the non-isothermal two-phase flow of water and air, and accounts for vapor pressure lowering effects. Fracture and matrix characteristic curves for liquid flow are described by the commonly used van Genuchten model (van Genuchten, 1980), while the relative permeability to gas is calculated from the Brooks-Corey formulation. Thermal conductivity is assumed to be a square-root function of liquid saturation, using a measured conductivity value at high saturation ("wet" conductivity) and a measured conductivity value at low saturation ("dry" conductivity) to define the relationship. Binary vapor-air diffusion rather than enhanced vapor diffusion is implemented.

The dual permeability method is applied to account for the combined effect of matrix and fracture flow. All hydrological properties and initial conditions are assumed to be homogeneous, except for the fracture permeability. We use an average permeability value for the major part of the SHT block, but also represent a local high-permeability feature that was identified from air-injection tests and borehole video logs during pre-heat characterization. The majority of the matrix and fracture property values are directly based on laboratory or field measurements; we refer to them as the base-case properties (see Section 3.3.5). No calibration to measured data from the SHT was performed. The simulation results presented in Section 3.4.1 and Section 3.4.2 of this report are obtained using the base-case model setup. In addition, we present results from a sensitivity study where the conceptual model of fracture-matrix interaction is changed or key hydrological properties of the fractured rock are varied (Section 3.4.3).

The simulation runs cover a 9-month period of heating the rock, and a 12-month period of natural rock cooling, after the heater is turned off. The heater is assumed to operate at a constant 3758 W, which was the average power during the operation of the SHT. A closer look at the time evolution of heater power reveals small fluctuations and a slightly declining trend (Figure 3.3-1); however, none of these is sufficiently significant to account for in the numerical model.

3.3.2 Model Domain

The computational domain for the thermo-hydrological simulations includes the actual test block plus significant rock volumes added in all directions to guarantee a proper definition of boundary conditions (Figure 3.3-2 and 3.3-3). The top and bottom boundaries of the model area are 14 m each from the heater axis; they are sufficiently far from the heater that they can safely represent infinity conditions (i.e., constant primary variables). The north and south boundaries extend to the outer wall of the bounding drifts, i.e., the Observation Drift on the north side and the Thermomechanical Alcove Extension on the south side. The distance from the heater centerline to the south boundary is 10.76 m, which is defined by the 6.26-m distance from the heater to the alcove inner wall plus the 4.5-m alcove width. The north boundary is at 11.59 m, defined by the 6.59-m distance to the Observation Drift wall and the 5.0-m drift width. The eastern boundary extends to the outer wall of the Thermomechanical Alcove; the western boundary is 17 m from the inner wall of the Thermomechanical Alcove, sufficiently far from the heater to represent a no-flow boundary for fluid, gas and heat.

3.3.3 Computational Grid Design

Grid generation is an important part of developing a complex 3-D model. The aim of grid generation is to achieve a proper balance between desired numerical accuracy and computational effort, both of which are controlled by the total number of gridblocks. In the SHT, the grid must be compatible with sharp gradients of temperature, saturation, and pressure that may occur at different distances from the heat source as time progresses. At the same time, geological features must be captured, and the special geometry of the test must be realistically represented.

Several automatic grid-generation modules have been developed to allow for accurate and efficient generation of 2-D and 3-D grids. In a first step, a 2-D vertical mesh is designed within the local XZ-plane, i.e., orthogonal to the heater centerline. Local mesh refinement is particularly important in this plane, because most of the heat produced is released transverse to the heater axis. In a second step, the complete three-dimensional SHT grid is created by appropriately extending several vertical 2-D planes into the third dimension and merging them.

Figure 3.3-4 shows an XZ-cross section of the grid. The origin of the coordinate system is at the collar of the heater hole. Fine gridding and radial symmetry is maintained around the heater hole up to a radius of 2.9 m, at which distance the grid is converted gradually to cartesian in order to better represent the boundaries of the drift and alcove walls. The size of the gridblocks increases with distance to minimize the number of computational elements. The radial increments start as small as 2.2 cm at the heater hole and increase to 50 cm at a distance of 5 m. This discretization is very fine close to the heat source in order to guarantee a proper representation of the physical processes, but rather coarse away from the heater in order to avoid excessive computational load. The Observation Drift and the Thermomechanical Alcove Extension are cut out from the model area, and their walls are treated as inner model boundaries.

Nineteen 2-D element planes are merged in the Y-direction to generate the entire 3-D mesh. (The Y-direction extends along the heater axis, perpendicular to the XZ-cross section shown above.) Figure 3.3-5 shows a horizontal cross section (i.e., XY-plane) of the grid at Z = 0.0. Starting from the Thermomechanical Alcove wall at Y = -5.5 m, the first two element planes represent the rock volume above and below the alcove (-5.5 m < Y < 0.0 m). The next five planes represent the 2-m standoff between the west wall and the heater (0.0 m < Y < 2.0 m). The following six planes represent the 5-m heater length (2.0 m < Y < 7.0 m). The last six planes extend from the heater to a no-flow boundary at Y = 17.0 m. The entire 3-D grid consists of about 30,000 gridblocks and more than 100,000 connections between them. Figure 3.3-5 also indicates the location of the fractured zone with higher permeability, which had been identified in the pre-heat characterization effort. The 40° strike azimuth feature is represented by extending the fracture zone over three different element layers in the XY-plane. In the Z-direction, the high-permeability zone extends from -2.8 m to 1.2 m. (Note that the displayed grid in Figure 3.3-5 does not show the actual interfaces between gridblocks in the finite difference discretization. The post-processing software automatically designs a mesh by connecting the center nodes of each finite difference grid. These post-processed meshes are depicted here.)

About 30 boreholes were drilled into the SHT block for passive monitoring and active testing. Several boreholes, in particular those specifically designed for temperature measurements, were grouted after instrumentation. Others, however, were left open for testing, for example those boreholes designed for displacement measurements. These open boreholes may act as conduits for vapor flux, and may possibly allow for significant gas-driven convective heat flow in axial direction. This phenomenon cannot be accounted for in the model, because boreholes are not explicitly represented in the numerical grid.

3.3.4 Boundary and Initial Conditions

The top and the bottom of the model domain are modeled using a constant primary variable boundary condition; i.e., pressure, saturation, and temperature in fractures and matrix are fixed at given values throughout the simulation period. All lateral boundaries are modeled as no-flow boundaries for heat, liquid, and gas. These definitions imply that the outer boundaries of the model domain are not affected by the heat source, which is a valid assumption because they are far enough away from the heater.

All the drifts included in the model domain—Observation Drift, Thermomechanical Alcove, and Thermomechanical Alcove Extension—are modeled by constant pressure, temperature, and saturation conditions, assuming that they are ventilated and the heating of the rock does not affect the parameters in the open drifts. No attempt was made to model the initial drying of the rock adjacent to tunnel walls due to ventilation. The relative humidity of the drifts is fixed so that the open void is in equilibrium with the adjacent rock at initial state. The drift walls are open for liquid and gas to escape from the model domain; however, no liquid or gas can enter the model domain from the alcoves.

The test block is insulated from the alcove walls with a low thermal conductivity material to minimize heat losses from the rock. This insulation is explicitly represented in our model, with a thickness of 15.2 cm, a thermal conductivity of 0.0447 W/(m^2 K), a density of 32 kg/m^3, and a heat capacity of 835 J/(kg K) (Birkholzer and Tsang, 1996, page 15). Note that in our model the insulation material allows moisture to escape from the test block in the form of both liquid water and vapor. A similar insulation material is used as a backfill in the heater hole for the 2-m standoff between the borehole collar and the heater element. The floor and the ceiling of the alcoves are not insulated; thus, they represent boundaries with constant primary variables.

Heater power is applied in the model at a constant rate throughout the entire heating period, starting from August 26, 1996, to May 28, 1997. The assumed power of 3758 W is the average for the heating period of 275 days and 2 hours. During the operation of the SHT, anomalous data were occasionally observed when the power to the heater was temporarily interrupted (Figure 3.3-1). Longer heater down times were observed on day 112 (15.8 hours), day 118 (23.1 hours), day 139 (24.6 hours, and day 202 (13.6 hours). The four long power outages were sufficiently strong as to temporarily influence the temperature data in nearby gages (Finley, 1997, page 15). Also, there was a slight trend of declining heater power over the 275 days of heating, probably due to the aging of heaters. However, none of the anomalies and trends observed was too severe, so that the constant heater power assumed in the model is a fair approximation.

The heater simulation runs start from a fully equilibrated initial situation in the test block. The initial conditions are a gas pressure of 87.0 kPa, a temperature of 25°C, a matrix liquid saturation of 0.92, and a fracture liquid saturation of 0.046. No geothermal and gas pressure gradients are assigned because of the small vertical extension of the model. A typical geothermal gradient of 0.02°C/m would only give a temperature difference of 0.56 degrees between the top and the bottom boundary, which is negligibly small compared to the perturbation enforced by the heater. This is similarly true for the potential gas pressure variation between the top and bottom of the model area. Also note that the ventilated alcoves surrounding the test block provide a constant barometric pressure boundary to the rock, so that the natural gas pressure field has already been altered at ambient state.

The chosen initial matrix liquid saturation of 0.92 is the average value for the tptpmn measured in cores from surface borehole SD9, which is in close proximity to the heater alcove (Flint, 1998, page 50, Table 9). This relatively high saturation is consistent with the laboratory data from grab samples obtained directly from the SHT block (Tsang et al., 1996, page 23, Table 3; Wang and Surez-Riviera, pages 17ff, Tables 3 and 4; also Chapter 2 of this report, Tables 2.5-1 and 2.5-2) where values ranging from 0.805 to 0.99 have been reported. The chosen fracture liquid saturation is not a measured value; it is derived from the assumption of thermodynamic equilibrium between the matrix and fracture continua at initial state. Applying the van Genuchten characteristic relationships and using the chosen characteristic properties for matrix and fractures (see Subsection 3.3.5), the matrix saturation of 0.92 results in a fracture saturation of 0.046 at equilibrated capillary pressure.

The initial values of gas pressure, saturation and temperature are also used to define the constant primary variable boundaries at the top/bottom of the model domain, and at the alcove walls. In prescribing saturation at the upper boundary, we implicitly define a gravity-driven percolation flux entering the model area from above. For the saturation values chosen to represent the initial state—0.92 in the matrix, 0.046 in the fractures—the percolation flux is quite small, on the order of 1 mm/yr or less, because the fractures are almost dry and non-conductive. This is somewhat smaller than current estimates of percolation at Yucca Mountain, which range from about 1 mm/yr up to 10 mm/yr. Our sensitivity studies indicate, however, that the thermo-hydrological situation in the SHT is only slightly affected by the actual amount of percolation, because the heat-induced fluxes are much larger than any reasonable estimate of percolation flux at Yucca Mountain.

3.3.5 Model Parameters

The hydrological and thermal input parameters used in the numerical simulations for the SHT are based mainly on laboratory or field measurements. All values are qualified if not otherwise indicated. Table 3.3-1 lists all the hydrological and thermal input values used for the SHT analyses. Table 3.3-2 gives the sources for these values and lists the Q status of the data.

For the base-case property set, site-specific measurements from the SHT block are used whenever possible; otherwise, data measured at other locations in the tptpmn unit are incorporated. In some cases, properties are estimated from the current calibration efforts for the UZ site-scale model (Bodvarsson et al., 1997, Chapter 6, page 6-1ff). With the exception of fracture permeability, all model parameters are assumed to be homogeneous. Note that most of the model parameters remain unchanged from the predictive modeling effort performed in 1996 (Birkholzer and Tsang, 1996, page 12, Table 3.3-1). No calibration to measured data from the SHT was performed; i.e., no parameter adjustment of measured property values was needed to arrive at a good agreement between measured and simulated temperature data. In addition to the base-case parameter set, we performed sensitivity studies by perturbing certain key parameters of the fractured rock.

Here we discuss the model parameters for the base-case property set item by item. Most matrix properties are measured on core samples from surface-based boreholes, representing an average over the different locations in the tptpmn unit. The matrix grain density of 2530 kg/m^3 is the particle density given in Flint (1998, page 44, Table 7). This value is consistent with laboratory measurements of cores from the Single Heater Test area (Tsang et al., 1996, page 23, Table 3; Wang and Suarez-Riviera, pages 17ff, Tables 3 and 4; also Chapter 2 of this report, Table 2.5-1 and 2.5-2). The average matrix porosity of all core measurements in the tptpmn is reported to be 0.11 (Flint, 1998, page 44, Table 7). Permeability data are available for surface boreholes SD9 and UZ16. The average matrix permeability given in Flint (1998, page 44, Table 7) is 4.0×10^{-18} m^2. Matrix van Genuchten parameters have been measured in three samples from surface borehole UZ16. The values given in Flint (1998, page 45, Table 8) are 6.4×10^{-7} Pa^{-1} for α, 1.47 for β, and 0.18 for residual liquid saturation. We use the measured residual

saturation value only for the relative permeability function. In the capillary pressure function we apply a zero residual saturation to avoid the extremely strong increase of capillary pressure at small saturations levels.

Fracture porosity and frequency were estimated by Sonnenthal et al. (1997, pages 7-9, 7-15, Tables 7.7, 7.15) based on ESF fracture mapping. We use a fracture porosity of 0.000124 and a fracture frequency of 1.88 1/m. The fracture permeability values are estimated from air-injection tests performed in the SHT block prior to heating, as previously discussed in Section 3.2.3. We assign the median of all measured air permeability values (i.e., 5.8×10^{-14} m^2) to most of the SHT block (Tsang et al, 1996, page 11, Table 1). In addition, we account for a zone of higher permeability (i.e., 5.2×10^{-12} m^2) at the southeast end of the heater element. No measurements of the van Genuchten properties of fractures are available. Here, we base our choice on average values for the tptpmn estimated from calibration efforts for the Yucca Mountain Site Scale Model (Bodvarsson et al., 1997, pages 6.32ff, A22ff, Tables 6.4.1-2, 6.5.1-1 through 6.5.5-1). Van Genuchten α-values calibrated with the UZ site scale model typically range from 10^{-5} Pa^{-1} to 10^{-3} Pa^{-1}. In our model, we use a value at the high end of this range, i.e. $\alpha = 10^{-3}$ Pa^{-1}, which represents a rather small capillarity in the fractures. This value is consistent with estimates derived in Sonnenthal et al. (1997, page 7-16, Table 7.13). The van Genuchten β is chosen to be 1.47, a value similar to the respective matrix parameter. Residual liquid saturation for the fracture continuum is chosen to be 0.01 in the relative permeability function, and zero in the capillary pressure function. Obviously, as the characteristic properties of the fractures have not been measured, the uncertainty associated with these parameters is significant. Therefore, in Section 3.4.3, we analyze the sensitivity of the simulated temperatures to some key hydrological properties, including van Genuchten properties for the fractures.

The thermal properties required to model the thermo-hydrological situation in the SHT are thermal conductivity (which may be temperature and saturation dependent) and heat capacity. Thermal conductivity is assumed to be a square-root function of liquid saturation, using two coefficients, a thermal conductivity value at low saturation ("dry") and at high saturation ("wet"). Site-specific conductivity measurements are available from six rock specimens taken from the thermal test domain in Alcove 5. Recent analyses of these data give a "dry" conductivity of 1.71 W/(m °K) and a "wet" conductivity of 2.14 W/(m °K) (Brodsky, 1998, page 16, Table 5). Due to a change in calibration procedure, however, these values are slightly higher than earlier estimates, approximately by 0.1 W/(m °K). In our model, we use earlier reported values, i.e., a "dry" conductivity of 1.67 W/(m °K) and a "wet" conductivity of 2.0 W/(m °K). These values are identical to the tptpmn-properties chosen for the Drift Scale Test model (Birkholzer and Tsang, 1997, page 20, Table 4.3-2). Note that the predictive model for the SHT (Birkholzer and Tsang, 1996, page 12, Table 3.3-1) did not distinguish between "dry" and "wet" thermal conductivity values; a constant 1.67 W/(m °K) was applied to all saturation conditions (Sobolik et al., 1996, page 17, Table 5). This approximation, however, proved to be unsatisfactory. The heat capacity of 953.0 J/(kg °K) was calculated based on experimentally determined values of thermal capacitance, given in Brodsky et al. (1997, page 48, Table 4-8) for different temperature ranges. The heat capacity of 953.0 J/(kg °K) used in the SHT model is very similar to the heat capacity of 948.0 J/(kg °K),

calculated by Francis (1997, page B-4, Table B-1) and Ho and Francis (1997, Table 2) for use in TSPA-VA. Francis (1997) and Ho and Francis (1997) used slightly different assumptions for the sample liquid saturation when deriving heat capacity from the experimentally determined thermal capacitance values.

Reasonable numbers for the vapor diffusion parameters are $D^{o}_{va} = 2.14 \times 10^{-5}$ m^2/s and $\theta = 2.334$, after Pruess and Tsang (1994, page 10, Table 1). A reasonable number for the tortuosity factor of the path followed during the gas diffusion process is $\tau = 0.2$. These parameters are non-Q, as no measurements exist; however, the effect of binary vapor-air diffusion is very small compared to other thermo-hydrological processes.

Note that the parameter distribution is assumed to be isotropic. We assign rock properties for all boreholes except for the heater hole, thus making the implicit assumption that wiring, grouting, and instrumentation in the test block do not affect the thermo-hydrological behavior. Possible chemical or mechanical alterations in response to the heating are not included in this study. However, thermal-mechanical coupled processes have been considered and analyzed by other SHT thermal testing team members (Sobolik et al., 1996; Finley, 1997). Chemical processes are studied and discussed in detail in Chapter 4 of this report.

3.4 Simulation Results and Comparison to Measured Data

Introducing a heat source into the unsaturated fractured tuff at Yucca Mountain may give rise to strong two-phase flow effects, typically characterized by the following:

(1) drying of the rock and vaporization of pore water close to the heater;

(2) vapor transport away from the heated area due to gas pressure build-up;

(3) condensation of the vapor in cooler regions outside of the drying zone;

(4) reflux of condensate to the vicinity of the heating due to capillary suction; and

(5) drainage of water away from the heated area due to gravity.

These processes are reflected in the spatial variation and temporal evolution of the liquid saturation in the rock mass. They also contribute to heat transfer in the near-field environment, as heat-induced gas and liquid fluxes may give rise to significant convective heat transport. For example, strong vapor-liquid counterflow may be reflected in a distinct "heat pipe" temperature signal, i.e., the temperature values remain at the nominal boiling point for some time before they continue to increase. The relative importance of convective heat transfer compared to heat conduction is related to the respective hydrological properties of the rock, as well as to the temporal and spatial scale of the heat perturbation. Careful analysis of SHT data from both active tests and passive monitoring can help constrain

hydrological properties of the fractured rock mass, and can serve to evaluate the applicability of different conceptual modeling approaches.

In this section, we present both a qualitative and quantitative discussion of SHT model results in comparison to field measurements from the heating and cooling phase of SHT. The simulated data are calculated with the base-case model described in Section 3.3; i.e., the results described below are obtained using a three-dimensional representation of the SHT, applying the dual-continuum model for fracture-matrix interaction, and assigning the rock properties given in Section 3.3.5. In Section 3.4.1, we present contour plots and profiles of simulated temperature, fracture, and matrix saturation in the rock at different stages during the test. This is intended to provide a basic understanding of the important processes related to the heating of the formation. We discuss the simulated results in a qualitative comparison with active and passive testing results. In Section 3.4.2, we provide a more detailed quantitative comparison of model results to measured data, specifically the temperature measurements in several instrumented boreholes. Statistical measures are applied to evaluate the "goodness-of-fit" between simulated and measured temperature. The impact of alternative fracture-matrix interaction concepts and different hydrological property sets is discussed in Section 3.4.3.

3.4.1 Qualitative Discussion of Simulation Results

Simulated temperature results for the SHT are presented in Figures 3.4-1 and 3.4-2 at 3 months and 9 months from the onset of heating, respectively. The figures include two graphs. The first graph is a contour plot on the YZ–plane showing a vertical cross section oriented orthogonal to the heater axis in the center of the 5-m-long heater element; i.e., at Y = 4.5 m in the plane of boreholes 16 and 18. The locations of boreholes 16 and 18, used for active and passive hydrological testing, are also indicated. The symbols along the borehole axis mark the positions of sensors for temperature, pressure, and relative humidity measurements. The second graph describes the temperature profile along the vertical axis at X = 0.0 m. The z-axes of both graphs are identical. All temperature values correspond to the matrix continuum; the fracture temperature distribution is almost identical.

Figures 3.4-1 and 3.4-2 show that rock temperature close to the heat source increases very rapidly after turning on the heat, resulting in strong localized perturbations. The maximum temperature has already reached about 275°C after 3 months of heating. At later stages, the temperature buildup is slower, reaching the maximum of about 300°C at the end of the nine-month heating period. The temperature distribution shows an almost perfect radial symmetry around the heater centerline, indicating that the heat transport is conduction-dominated. The 50°C-isotherm is at a radial distance of about 2.0 m at 3 months of heating, and moves out to about 3.3 m at 9 months from the onset of heating. The zone of temperature above the nominal boiling point, however, is much smaller, extending to approximately 1.2 m from the heater at the end of the heating period. A sufficiently large zone of boiling is an important feature of the test, because it gives rise to significant moisture redistribution. The very good match between the simulated and measured temperature data in the SHT block is discussed in the following Subsection 3.4.2.

Figures 3.4-3 through 3.4-6 show simulated liquid saturation contours after 3 months and 9 months of heating in the fracture and matrix continuum, at the same vertical cross section. Vertical saturation profiles are also presented. During heating, moisture is driven by the gas pressure gradient away from the boiling zone in the form of vapor, mainly through the fractures because of the low matrix conductivity. As a result, the rock close to the heater is dry, with saturation values below residual. At the end of the heating period, drying has extended to a radial distance of about 1.2 m from the heater. In cooler regions, the vapor condenses at the fracture walls, resulting in an increase of liquid saturation in both fractures and matrix. Fracture saturation increases to values of about 0.6 at 3 months of heating, from an initial saturation of only 0.046. Strong downward drainage flux is noticeable below the heater, indicating that the capillary pressure gradient in the fractures is overcome by gravity. In the matrix, the simulated saturation build-up in the condensation zone is less apparent and less extended than in the fractures. Apparently, the vapor condenses and flows in the fractures faster than it is drawn into the matrix, so that only a small fraction of condensate imbibes into the rock pores. This leads to a condition of disequilibrium between fractures and matrix. The rock matrix is drier above the heater than below, not because of gravity-driven liquid flux in the matrix, but because of the downward drainage in the fractures and subsequent imbibition into the matrix pores. The thermally induced liquid fluxes are orders of magnitude higher than the ambient percolation flux at Yucca Mountain. Comparison of the 3-month with the 9-month results indicates that most of the moisture redistribution occurs during the first months of heating; the heat-driven processes are slower in the later stages of the test.

Figure 3.4-7 presents the simulated rock temperature after about 1 year into the test, i.e., at 3 months from the onset of the cooling phase. The rock mass has cooled off substantially; the maximum temperature in the test block is slightly above 40°C. Figures 3.4-8 and 3.4-9 show the saturation distribution in fractures and matrix after 3 months of the cooling. Because the rock temperature drops below nominal boiling almost immediately after the heating stops, vaporization and condensation processes have disappeared. The strongly dynamic nature of flow during heating becomes less pronounced, and the pressure and saturation gradients tend to equilibrate. This equilibration process is very slow in the matrix so that the moisture redistribution established during heating is still apparent after 3 months of cooling. The dominant mode of fluid movement during cooling is capillary-driven flux in the matrix, mainly directed toward the heater, and slowly rewetting the dry-out region. Gravity drainage in the fractures and matrix imbibition probably occurs only during the early stages of cooling, when fractures and matrix are not in equilibrium.

The redistribution of the moisture content described by the numerical model is consistent with the results of active and passive hydrological testing (see Chapter 2). Active tests, such as cross-hole radar tomography and air injection, had been conducted prior to and periodically during the SHT. Radar tomography was performed in boreholes 15, 17, 22, 23; air-injection tests were performed in boreholes 16 and 18. All these boreholes are orthogonal to the heater axis and located in the mid-plane of the heater element at approximately Y = 4.5 m. Radar tomography data probes the change in water content in the matrix (which is strongly related to the porosity), while air permeability tests give information about

liquid saturation changes in the fractures. Continuous passive hydrological monitoring of pressure and relative humidity was performed throughout the entire test period at four locations in boreholes 16 and 18, respectively.

Cross-hole radar surveys were carried out before the onset of heating, and then after about 5 months, 7 months and 9 months of heating (Section 2.3). The radar velocity fields produced from tomographic inversion at 5 months show an increase of velocity close to the heater and a decrease about 1 m away from the heater toward the alcove walls. A radar velocity increase is indicative of liquid saturation decrease in the matrix, while velocity decrease the opposite. Thus the survey is consistent with the thermo-hydrological conditions of a drying zone around the heat source and a condensation zone commencing about 1 m away, as obtained by the simulations (Figures 3.4-3 through 3.4-6). The tomograms at 7 and 9 months show a further velocity increase near the heater compared to the 5-month results, but no significant changes in the areas beyond the 1-m radius. This indicates a more extended drying zone, but a rather constant spatial extent of the condensation zone, and is in agreement with simulated results that show most of the liquid saturation build-up occurring in the first 3 months of heating. Another survey was performed in January 1998, about 7 months into the cooling phase of the test. The test results still show a drying zone, not too different from that delineated by the 7- and 9-month velocity fields, indicating less dynamic thermo-hydrological processes after the heat is turned off.

The formation of a zone with increased saturation during the first few months of heating is also corroborated by the air permeability data obtained during heating and cooling in boreholes 16 and 18 (Section 2.1.2). To demonstrate the qualitative agreement between simulation and test results, we shall analyze the simulated thermo-hydrological situation in the vicinity of borehole 16 in more detail. Figures 3.4-10 through 3.4-13 present temperature and saturation measured along this borehole at 3 and 9 months of heating, and at 3 months and months of cooling. Air-injection tests were carried out in three different zones approximately extending from sensor 16-1 to 16-2 (Zone 1), from 16-2 to 16-3 (Zone 2), and from 16-4 (Zone 3) all the way to the end of the hole. The location of the sensors (pressure transducers and humidity sensors) is given in the figures to provide better orientation. The simulation results show a significant increase in fracture liquid saturation in Zone 3 of borehole 16 at 3 and 9 months of heating. During cooling, however, this situation changes; the fracture saturation drops almost instantly to pre-test values as soon as the heater is turned off. These simulation results are in good agreement with the measured data from air injection tests, shown in Figure 2.1-4. As fracture liquid saturation increases in the condensation zone during heating, one would expect that air permeability should decrease. Indeed, after 3 months of heating, the measured air permeability values in Zone 3 have decreased by a factor of 4 in borehole 16 and a factor of 2 in borehole 18, compared to the pre-heat values. For the rest of the heating period, the measured permeabilities remain essentially constant. Then, as soon as the heat-induced vaporization and condensation processes disappear during the cooling phase, the air permeabilities increase to values equal or higher than the pre-heat measurements. Little change in air permeability is observed in the other injection zones in boreholes 16 and 18 during the entire test, because the distance to the heater is too large for it to be significantly affected.

Additional air permeability measurements were performed in January 1998, i.e., seven months after turning off the heat (Section 2.1.3). The measured permeabilities exhibited a consistent, yet small increase compared to the pre-heat values. This increase cannot be attributed to thermo-hydrological effects, because the fracture saturation before and after heating is fairly similar. It can be possibly attributed to mechanical processes resulting in microfracturing or fracture opening during the test. Such effects are not accounted for in the numerical model.

Our simulation results show that all sensors in boreholes 16 and 18 remain in an environment of high matrix saturation during the entire heating period, as the dry-out zone does not extend to the sensor locations (Figure 3.4-10 through 3.4-13). Therefore, the relative humidity readings from passive monitoring should effectively register 100%. However, as pointed out in Section 2.2.2, this is only the case for sensor 18-4. Sensor 16-4 ceased to function properly beginning November 8, 1997; the other sensors in boreholes 16 and 18 exhibit relative humidity readings below 96%. This is probably related to drying from ventilation in the Thermomechanical Alcove Extension, which is not accounted for in our model.

Because gas pressure buildup occurs only in the boiling area close to the heater, which is not intersected by boreholes 16 and 18, the simulated pressure sensors in boreholes 16 and 18 do not register readings much different from the ambient value. This again is consistent with the measured data, except for sensor 4 in borehole 16, where pressure buildup was observed during the heating phase of the test (Figure 2.2-4). This, however, was not a result of elevated gas pressure, but related to the influx of condensate into the bottom zone of borehole 16, resulting in a hydrostatic pressure buildup. The model results suggest an area of high fracture saturation and significant liquid flow processes in the vicinity of Zone 3, indicating that water seepage into the packed-off borehole interval is indeed a possibility. No water was collected in borehole 16 during the cooling phase of the test, as the vaporization-condensation processes had ceased and the fracture saturation had significantly dropped.

Rock samples taken from dry-drilled boreholes at about 7 months into the cooling phase were analyzed for porosity, density, and moisture content (Section 2.5.2, Figure 2.5-1). Some of these samples were located in the dry-out zone close to the heater; others were taken from the condensation zone. The matrix saturation data derived from these measurements give values for the dry-out zone in the range of 10% to 30%, consistent with the very slow rewetting process simulated by the model. The model matrix saturation in the dry-out zone is about 4% at the end of heating period, about 7% after 3 months of cooling and about 10% after 9 months of cooling. In the condensation zone, the measured matrix liquid saturation is approximately in the range of the pre-heat data (taking into account that the liquid saturation can differ by 9% between dry-drilled and wet-drilled cores, as discussed in Section 2.5.1.2), in some cases slightly lower. Overall, matrix cores taken from below the heater horizon have higher saturation than cores taken from above the heater horizon (Figure 2.5-1). These findings again are in good agreement with the model results: during heating, most of the condensate is predicted to drain through the fractures, limiting the effect of matrix imbibition. Therefore, matrix saturation increases only slightly from the

initial value of 0.92 to a maximum value of about 0.95, with higher saturation obtained below the heater than above it (Figures 3.4-5 and 3.4-6). During cooling, the simulated liquid and gas flow processes are very slow; thus, the moisture redistribution established during heating remains almost unchanged through several months of cooling (Figure 3.4-9). However, pore water from the condensation zone is slowly driven back towards the dry-out zone, so that matrix saturation in the vicinity of the dry areas can decrease below the pre-heat value. This effect can clearly be seen from the simulated results in Figures 3.4-12 and 3.4-13, where the entire bottom section of borehole 16 features matrix saturation values smaller than the pre-heat value of 0.92.

3.4.2 Quantitative Comparison of Measured and Simulated Temperature

Hourly temperature data are available at multiple locations within the SHT block, providing a unique opportunity to analyze the spatial and temporal evolution of the thermo-hydrological processes in fractured tuff. Although heat conduction is the dominant heat transfer process, heat transport due to gas or liquid flow can also influence the temperature field, as evidenced by subtle, sometimes strong temperature "plateaus" near the nominal boiling point. Detailed analysis of the numerous temperature measurements in the SHT can help identify and constrain moisture redistribution processes, and comparison between measured and modeled temperature data can serve to determine the accuracy of the thermo-hydrological model and the adyquacy of the simulation input parameters.

3.4.2.1 Discussion of Temperature Profiles

The continuous temperature measurements from the SHT allow the display of data either as temperature profiles at a given time or as temperature evolution at a particular spatial location. Figures 3.4-14 and 3.4-15 present snapshots after 3 months and 9 months of heating, for the subset of temperature data measured close to the mid-plane of the heater, at Y = 4.5 m. Measured data points are indicated by symbols. The figures also show simulated results, which are extracted from the 3-D grid for a horizontal sampling line at Y = 4.5 m. The simulated results have separate curves for matrix (solid line) and fracture (dashed line) temperature. The measured data are compared to the matrix simulation results, as most of the sensors are placed in grouted holes and would thus represent the temperature response of non fractured rock. Temperature is displayed as a function of radial distance from the heater hole.

The simulated matrix and fracture temperature are similar except near the nominal boiling point, where the fracture curve shows a narrow plateau, indicative of substantial heat transfer contributions from vapor-liquid counterflow. This two-phase heat pipe region centers around 0.8 m radial distance from the heater at 3 months of heating, and moves out to about 1.2 m at the end of 9 months of heating. None of this behavior can be seen in the simulated matrix temperatures. Obviously, the assumed thermal and hydrological properties in the matrix do not promote heat pipe effects. It is unfortunate that there is a lack of measured data at these distances. Nevertheless, the simulated temperatures compare favorably with the measured data.

Figure 3.4-16 gives a similar comparison of measured and simulated data for the cooling phase, at 3 months after heater turn-off. The drastic temperature drop from the heating phase temperatures is well represented, but the simulated results exhibit a slight overprediction compared to the measured data. Possible reasons are discussed in Section 3.4.3.

3.4.2.2 Discussion of Temperature Evolution

Figure 3.4-17a through 3.4-17d present the time evolution of temperatures over a 15-month period (9 months of heating and 6 months of cooling), for sensors close to the center-plane of the heater in boreholes parallel to the heater axis. Radial distances between the heater and the sensors are 0.34 m for borehole 2, 0.68 m for borehole 3, 1.5 m for borehole 4, 0.42 m for borehole 8, 0.67 m for borehole 9, 1.51 m for borehole 10, 0.73 m for borehole 11, and 0.70 m for borehole 12. The majority of these boreholes are grouted, with the exception of boreholes 2, 3, and 4, which are open holes to allow for mechanical displacement measurements. The temperature in the open holes may be somewhat affected by convective heat transfer within the boreholes. Generally, the temperature data show very subtle, if any, heat pipe effects, indicating that the dominant heat transfer mechanism operating in the SHT is thermal conduction. In borehole 9, for example, the temperature increases to nominal boiling within about 50 days, but then continues to increase without the evidence of a significant temperature "plateau." The other sensors registering temperatures above 100°C show similar behavior; it seems that the rock properties in the SHT do not allow for appreciable liquid reflux from the condensation zone back to the heater. The curves also exhibit a drastic drop of temperature as soon as the heater is turned off. The down spikes in the measured data register incidences of power outage, which have not been accounted for in the model.

Comparison between the measured and the simulated temperature evolution shows very good overall agreement for the heating phase. The observed behavior of only minor heat pipe effects is well captured in the simulated data, and there is no general trend of over- or underpredicting the measurements. Some of the observed discrepancies are probably related to the model assumption of homogeneous properties. In borehole 11, for example, the simulation overpredicts the measured temperature, possibly because the assumed fracture continuum permeability of 5.85×10^{-14} m^2 is two orders of magnitude smaller than the measured air-permeability value at this borehole. A local increase of fracture permeability in the model would promote heat transfer by convection and result in a lower temperature close to the borehole. During the cooling phase, the agreement between model results and data is generally good, but the numerical results show a small but consistent temperature overprediction compared to the measured data.

3.4.2.3 Discussion of Model Accuracy

The accuracy of the thermo-hydrological model is evaluated both visually and by statistically analyzing temperature differences between simulation and measured data. This analysis is performed for all SHT sensors, except for a few gages that exhibit obviously erroneous behavior. Figure 3.4-18 visualizes possible systematic errors in the model results by presenting the temperature residuals as a function of the measured temperature. This procedure is performed at 3 months and 9 months from the onset of heating,

and at 3 months from heater turn-off. We can see that, for the heating period, (1) most of the temperature residuals are within a ±10 °C, (2) the scatter of data is larger for the high-temperature range, and (3) there is no general trend of over- or underpredicting data. In evaluating the simulation results, one should keep in mind that the model uses homogeneous properties for the entire block, so that local heterogeneity is not accounted for. These and other simplifying assumptions, such as neglecting the presence of boreholes or relatively coarse gridding in the Y-direction, give rise to such temperature discrepancies. It is the general trends that have to be accurately simulated by a model, not the temperature at each individual location. Thus, we may conclude that the overall model accuracy is very good for the heating phase. During cooling, most of the residuals have positive values, indicating a systematic problem where the simulated values are consistently too high.

We shall further elaborate on the model accuracy by applying simple statistical measures for the goodness of fit between simulation and measurement. Two statistical measures for model evaluation have been proposed by the Thermal Testing Teams in participating laboratories: the Mean-Error (ME) and the Root-Mean-Square-Error (RSME). The Mean-Error is simply the average of the temperature residuals for all gages; a model would not feature a systematic error of consistently over- or underestimating data if the ME's were close to zero. Positive and negative values would indicate model overprediction and underprediction, respectively, of the measured data. The RSME is similar to a standard deviation; the smaller the RSME, the better the overall model fit. It was suggested to apply these measures at discrete times throughout the test, and to use a weighting scheme based on the frequency of temperature measurements in given temperature subranges. The definitions of ME, RSME, and the weighting scheme used are presented in the Appendix.

We applied the statistical procedures at three times: after 3 and 9 months of heating, and after 3 months of cooling. Results are given in Table 3.4-1. Mean-Errors and the Root-Mean-Square-Errors are presented for the entire temperature range, and for two temperature windows below and above nominal boiling. Considering all sensors, the RSME is 4.7°C at 3 months and 4.6°C at 9 months, which is fairly small compared to the large range of temperatures obtained in the SHT. The ME calculated for all sensors suggests a very modest underestimation of temperature data by the model; on average, the model results are 1.7°C too low at 3 months and 0.3°C too low at 9 months. Separate analysis for the two temperature windows above and below boiling indicates a similarly good agreement between measured and model data. We may conclude that the model represents the important thermo-hydrological processes in the SHT quite well, because possible systematic problems would become clearly evident in the above-boiling temperature range, i.e., in a range where heat-convection processes are very important. The model is less accurate during the first several months of cooling. At 3 months after heater turn-off, the RSME is 2.5°C. The ME indicates a consistent trend of overestimating the measured data, by 1.9°C on average.

3.4.3 Sensitivity Analysis

The good agreement between the measured data and the simulated results shown in the previous sections indicates that the thermo-hydrological response of the SHT is well represented by the numerical model. While heat conduction accounts for most of the temperature rise, effects of thermo-hydrological coupling cannot be ignored in the interpretation of the measured data. In particular, the choice of different parameter values of the hydrological properties can play a significant role in affecting the simulation results. The spatial heterogeneity and uncertainty of the hydrological properties is large, particularly in the fractures. In this section, we investigate the sensitivity of the simulated temperatures to some key properties of the rock. Insight from these studies can serve to constrain these hydrological properties. In addition, we study the importance of percolation flux, the effect of initial saturation in the rock, and the impact of different conceptual models for fracture-matrix interaction.

One must keep in mind that findings from this sensitivity study are specific to a small-scale experiment, and cannot readily be applied to larger problems, such as the Drift Scale Test or the entire repository. In the SHT, the impact of the thermal perturbation is very localized and intense. The strong perturbation of the thermo-hydrological system may accentuate the differences in model prediction from alternative conceptual models and different hydrological properties.

3.4.3.1 Thermo-Hydrological Parameters

Our sensitivity study is performed in two dimensions for a vertical plane orthogonal to the heater axis at Y = 4.5 m. Results from a 2-D model cannot exactly represent the actual 3-D behavior of the rock mass; the 2-D temperature response overestimates the 3-D system behavior. However, 2-D simulations have considerable merit in a sensitivity study. They are instructive in uncovering the relative importance of parameters and processes, while allowing for more efficient computation and data handling compared to a fully 3-D study. From the base-case properties used before, only one parameter at a time is varied, while all other parameters are kept constant. Sensitivity is evaluated by analyzing the temperature history in the rock matrix measured at a radial distance of 0.67 m from the heater, representing the location of borehole 9 in relation to the heater.

Figure 3.4-19 shows simulation results for the base-case matrix permeability and for cases where the matrix permeability is increased and decreased by one order of magnitude. The increase of matrix permeability results in a large suppression of temperature, arising from (1) increased imbibition of condensate from the fractures into the matrix, and (2) increased liquid flow back to the heater area through the matrix continuum. Lowering the matrix has negligible effect because the base-case value is already small enough such that only minor imbibition and liquid reflux is present. Figure 3.4-20 presents sensitivity of temperature to fracture permeability. Higher fracture permeability promotes increased convective heat transport by removal of vapor from the heater area, giving rise to lower temperatures. Lower permeability in the fractures does the reverse, resulting in higher temperature. Overall, the

temperature evolution is less sensitive to an increase by one order of magnitude in the fracture permeability than in the matrix permeability.

Figure 3.4-21 shows the simulated temperature response when the matrix α-values are varied by one order of magnitude compared to the base case. The α-value is a fitting parameter for the van Genuchten characteristic function, inversely corresponding to the potential strength of capillary suction. A smaller α-value implies a stronger capillary suction in the matrix, which promotes imbibition of condensate from the fracture walls into the matrix. Thus, more water is available in the matrix to flow toward the heater area, resulting in increased convective heat transfer and lowering of the temperature. A larger α-value has the opposite effect; however, a one-order-of-magnitude increase has rather small impact on the temperatures. As discussed earlier, the base-case matrix properties allow for little matrix imbibition and small liquid reflux due to the small matrix permeability, so that the effect of a reduction in capillarity is negligible. Sensitivity to the fracture α-value is shown in Figure 3.4-22. The effect on temperature is similar in trend, but smaller in magnitude compared to that of changing the matrix α-value.

The examples shown above demonstrate that one order of magnitude variation in some of the key properties of the rock can significantly alter the simulated temperature of the SHT. One-order-of-magnitude variation is well within the limit of the spatial heterogeneity and uncertainty of the hydrological properties within the fractured welded tuff. In particular, one can conclude from the above analysis that property sets with high matrix permeability and strong capillarity in fractures and matrix are not likely to represent the SHT thermo-hydrological situation. All these cases tend to overestimate vapor-liquid counterflow and to underestimate the observed temperatures.

Further analysis was conducted to study the sensitivity of the temperature evolution to the characteristic curve parameter β, to the ambient percolation flux at Yucca Mountain, and to initial matrix saturation in the SHT block. Changes in van Genuchten β, a fitting parameter related to the aperture distribution of fractures, hardly affect the simulated temperature. Similar results were obtained for percolation flux, as varying the flux range from 0.1 mm/yr to about 20 mm/yr would change the initial fracture saturation in the SHT block, but not affect the temperature response. This is because all reasonable values of percolation at Yucca Mountain are negligibly small compared to the thermally induced fluxes in the SHT. In contrast, the initial matrix saturation of the SHT block does have an impact on temperature. Smaller initial matrix saturation results in higher temperature, because less liquid is available in the matrix pores for vaporization and subsequent condensation.

3.4.3.2 Fracture-Matrix Interaction

For comparison with the DKM modeling results presented so far, we apply an alternative conceptual model for fracture-matrix interaction, namely the ECM concept. ECM is a simplified approach where thermo-hydrological equilibrium is assumed at all times between fractures and matrix. It allows for fast,

computationally efficient simulation of thermo-hydrological processes in fractured rock. The simulation runs are performed using a 3-D representation of the SHT.

First, we shall compare measurements to numerical simulation results analyzing the time evolution of temperature for the different conceptual models, using the center gage in borehole 9 as an example (Figure 3.4-23). Note that the ECM results display only one temperature curve due to the local equilibrium assumption, while DKM has separate curves for fracture and matrix temperatures. For both models, the general agreement between the measured and simulated data is good, indicating that the thermo-hydrological response of the SHT is well represented. However, the ECM results display a subtle heat pipe signal, which retards the temperature increase at nominal boiling for a certain time and gives rise to an underestimation of temperature for the remaining heating period. In contrast, the matrix temperature curves obtained with the DKM match the measured data curve exactly.

Analysis of the simulated moisture redistribution processes demonstrates more substantial differences between the model concepts. Figure 3.4-24 shows matrix saturation contours in a vertical plane at Y = 4.5 m after 3 months of heating, simulated using ECM. This is to be compared to Figure 3.4-5 for the DKM results. In both cases, drying occurs up to a radial distance of about 1 to 1.5 meters from the heater; beyond that is the condensation zone where liquid saturation is higher than at ambient conditions. However, while strong gravity drainage in the fractures is obtained using DKM, indicated by the saturation build-up below the heater, no gravity drainage is observed using the ECM. The ECM concept involves the crucial assumption that pressure equilibrium between the fractures and matrix is maintained at all times. As a result, gravity driven liquid flow in the fractures tends to be underestimated, because vapor condensing on the fracture walls is readily imbibed into the matrix pores and driven back towards the heater. Because no water drains through the fractures, the condensate accumulates in matrix pores and gives rise to matrix saturation values close to 1. However, hydrological data suggest that most of the condensate indeed drains away from the test area so that matrix saturation cannot significantly build up in the condensation zone, evidenced for example in the geophysical data or in the post-test core sample analysis. We may conclude that the DKM seems to be much better suited in realistically representing thermo-hydrological processes in the SHT than the ECM. We should point out, however, that the DKM has a tendency to underestimate fracture-matrix interaction particularly at early times, due to the assumption of a linear gradient between fractures and matrix. This could be improved by analysis using the more rigorous, yet computationally exhaustive MINC method (Birkholzer and Tsang, 1998).

3.4.3.3 Discussion on Cooling Phase Results

As mentioned earlier, the modeled temperatures show a consistent trend of overpredicting the measured data during the first several months of cooling. Because heat-conduction processes are less significant after the heater has been turned off, the discrepancy between simulated and measured data is probably not attributed to hydrological processes being misrepresented by the model, but more likely related to model assumptions and parameters of the thermal processes. For example, insulation of the test block may be

less effective than assumed in the model, "wet" thermal conductivity of the rock may be underestimated, or heat capacity of the rock may be overestimated. In the first two cases, thermal energy would more efficiently be driven away from the test block, resulting in faster cooling. The third possibility suggests that the amount of heat stored in the test block is smaller than assumed; therefore temperature would decrease more rapidly after turning off the heat. Scoping simulations indicate that all these possibilities contribute to improving the model results. At this point, however, though we suggest possible reasons for the discrepancy between modeled and measured data, there are no data to support or refute any or all the above hypotheses.

3.5 Summary and Conclusions

The Single Heater Test (SHT) is the first of two *in-situ* thermal tests included in the site characterization program for the potential underground nuclear waste repository at Yucca Mountain. The extensive data available from this test provide a unique opportunity to improve our understanding of the thermo-hydrological processes in the natural setting of the repository rocks and validate our conceptual and numerical model. We have simulated the SHT using a three-dimensional numerical model of the fractured tuff in the heater vicinity, and compared the simulation results to field data. The fractured rock is modeled by the dual-permeability scheme, assuming a continuum behavior in fractures and rock matrix. As much as possible, site-specific thermal and hydrological data have been used as input parameters. The model has not been calibrated to measured SHT data in order to derive a "best-fit" property set.

A very good agreement was obtained between the measured and simulated temperature data, showing that the thermo-hydrological response in the SHT is well represented by the numerical model. Both the measured and simulated temperatures suggest that while heat is mainly transported by conduction, the contribution from thermo-hydrological coupling is also important. Overall, the signature of convective transport due to heat-induced vapor and liquid fluxes is very subtle, indicating that the hydrological properties of the matrix and fractures in the SHT are such that they do not promote significant vapor-liquid counterflow during the heating phase. Detailed analysis of the measured and modeled temperature data indicates that the average model error over all gages is in the range of a few degrees centigrade. Slight discrepancies occurring at certain temperature gages may be in part attributed to local heterogeneity, which is not accounted for in the model.

Qualitatively, the model results show good agreement with field measurements of moisture redistribution in the rock mass. In the heating phase, the model predicts a dry-out zone of about 1.2 m extent close to the heater, and a condensation zone further away with strong increase in fracture saturation, which gives rise to significant gravity drainage through the fractures. The simulated matrix saturation increases only slightly in the condensation zone, since most of the condensate drains away before it is imbibed into matrix pores. During cooling, the dynamic nature of moisture redistribution becomes less pronounced,

and very slow rewetting of the dry-out regions occurs. Field data from air injection tests, radar tomography, and post-heating core analyses are consistent with these model findings: during heating, the increase of fracture saturation due to condensation is evidenced by a significant reduction in air permeability. Radar tomography data, supported by analysis on rock samples, show a dry-out zone developing close to the heater and a zone of slightly increased matrix liquid saturation further away. They also show that the moisture content in the matrix is larger below the heater than above, suggesting that gravity drainage through the fractures is present during the heating phase. Measurements of core moisture content conducted after 7 months of cooling give saturation values of 10% to 30% in the dry-out zone, supporting the model results of a very slow rewetting after the heater has been turned off.

A sensitivity study was carried out to gain a better understanding of how the coupled thermo-hydrological processes in the repository formation are affected by rock properties and model conceptualization. Results of the sensitivity study provide constraints on key hydrological parameters of the fractured rock mass, namely on permeability and capillarity values in the fractured rock. In particular, property sets with high matrix permeability, and strong capillarity in the fractures and the matrix, cannot realistically represent the SHT thermo-hydrological situation. Other parameters, such as the ambient percolation flux, have only limited impact on measured temperature, and thus cannot be constrained by comparing model results with the measured data. Studies performed using the ECM conceptualization of the fractured rock show that this simple fracture-matrix interaction concept does not accurately represent the thermo-hydrological situation in the SHT. The ECM scheme underestimates gravity drainage in the fractures and overpredicts effects of vapor-liquid counterflow, giving rise to a less accurate simulation of the temperature field.

Acknowledgement

We thank George Moridis, Sumit Mukhopadhyay, Don Mangold, and Dan Hawkes for their review of the manuscript and comments for improvement.

References

Birkholzer, J. T. and Tsang, Y.W. 1998. "Numerical Analysis of Thermo-Hydrological Conditions in the Single Heater Test at Yucca Mountain." *Proceedings of TOUGH Workshop '98.* Berkeley, California: Lawrence Berkeley National Laboratory. MOL.19980715.0257.

Birkholzer, J.T. and Tsang, Y.W. 1997. *Pretest Analysis of the Thermo-hydrological Conditions of the ESF Drift Scale Test.* Yucca Mountain Project Level 4 Milestone SP9322M4. Berkeley, California: Lawrence Berkeley National Laboratory. MOL. 19971201.0810.

Birkholzer, J.T. and Tsang, Y.W. 1996. *Forecast of Thermo-hydrological Conditions and Air Injection Test Results of the Single Heater Test at Yucca Mountain.* Yucca Mountain Project Level 4 Milestone SP918M4, Report LBNL-39789, UC-814. Berkeley, California: Lawrence Berkeley National Laboratory. MOL.19971124.0089.

Bodvarsson, G.S.; Bandurraga, T.M.; and Wu, Y.S., eds. 1997. *The Site Scale Unsaturated Zone Model of Yucca Mountain, for the Viability Assessment.* Yucca Mountain Project Level 4 Milestone SP24UFM4, Report LBNL-40376. Berkeley, California: Lawrence Berkeley National Laboratory. DTN: LB970601233129.001 (Q). MOL.19971014.0232.

Brodsky, N. S. 1996. *Thermal Properties of Test Specimens from the Single Heater Test Area in the Thermal Testing Facility at Yucca Mountain, Nevada.* Report prepared for the Yucca Mountain Site Characterization Project. Albuquerque, New Mexico: Sandia National Laboratories. MOL.19961029.0115.

Brodsky, N.S. 1998. *Laboratory Measurements of Thermal Conductivity as a Function of Saturation State for Welded and Nonwelded Tuff Specimens.* Report prepared for the Yucca Mountain Site Characterization Project. Albuquerque, New Mexico: Sandia National Laboratories. MOL.19980825.0288.

Department of Energy (DOE) 1993. *Reference Information Base (RIB).* Yucca Mountain Site Characterization Project, YMP/93-02m/Rev. 3. DTN: MO9212RIB00028.003 (NQ).

Finley, R. 1997. *Evaluation and Comparative Analysis of Single Heater Test Thermal and Thermomechanical Data: Third Quarter Result.* Yucca Mountain Project Milestone SP9268M4. Albuquerque, New Mexico: Sandia National Laboratories. DTN: SNF35110695001.008. MOL.19980209.0374.

Flint, L.E. 1998. *Characterization of Hydrogeologic Units Using Matrix Properties, Yucca Montain, Nevada.* Yucca Mountain Project Milestone 3GUP603M. U.S. Geological Survey Water Resources Investigation Report 97-4243. Denver, Colorado: U.S. Geological Survey. MOL. 19980429.0512.

Francis, N.D. April 16, 1997. Memo from author to distribution. "The Base-Case Thermal Properties for TSPA Modeling." Albuquerque, New Mexico: Sandia National Laboratories.

Ho, C.K. and Francis, N.D. August 7, 1997. Memo from authors to distribution. "Correction to Base-Case Thermal Properties for TSPA-VA Modeling." Albuquerque, New Mexico: Sandia National Lanboratories

Pruess, K; Simmons, A.; Wu, Y.S.; and Moridis, G.J. 1996. *TOUGH2 Software Qualification Report.* Report LBL-38383. Berkeley, California: Lawrence Berkeley National Laboratory. MOL.19960610.0010-0020.

Pruess, K. and Tsang, Y.W. 1994. *Thermal Modeling for a Potential High-Level Nuclear Waste Repository at Yucca Mountain, Nevada.* Report LBL-35381, UC-600, Berkeley, California: Lawrence Berkeley National Laboratory. NNA.19940427.0248.

Pruess, K. 1991. *TOUGH2—A General Purpose Numerical Simulator for Multiphase Fluid and Heat Flow.* Report LBL-29400, UC-814. Berkeley, California: Lawrence Berkeley National Laboratory. NNA.19940202.0088.

Pruess, K.; Wang, J.S.Y.; and Tsang, Y.W. 1990. "On the Thermohydrologic Conditions near High-Level Nuclear Wastes Emplaced in Partially Saturated Fractured Tuff, Part 2. Effective Continuum Approximation." *Water Resour. Res., 26* (6), 1249-1261. NNA.19891026.0084.

Pruess, K. and Narasimhan, T.N. 1985. "A Practical Method for Modeling Fluid and Heat Flow in Fractured Porous Media." *Soc. Pet. Eng. J.*, 25 (1), 14-26. NNA.19890522.0235

Sobolik, S.R.; Francis, N. D.; and Pott, J. 1996. *Pre-Experiment Thermo-Hydrological-Mechanical Analyses For The ESF Single Heater Test.* Letter Report SLTR96-0004. Albuquerque, New Mexico: Sandia National Laboratories. MOL.19980128.0366.

Sonnenthal, E.L.; Ahlers, C.F.; and Bodvarsson, G.S. 1997. "Fracture and Fault Properties for the UZ Site-Scale Flow Model." *In:* G.S. Bodvarsson, T.M. Bandurraga, and Y.S. Wu, eds. *The Site-Scale Unsaturated Zone Model of Yucca Mountain, Nevada, for the Viability Assessment*, Chapter 7. Yucca Mountain Project Level 4 Milestone SP24UFM4. Report LBNL-40376, UC-814. Berkeley, California: Lawrence Berkeley National Laboratory. LB970601233129.001 (Q). MOL.19971014.0232.

Tsang Y. W., Wang, J.; Freifeld, B.; Cook, P.; Suarez-Rivera, R.; and Tokunaga, T. 1996. *Letter Report on Hydrological Characterization of the Single Heater Test Area in the ESF.* Yucca Mountain Project Level 4 Milestone OS327322D1. Berkeley, California: Lawrence Berkeley National Laboratory. LB960500834244.001 (Q). MOL.19971119.0549.

Tsang, Y.W. and Birkholzer, J.T. 1997. *Interpreting the Thermal-Hydrological Response of the ESF Single Heater Test.* Yucca Mountain Project Level 4 Milestone SP9267M4. Berkeley, California: Lawrence Berkeley National Laboratory. MOL.19971204.0759.

Wang, J.S.Y. and Suarez-Rivera, R. 1997. *Laboratory Test Results of Hydrological Properties from Dry Drilled and Wet Drilled Cores in the Drift Scale Test Area and in the Single Heater Test Area of the Thermal Test Facility.* Yucca Mountain Project Level 4 Milestone SP5130M4. Berkeley, California: Lawrence Berkeley National Laboratory. LB970500123142.003 (Q).

Wu, Y.S.; Ahlers, C.F.; Fraser, P.; Simmons, A.; and Pruess, K. 1996. *Software Qualification of Selected TOUGH2 Modules*. Report LBL-39490 UC-800. Berkeley, California: Lawrence Berkeley National Laboratory. MOL.19970219.0100-0105.

Van Genuchten, M.T. 1980.."A Closed-Form Equation for Predicting the Hydraulic Conductivity of Unsaturated Soil." *Soil Science Soc. Am. Journal, 44* (5), 892-898. NNA.19890522.0287.

Appendix

The temperature gages in the SHT block are associated with a measured temperature value, $T_{mea,i}$, and a modeled temperature, $T_{sim,i}$, the latter obtained by spatial interpolation from the model grid nodes. At a given instant in time, the *Mean-Error (ME)* can be evaluated from

$$ME = \frac{\sum_{i=1}^{N} w_i \left(T_{sim,i} - T_{mea,i}\right)}{\sum_{i=1}^{N} w_i}, \qquad (1)$$

where N is the number of temperature gages used in the analysis, and w_i is the weighting factor given to the i^{th} temperature gage. On average over a given temperature range, a model would *not* feature a systematic error of consistently over- or underestimating data, if the *ME* is equal to zero for that temperature range. The *Root-Mean-Square-Error (RMSE)* is given by

$$RMSE = \left(\frac{\sum_{i=1}^{N} w_i \left(T_{sim,i} - T_{mea,i}\right)^2}{\sum_{i=1}^{N} w_i} \right)^{1/2} \qquad (2)$$

The smaller *RMSE*, the better is the model fit to the data in a given temperature range.

The weighting factors, w_i, used in Eqs. (1) and (2), are based on a frequency analysis of the temperature measurements, acknowledging that the sensors are not uniformly distributed throughout the test block. It is desired to give equal importance to all temperature sub-ranges in the total range of temperatures observed. For example, in case only a few temperature gages are located in the "hot" zone close to the heater compared to numerous sensors located in "colder" areas, data in the "hot" temperature sub-range should get a larger weighting factor than data in the "colder" sub-range. We decided to divide the total range of temperature measurements into 20 equally sized temperature sub-ranges, then calculate the number of measurements falling into each sub-range, and finally define the weighting factors for each sub-range as the inverse of the number of occurrences in that sub-range, namely

$$w_j = 1/N_o, \qquad (3)$$

where j denotes the temperature sub-range considered, and N_o gives the number of occurrences within this sub-range. Note that Eq. (3) can not be applied if there is no occurrence in a certain sub-range; however, no weighting factor is needed in this case.

Tables

Table 3.3-1 Hydrological and thermal input values.

Parameter	Value	Comments
Matrix Porosity	0.11	tptpmn-average
Matrix Permeability	4.0×10^{-18} m^2	tptpmn-average
Matrix van Genuchten parameter α	6.4×10^{-7} Pa^{-1}	tptpmn-average
Matrix van Genuchten parameter	1.47	tptpmn-average
Matrix Residual Liquid Saturation	0.18	tptpmn-average
Matrix Grain Density	2530.0 kg/m^3	tptpmn-average
Initial Matrix Liquid Saturation	0.92	SHT lab measurements; SD9 tptpmn-average
Fracture Porosity	0.000124	UZ site scale model
Fracture Permeability (low permeability background)	5.85×10^{-14} m^2	SHT air-injection tests
Fracture Permeability (high-permeability feature)	5.2×10^{-12} m^2	SHT air-injection tests
Fracture van Genuchten α	1.0×10^{-3} Pa^{-1}	UZ site scale model
Fracture van Genuchten β	1.47	UZ site scale model
Fracture Residual Liquid Saturation	0.01	UZ site scale model
Initial Fracture Saturation	0.046	Equilibrium with matrix
Fracture Frequency	1.88 1/m	UZ site scale model
Rock Mass Thermal Conductivity $C(S_l) = C_{dry} + (C_{wet} - C_{dry})\sqrt{S_l}$	C_{dry} = 1.67 W/(m °K) C_{wet} = 2.0 W/(m °K)	Alcove 5 lab measurements*
Rock Mass Heat Capacity	953.0 J/(kg °K)	tptpmn-average
Vapor Diffusion Coefficient D^o_{va}	2.14×10^{-5} m^2/s	Standard values after Pruess and Tsang (1994)
Temperature dependence θ	2.334	
Tortuosity Factor	0.2	

* Recent analyses performed at Sandia National Laboratories give a "dry" conductivity of 1.71 W/(m °K) and a "wet" conductivity of 2.14 W/(m °K) (Brodsky, 1998, page 16, Table 5). Due to a change in calibration procedure, these values are slightly higher than earlier estimates, approximately by 0.1 W/(m °K). In our model, we use earlier estimates, i.e., a "dry" conductivity of 1.67 W/(m °K) and a "wet" conductivity of 2.0 W/(m °K).

Table 3.3-2. Data sources and Q status.

Data Type	Q Status	DTN/AN
Core measurements from surface boreholes, in Flint (1996); matrix porosity, permeability, van Genuchten properties, grain density, initial saturation	Q	TIC 236515
Core measurements from SHT block, in Tsang et al., 1996; matrix initial saturation, porosity, grain density	Q	DTN LB960500834244.001
Core measurements from SHT block, in Wang and Suarez-Riviera, 1997; matrix initial saturation, porosity, grain density	Q	DTN LB970500123142.003
Pre-heat air-injection tests for the SHT block, in Tsang et al., 1996; fracture permeability	Q	DTN LB960500834244.001
Calibrated properties for UZ site scale model layers, in Bodvarsson et al., 1997; fracture van Genuchten properties	Q	DTN LB970601233129.001
Analysis of ESF fracture mapping data, in Sonnenthal et al., 1997; fracture van Genuchten α, fracture frequency and spacing, porosity	Q	DTN LB970601233129.001
Core measurements on Alcove 5 rock specimens, in Brodsky, 1998; thermal conductivity	Q	MOL.19971125.0845
Core measurements from surface boreholes, in Brodsky et al., 1997; heat capacity	Q	DTN SNL01A05059301.005
Vapor diffusion parameters, in Pruess and Tsang, 1994; vapor diffusion coefficient, factor for temperature dependence	NA	NNA.19940427.0248

Table 3.4-1 Error analysis.

Criterion	Range	3 months	9 months	12 months (cooling)
Root-Mean-Square-Error (°C)	All Temp.	4.7	4.6	2.5
Mean-Error (°C)	All Temp.	-1.7	-0.3	1.9
Root-Mean-Square-Error (°C)	Temp. < 97 °C	4.5	3.0	2.5
Mean-Error (°C)	Temp. < 97 °C	-1.5	0.9	1.9
Root-Mean-Square-Error (°C)	Temp. > 97 °C	5.0	5.0	N/A
Mean-Error (°C)	Temp. > 97 °C	-2.0	-1.7	N/A

Figures

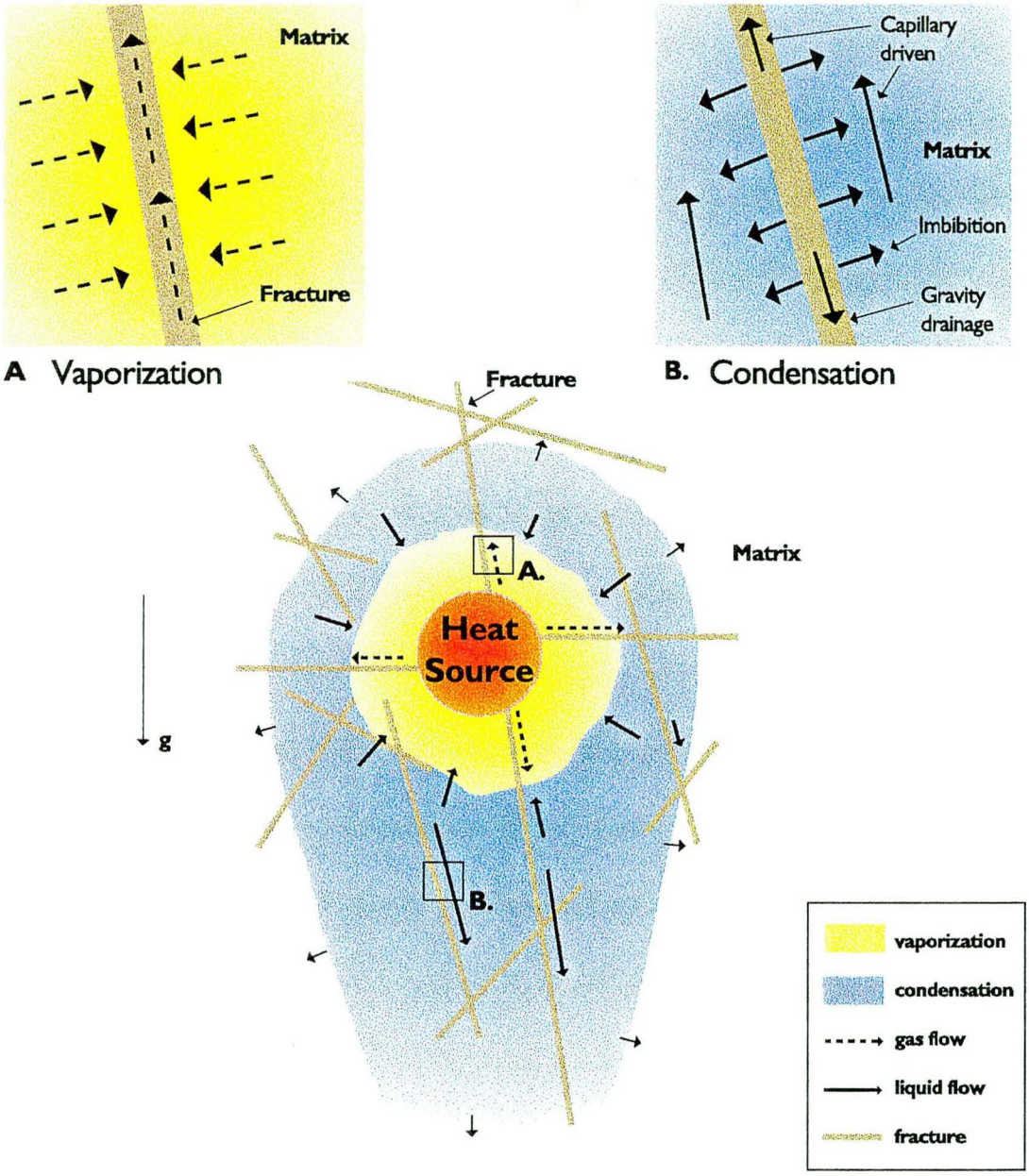

Figure 3.2-1 Potential thermo-hydrological processes in fractured tuff after emplacement of a heat source

Conceptual Models for Fracture-Matrix Interaction

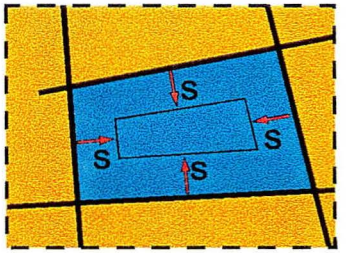

Concept	Capillary Pressure	Interflow
ECM (1 Continuum)	Equilibrium ($P_F = P_M$)	Infinitely Fast
DKM (2 Continua)	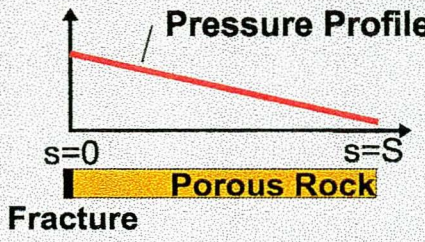	proportional to pressure difference
MINC (Multiple Continua)	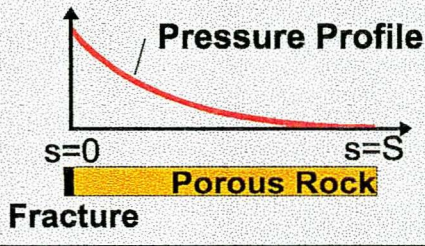	proportional to interface gradient

Figure 3.2-2 Conceptual models for fracture-matrix interaction (ECM, DKM and MINC)

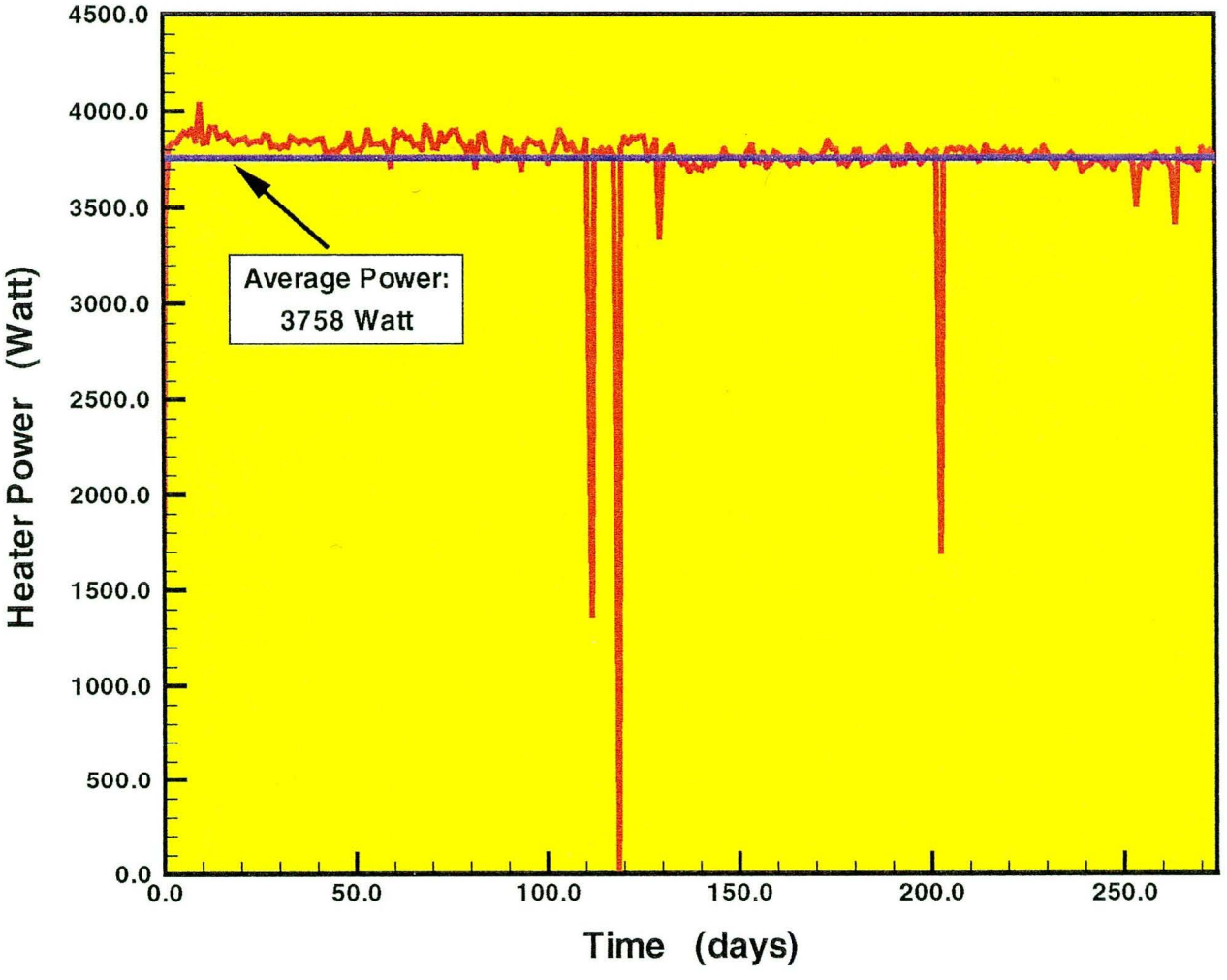

Figure 3.3-1 Heater power during operation of the test

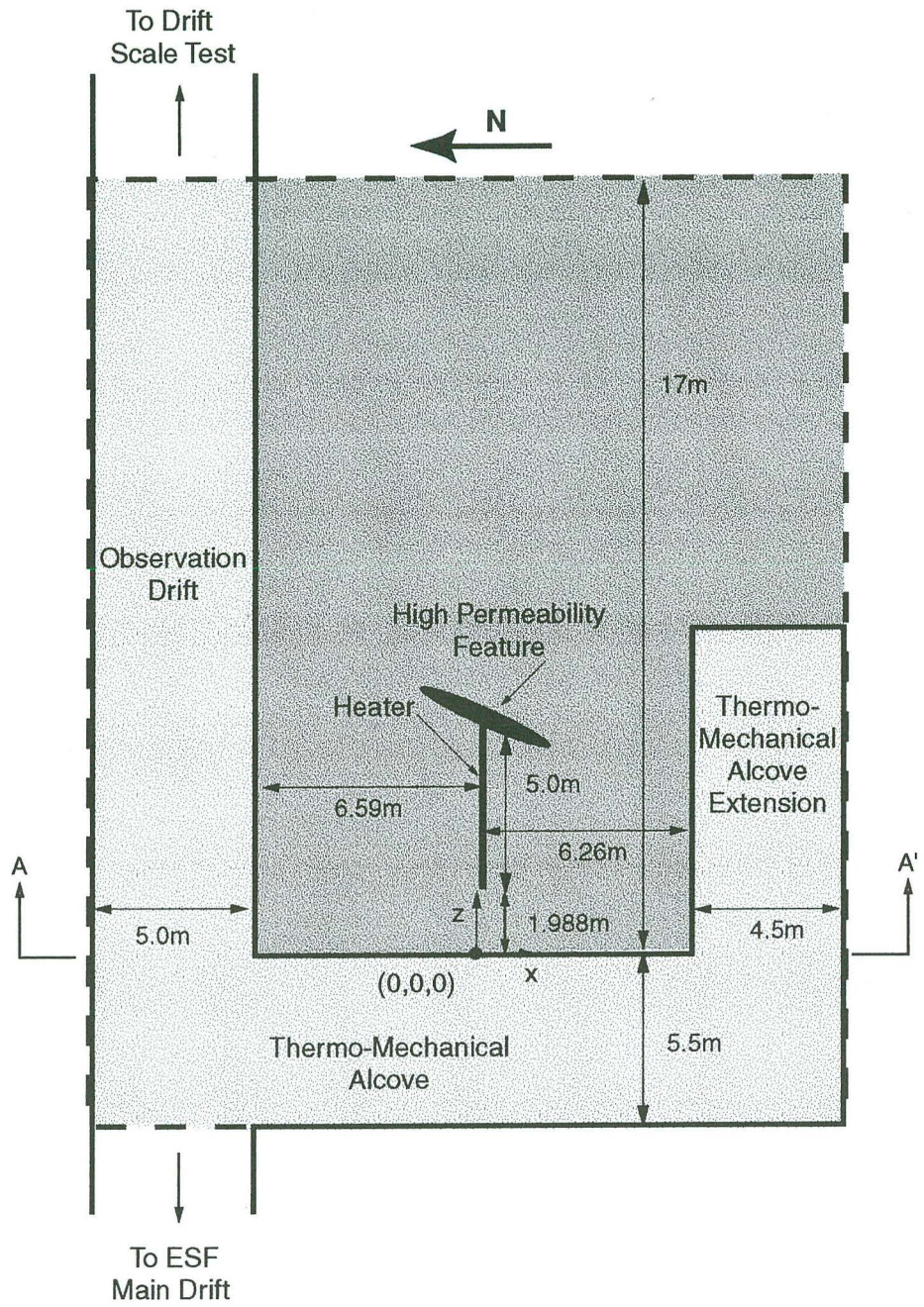

Figure 3.3-2 Boundaries of SHT model domain in a plan view. The shaded areas indicate the model domain extension.

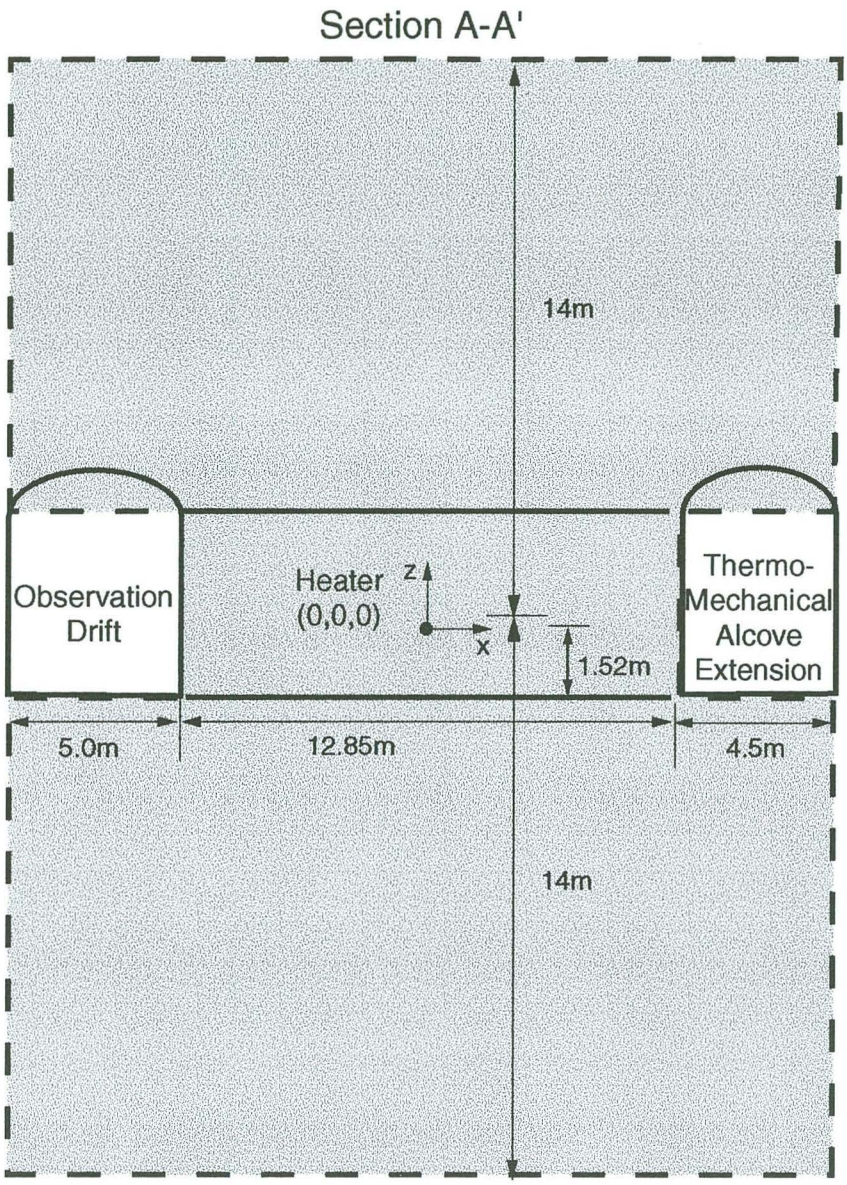

Figure 3.3-3 Boundaries of SHT model domain in a vertical cross-section. The shaded area indicates the model domain extension.

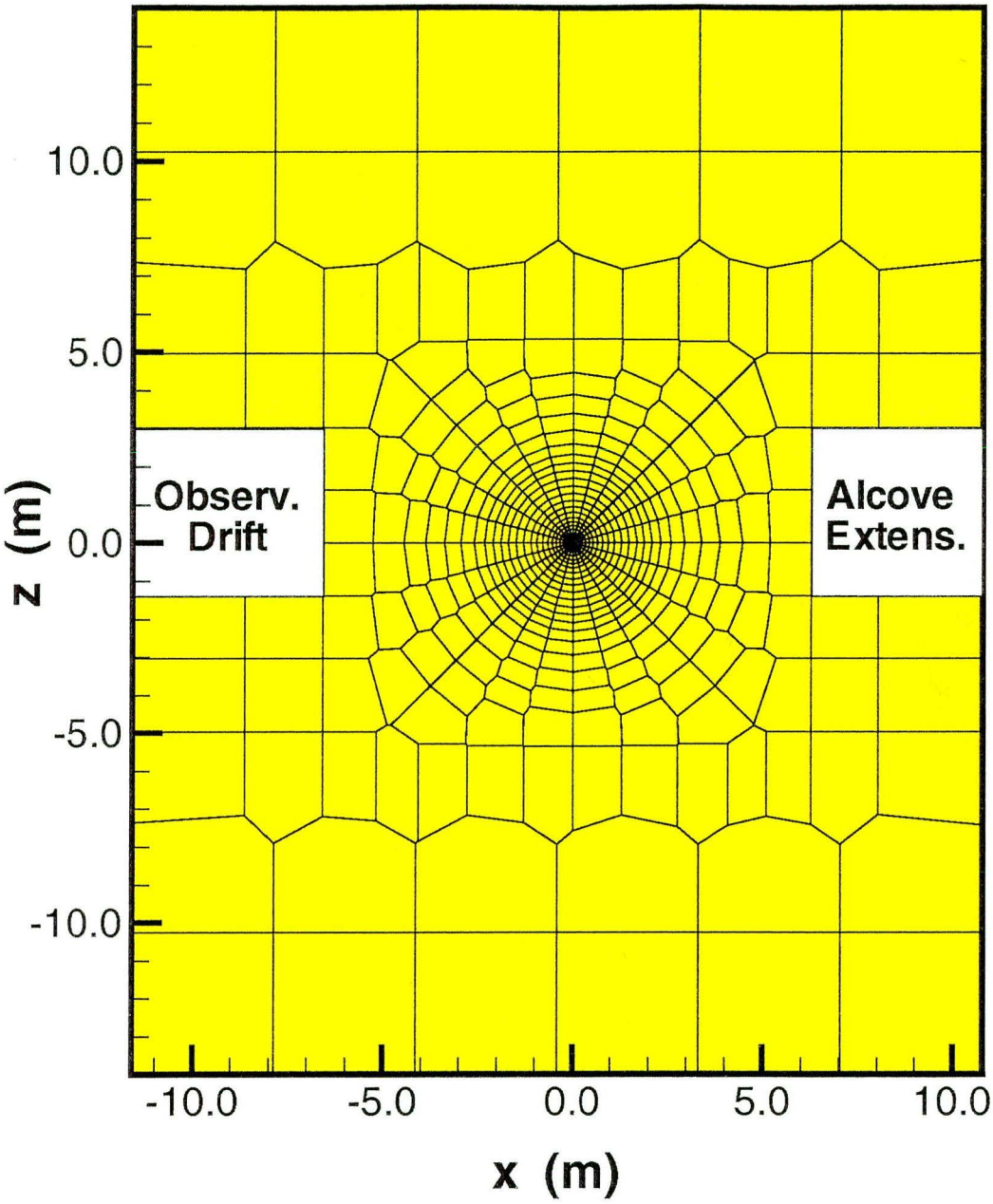

Figure 3.3-4 Discretization of SHT model in a vertical cross-section

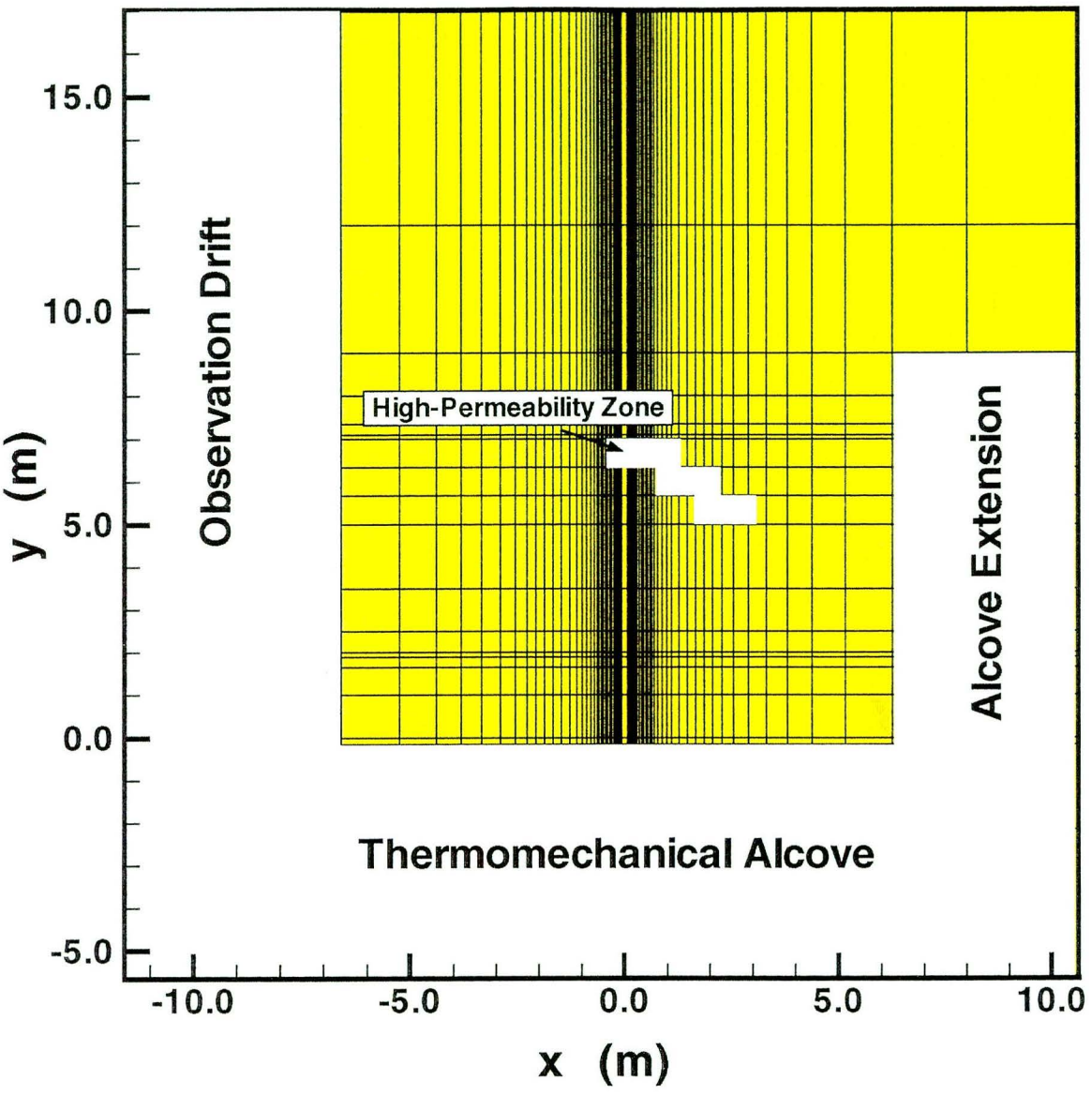

Figure 3.3-5 Discretization of SHT model in a plan view

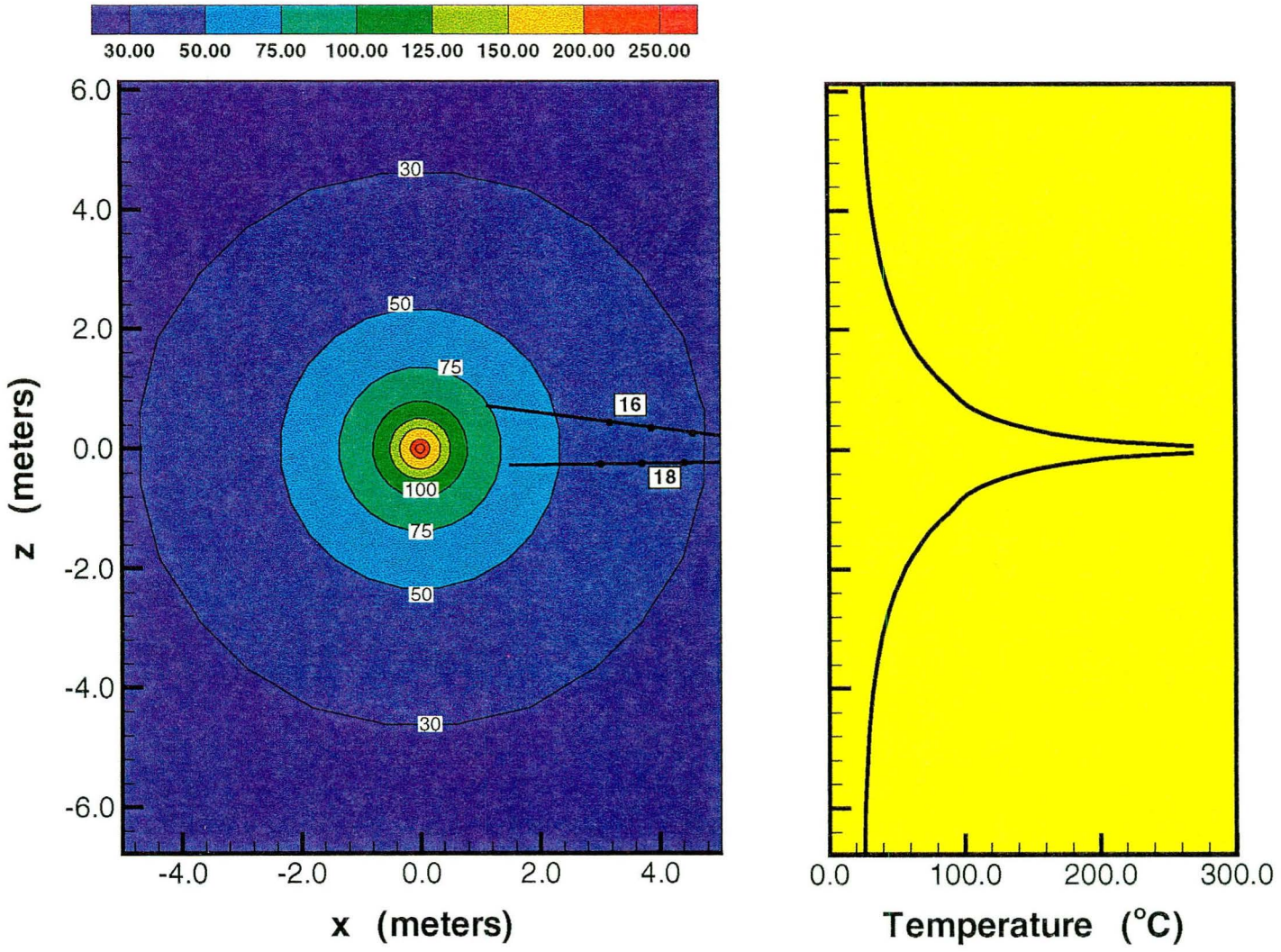

Figure 3.4-1 Simulated matrix temperature after 3 months of heating in XZ–cross section at Y = 4.5 m

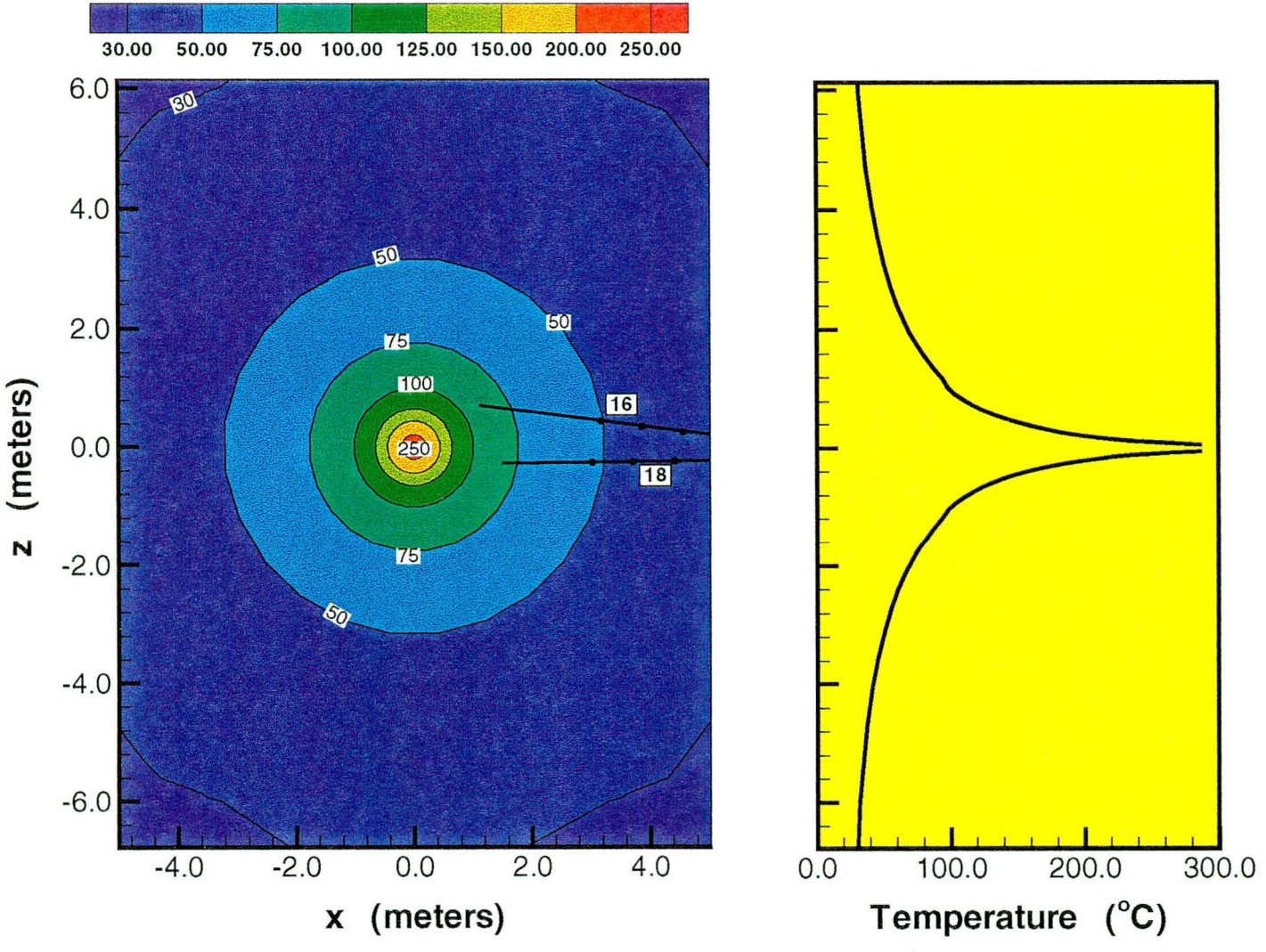

Figure 3.4-2 Simulated matrix temperature after 9 months of heating in XZ–cross section at Y = 4.5 m

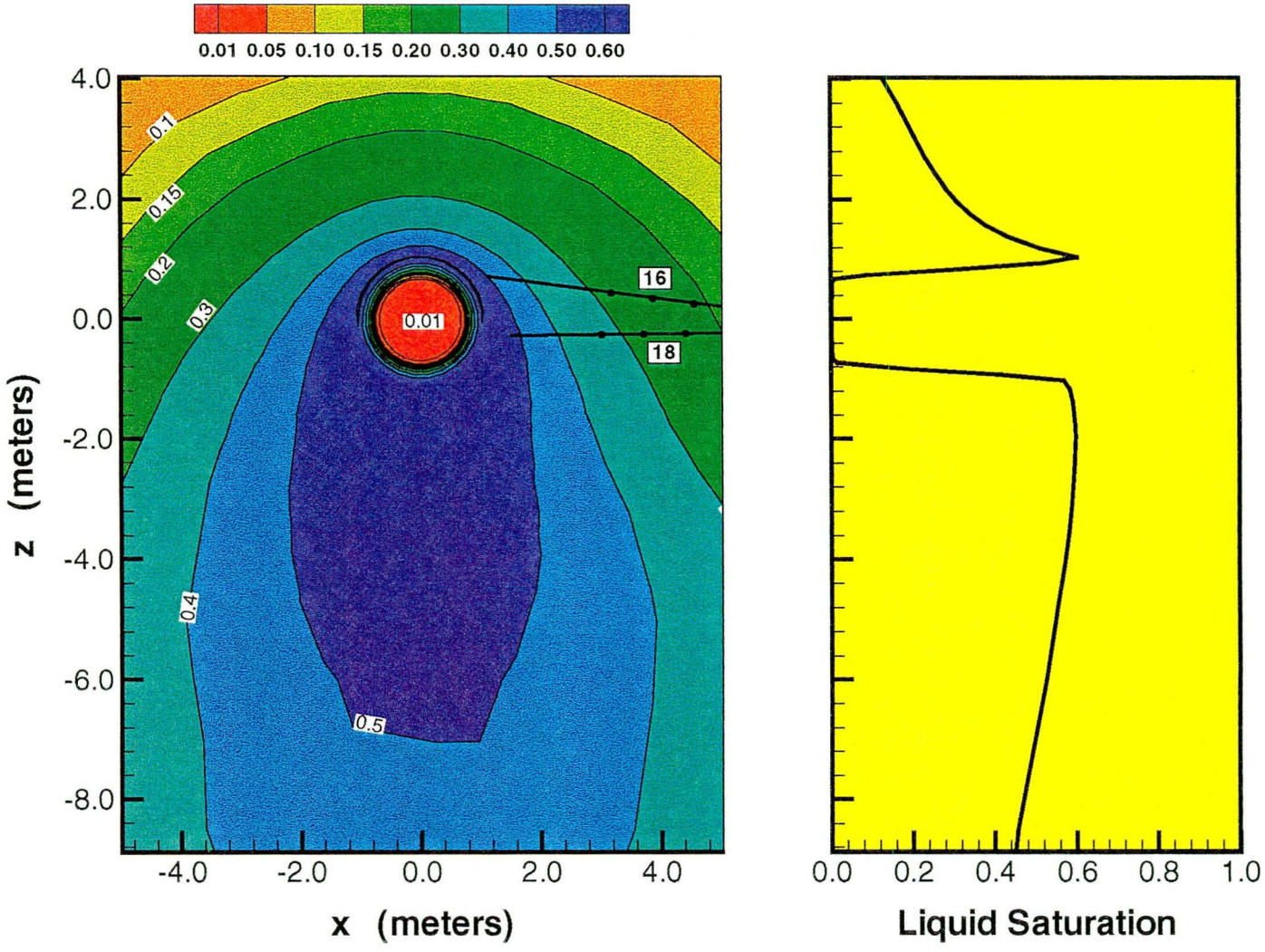

Figure 3.4-3 Simulated fracture liquid saturation after 3 months of heating in XZ–cross section at Y = 4.5 m

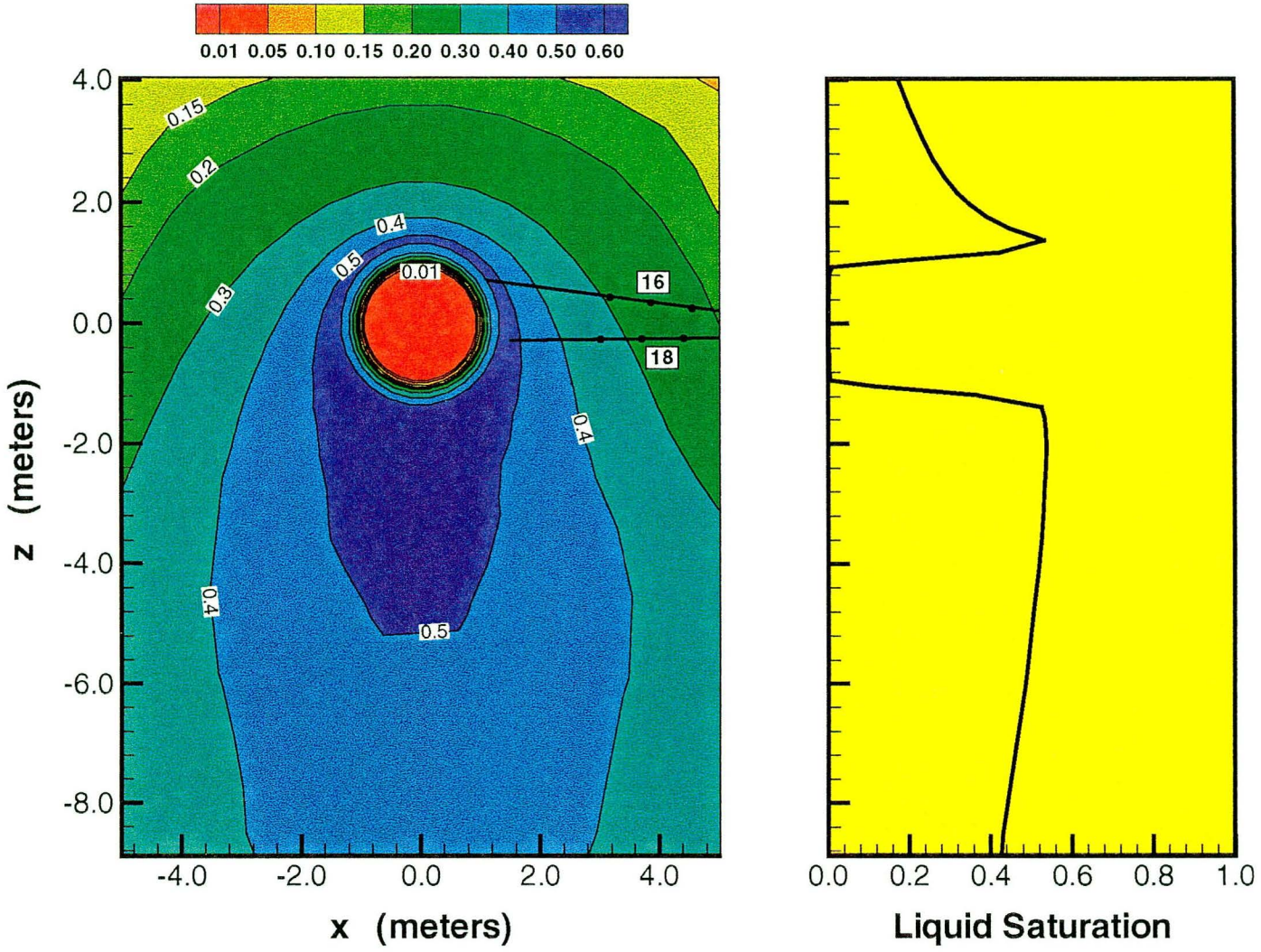

Figure 3.4-4 Simulated fracture liquid saturation after 9 months of heating in XZ–cross section at Y = 4.5 m

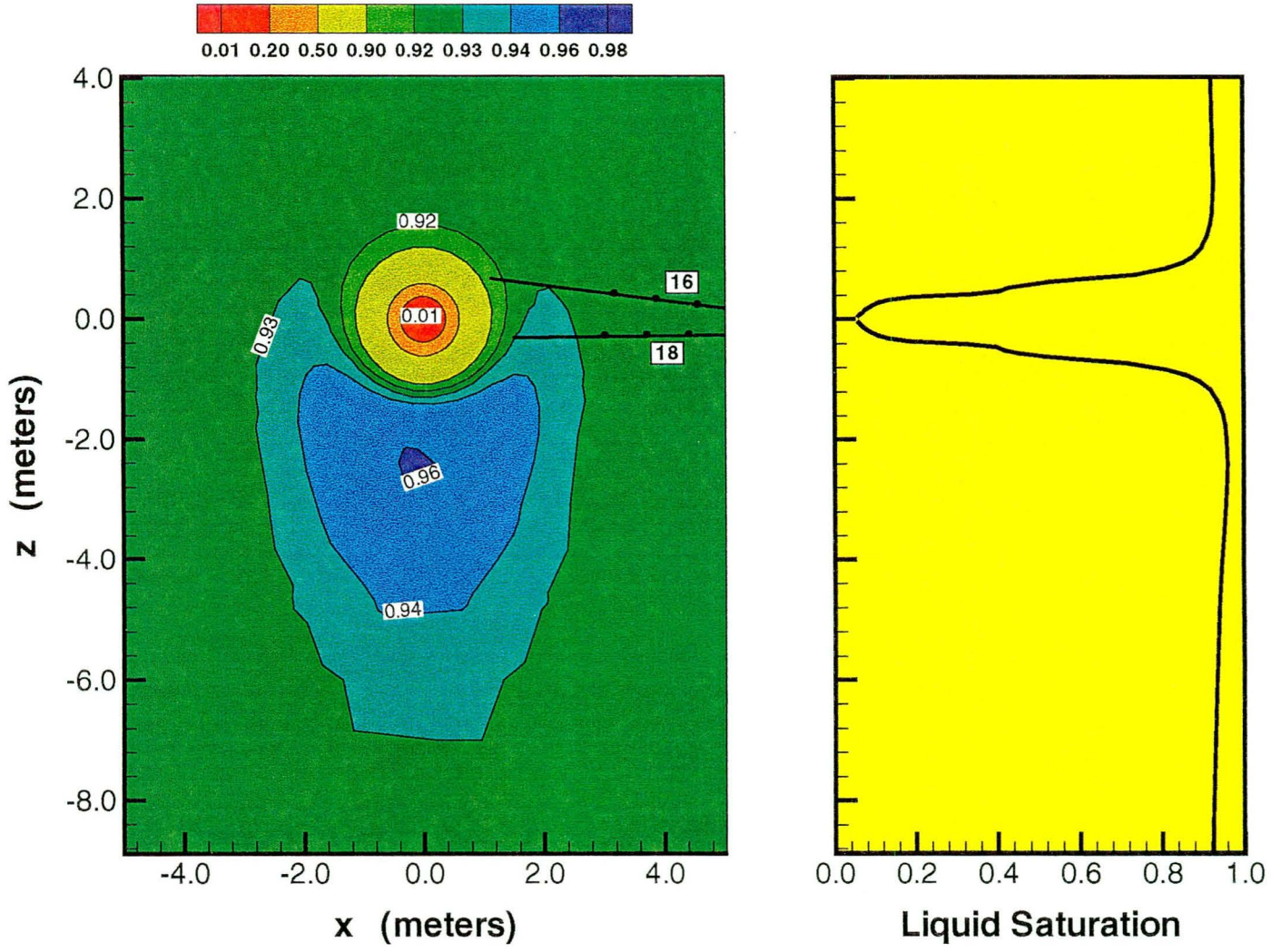

Figure 3.4-5 Simulated matrix liquid saturation after 3 months of heating in XZ–cross section at Y = 4.5 m

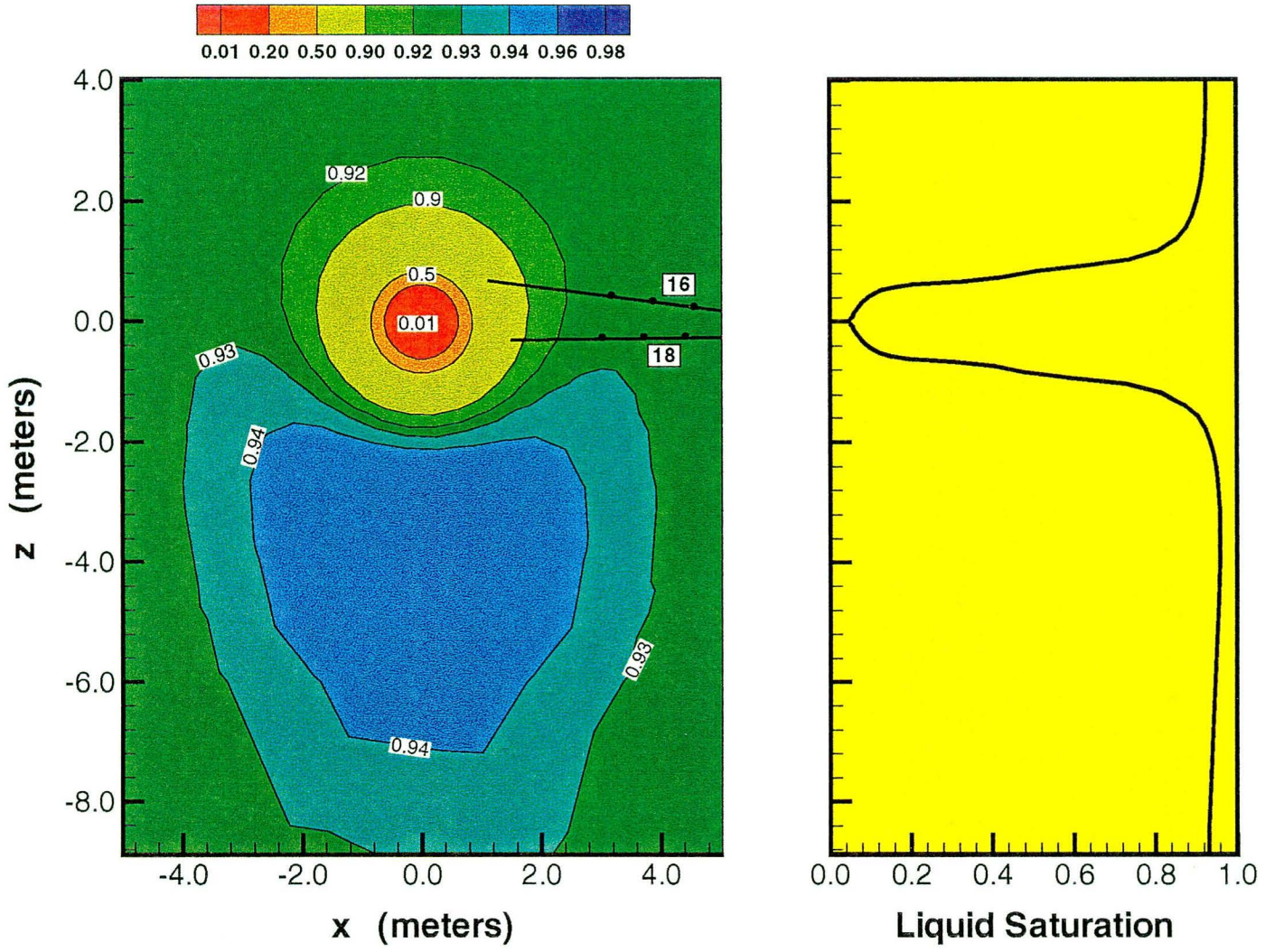

Figure 3.4-6 Simulated matrix liquid saturation after 9 months of heating in XZ–cross section at Y = 4.5 m

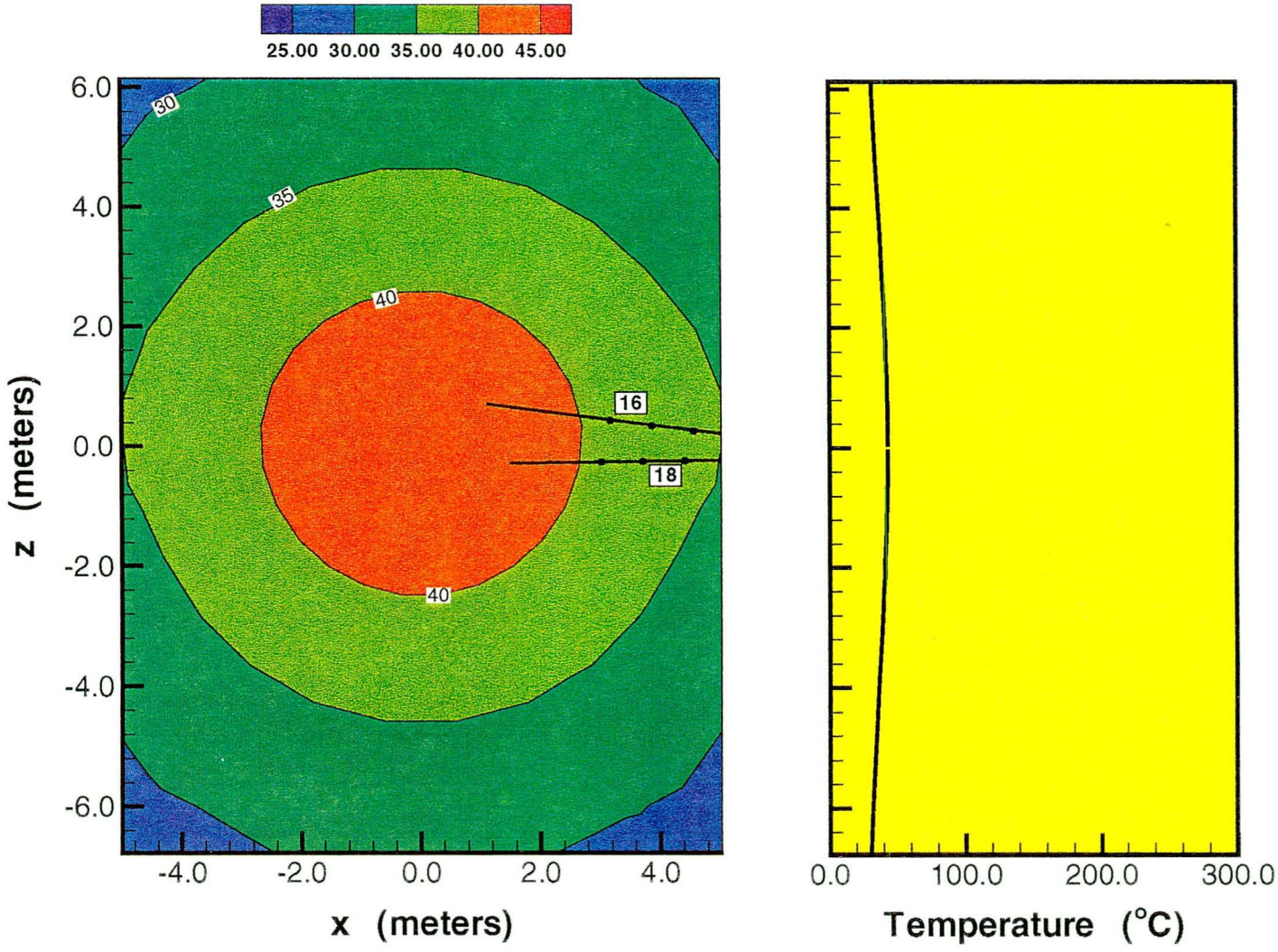

Figure 3.4-7 Simulated matrix temperature after 3 of cooling in XZ–cross section at Y = 4.5 m

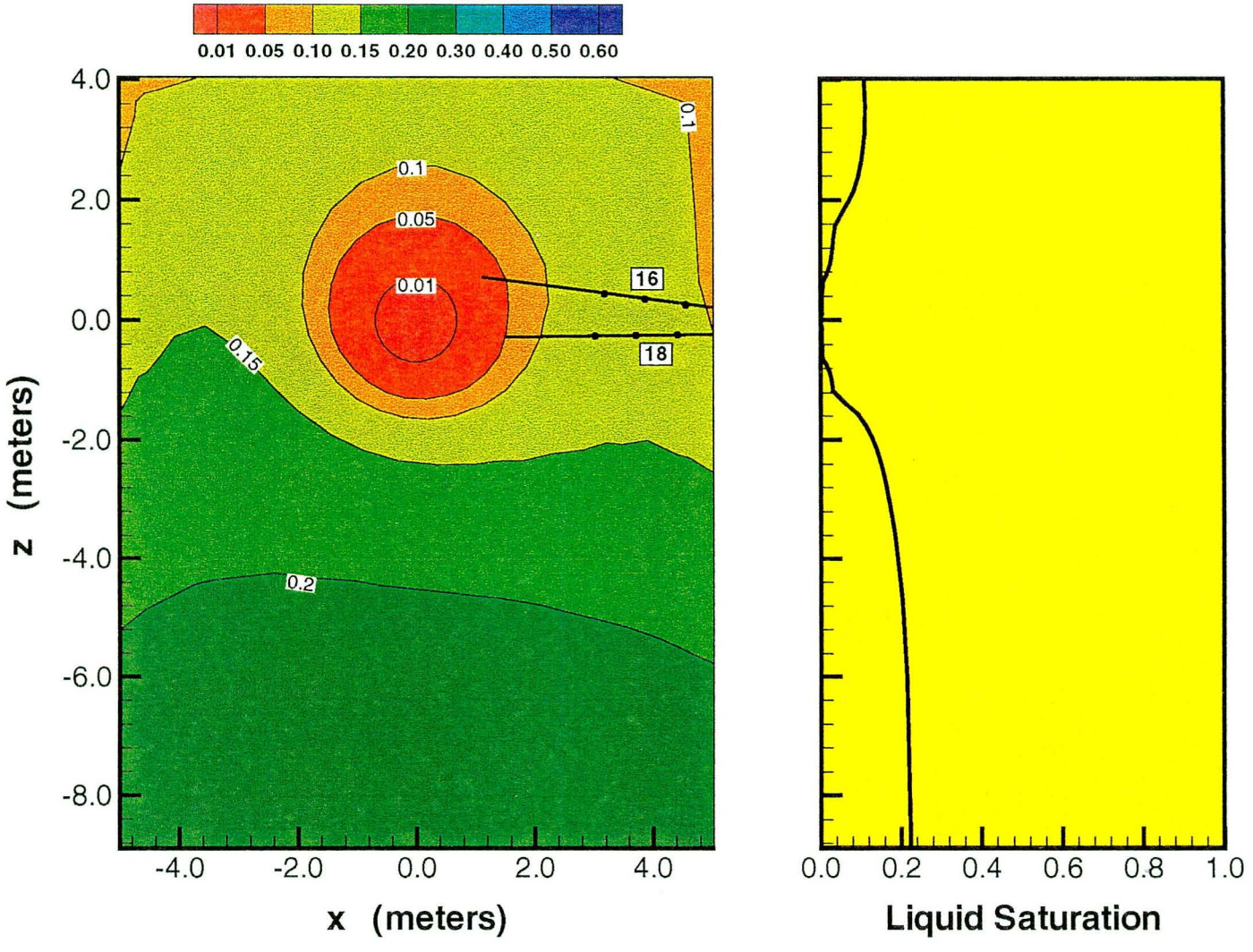

Figure 3.4-8 Simulated fracture liquid saturation after 3 of cooling in XZ–cross section at Y = 4.5 m

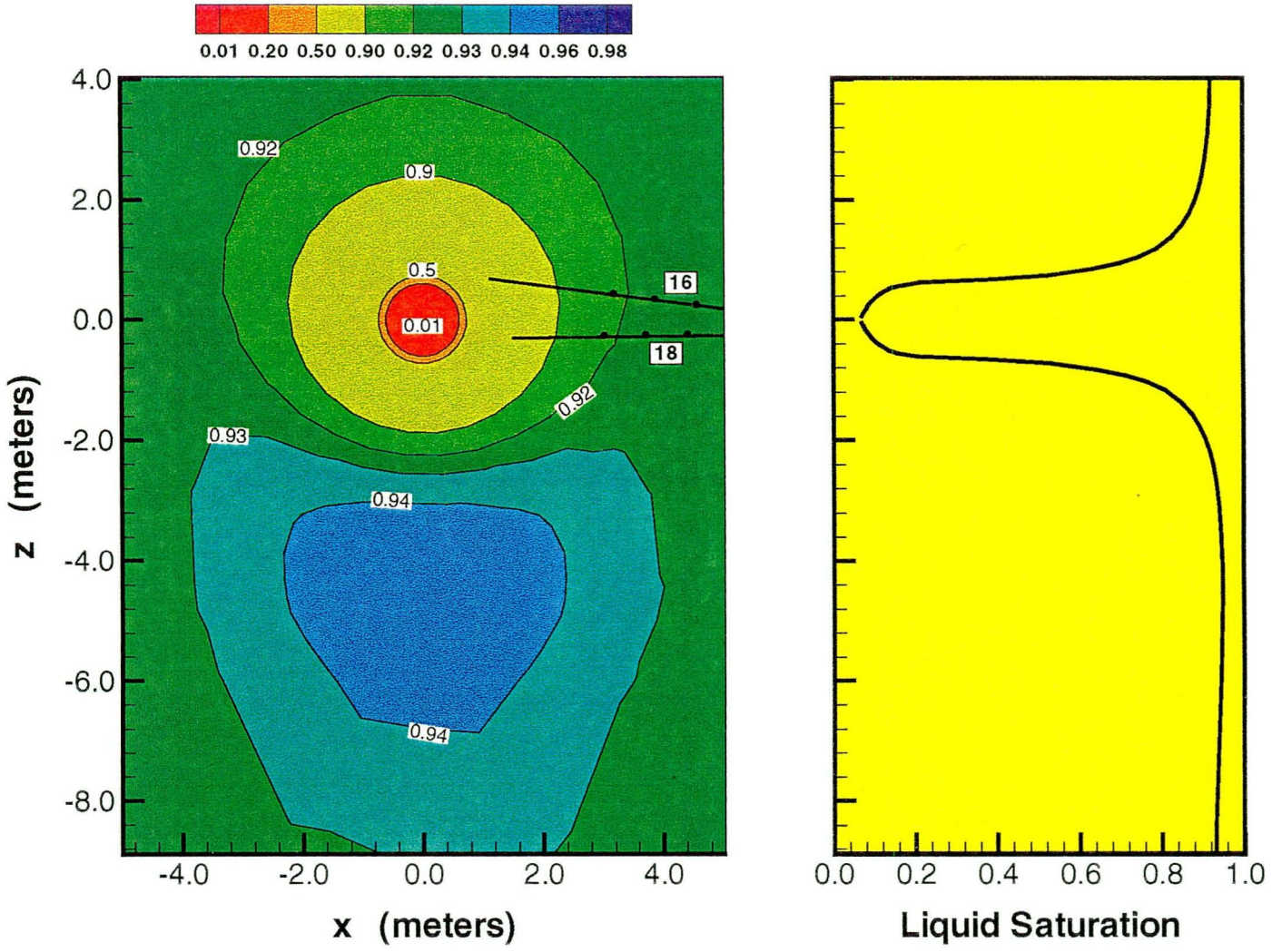

Figure 3.4-9 Simulated matrix liquid saturation after 3 of cooling in XZ–cross section at Y = 4.5 m

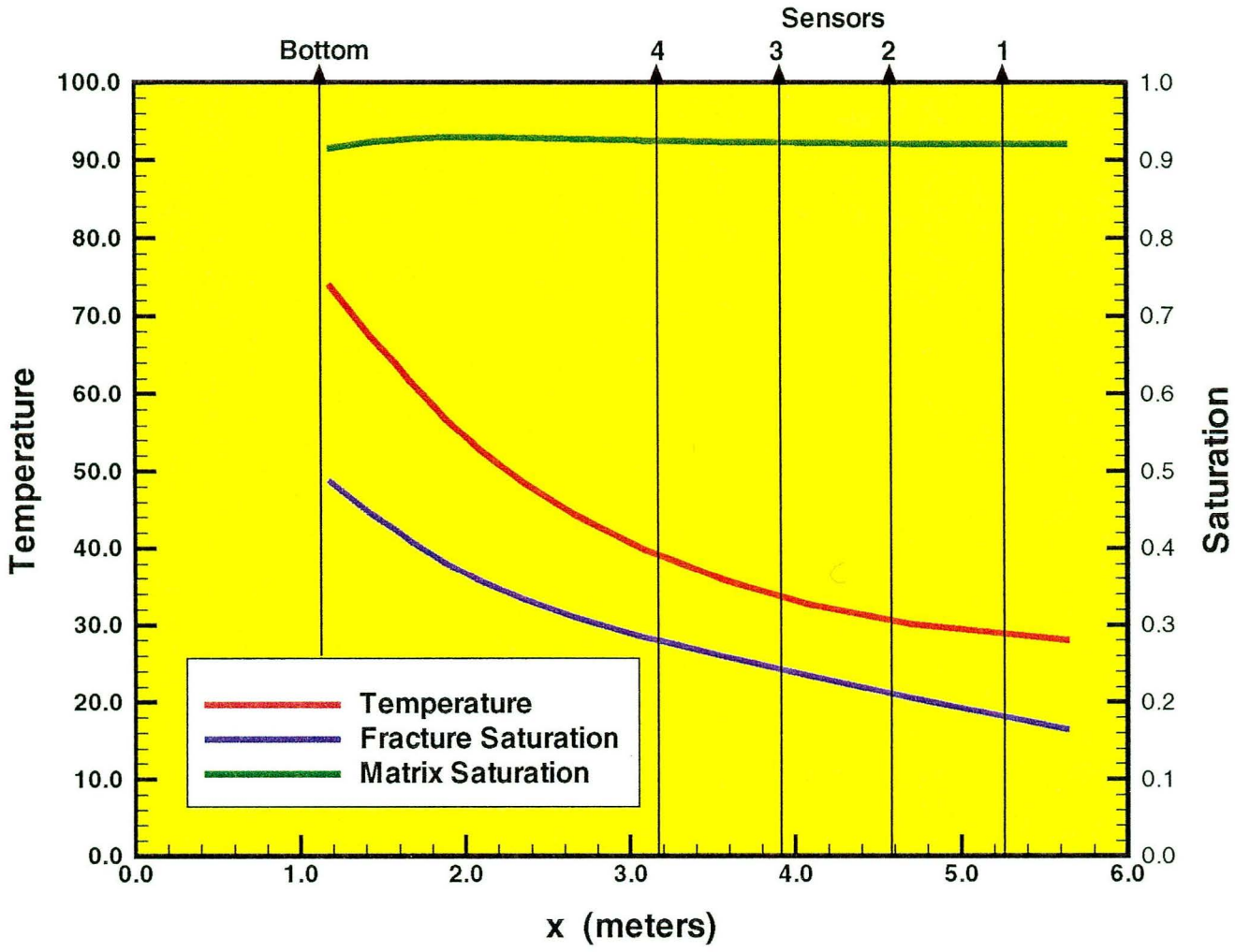

Figure 3.4-10 Simulated temperature and saturation along borehole 16 after 3 months of heating

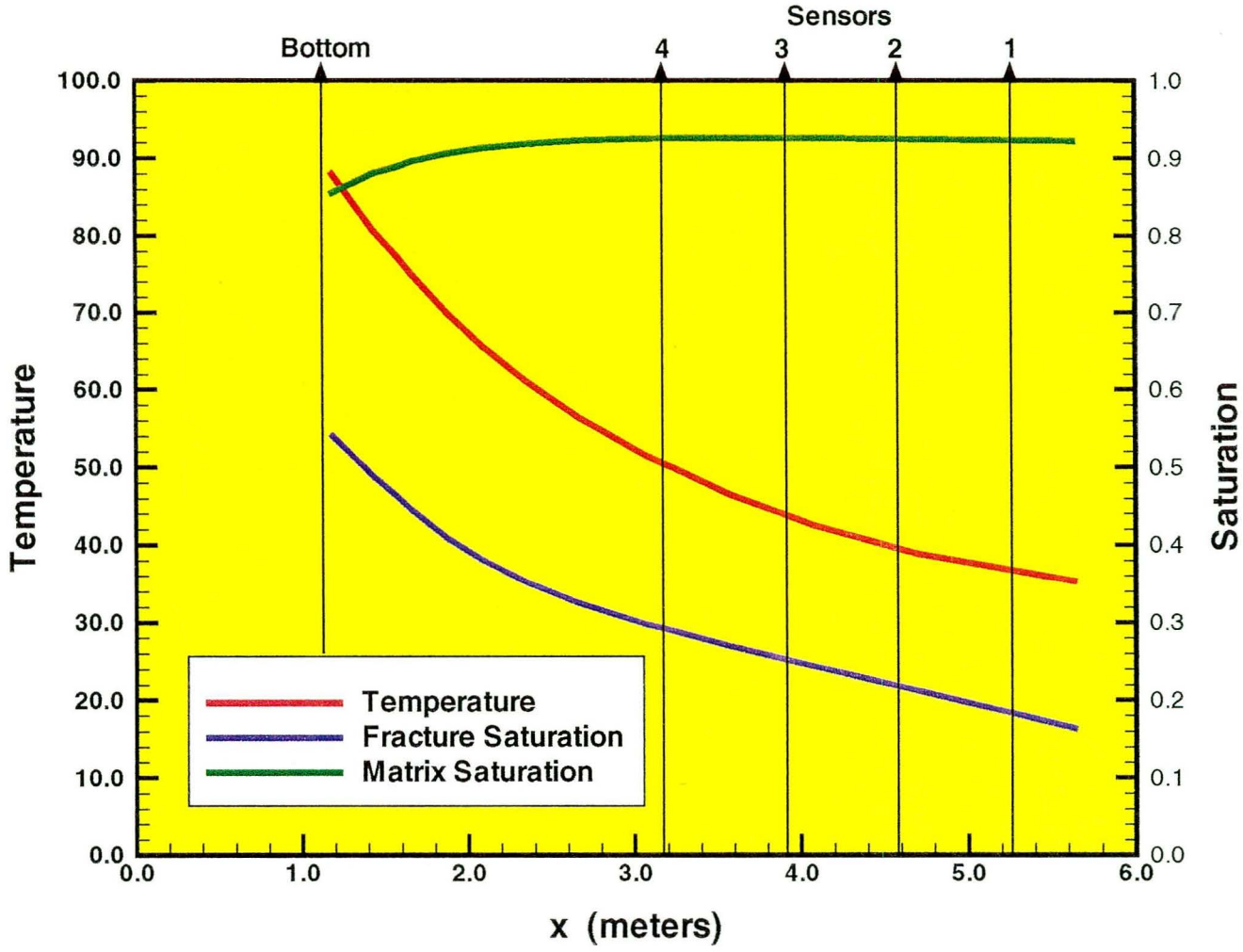

Figure 3.4-11 Simulated temperature and saturation along borehole 16 after 9 months of

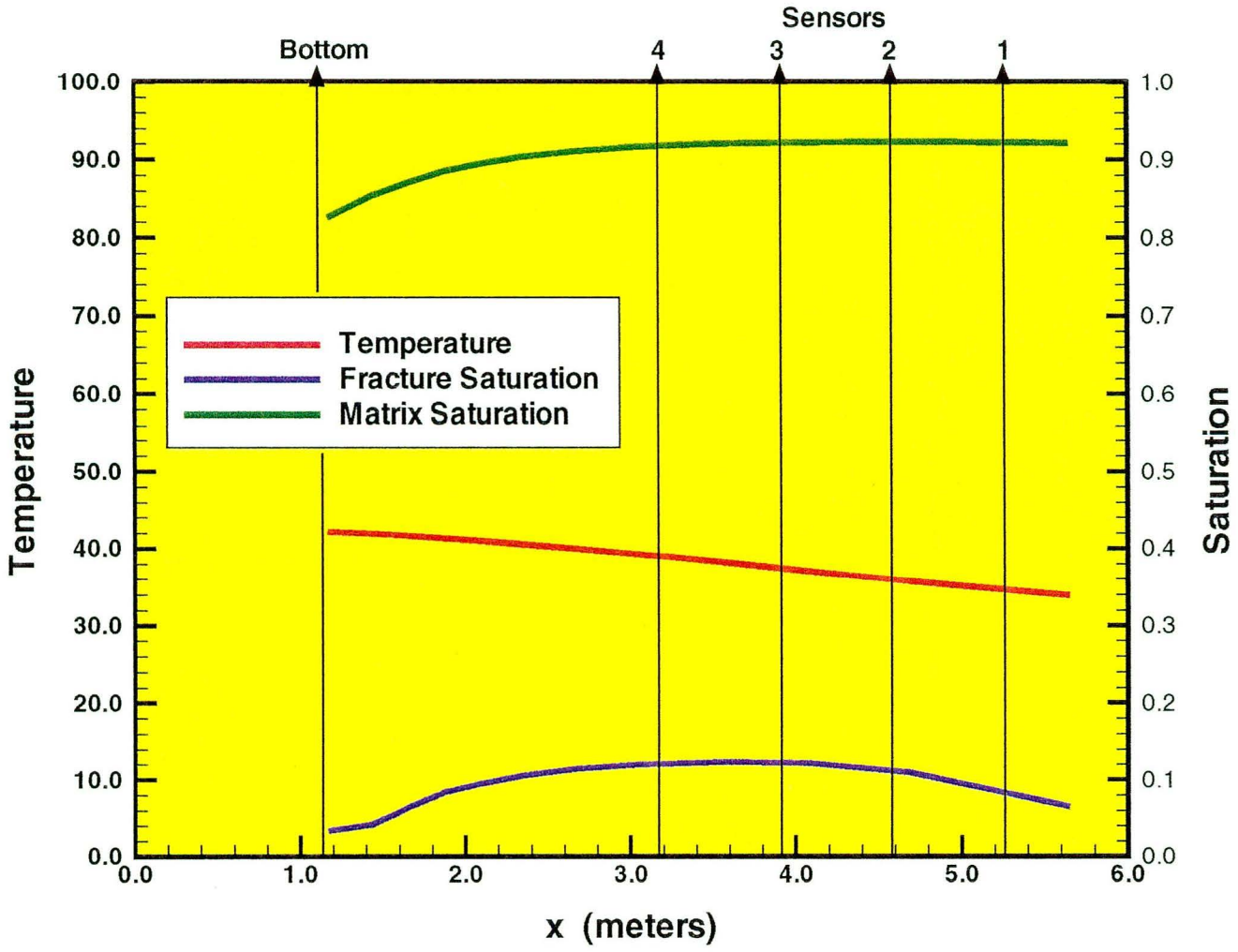

Figure 3.4-12 Simulated temperature and saturation along borehole 16 after 3 months of cooling

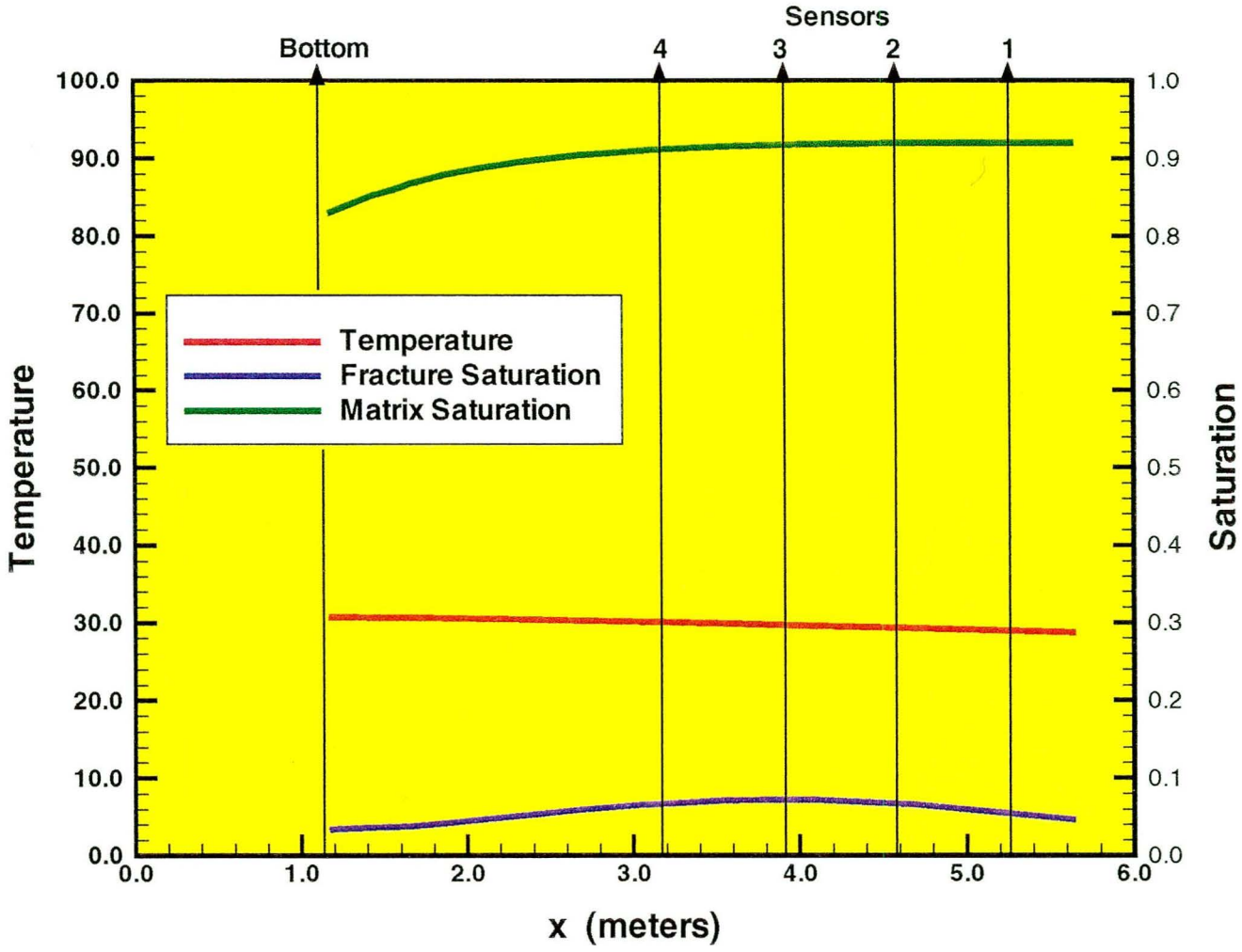

Figure 3.4-13 Simulated temperature and saturation along borehole 16 after 9 months of cooling

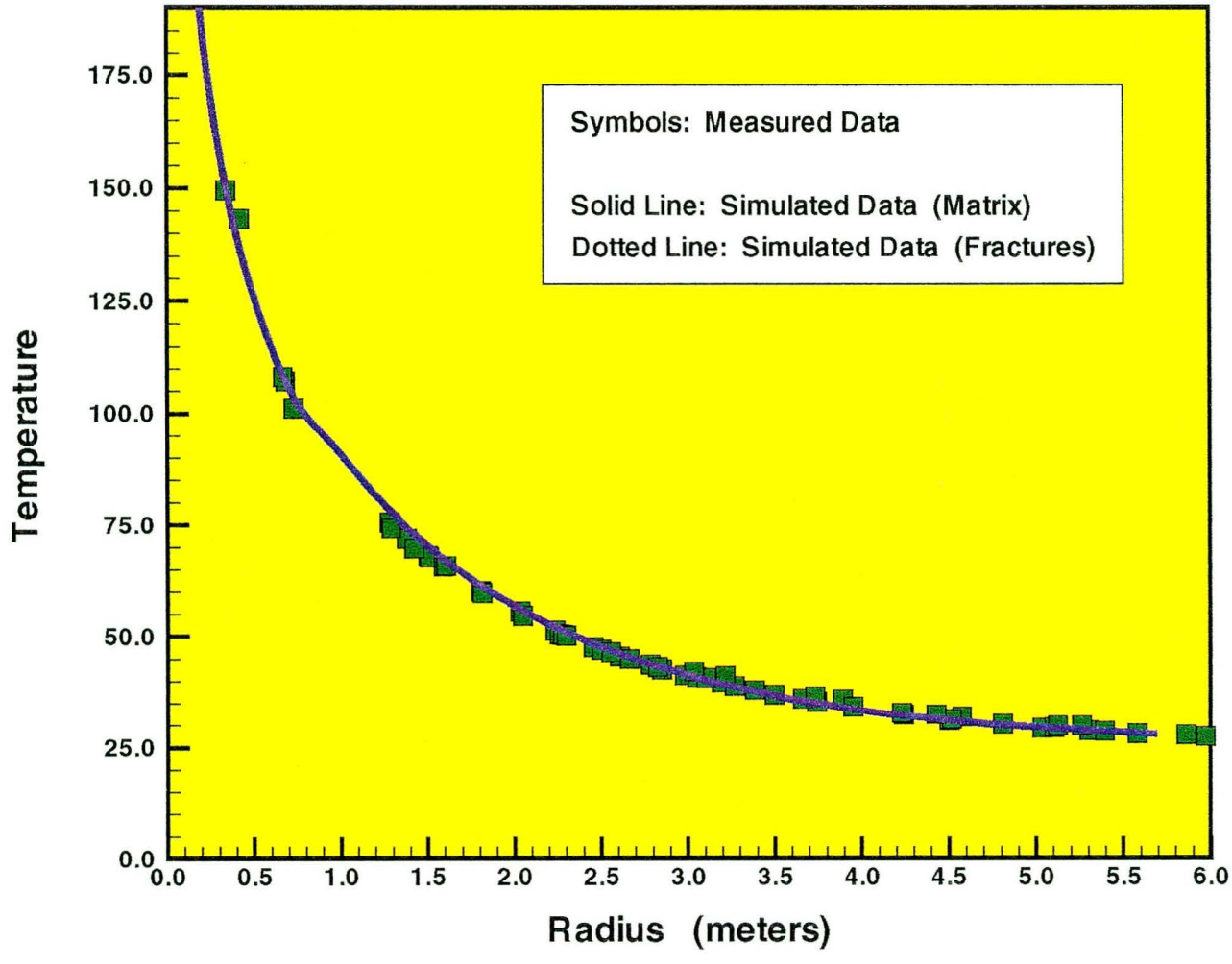

Figure 3.4-14 Measured and simulated temperature after 3 months of heating, for temperature sensors in the center-plane of the SHT block at Y = 4.5 m

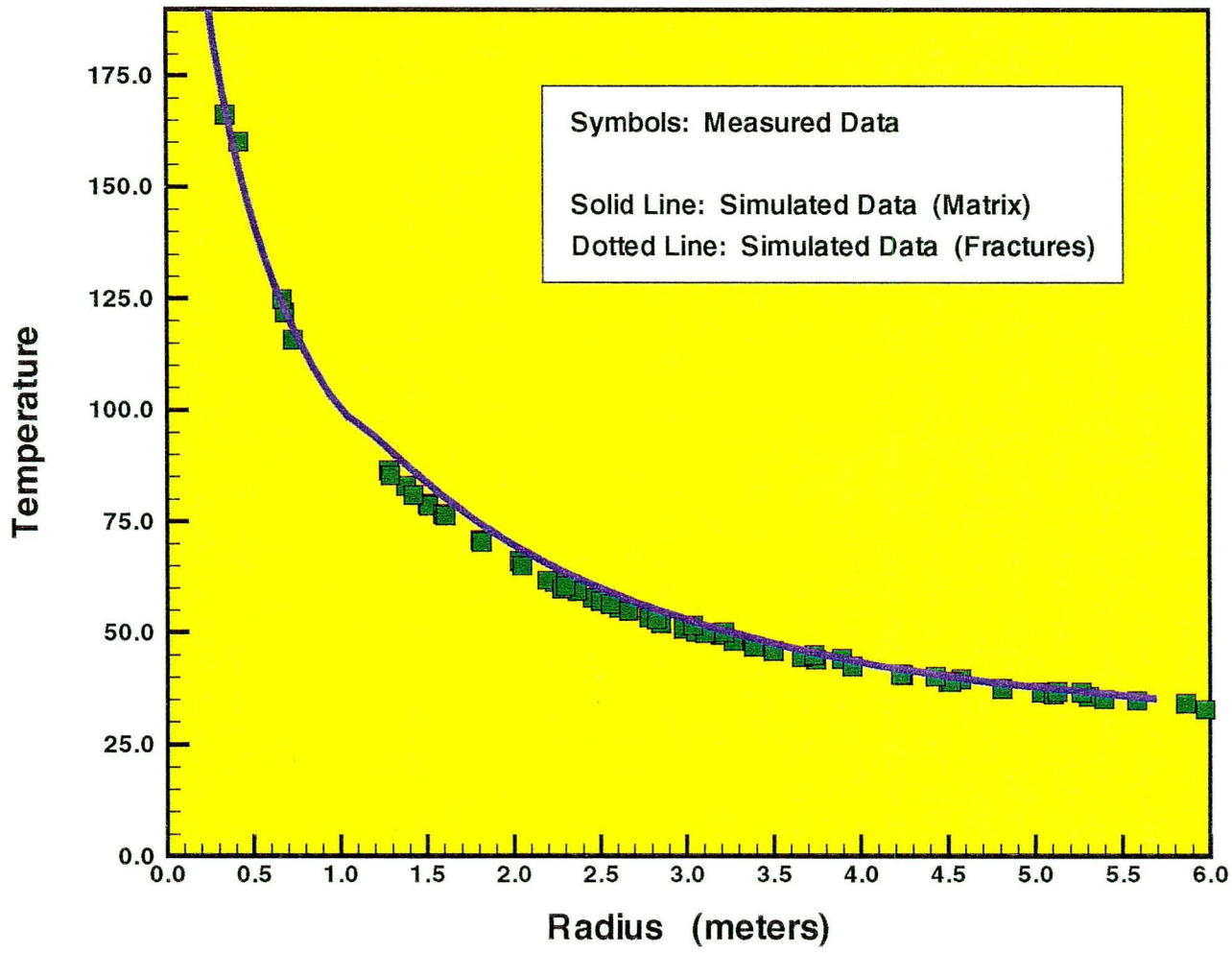

Figure 3.4-15 Measured and simulated temperature after 9 months of heating, for temperature sensors in the center-plane of the SHT block at Y = 4.5 m

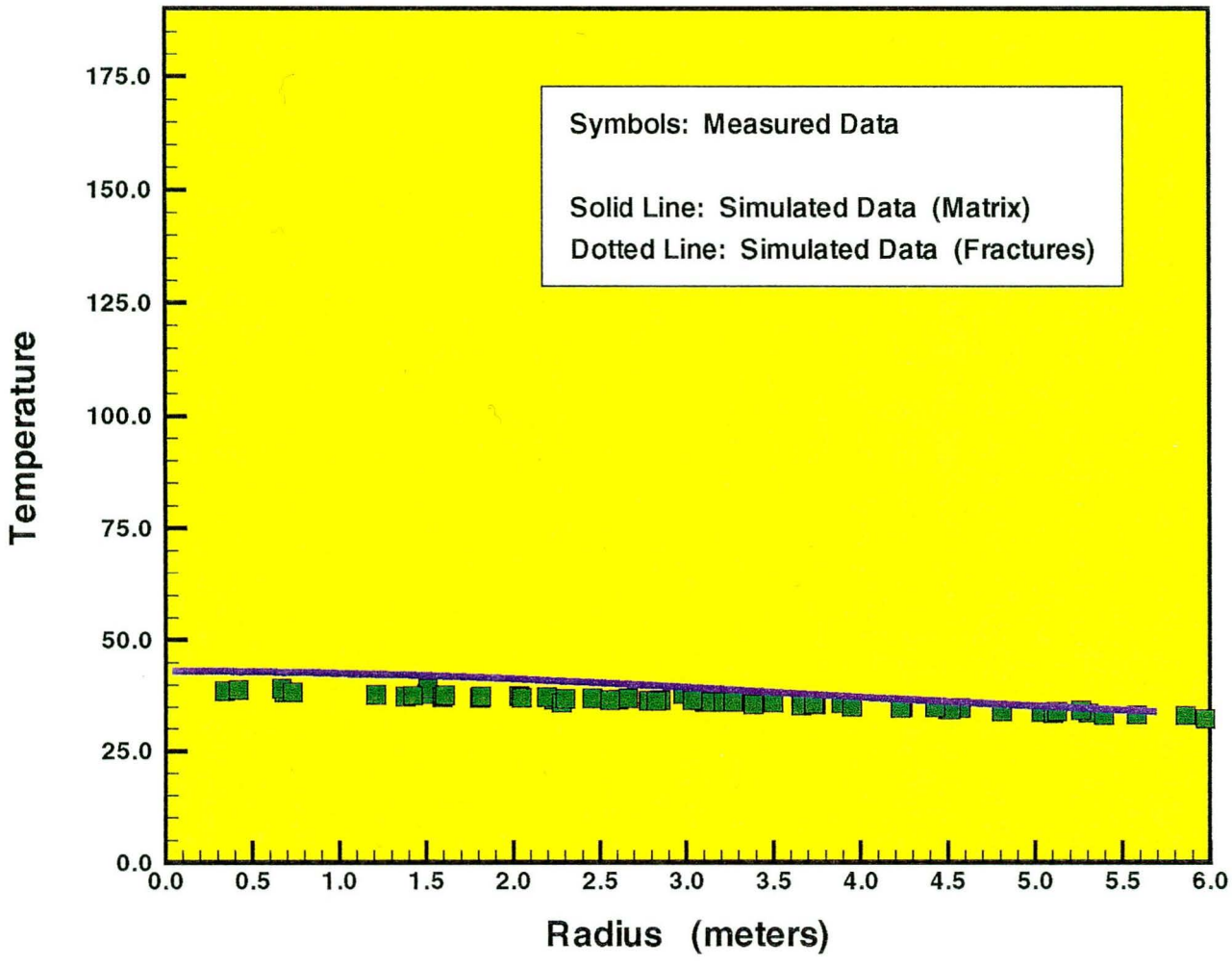

Figure 3.4-16 Measured and simulated temperature after 3 months of cooling, for temperature

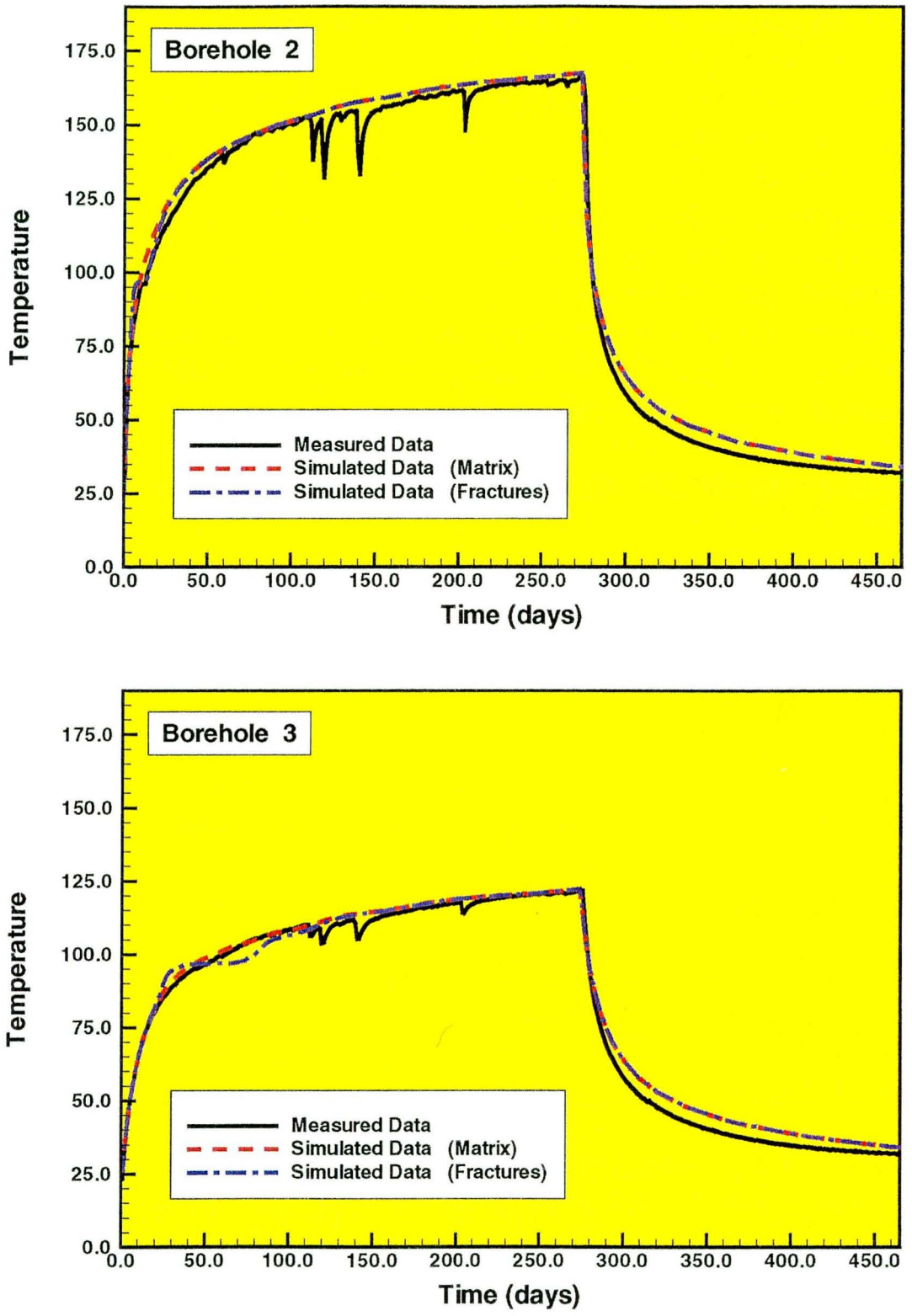

Figure 3.4-17a Measured and simulated temperature history in boreholes 2 and 3, for temperature sensors in the center-plane of the SHT block at Y = 4.5 m

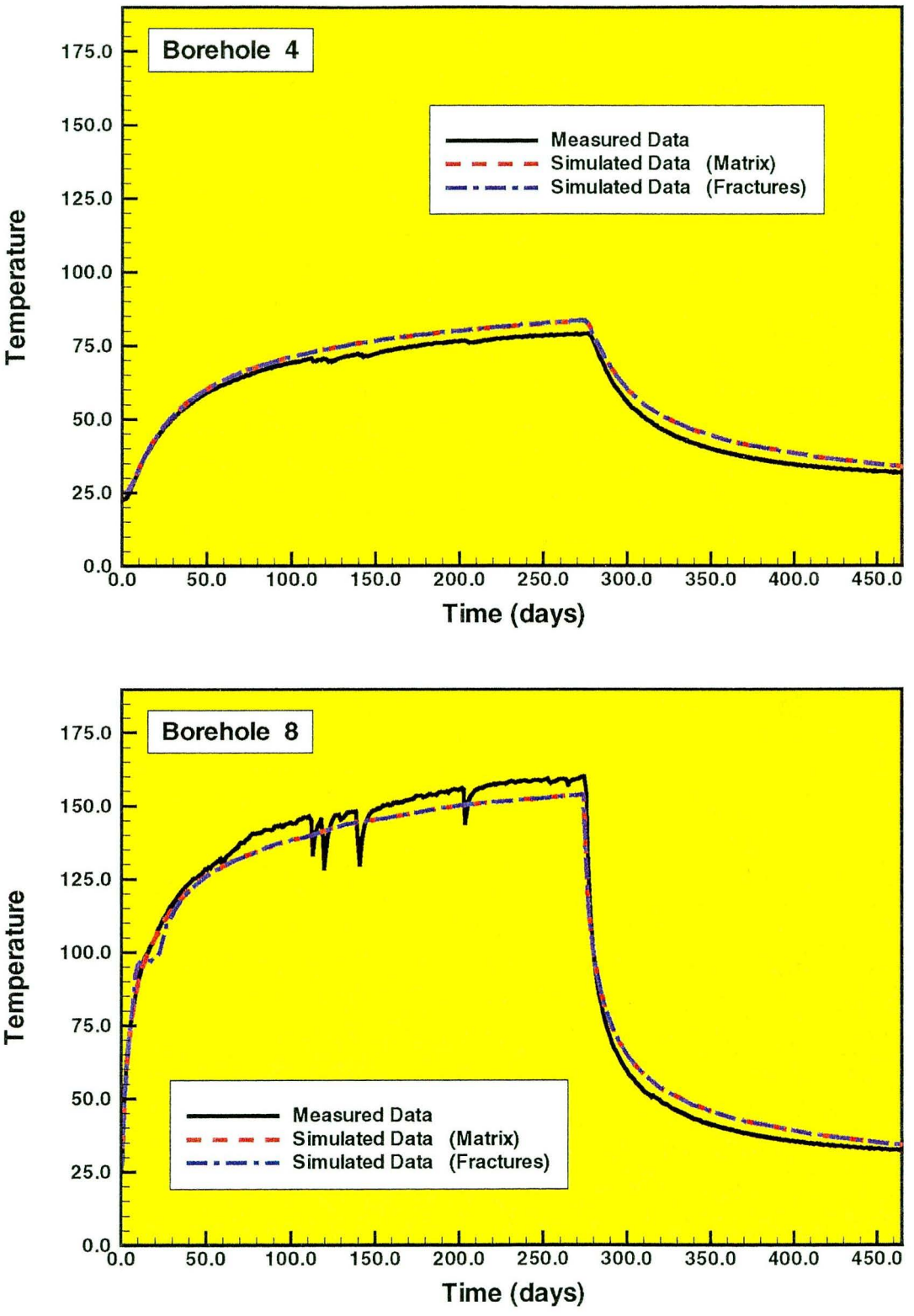

Figure 3.4-17b Measured and simulated temperature history in boreholes 4 and 8, for temperature sensors in the center-plane of the SHT block at Y = 4.5 m

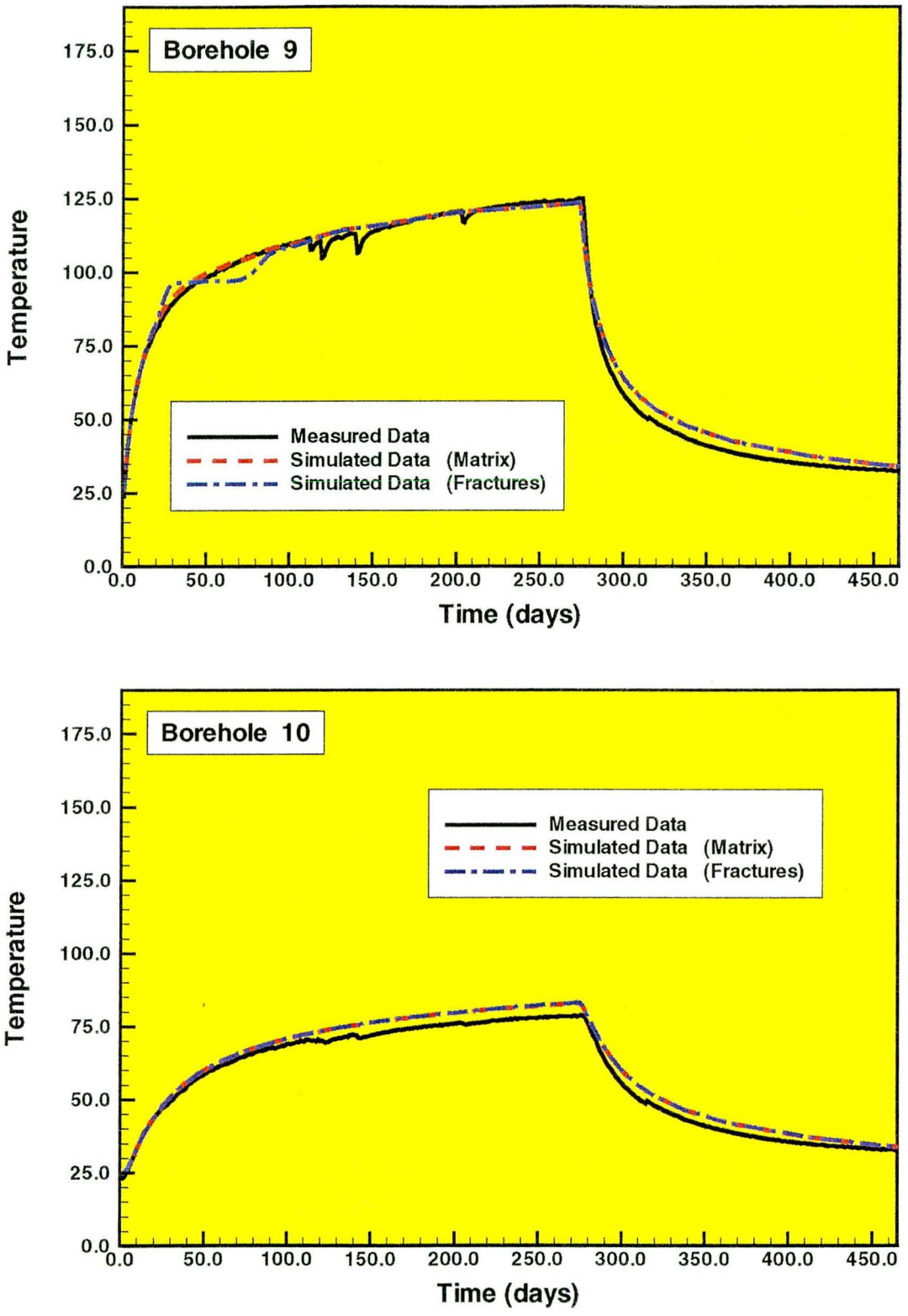

Figure 3.4-17c Measured and simulated temperature history in boreholes 9 and 10, for temperature sensors in the center-plane of the SHT block at Y = 4.5 m

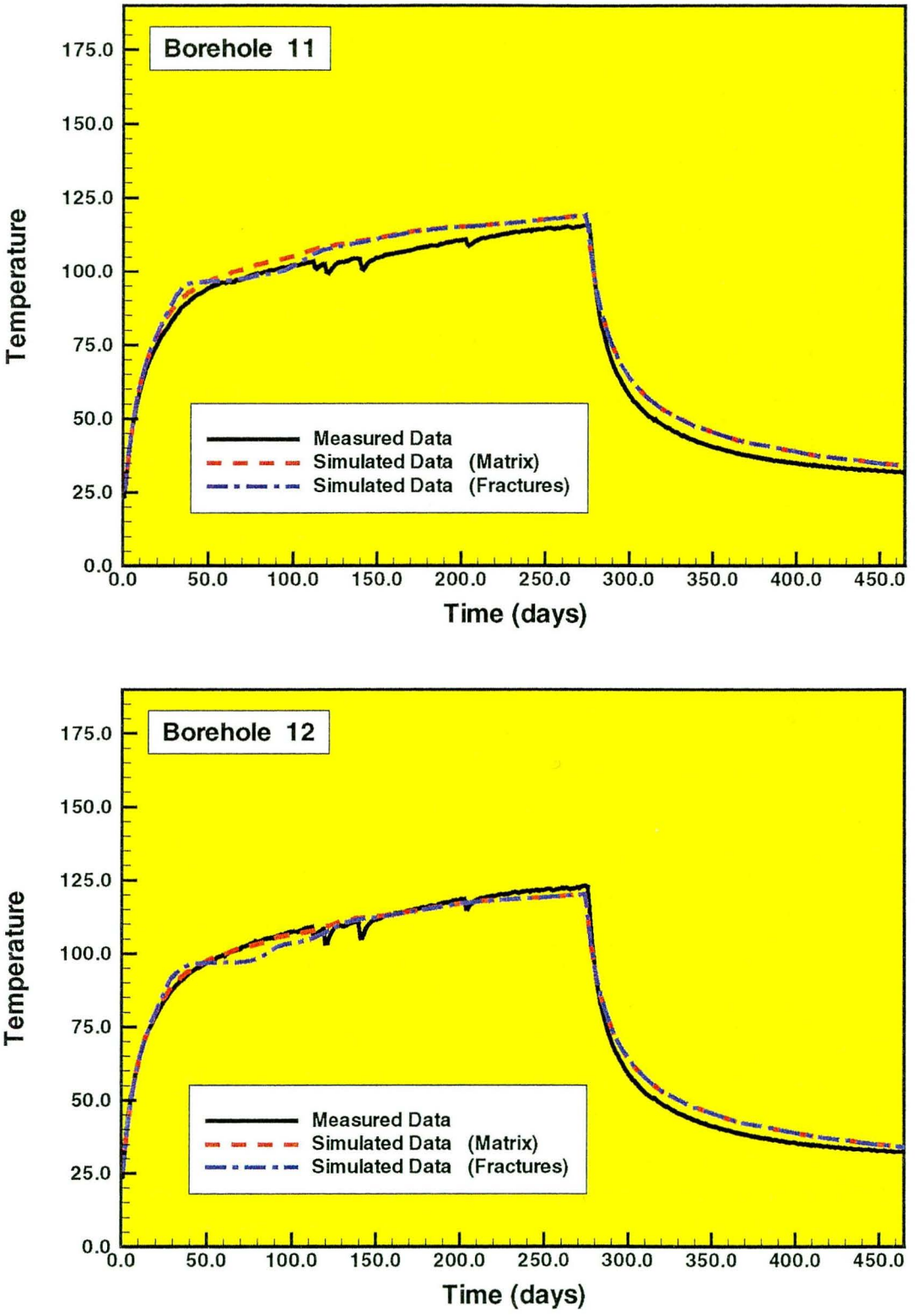

Figure 3.4-17d Measured and simulated temperature history in boreholes 11 and 12, for temperature sensors in the center-plane of the SHT block at Y = 4.5 m

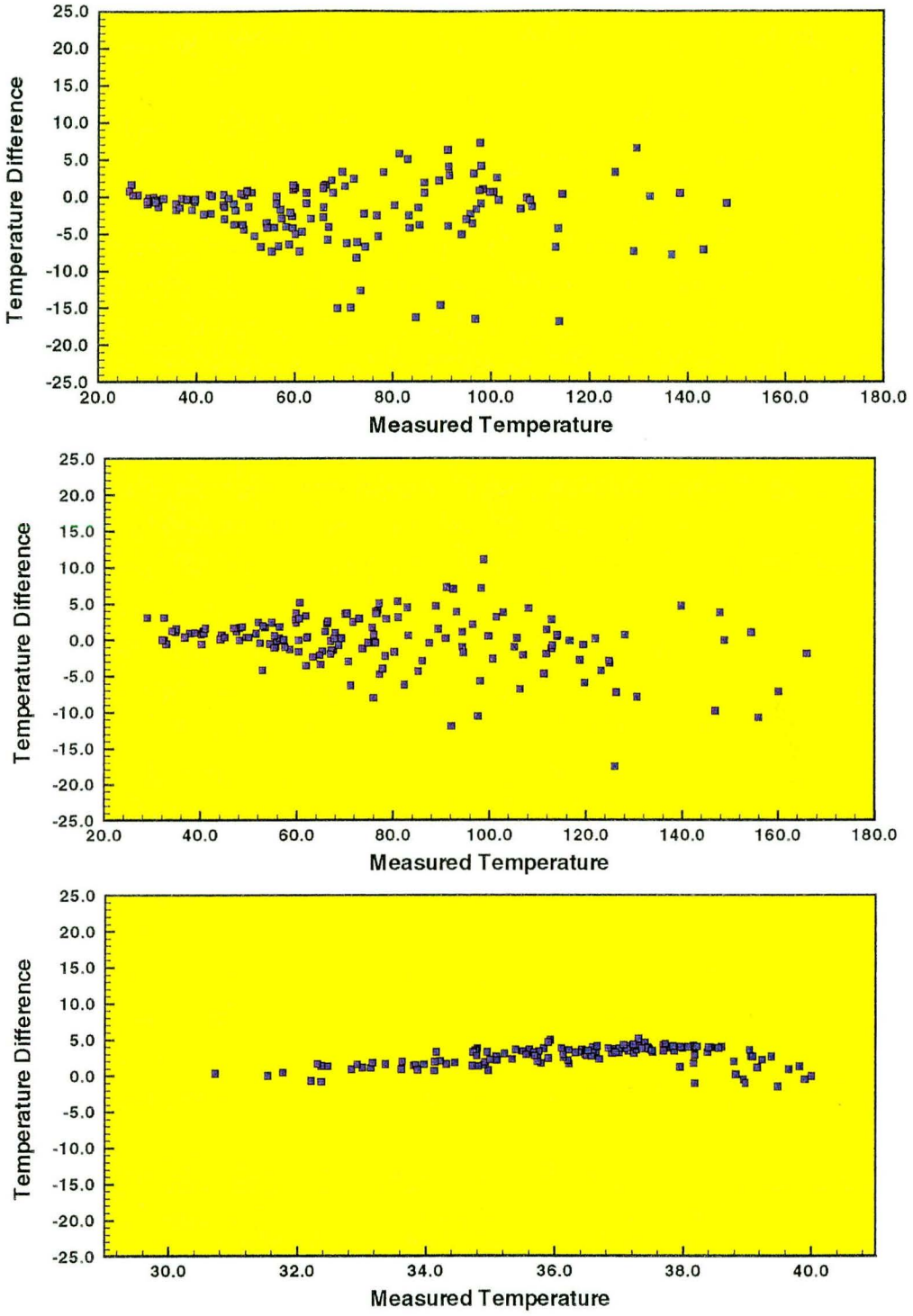

Figure 3.4-18. Difference between the simulated and the measured temperature as a function of measured temperature. The top graph, center graph and bottom graph show results at 3 months, 9 months of heating, and

3 months into cooling, respectively.

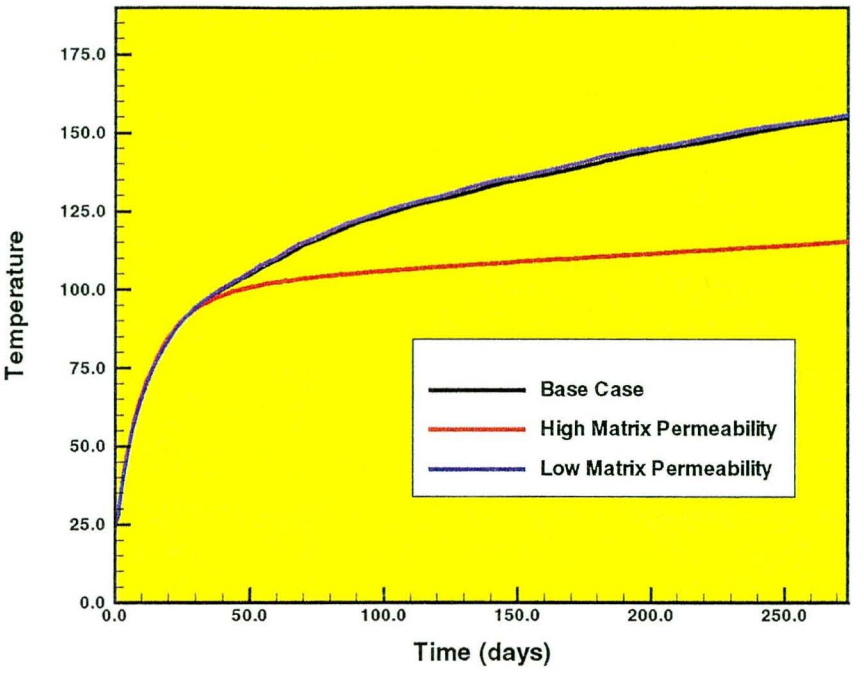

Figure 3.4-19 Sensitivity of temperature to a one-order-of-magnitude change in matrix permeability

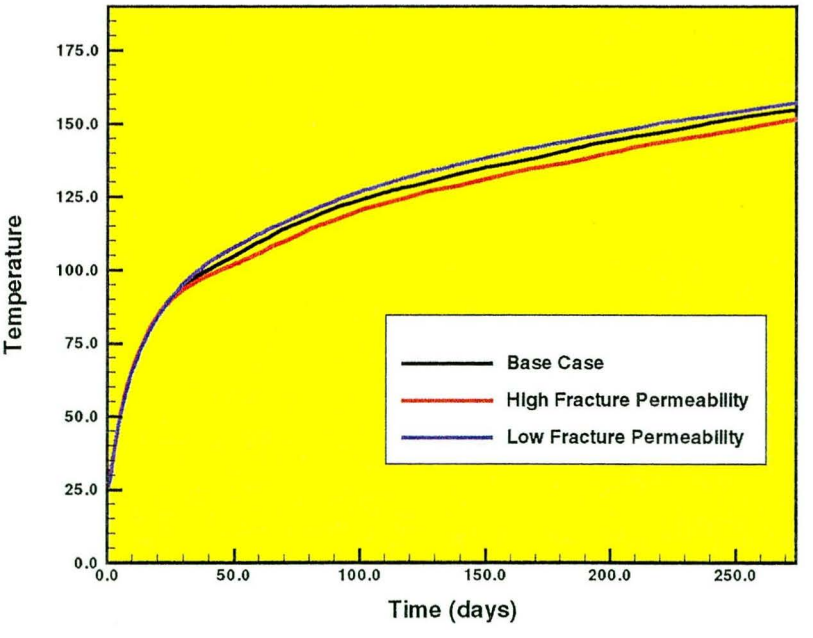

Figure 3.4-20 Sensitivity of temperature to a one-order-of-magnitude change in fracture permeability

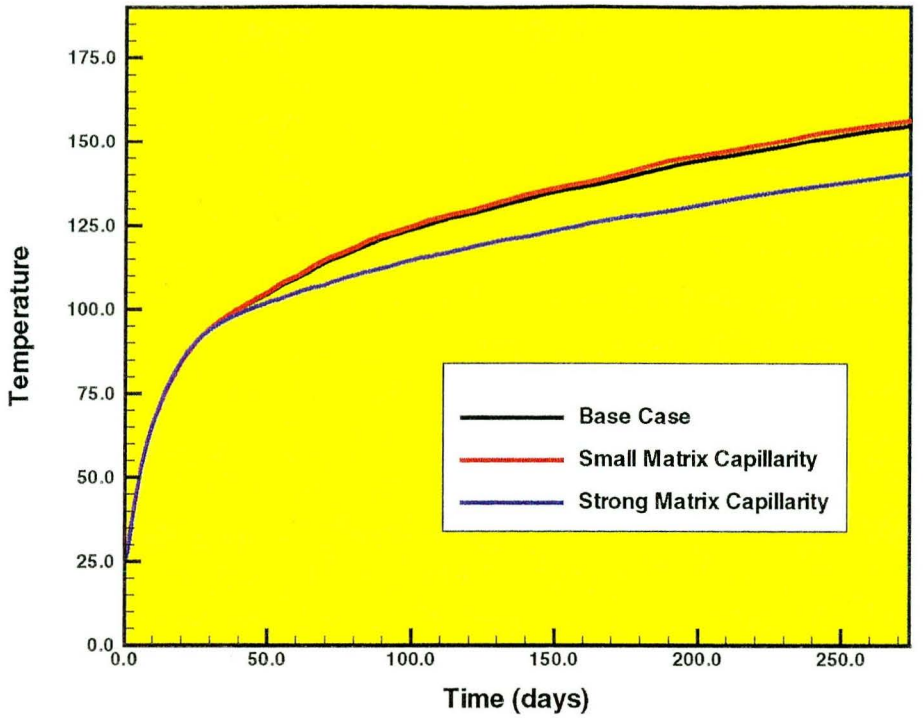

Figure 3.4-21 Sensitivity of temperature to a one-order-of-magnitude change in matrix α - parameter

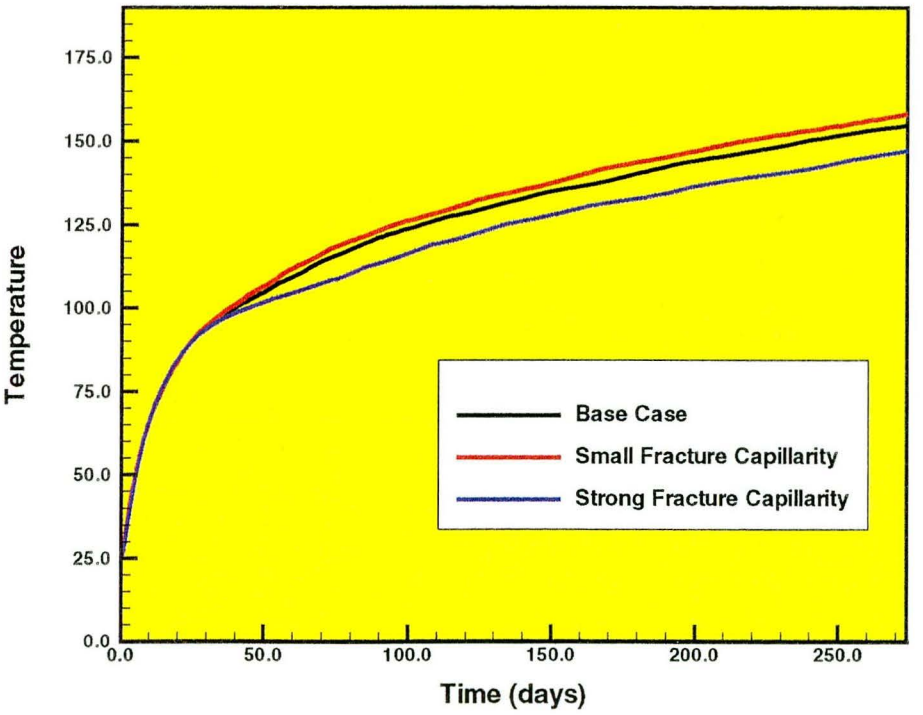

Figure 3.4-22 Sensitivity of temperature to a one-order-of-magnitude change in fracture α - parameter

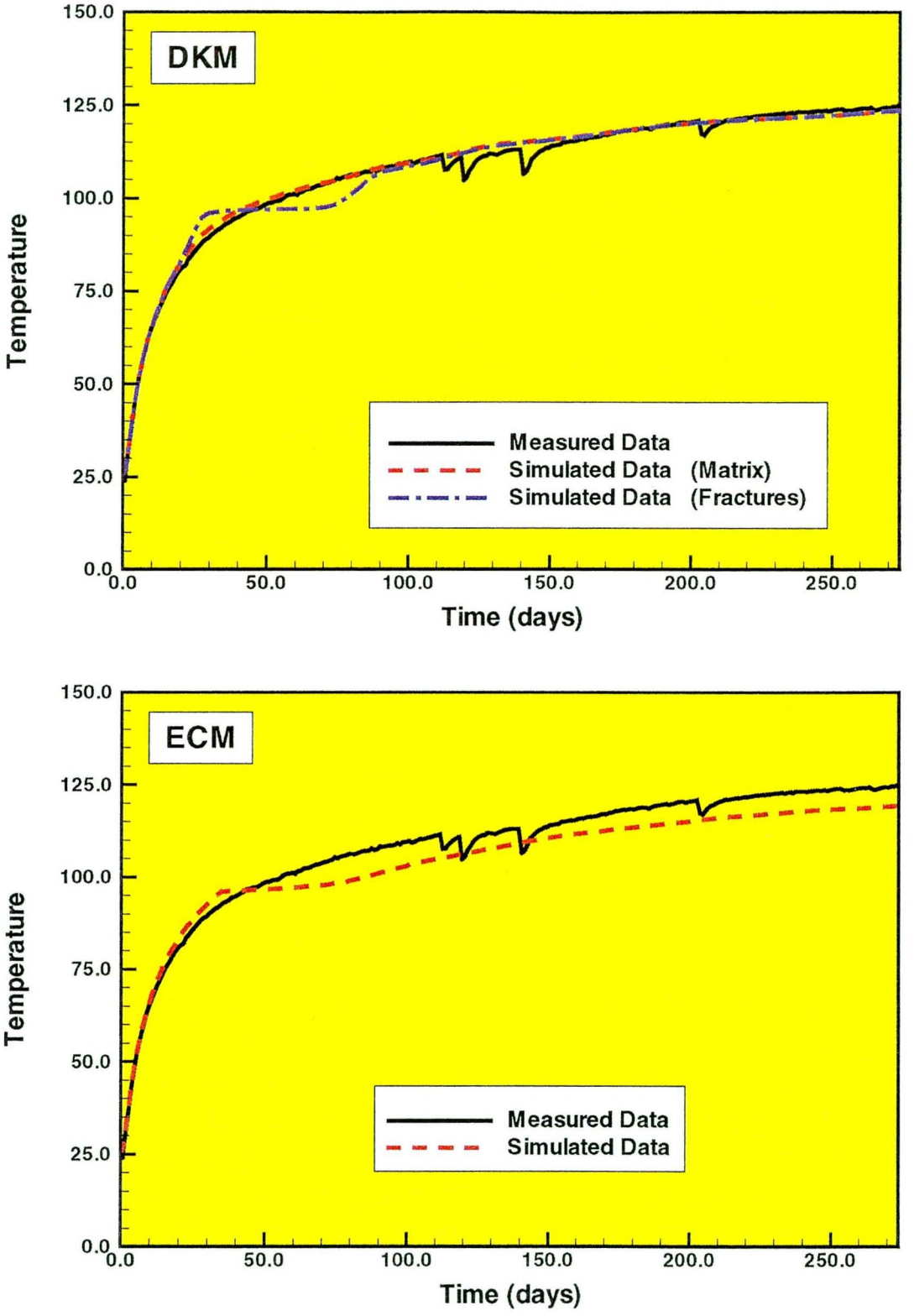

Figure 3.4-23 Measure versus simulated temperature history for DKM and ECM

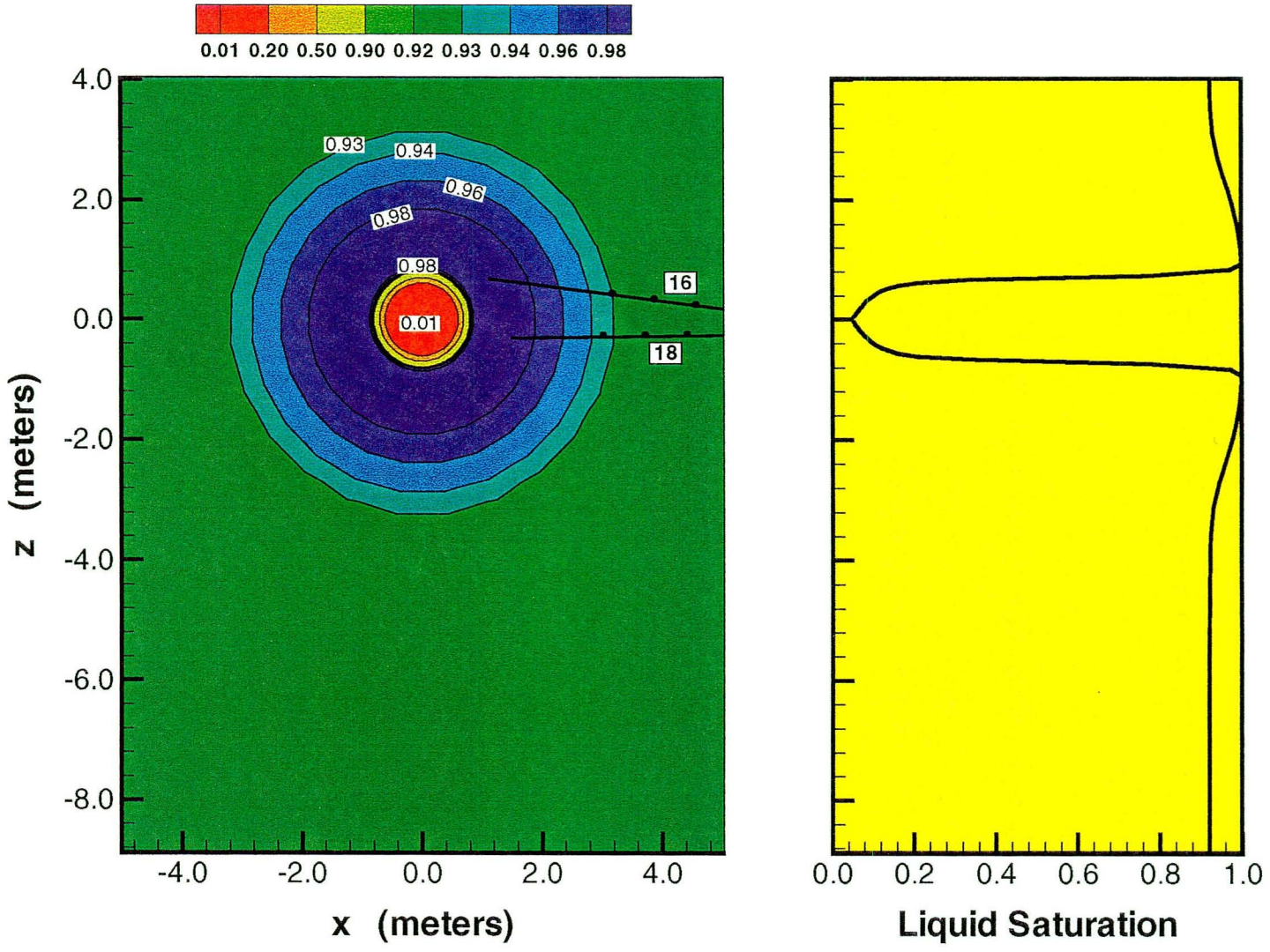

Figure 3.4-24 Simulated matrix liquid saturation at 3 months of] heating in XZ–cross section at Y = 4.5 m, using ECM

This page intentionally left blank.

Chapter 4 Interpretive Analysis of the Thermo-Hydrological-Chemical Aspects of the Single Heater Test

N. Spycher, E. Sonnenthal, and J. Apps

4.1 Introduction

This chapter focuses on modeling the thermal, hydrological, and chemical (THC) processes accompanying the Single Heater Test (SHT) and on interpreting the geochemical data collected during this test. This analysis is performed on the basis of thermal and hydrological data discussed in Chapter 3 of this report, previous geochemical studies, and a conceptual model of THC processes developed from previous modeling efforts.

The geochemical data available from the SHT are limited to two sets of analyses of water samples collected in borehole 16 and new mineralogical data from overcoring borehole 16 and borehole 2 after completion of the test. The interpretive analysis presented here is therefore limited and will be supplemented by more extensive geochemical data from the currently ongoing Drift Scale Test (DST) as these become available. For the present time, the results of simulations discussed in this chapter will be useful in supplementing previous studies of borehole-16 water and in further understanding of THC processes that may have implications for the assessment of repository performance and waste package design.

The objective and background for this interpretive study are stated below in this section. Specifics on the QA status of data and computer programs used specifically in this chapter are presented in Section 4.2. These supplement the general QA status of data and programs stated in Chapter 1 of this report. Mineralogical and water chemistry data collected as part of the test are discussed in Section 4.3 and provide a basis for input data to numerical simulations presented in Section 4.5. In Section 4.4, the THC processes affecting the test are summarized to provide a context for interpretation of simulation results. Coupled THC simulations of the SHT are presented in Section 4.5, which also includes details on the numerical model and input data. In Section 4.6, modeling results are compared with mineralogical and water chemistry data collected during the test. Conclusions are stated in Section 4.7.

4.1.1 Objective

The objective of this study is primarily to improve our understanding of THC processes accompanying the SHT, as these processes may have direct implications on the design and long-term performance of a nuclear waste repository at Yucca Mountain. By comparing field geochemical data with results of numerical simulations, our goal is also to determine whether the quantitative methods and input data used in our current THC models are adequate to provide reliable long-term predictions of repository performance.

4.1.2 Background and Previous Studies

The SHT was the first test conducted as part of the ESF Thermal Tests. The latter comprise both the SHT and the DST, which were designed to study the *in situ* thermal, hydrological, mechanical and chemical responses of the proposed repository's host rock to heating. The heating phase of the SHT started on August 26, 1996, and lasted until May 28, 1997 (nine months). Test data were collected during the heating phase as well as during a following cooling period, which ended the first week of January 1998. Details on the SHT design and setup can be found in previous chapters of this report and references therein.

The SHT was primarily designed to collect thermal, mechanical, and hydrological data. The test was not designed to collect water samples, nor to provide extensive post-test mineralogical data. Ninety chemical sensors were installed for the SHT, but all either failed or could not be used because of calibration problems (CRWMS, 1997, p. 5-53). Several existing boreholes (e.g. 2 and 16) were overcored during post-test characterization to provide mineralogical data on the test alteration products. Mineralogical effects of the SHT were concentrated only on overcores of drillholes that were not originally filled with grout. Analyses of overcores from originally grouted drillholes were not completed because the interaction of the grout with surrounding rock makes the identification of SHT water/rock interaction products essentially impossible (Levy et al., 1998, p. 3).

The only currently available detailed analyses of post-test alteration products is presented by Levy et al. (1998, pp. 22 to 24). These authors based their study on SEM and XRD analyses of overdrilled cores ESF-TMA-PTC-MPBX-1 (drilled over borehole 2) and ESF-TMA-PTC-NEU-2 (drilled over borehole 16) (see also Figures 1.1-1 and 1.1-2 in Chapter 1 of this report), and were able to identify several mineral phases deposited during the test (Section 4.3). However, these authors stress the need for additional specific characterization of pre-test core samples to fully understand their post-test analyses.

During air-permeability testing on November 25, 1996, fluid was observed in injection line 16-4 of borehole 16 and subsequently sampled for chemical analysis. Additional samples were also collected from the same location on February 4, 1997, providing a second set of water analyses (Section 4.3). An interpretation of these analytical data was completed by Glassley (1997) and Glassley and DeLoach (1997). These authors carried out geochemical simulations as part of their evaluation and concluded the

water consisted of steam condensate which underwent some, although minimal, chemical interaction with surrounding rock. Analyses of gas samples to help constrain the water chemistry and further evaluate the origin of water in borehole 16 were not conducted because gas analyses were not part of the SHT project scope. Therefore, the two sets of water samples from borehole 16 constitute the only data providing direct insight into the chemistry of pore/fracture water during the SHT.

4.2 QA Status of Work

The work completed for this study was performed under the Yucca Mountain Project (YMP) Quality Assurance Program procedures. It is documented in YMP Scientific Notebooks listed in Chapter 1 of this report. The input and output data for computer simulations presented here, as well as the computer program used for these simulations, were submitted to the technical database with identification DTN:LB980901123142.005.

Specifics on the QA status of data and computer programs used specifically in this chapter are presented in this section. These supplement the general QA status of data and computer programs stated in Chapter 1 of this report.

4.2.1 QA Status of Data

The data used as input to modeling in this report come from a variety of qualified and unqualified sources. Supporting data for some calculations were drawn from scientific literature cited in the reference section. The QA status of specific analytical data is provided in Table 4.2.1. Other data were used as follows:

1. Hydrologic parameters and other specifications of the SHT were taken from Chapter 3 of this report (with Q status further described in Chapter 1 of this report), and from Birkholzer and Tsang (1996, pp. 8 to 12, 28).

2. Kinetic data were adapted from sources discussed in Section 4.5.4.5. These data are unqualified.

3. The thermodynamic database was developed as part of a previous study (Sonnenthal et al., 1998a, pp. 23 to 28) with addition of new data in Section 4.5.4.4. It is considered preliminary.

4. The pore-water-chemistry data were taken from Sonnenthal et al. (1998a, p. 63). These data are also preliminary.

All model output data are considered to be the results of exploratory calculations that are semi-quantitative at best because of the large uncertainty of input data.

Table 4.2-1. Analytical Data Sources and Q Status

Data Type, Organization, and Principal Investigator	Q Status	DTN/ACCN (if available)
XRD Mineralogy, LLNL, Roberts and Viani (1997)	Y	DTN LL980106404244.050
SEM-EDX, XRD Mineralogy, LANL, Levy et al. (1998)	N	NA
Mineralogy, USGS, Paces et al. (1998)	Y	DTN GS980308315215.009
UZ Pore-Water Analyses, USGS, Yang et al., 1996a,b	Y Y	MOL. 19970715.0408 (a) DTN GS970208312271.002 (b)
Borehole-16 Water Analyses, LLNL, Glassley (1997), Glassley and DeLoach (1997)	Y Y	DTN LL970409604244.030 DTN LL970703904244.034
Gas CO_2 analyses, LBNL, Conrad (1998)	N	NA

NA= Not Available; Y= qualified, N= unqualified data.

4.2.2 QA Status of Computer Programs

TOUGHREACT (Section 4.5.1) is the computer program used for all numerical simulations presented in this chapter. The qualification of TOUGHREACT is currently underway, and the code cannot be considered Q at this time. Nevertheless, several benchmark tests have been performed to verify the overall behavior of the geochemical reaction and transport modules of this numerical model (Sonnenthal et al., 1998a, pp. 40 to 45; Xu et al., 1998, pp. 10 to 14). The results of these tests will be incorporated into the software qualification of TOUGHREACT for the Yucca Mountain Project.

SUPCRT92 (Johnson et al., 1992) was used for computing solubility products of zeolites (Section 4.5.4). This software cannot be considered Q at this time.

4.3 Geochemical Data from the SHT

Mineralogical and water chemistry data collected during the SHT are summarized here to provide a basis for input data to numerical simulations (Section 4.5) and to provide a context for interpretation of simulation results (Section 4.6).

4.3.1 Mineralogical Data

Mineralogical analysis of pre-DST core samples by bulk x-ray diffraction were conducted by Roberts and Viani (1997, p. 9) and provide the basis for mineral volume fractions input in simulations. The most common minerals, in order of decreasing abundance, are K-feldspar, plagioclase, cristobalite and quartz, with minor amounts of zeolites. Calcite was found almost exclusively in fractures (Paces et al., 1998). Estimated volume fractions of these minerals in both matrix and fractures are given in Section 4.5.4.2.

Six- to ten-inch diameter overcore of boreholes 2 and 16, recovered during post-test characterization, were examined by Levy et al. (1998, pp. 8 to 15) using X-ray diffraction (XRD), scanning-electron microscopy (SEM) and energy-dispersive X-ray spectroscopy (EDX) methods. In the course of this examination, they identified stellerite, a calcium-rich zeolite, as the predominant zeolitic phase. This zeolite was found to line fractures, and was also observed dispersed in the highly porous matrix adjacent to lithophysae. In both these occurrences, stellerite was interpreted as a primary mineral (pre-test). SEM images indicated that the stellerite was "intergrown with, and/or overgrown by K-rich alkali feldspar crystals mostly ≤10 μm across, accompanied by smectite and silica" (Levy et al., 1998, p. 10). Although the stellerite paragenesis is not certain, it probably formed at a late stage of hydrothermal activity during the terminal phase of deuteric alteration of the Topopah Spring welded tuffs (TSw), and quite possibly at temperatures less than 100°C. $^{87}Sr/^{86}Sr$ ratios of strontium substituting for calcium in the stellerite would probably aid in determining whether the source of the calcium was from the tuff itself or of later pedogenic provenance. The stellerite probably shares similar genetic affinities with heulandite and mordenite, other calcium-rich zeolites observed sparingly and lining fractures within the TSw (e.g., Carlos, 1985, 1989, 1993, 1994; Levy and O'Neil, 1989; Carlos et al., 1991; Carlos et al., 1995a,b).

From the above observations, it was assumed for simulations presented later that stellerite is present in fractures (25 percent by volume), but not in the matrix. Other zeolites were assumed absent from the initial pre-test mineral assemblage but were included in simulations as possible reaction products (Section 4.5.4.2).

Levy et al. (1998, pp. 12 to 15) also identified gypsum, amorphous silica, and calcite as test alteration products (Section 4.6). These minerals were included as possible reaction products in computer simulations (Section 4.5.4.2).

4.3.2 Water Analyses

Two water samples were collected from borehole 16, one on November 25, 1996, and another on February 4, 1997. Both samples were collected from injection line 16-4 of this borehole (zone 3 in Figure 2.1-3 in Chapter 2 of this report). The water was considered to be a condensate that had drained through fractures into the borehole (Glassley and DeLoach, 1997, p. 6). Chemical analyses of the waters are documented in the Single Heater Test Status Report (CRWMS, 1997, p. 5-49). Analyses of the waters, as described in the latter report, are reproduced here in Table 4.3-1.

On the basis of geochemical simulations using v.7.2a of EQ3/6 (Wolery, 1992), Glassley and DeLoach (1997, p. 3 to 6) and Glassley (1997, p.3) concluded that the waters showed interaction with calcite and some dissolution of feldspars. The waters showed much more dilute concentrations than other waters collected at Yucca Mountain, suggesting their origin as condensates that had undergone only limited water-rock interaction. Glassley and DeLoach noted an inconsistency between the higher than expected sodium concentration in the collected samples relative to their model results and attributed this to uncertainties in the dissolution kinetics for plagioclase. Potassium concentrations, however, were well-described by dissolution of K-feldspar. The calcium concentrations were thought to reflect the interaction of calcite with water where pH is controlled externally, probably by elevated CO_2 partial pressures (P_{CO2}) near the boiling zone (Glassley, 1997, p. 3; CRWMS, 1997, p. 5-52). It was pointed out in the latter reference that the CO_2 could have been derived from carbonate minerals, boiling of water, or movement of CO_2-rich pore gases.

Strontium isotopic ratios ($^{87}Sr/^{86}Sr$) in borehole-16 waters (CRWMS, 1997, p. 5-49) were also similar to those observed in calcite at Yucca Mountain (Paces et al., 1998), indicating that very little reaction with the tuff matrix took place, which would have shifted the waters to higher ratios. Strontium concentrations in the water are also consistent with significant calcite interaction, because they are much higher than would be expected by dilution (Sonnenthal, 1997).

Oxygen and deuterium isotopic ratios plotted near the meteoric water line (CRWMS, 1997, p. 5-51) indicating that the water was likely formed by near complete boiling and subsequent condensation of water (Sonnenthal, 1997). Another possibility may be that the condensate waters were originally lighter in isotopic composition, and subsequently reequilibrated with matrix pore waters before collection.

Table 4.3-1 Analyses of water samples from the Single Heater Test. Data taken from Table 5-19 of the Single Heater Test Status Report (CRWMS,1997, pp.5-49).

	Suite 1 (November 25, 1996)				**Suite 2 (February 3, 1997)**	
	SHT Borehole 16		**SHT Borehole 16**	**USGS Analyses**	**SHT Borehole 16**	
	LLNL Data	**LBNL Data**	**LANL Data**		**LLNL Data**	**LBNL Data**
Na (mg/l)	16				13.9	
Si (mg/l)	16.8				17.4	
Ca (mg/l)	13				9.76	
K (mg/l)	2.5	2.69			2.5	
Mg (mg/l)	1.63				1.16	
pH	6.2				6.9	
HCO_3 (mg/l)	188 *					
F (mg/l)	0.44				0.12	
Cl (mg/l)	2.54		2.1		1.45	
S (mg/l)	0.71					
SO_4 (mg/l)	1.83		1.5		0.42	
PO^{3-}_4 (mg/l)	<0.03				<0.4	
Nitrate (mg/l)	<0.01				0.15	
NO_3 (mg/l)	1.1				<0.4	
Li (mg/l)	<0.03				<0.03	
B (mg/l)	0.37				0.74	
Al (mg/l)	<0.06				<0.06	
Fe (mg/l)	0.74				0.13	
Sr (mg/l)	0.2	0.1850		0.22	0.14	
Rb (mg/l)		0.0066				
Br (mg/l)	<0.2		0.008		<0.4	
del D	-101.7	-95.00		-93.1	-99.6	-94
del ^{18}O	-12.8	-11.80		-13.1	-12.9	-13.1
Tritium	0.44+0.19 TU		<0.3 TU			
$^{87}Sr/^{86}Sr$		0.71243		0.71240		
U (mg/l)				0.0001013		
$^{234}U/^{238}U$				8.03200		

* From charge balance

4.4 Conceptual Model of THC Processes affecting the SHT

The thermal, hydrological and chemical processes resulting from heating the host-rock during the SHT are briefly reviewed in this section, with a particular emphasis on water-gas-rock interaction processes that govern the behavior of the chemical system in the test area. The THC processes that may occur during thermal tests have been previously investigated by Glassley and DeLoach (1997) and Glassley (1997) for the SHT, and by Sonnenthal et al. (1998a, pp. 46 to 72; 1998b, pp. 3-1 to 3-12) for the DST. Additional studies of THC processes at repository scale for the Yucca Mountain project have been presented by Glassley (1998a, pp. 5-24 to 5-27; 1998b, pp. 5-52 to 5-56; 1998c, pp. 5-68 to 5-78), Whitbeck and Glassley (1998, pp. 5-42 to 5-52), and Nitao (1998, pp. 5-57 to 5-67). We draw from the investigations of these authors to develop a conceptual model that can be used as a basic framework for interpretive analyses presented in sections 4.5 and 4.6. The THC processes accompanying the SHT and other thermal tests are similar to those anticipated to affect the proposed repository at Yucca Mountain and, therefore, are important for the assessment of long-term repository design and performance.

The evolution of the chemical regime in the unsaturated zone surrounding the SHT is closely related to the hydrologic regime driven by the heating and cooling stages of the test. The main THC processes affecting the SHT (and, by analogy on a larger scale, the proposed repository) are schematically illustrated in Figure 4-1. Several zones are identified. The dryout zone extends immediately around the heat source, surrounded by a boiling zone, then by a condensation zone. Within the zones of boiling and condensation may lie an isothermal region where reflux is important, termed the "heat pipe" region. A drainage zone extends at some distance beneath the heat source, where water accumulates from drainage of steam condensate into fractures. In addition, recent simulations of the DST (which is essentially a longer version of the SHT) seem to indicate the formation of a CO_2 halo expanding away from the heat source as CO_2 is volatilized from pore and fracture waters in hot areas (Sonnenthal et al., 1998a, p. 64 and 1998b, pp. 3-8; Conrad, 1998).

Each zone of the conceptual model is associated with typical chemical processes, as discussed in separate sections below. It is important to realize that in a natural setting such as the environment of the SHT, rock fracture and matrix heterogeneities are likely to result in more irregular zoning patterns than those shown on Figure 4-1 or resulting from the simulations presented in Section 4.5. Therefore, at a given time in a real system, the transition from dryout to boiling, condensation, or drainage zones could occur closer to the heat source in some areas than in others.

4.4.1 The dryout zone

During the heating stage of the test, rocks are heated significantly above the water boiling point, and evaporation and boiling of pore waters takes place. Areas close to the heat source eventually dry out, precipitating all salts previously in solution. This zone is currently not of primary interest in our study of

THC processes because it is absent of aqueous geochemical processes. However, upon rewetting during cool-down, the dissolution of salts precipitated previously in this zone is likely to affect the chemical behavior of fluids imbibed in this zone.

4.4.2 The boiling zone

The boiling zone comprises the area between the dryout zone and the condensation zone, where pore water is boiling but dryout conditions are not reached. If the boiling zone becomes significant in size, it can develop into a "heat-pipe" zone, which is essentially a zone of nearly constant temperature where pore water is continuously boiled, driven away as steam, condensed and refluxed back towards the heat source. Water saturation in fractures and matrix typically decrease from the outer edge of the boiling zone (or if present, heat-pipe zone) towards the dryout zone. CO_2 volatilization generally results in a pH increase of boiling waters (Sonnenthal et al., 1998a, p. 55) from the reaction

$$HCO_3^- + H^+ \rightarrow CO_{2\,(gas)} + H_2O \qquad (4.4.1)$$

although the development of heat-pipe effects may result in pH remaining nearly constant or increasing only slightly in the heat-pipe zone (Sonnenthal et al., 1998b, p. 3-48). The pH increase, together with the higher temperature, generally results in the precipitation of calcite and dissolution of silica phases in the boiling zone. Along with extreme evaporation and boiling, saturation with respect to calcium and magnesium sulfates and hydrated silicates may also occur.

Within a dual permeability framework (fractures and matrix), the salt concentration of solutions in fractures in the boiling zone can greatly increase due to evaporative concentration, even though the liquid saturation in those fractures may not decrease significantly. This is caused by an inflow of matrix water into fractures and subsequent boiling of this water in the fractures, with constant replenishment of water from the matrix keeping the saturation from decreasing. This phenomenon was reproduced in the numerical simulations presented in Section 4.5 and can produce very high salt loads where the boiling zone meets the dryout zone (typically a very thin zone, in the order of a few centimeters in the SHT simulations).

4.4.3 Condensation zone

A condensation zone occurs beyond the volume of rock in which boiling takes place. Although the boiling point of water at Yucca Mountain is near 95°C, the condensation boundary temperature may be modified by capillary action and dissolved salts. The main chemical processes affecting the condensation zone include dilution of pore waters with condensate, pH decrease due to uptake of CO_2 from the vapor phase (reverse of Reaction 4.4.1), enhanced dissolution of calcite, and precipitation of silica phases at declining temperatures in places where the aqueous liquid drains toward cooler regions. The condensation zone would technically include the outer edge of a heat-pipe region. However, it typically

extends much farther than the latter, and may occur from the condensation of H_2O vapor resulting from evaporation alone, without boiling.

4.4.4 Drainage Zone

Our current conceptual model of the SHT includes a drainage zone mostly beneath the heat source (Figure 4-1). This zone results from steam condensation in fractures surrounding the heat source followed by gravity-driven downward flow, which causes the water saturation in fractures below the heat source to increase more than elsewhere around the heated area (see also Chapter 3 of this report). Because the water draining in fractures originates from steam condensation, its pH is typically lower than in matrix water because of CO_2 uptake from the vapor phase upon condensation. As a result, more dissolution of calcite and other pH-dependent mineral phases is expected to occur in the drainage zone than elsewhere in the test area. However, drainage below the heat source occurs towards cooler areas and is expected to induce the precipitation of silicates in this zone. Therefore, the net effect on overall porosity changes in the drainage zone may vary depending on the amounts of minerals precipitating by cooling versus those dissolved by the lower-pH draining water.

4.4.5 CO_2 Halo

Simulations of the DST presented by Sonnenthal et al. (1998a, p. 64 and 1998b, pp. 3-8) indicate the formation of a CO_2 halo expanding away from the heat source with time, as CO_2 volatilized from matrix water is transported in fractures (mainly by advection) away from the hot areas. Data collected from the DST indicate that this halo is present (Conrad, 1998). In a natural setting, it is likely that CO_2 and steam flow along preferential fracture pathways result in localized areas of increased CO_2 partial pressures without necessarily creating a complete halo around the heat source. The zones of increased CO_2 partial pressures typically correspond to zones of decreased pH, and therefore increased calcite dissolution.

4.4.6 Zoning During Cooling Phase

During the cooling phase of the test, the boiling and condensation zones retreat towards the location of the initial heat source. As the boiling front retreats, a coating of mineral precipitates may be deposited along fractures and perhaps to some degree into the rock matrix. Above the location of the initial heat source, the downward- retreating front may induce redissolution of previously precipitated salts, and concentration of the salt load at the migrating front.

During cool-down, the water composition is dominated by condensate and its actual composition depends on the extent of rock-water interaction. Waters of this more evolved nature are most likely to interact with repository materials.

4.5 Quantitative Analysis of THC Processes

Numerical simulations of coupled THC processes affecting the SHT are presented in this section. These simulations follow the development of the conceptual and numerical models for THC processes presented for the DST by Sonnenthal et al. (1998a, pp. 57 to 63 and 1998b, pp. 3-5 to 3-11). In addition, limited water sampling and post-test mineralogical studies have provided data (Section 4.3) for which comparisons to the simulations can be made to assess the reliability of the model and its input data.

The basis of the thermo-hydrologic model used here is the two-dimensional dual-permeability mesh and thermohydrological parameters described in Birkholzer and Tsang (1996, pp. 8 to 12, 15 to 20, and p. 28) and further discussed in Chapter 3 of this report. A conceptual model for treating the rate-limited reactions of minerals, gas, and water coupled to the thermohydrologic calculations is presented in Sonnenthal et al. (1998a, p. 37-40). Details on numerical methods can be found in Pruess and Xu (1998) and references therein.

4.5.1 Numerical Model and Processes Considered

The numerical model used for this study is TOUGHREACT (Pruess and Xu, 1998; Xu et al., 1997 and 1998). The original computer program was modified and enhanced as part of this effort to study THC processes in the SHT. TOUGHREACT considers heterogeneous chemical systems including an arbitrary number of primary chemical species and minerals. The precipitation and dissolution of minerals is computed under equilibrium and/or kinetic (i.e., non-equilibrium) constraints. Also considered is the transport of an arbitrary number of gases (such as CO_2) in an air/vapor phase at equilibrium with the aqueous solution. Within the dual-permeability framework considered here (fractures and matrix), gases in each medium are in equilibrium with the fluid in that medium.

An important aspect of TOUGHREACT is that its core structure is the TOUGH2 code (Chapter 3 of this report), enabling it to treat various geochemical processes in the framework of dual permeability/porosity, multiple-interacting continua (MINC), and equivalent continuum formalisms for fractured porous media, along with the transport of water, air, and heat. The full equations for heat, water, and gas flow are solved simultaneously, followed by the transport (advection-diffusion) of primary aqueous and gaseous chemical species in a sequential fashion, and then by the solution of the chemical system at each gridblock. Thus, the full multiphase thermohydrologic system is solved as in the modeling presented in Chapter 3 of this report, along with solving the rate-limited precipitation and dissolution of solid phases and the speciation of aqueous and gaseous species.

The geochemical and transport calculation methods incorporated in TOUGHREACT have been enhanced as part of this study to deal with boiling conditions and rock matrix-fracture interactions such as those arising from the Yucca Mountain thermal tests. Coupled processes included in the simulations include:

- Reactive advection-diffusion of CO_2 in the vapor phase

- Reactive advection-diffusion of aqueous species (up to 10 primary components and over 30 derived aqueous species for the present case)

- The precipitation and dissolution of minerals under kinetic and/or equilibrium constraints (up to 18 minerals for the present case)

- Coupled flow, transport, and chemical reaction within a dual permeability framework (matrix/fractures) where differing mineralogies in matrix and fractures (and in respective subdomains as necessary) are specified

- Full interaction between chemical processes in matrix and fractures (e.g., CO_2 volatilization from the matrix water and condensation/dissolution into fracture water; differing mineral precipitation and dissolution patterns in fractures and matrix, depending on the hydrochemical interactions between these two media)

- All thermal and hydrological processes discussed in Chapter 3 of this report, with the minor difference that no vapor pressure lowering due to capillary pressure was considered for the simulations presented here (i.e., the TOUGH2 module EOS3 was used while simulations in Chapter 3 of this report were carried out with module EOS4).

The effect of porosity change (from mineral precipitation/dissolution) on matrix and fracture permeability is not currently considered in the model. For the simulations presented here (which cover a short time frame), the amount of mineral precipitation and dissolution is very small compared to the matrix and fracture porosities, so that the mineral precipitation or dissolution effects on permeability can be assumed negligible.

Before reaching complete dryout conditions, chemical interactions stop being computed when the liquid saturation drops below 10^{-4} and/or the ionic strength of the solution exceeds 2. This is because chemical reactions cannot be computed without an aqueous phase present, and calculation methods are not suitable for elevated ionic strengths.

4.5.2 Grid and Boundary Conditions

The numerical results presented in this report are based on the two-dimensional dual-permeability grid, thermohydrologic parameters, and boundary conditions for the SHT developed by Birkholzer and Tsang (1996, pp. 15 to 20, 28) and as improved and further discussed in Chapter 3. The computational mesh is shown in Figure 4-2.

4.5.3 Thermal, Hydrological, and Transport Input Parameters

Details on the heating schedule, thermohydrologic parameters and grid generation can be found in Chapter 3.0 and in Birkholzer and Tsang (1996). Briefly, the base case model considers heating at approximately 94 percent full power for the first nine months of the test (3.758 KW), followed by eight months of cooling without heat input. Maximum temperatures in the dryout zone reached over 300°C during the test. The cooling phase of SHT ended approximately seven months after the heat source was turned off. The model was run for an eighth month of cooling to provide final results that coincide approximately with the time when boreholes 2 and 16 were overcored.

Although the rock properties and lithologic units vary over the area of influence of the SHT, they are assumed to be uniform for the simulations, and equivalent to the properties of the Tptpmn lithologic unit of the Topopah Spring tuff (Birkholzer and Tsang, 1996, pp. 8 to12). For the simulations presented in this report it is assumed that there is no percolation flux at the top of the model boundary for the entire period of the SHT. This assumption is considered appropriate because the percolation flux is very small (in the range of a few millimeters per year) compared to the duration of the test simulations (seventeen months). The bottom boundary and all drifts are considered to have a constant pressure and temperature, and therefore they are also assumed to have a constant chemical composition.

The diffusion coefficient of aqueous species was estimated to be 10^{-9} m^2/sec from data in CRC (1981, p. F-53). The coupled flow-transport-reaction calculation methods assume that the diffusion coefficient is the same for all aqueous species (e.g. Steefel and Lasaga, 1994, p. 537). The diffusion coefficient of CO_2 in the vapor phase was estimated to be 2×10^{-5} m^2/sec from data at 0°C in CRC (1981, p. F-53) extrapolated to an average temperature of 50°C using methods in Lyman et al. (1990, Equations 17-11 and 17-16, and references therein). The tortuosity was assumed to be 0.2 in fractures and matrix. This parameter cannot be exactly determined, and a value of 0.2 is within a typical range of values (e.g. Bear, 1972).

4.5.4 Chemical Input Parameters

Model input parameters for chemical processes considered in the coupled THC simulations include starting water and gas compositions, initial fracture and matrix mineralogies, other secondary mineral phases that may form as the result of THC processes, and thermodynamic and kinetic data for all considered reactive minerals, gases, and aqueous species. Except for mineral reactive surface areas and new thermodynamic data as discussed in the following subsections, these chemical input parameters were the same as those employed in THC simulations presented in Sonnenthal et al. (1998a, p. 58 to 63) for the DST. These data are summarized below. The modeled chemical system is assumed to be initially homogeneous with respect to mineral proportions, pore water chemistry, and all other geochemical parameters.

The Thermomechanical Alcove Extension and the Observation Drift were treated as zones without mineral reactions, but with a constant CO_2 partial pressure fixed at the value shown in Table 4.5.1 (approximately 1430 ppmV). This value is somewhat elevated compared to ambient concentrations (around 450 ppmV) measured by Conrad (1988) in the observation drift of the DST. This may result in predicted CO_2 partial pressures that are somewhat overestimated near the alcoves. However, in the proximity of the heater, the effect of the alcove boundary on calculated P_{CO2} is not believed to be significant.

4.5.4.1 Initial Water and Gas Compositions

The starting matrix and fracture water compositions were assumed to be identical. The starting water composition (Table 4.5.1) was averaged from analyses of samples collected in boreholes UZ-16, SD-9, and SD-12 derived from Yang et al. (1996a, pp. 14 to 15 and 1996b, p. 12). Detailed discussions of these pore water compositions can be found in these references and in Apps (1997); a discussion of the averaging technique and rationale for it can be found in Sonnenthal et al. (1998a, pp. 62 to 63).

For consistency with the starting water composition, the initial CO_2 concentration in fractures and matrix pores was calculated to reflect the partial pressure at equilibrium with the pore water (Table 4.5.1) at 25 °C and atmospheric pressure of 1 bar, corresponding to a concentration of approximately 1430 ppmV.

Table 4.5.1. Initial matrix and fracture water composition for TOUGHREACT simulations (Sonnenthal et al., 1998a, p. 63). A subset of these concentrations was used for some of the simulations, as described in the text.

	Average (mg/L)
Ca	27
Mg	5
Na	91
HCO_3^-	191 (219*)
Cl^-	41
NO_3^-	13
SO_4^{2-}	40
SiO_2	60
Al	1×10^{-6}**
K	4**
pH	8.2
P_{CO2} (bars)	1.43×10^{-3} (calculated at 25 °C)

* Adjusted for charge balance

** Estimated

4.5.4.2 Mineralogy

Initial matrix and fracture mineralogies are shown in Table 4.5.2. The primary distinction between fractures and matrix is the presence of stellerite (a zeolite observed to amount up to 25 percent volume in fractures) and small amounts of calcite and illite in fractures, and absence of these minerals in the matrix.

The volume fractions of minerals in matrix were estimated from bulk mineral abundances reported by Roberts and Viani (1997, p. 9) and Levy et al. (1998, p. 22) and an assumed effective mineral reactive volume fraction of 0.85. The abundances of mineral end members albite and anorthite were recalculated based on the An content of albite given by Johnson et al. (1998, Table 6).

To our knowledge, systematic analyses of fracture mineralogies in the Topopah Spring welded tuff have not been reported. For this reason, the volume fractions of minerals in fractures were assumed the same as those in the matrix, but normalized to include 2 %(vol.) calcite based on a range of observations by Paces et al. (1998), and an estimated 5 %(vol.) volume illite (arbitrary) to account for clay minerals. The

volume fractions were then renormalized to include an additional 25 %(vol.) stellerite estimated from a range of values reported by Levy et al. (1998, p. 22).

Table 4.5.2 Initial mineral volume fractions assumed in TOUGHREACT simulations. Minerals with zero volume fractions are included in the simulations as possible reaction products not initially present at the start of simulations.

Minerals	**Vf (matrix)**	**Vf (fractures)**
Quartz	0.0967	0.0746
Cristobalite-α	0.2179	0.1681
Am. SiO_2	0.0	0.0
Calcite	0.0	0.015
Microcline	0.2860	0.2201
Albite-low	0.2374	0.1831
Anorthite	0.0079	0.0065
Kaolinite	0.0	0.0
Illite	0.0	0.0038
Sepiolite	0.0	0.0
Smectite-Na	0.0	0.0
Smectite-K	0.0	0.0
Smectite-Ca	0.0	0.0
Smectite-Mg	0.0	0.0
Stellerite	0.0	0.25
Heulandite	0.0	0.0
Mordenite	0.0	0.0
Gypsum	0.0	0.0

4.5.4.4 Thermodynamic Data

Solubility products of albite, k-feldspar (microcline), illite, smectites, kaolinite, sepiolite, calcite, quartz and cristobalite were identical to those recomputed in Sonnenthal et al. (1988a, p. 28 and references therein). Solubility products of zeolites were computed as part of the present study as described below. Data for other minerals and aqueous phases were taken from the EQ3/6 database (Wolery, 1992), which consists mostly of data from SUPCRT92 (Johnson et al., 1992) and from Pokrovskii and Helgeson (1995).

In modeling the THC evolution of the SHT, it is desirable to incorporate any phases that might participate either as reactants or products (precipitates) during the course of the test. As mentioned in Section 4.3.1, the zeolite minerals heulandite, mordenite and stellerite were identified in core samples from the SHT area. The inclusion of these minerals in the thermodynamic database of the TOUGHREACT code is therefore appropriate, as any one could participate in modifying the chemical

evolution of the system. Fortunately, the $\Delta G^{o}_{f,298}$, $\Delta G^{o}_{f,298}$, $S^{o}_{f,298}$ and V^{o} of these zeolites have been calculated (Chipera and Apps, 1998), affording a basis for calculating their solubility products as a function of temperature. The calculations were conducted as follows:

1. The Maier and Kelley (1932) heat capacity function for each zeolite was calculated according to the procedures recommended by Helgeson et al. (1978)

2. $\Delta G^{o}_{f,298}$, $\Delta G^{o}_{f,298}$, $S^{o}_{f,298}$, V^{o} and the Maier-Kelley heat capacity function terms for each zeolite was entered in the SPRONS96.DAT database of SUPCRT92 (Johnson et al., 1992)

3. The dissolution reaction product constants with respect to each zeolite were calculated with respect to the aqueous species and quartz as a reaction product calculated along the saturation curve for water at 0, 25, 60, 100 and 150°C.

4. The final solubility products at the above-indicated temperatures were calculated by addition of the quartz solubility products calculated from the equation by Rimstidt (1997). In this way, the application of erroneous data for $SiO_2(aq)$, presently in the SPRONS96.DAT database could be conveniently circumvented.

A summary of the thermodynamic properties of heulandite, mordenite and stellerite used to calculate their solubility products is given in Table 4.5.3.

Table 4.5.3. Summary of Thermodynamic Properties of Calcium-Rich Zeolites

Mineral Name	Chemical Formula ⑩	$\Delta G^{o}_{f,298}$ ¶ (kcal.mol^{-1})	$\Delta H^{o}_{f,298}$ ¶ (kcal.mol^{-1})	S^{o}_{298} ¶ (kcal.mol^{-1}.K^{-1})	V^{o} ¶ (cm^3.mol^{-1})	Maier-Kelley C^{o}_{p} Coefficients. ①④		
						a (cal.mol^{-1})	B x 10^3 (cal.mol^{-1}.K^{-2})	c x 10^{-5} (cal.mol^{-1}.K)
Heulandite	$(K_{0.4}Na_{1.0}Ca_{3.3})Al_{8.0}Si_{28.0}O_{72}\bullet 26H_2O$	-9440.15	-10251.20	743.28	1266.4	784.86	281.59	103.83
Mordenite	$(K_{0.9}Na_{2.1}Ca_{1.5})Al_{6.0}Si_{30.0}O_{72}\bullet 22H_2O$	-9055.23	-9814.05	708.05	1273.5	697.62	289.84	102.86
Stellerite	$(Ca_{3.9}Na_{0.1})Al_{7.9}Si_{28.1}O_{72}\bullet 28H_2O$	-9550.69	-10389.20	770.63	1331.0	766.78	278.58	103.28

⑩ From Broxton et al. (1986) for heulandite and mordenite. From Carlos et al. (1995a) for stellerite.
¶ From Chipera and Apps (1998).
① $C^{o}_{Pr} = a + bT - cT^{-2}$ (Maier and Kelley, 1932).
④ Coefficients from oxide compounds and zeolitic water according to the method prescribed by Helgeson et al. (1978).

A tabulation of the calculated solubility product constants for the three zeolites is given in Table 4.5.4 for the following reactions:

Heulandite: $(K_{0.4}Na_{1.0}Ca_{3.3})Al_8Si_{28}O_{72} \cdot 26H_2O + 32H^+ =$

$$0.4K^+ + Na^+ + 3.3Ca^{2+} + 8Al^{3+} + 28SiO_2(aq) + 42H_2O \qquad (4.5.1)$$

Mordenite: $(K_{0.9}Na_{2.1}Ca_{1.5})Al_6Si_{30}O_{72} \cdot 22H_2O + 24H^+ =$

$$0.9K^+ + 2.1Na^+ + 1.5Ca^{2+} + 6Al^{3+} + 30SiO_2(aq) + 34H_2O \qquad (4.5.2)$$

Stellerite: $(Ca_{3.9}Na_{0.1})Al_{7.9}Si_{28.1}O_{72} \cdot 28H_2O + 31.6H^+ =$

$$3.9Ca^{2+} + 0.1Na^+ + 7.9Al^{3+} + 28.1SiO_2(aq) + 43.8H_2O \qquad (4.5.3)$$

4.5.4. Solubility Products, K_s, of Calcium-Rich Zeolites

Mineral Name	**$\log K_s(T_{°C})$**				
	0	25	60	100	150
Heulandite	-2.359	-10.134	-18.927	-26.742	-34.237
Mordenite	-35.232	-37.805	-40.592	-42.886	-44.881
Stellerite	-5.397	13.261	-22.147	-30.036	-37.598

To illustrate the procedure adopted with respect to steps 3 and 4 above, stellerite is used as an example. The equation to describe the solubility of stellerite with respect to quartz and aqueous species is:

$$(Ca_{3.9}Na_{0.1})Al_{7.9}Si_{28.1}O_{72} \cdot 28H_2O + 31.6H^+ =$$

$$3.9Ca^{2+} + 0.1Na^+ + 7.9Al^{3+} + 28.1SiO_2\,(s) + 43.8H_2O \qquad (4.5.4)$$
$$\text{(quartz)}$$

The dissolution reaction constants for this reaction were calculated as described above. To these constants, corresponding solubility product constants for the reaction:

$$28.1SiO_2(s) = 28.1SiO_2(aq) \qquad (4.5.5)$$
$$\text{(quartz)}$$

were added to yield solubility product constants for the stellerite dissolution (reaction 4.5.3). Similar procedures were adopted for heulandite and mordenite.

4.5.4.5 Kinetic Data

Kinetic data and references are shown in Table 4.5.5. For each mineral, surface areas used in calculating reaction rates were multiplied by the volume fraction of the mineral in the starting fracture and matrix mineral assemblages. Minerals absent from the starting assemblages had their surface areas divided by 100. This is a departure from the simulations presented in Sonnenthal et al. (1998a, pp. 63 to 70 and 1998b, pp. 3-7 to 3-12) in which larger surface areas (Table 4.5.5) were used, and which seemed to result in overestimated mineral reaction rates.

Table 4.5.5 Dissolution and precipitation rate law parameters and reactive surface areas for minerals. Data from Whitbeck and Glassley (1998, p. 5-42) and from Table 3 of Johnson et al. (1998), and references therein as shown below. Dissolution and precipitation rate laws are discussed in footnote.

Minerals	**k_0 (mol/m^2 s)**	**E_a (kJ/mol)**	**S (m^2/kg H_2O)**	**Original Reference**
Quartz	1.2589e-14	87.5	71.07	Tester et al. (1994), Johnson et al. (1998)
Cristobalite-α	3.1623e-13	69.08	71.07	Rimstidt and Barnes (1980), Johnson et al. (1998)
Am. SiO_2	7.944e-13	62.8	142.14	Rimstidt and Barnes (1980), S estimated
Calcite	1.0e-11	41.87	71.07	Glassley (1998c), S estimated
Gypsum	equilibrium	equil.	equil.	
Microcline	1.0e-12	57.78	142.4	Whitbeck and Glassley (1998), S estimated from Johnson et al. (1998)
Albite-low	1.0e-12	67.83	104.2	Whitbeck and Glassley (1998)
Anorthite	1.0e-12	67.83	124.6	modified after Whitbeck and Glassley (1998)
Kaolinite	1.0e-13	62.80	142.4	Whitbeck and Glassley (1998), S estimated
Illite	1.0e-14	58.62	142.4	assumed equal to muscovite as given in Johnson et al. (1998), S estimated
Sepiolite	1.0e-14	58.62	142.4	assumed equal to illite
Smectite-Na	1.0e-14	58.62	142.4	assumed equal to illite
Smectite-K	1.0e-14	58.62	142.4	assumed equal to illite
Smectite-Ca	1.0e-14	58.62	142.4	assumed equal to illite
Smectite-Mg	1.0e-14	58.62	142.4	assumed equal to illite
Heulandite	1.99e-12	62.802	124.6	Ragnarsdottir (1993) from Whitbeck and Glassley (1998), S assumed to be the same as anorthite
Stellerite	1.99e-12	62.802	124.6	assumed equal to heulandite
Mordenite	1.99e-12	62.802	124.6	assumed equal to heulandite

For amorphous silica, precipitation rate law from Rimstidt and Barnes (1980): $\log k = -7.07 - 2598/T_K$, and reactive surface area set twice that of the other silica phases. Dissolution and precipitation rate law for other minerals: $k = k_0 \exp[-E_a/R(1/T_K - 1/298.15)]$. All other kinetic minerals were given the same rate law for precipitation as dissolution, except quartz and cristobalite, for which precipitation was suppressed.

4.5.5 Numerical Simulations

Two simulations are presented that are likely to bound the range of geochemical behavior expected for the SHT. The primary difference between them is that the first simulation (KIN05) does not consider aluminosilicate minerals, while the second one (KIN04) considers several of these minerals, including feldspars, various clay minerals, and zeolites. These minerals can have a substantial effect on pH and water chemistry, and because their thermodynamic and kinetic properties are subject to much uncertainty due to their inherent great compositional and structural variability, morphology, and solid solution behavior, their importance in the evolution of condensate water chemistry will require further refinement through modeling and data collection from the ongoing DST.

The simulations were carried out over a simulated time period of 521 days (nine months of heating followed by eight months of cooling). Each simulation is discussed separately below.

4.5.5.1 Calcite-Silica-Gypsum System

This simulation considered the following chemical system:

- Aqueous components: H^+, H_2O, Na^+, Cl^-, HCO_3^-, Ca^{++}, $SiO_{2(aq)}$ and SO_4^{--} and their derived species
- Minerals: calcite, gypsum, amorphous silica, quartz, and alpha-cristobalite
- Gases (in H_2O vapor): CO_2

Simulation results are shown for fractures as vertical 2-D cross sections on Figures 4-3 through 4-12. These results are discussed below and further compared with measured data in Section 4.6.

For this simulation, results for the matrix are not presented because fluids flow essentially in fractures where the most relevant and interesting hydrochemical processes take place. However, the inclusion of matrix-fracture interactions in the simulations is very important because the matrix acts as a source of vapor, CO_2, and other components in fractures. Computed aqueous phase compositions and mineral precipitation/dissolution trends in the matrix and fractures are presented for the second simulation (Section 4.5.5.2).

Distributions of temperature and liquid saturation in fractures are shown at 91 days after the initiation of heating (Figure 4-3), coinciding with the date of the first water sample collection from borehole 16. The projected location of this borehole traverses a range of elevated liquid saturations, which is consistent with observations of water drainage into the borehole. The computed CO_2 partial pressure (P_{CO2}) is also elevated through much of the length of the borehole (Figure 4-4), owing to strong degassing of CO_2 in the rock closer to the heater. The strong degassing of CO_2 and subsequent redissolution into condensate waters farther from the borehole leads to a large drainage region of lower pH waters below the heater,

and a small region above it (Figure 4-5). Along borehole 16, the computed pH varies from the ambient value of about 8.2 at the alcove to about 7 at the end of the borehole (closest to the heater). Condensate waters around and below the heater have pHs mostly below 7, down to a minimum of 6.55. Calcite dissolution in fractures (Figure 4-6) is most pronounced in this same region of low pH, with a larger amount of precipitation in the boiling and dryout regions, as a consequence of its decreased solubility at higher temperatures and higher pH in these regions.

At the time of the second water sample collection, 161 days after initiation of heating, the computed distributions of temperature and fracture liquid saturations are similar but expanded outward from the previous snapshot in time (Figure 4-7). The region of decreased P_{CO2} at the boiling front has moved outward to the end of borehole 16 (Figure 4-8), although most of the borehole still traverses the outer region of higher P_{CO2}. The drainage region below and partially around the heater exhibits the lowest pH values (to a minimum of about 6.6), as at 91 days, and this region has progressed well into the part of borehole 16 closest to the heater (Figure 4-9). The computed extent of calcite dissolution (Figure 4-10) increased significantly since the time of 91 days (when the first water sample was collected), with the last 2 meters of borehole 16 in the main region of dissolution.

At 521 days, eight months after the heat source was turned off (coinciding with the time when overcoring took place) the mineral distributions are basically stabilized, because temperatures have decreased substantially, thus retarding reaction rates. Changes in computed calcite amounts at 521 days (Figure 4-11) indicate the strongest dissolution occurs in a symmetric pattern around the heater with comparatively lesser but more extended dissolution in the drainage region below the heater. About the same magnitude of precipitation is concentrated about 1.5 meters above the heater, just touching the end of borehole 16. Cristobalite dissolution is also predominant in a narrow region around the heater (Figure 4-12). In the drainage region, it shows a much more restricted extent of dissolution than calcite. The difference in the pattern of calcite and cristobalite dissolution in the drainage region is due to the increased solubility of calcite at lower-temperatures and lower pH. Water draining from the heater has a lower pH, and also equilibrates thermally with the lower temperature rock as it flows downward. Cristobalite solubility and reaction rates decrease with decreasing temperature and are little affected by pH (in near neutral waters), and therefore the drainage waters dissolve very little cristobalite once they leave the high temperature region.

Gypsum and amorphous silica were predicted to precipitate at a few grid nodes directly adjacent to the dryout zone, at near-zero liquid saturations. Contour plots of these restricted occurrences are not presented. Gypsum forms in our model by evaporative concentration of calcium and sulfate upon boiling at an elevated temperature. As discussed later (Section 4.6), the observed deposition of gypsum in the vicinity of the SHT is more widespread than predicted by the model, and probably resulted from evaporation at low temperature.

4.5.5.2 Calcite-Silica-Gypsum-Aluminosilicates System

This simulation considered the following chemical system:

- Aqueous components: H^+, H_2O, Na^+, Cl^-, HCO_3^-, Ca^{++}, $SiO_{2(aq)}$, SO_4^{--}, K^+, Mg^{++} and AlO_2^- as well as their derived species

- Minerals: calcite, gypsum, amorphous silica, quartz, alpha-cristobalite, low albite, K-feldspar (microcline), illite, kaolinite, smectites (Ca, Na, Mg, and K phases), and zeolites (stellerite, heulandite, and mordenite)

- Gases (in H_2O vapor): CO_2

Simulation results are shown as vertical 2-D cross sections (Figures 4-13 through 4-27), a vertical profile through the heater at a time of 161 days (Figures 4-28 through 4.30), and time profiles for a point in the vicinity of borehole 16, zone 16-4 (Figures 4-31 though 4-35). These results are discussed below and further compared with measured data in Section 4.6.

In this simulation the thermohydrological conditions are identical to those shown previously. In the considered geochemical system, chloride is a nonreactive (conservative) species and it is therefore a useful indicator of the extent of dilution by condensate waters, the extent of evaporation, and the equilibration of matrix and fracture pore waters. Figure 4-13 shows the computed distribution of chloride concentrations at 91 days, showing the very strong dilution around the heater borehole and in the condensate waters draining below the heater. Concentrations of chloride in fracture pore waters are initially about 40 mg/liter (Table 4.5.1) and are computed to decrease to much less than 1 mg/liter in the most dilute waters (Figure 4-13). In areas where the liquid saturations reach the minimum allowable value for chemical calculations (10^{-4}), computed chloride concentrations are as high as 16,000 mg/liter. These areas are, of course, very limited in extent.

The computed increase in P_{CO2} away from the heat source in fractures is much less than in the previous simulation, owing to increased consumption of aqueous carbonate species and hydrogen ion by mineral reactions such as feldspar dissolution and increased calcite precipitation from anorthite breakdown (Figure 4-14). A region of decreased P_{CO2} around the heater is due to degassing. In the dryout zone, there is a large increase in P_{CO2}. However, the large P_{CO2} is calculated as the value reflecting equilibrium with the last residual water phase, and may be subject to greater numerical errors than in areas of less extreme hydrochemical changes. As discussed later, the P_{CO2} increase just before dryout may reflect an influx of CO_2 from the matrix into fractures that is greater than the rate of CO_2 consumption and advection in fractures.

The CO_2 dissolution in condensates leads to lower pH waters that drain below the heater (Figure 4-15). The lowest pH values attained are about 7.1 compared to 6.55 in the previous model that did not consider aluminosilicate minerals. The pH is also lower than initial values in a thin condensation zone above the heater (Figure 4-15). However, further above the heater, the pH becomes slightly higher than initial values due to evaporative loss of CO_2.

After 161 days the region of highly dilute condensate waters has increased (Figure 4-16) and encompassed the last 1 to 1.5 meters of borehole 16. A large region of dilute waters has also drained several meters into the fractures underlying the heater. Areas of increased P_{CO2} are evident several meters above and below the heater, with the regions near the alcoves remaining near starting P_{CO2} due to buffering with the gas phase in the alcoves (Figure 4-17). Lower pH water has drained to the base of the model domain (about 12 meters below the heater), and the area of slightly increased pH above the heater has enlarged (Figure 4-18).

Distributions of some of the more abundant mineral phases are shown in Figures 4-19 to 4-27 for the final simulation time of 521 days. Absolute volume percentage change in cristobalite (Figure 4-19) is similar to that seen in the first simulation, although the region of dissolution extends further from the heater in the case with aluminosilicate minerals. It is likely that the precipitation of other silica-bearing minerals (notably zeolites) tends to lower silica concentrations further from the heater and therefore result in an increased dissolution rate for cristobalite. Calcite dissolution is also slightly greater (Figure 4-20) than in the first simulation. This was unexpected because the pH is higher in the condensation and drainage zones in this second simulation. However, it can be explained by the depletion of calcium in solution to form calcium zeolites.

Dissolution of feldspar minerals (microcline and albite) occurs dominantly within the narrow reflux zone near the heater (Figures 4-21 and 4-22) with some increased dissolution in the drainage zone below the heater. Precipitation of albite and microcline is predicted in the dryout region, however, slow nucleation and growth kinetics may limit the actual precipitation in the SHT. Clay mineral precipitation is directly related to the dissolution of feldspars, as seen in the plot of kaolinite (Figure 4-23), with the most precipitation in the combined condensation-drainage zones below the heater due to generally lower pH within this region. Ca-smectite (4.24) shows a larger region of precipitation (yet volumetrically much less) owing to the pH and temperature dependences of reactions involving calcium (the major calcium bearing minerals are calcite, anorthite, and stellerite).

Stellerite, which is an abundant calcium zeolite mineral coating fractures in the SHT (Levy et al., 1998) shows precipitation over a large region away from the heater (Figure 4-25), unlike other minerals. This could be caused by CO_2 transport, as zones of increased P_{CO2} away from the heater display a decreased pH, thus an increased solubility of calcite and a resulting increase in available calcium in solution to form stellerite. This mineral is predicted to undergo dissolution very close to the heater in the highest temperature regions. Another zeolite that may be more abundant in other areas of Yucca Mountain is

heulandite. The total volumes of heulandite precipitated in the model simulations are very small, yet the distribution is quite unique (Figure 4-26). As one moves away from the heater, it varies from nearly zero precipitation, to a greater amount of crystallization, and then a zone of nearly zero crystallization, followed again by another large zone of greater precipitation. Such patterns of mineral precipitation, both in time and space, are characteristic of complex chemical systems that cannot be predicted by thermal stability alone.

Other minerals that are found at the edge and in the dryout zone are gypsum and amorphous silica. These phases are too localized in abundance to be shown in a contour plot, but they are seen to form where increased concentrations of sulfate and silica, respectively, eventually lead to precipitation as liquid saturations decrease during the motion outward of the boiling isotherm.

In addition to understanding the coupled chemical system accompanying the SHT, one of the important aspects of long-term repository behavior is the change in porosity and permeability over time. Although the SHT was very short in duration, it can yield some information on the effective rates of reaction under thermohydrologic conditions and the possible distribution of porosity changes around a heated drift over a short period of time. The total porosity change (sum of all the mineral changes) for the fracture medium is shown in Figure 4-27. As would be expected from the distribution of the minerals shown in the previous figures, the greatest porosity increase takes place in the condensation-reflux zone in a narrow band about 2 meters away from the heater. Porosity decreases near the heater in the dryout zone, and most significantly in a broad region below the heater, where a combination of increased drainage through this region and moderate temperatures lead to greater precipitation of phases such as clays and zeolites, relative to the dissolution of feldspars, silica phases, and calcite.

To further examine the geochemical system around the heater, computed profiles of temperature, liquid saturation, aqueous species concentrations and mineral abundances in fractures are shown on Figures 4-28 through 4-30 for a simulated time of 161 days. This time corresponds to the time after which the second set of water samples was collected in borehole 16. The location of the vertical profile is shown on Figure 4-3. Graphs are presented with the distance from the heater plotted as the X axis. Therefore, the X axis of these plots needs to be aligned with the profile in Figure 4-3 for true spatial representation (i.e., approximately 90-degree rotation).

Most of the previously discussed observations are relayed in the profiles. At the time considered (161 days), the dryout zone extends to approximately one meter away from the heater. Around the dryout zone, a narrow heat-pipe zone of approximately half a meter width has developed (Figure 4-28a). Accordingly, the liquid saturation drops quickly to zero within this narrow area (Figure 4-28b). Chemical reactions are computed only for zones above a liquid saturation of 10^{-4} (and/or ionic strength below 2), and for this reason no aqueous chemistry and mineral data are shown in the profiles in the zone where the liquid saturations are below this limit.

As mentioned earlier, the chloride concentration profile (Figure 4-29) is a useful indicator of dilution in the condensation zone, and evaporative concentration in the narrow boiling (heat pipe) zone closer to the heater. The concentrations of other species follow profiles that differ more or less from the chloride trend depending on the degree of water-rock interaction affecting these species. Calcium becomes strongly depleted in solution near the heater. This is not reflected in concentrations measured in water from borehole 16 (Section 4.6). This could be due to a too-low calcite dissolution rate and/or too high precipitation rates of calcium zeolites. By comparing calcium concentrations computed with and without aluminosilicate minerals (see also Section 4.6) and concentrations from simulations assuming calcite at equilibrium (not presented here), it appears that, in the case of these simulations, the calcium depletion is primarily due to overestimating the precipitation rates of zeolites. This could have resulted from overestimating the reactive surface areas of these minerals.

The pH is lower below the heater (negative X values on Figure 4-29b) than above it, due to increased drainage of less alkaline condensed water in this zone. The pH trend reflects some increase towards the heater due to evaporative loss of CO_2 with temperature (Reaction 4.4.1), followed by a sharp decrease at the front of the condensation zone (where dilution is maximum), then a steep increase in the boiling zone from intense CO_2 volatilization. Away from the boiling zone, the P_{CO2} displays a trend which is inverse that of pH, as would be expected from Reaction 4.4.1. Closer to the heater, the trends of pH and P_{CO2} become similar. The sharp P_{CO2} increase upon near dryout is likely to be caused by a strong influx of CO_2 from the matrix that cannot dissipate (through advection and/or diffusion) or be consumed by mineral reactions in fractures faster than the rate of boiling. However, the magnitude of the calculated P_{CO2} at this location may be unrealistic because assumptions for computing the system chemistry very near the dryout zone may no longer hold.

Computed mineral abundances along the profile show the dissolution of feldspars and precipitation of kaolinite and stellerite (Figure 4-30a) in a zone extending from approximately one to four meters away from the heater. An example of feldspar dissolution reaction can be written as:

$$2NaAlSi_3O_8 + H_2O + 2H^+ \rightarrow Al_2Si_2O_5(OH)_4 + 4SiO_2(aq) + 2Na^+ \qquad (4.4.2)$$
(albite) (kaolinite)

Reaction 4.2 is favored by lower pH and dilution, which is consistent with the greater amount of kaolinite computed below the heater (where the pH is lower and dilution greater) than above it. Stellerite may also form from feldspar dissolution according to the following reaction, which is not pH dependent:

$$2NaAlSi_3O_8 + SiO_2(aq) + Ca^{++} + 7H_2O \rightarrow CaAl_2Si_7O_{18} \cdot 7H_2O + 2Na^+ \qquad (4.4.3)$$
(albite) (stellerite)

However, lower pH and dilution favor its dissolution to form kaolinite below the heater:

$$\underset{\text{(stellerite)}}{CaAl_2Si_7O_{18} \cdot 7H_2O} + 2H^+ \rightarrow \underset{\text{(kaolinite)}}{Al_2Si_2O_5(OH)_4} + 5SiO_2(aq) + Ca^{++} + 6H_2O \qquad (4.4.4)$$

Calcite and cristobalite dissolve to a lesser extent than feldspars close to the heater (Figure 4.30a). As mentioned earlier, stellerite precipitation rates may have been overestimated because calculated calcium concentrations are much lower than those observed in water samples from borehole 16 (Section 4.6). Other minerals dissolve (quartz) or precipitate (clays, zeolites other than stellerite) in very small quantities (Figure 4-30b). Reactions such as 4.4.2 or 4.4.4 appear to be primarily driven by reaction rates and dilution (as opposed to pH) and result in the solution pH being generally higher (by consuming hydrogen ion) than in the previous simulation, which did not consider aluminum silicates.

To illustrate the simulated chemical processes through time, profiles similar to those discussed above were plotted as a function of time, for a point location shown on Figure 4-3. This location was chosen in the vicinity of borehole 16, zone 16-4. Dryout conditions were never reached at this point during the length of the simulated test. Results are presented in Figures 4-31 through 4-35 for fractures and matrix and show that fracture and matrix waters exhibit significantly different aqueous chemistries.

The observations and reactions described above for the spatial profiles of fracture waters (Figures 4-27 through 4-30) can be applied to the time profiles as well. Dilution in fractures increases with time as the system heats up and steam condenses in fractures. This is shown by computed increasing liquid saturations (Figure 4-31b) and decreasing chloride concentrations (Figure 4-32a) in fractures with time until the heat source is turned off at approximately 275 days. At this time, fractures drain resulting in a steep decrease in their liquid saturation because no more steam is being generated. Accordingly, the concentrations of chloride and other unreactive species quickly rise (Figure 4-32a) by equilibration with matrix water closer in composition to the initial water.

The computed water chemistry trends in the matrix are significantly different than in fractures because condensation and dilution effects are not as important in the matrix. The permeability of the matrix is also quite low, and thus the rates of liquid flow are much less than in fractures. Consequently, the matrix water chemistry exhibits trends more similar to those that would be predicted by simple heating (i.e., geochemical mass-transfer without fluid flow). At the start of the simulated test, the pH decreases with time as water dissociates and calcite precipitates with increasing temperature, until the volatilization of CO_2 becomes significant enough to reverse these trends and increase the pH (Reaction 4.4.1). Accordingly, the computed P_{CO2} trend in the matrix is inversely related to the pH trend (Figure 4-33b). The pH increases with time, and somewhat more so after the heat is turned off because the system remains warm and CO_2 keeps volatilizing into fractures that now have a higher gas saturation (CO_2 advected faster away from the system).

The higher pH in the matrix water results in different computed mineral abundances in matrix (Figure 4-35) compared to those in fractures (Figure 4-34). Notably, there is proportionally more heulandite, mordenite, and sepiolite precipitation, less feldspar dissolution, and more quartz and cristobalite dissolution in the matrix than in fractures. In all cases, as discussed previously, the computed mineral volume changes are too small (over the length of the test) to have any significant effect on either the fracture or matrix permeability.

Results of simulations are further discussed with respect to the composition of water from borehole 16 in the next section.

4.6 Interpretation and Discussion

Calcite, gypsum, and amorphous silica were found in post-test mineralogical analyses of ESF-TMA-PTC-NEU-2 (overcore of borehole 16) (Levy et al., 1998, p. 23) and attributed to reactions that occurred during the SHT. These authors have identified two possibilities for the origin of these evaporite minerals (p. 16): (1) formation during water-rock interaction at elevated temperatures, and (2) precipitation during post-test evaporation. They conclude (p. 17) that the distribution and textural attribute of these minerals suggest they formed through evaporation of the remaining waters during the post-test cool-down period. For this reason, a direct comparison of these precipitates cannot be made to the modeled mineral precipitates unless it can be shown that they crystallized at high temperatures.

Some comparison can be made of the last minerals predicted to form in the dryout zone at small liquid saturations (but at boiling temperatures) to those found in overcores of boreholes 2 and 16, as some of the phases are likely to be the same as those formed by evaporation at temperatures below boiling. At the boiling front, precipitated minerals in the model simulations include calcite, gypsum, minor amorphous silica, and minor quantities of clay minerals and zeolites. As mentioned above, calcite, gypsum, and amorphous silica were found in post-test mineralogical analyses. The other phases are also expected to form under evaporative conditions or dryout during boiling. However, borehole 16 was outside the dryout region and therefore never experienced the final dryout due to boiling. These phases were not calculated to form at the location of borehole 16 because computed liquid saturations were too high (and concentrations too small) for amorphous silica and gypsum to precipitate, and the pH of condensate waters was too low for calcite precipitation at these locations. This is corroborated by the compositions of the waters collected in borehole 16, which were relatively dilute, and strongly undersaturated with respect to gypsum, calcite, and amorphous silica. Therefore, in agreement with Levy et al. (1998, p. 17), we conclude that the phases observed in the post-test mineralogical studies most likely formed through evaporation of the remaining waters in the borehole, sometime after the test was completed.

Table 4.6.1 Comparison of water compositions measured in borehole 16 (BH-16) to concentrations computed in model Zones A, B, and C shown on Figure 4-36. Simulation with aluminosilicate minerals

(KIN04). Concentrations are listed in order of decreasing temperature within each zone, and correspond to the data shown graphically on Figure 4-37.

		Calculated - 91 days			**Measured 11/25/96**
		Zone A	Zone B	Zone C	BH-16
Temperature	deg.C	88 - 73	68 - 58	80 - 68	
Liquid Saturation		0.66 - 0.49	0.47 - 0.40	0.61 - 0.63	
pH		7.7 - 8.2	8.1 - 8.1	7.3 - 7.4	6.2
Ca	mg/l	0.19 - 0.00	0.00 - 0.72	0.21 - 0.18	13
Mg	mg/l	0.00 - 0.77	1.5 - 3.7	0.00 - 0.08	1.63
Na	mg/l	2.8 - 57	65 - 92	4.7 - 9.3	16
Cl	mg/l	0.64 - 17	20 - 33	1.2 - 2.6	2.54
Si	mg/l	4.0 - 7.8	7.1 - 5.1	3.3 - 3.4	16.8
HCO3	mg/l	4.2 - 99	115 - 172	9.6 - 19	188*
SO4	mg/l	0.63 - 17	20 - 32	1.2 - 2.6	1.83
K	mg/l	0.88 - 2.0	2.4 - 8.8	0.68 - 0.76	2.5
Al	mg/l	0.85 - 0.26	0.15 - 0.01	0.38 - 0.16	< 0.06
		Calculated - 161 days			**Measured 2/3/97**
		Zone A	Zone B	Zone C	BH-16
Temperature	deg.C	96 - 90	83 - 72	95 - 83	
Liquid Saturation		0.34 - 0.63	0.57 - 0.46	0.42 - 0.60	
pH		7.8 - 7.7	8.1 - 8.3	7.6 - 7.6	6.9
Ca	mg/l	0.21 - 0.23	0.01 - 0.00	0.25 - 0.16	9.76
Mg	mg/l	0.00 - 0.00	0.00 - 0.12	0.00 - 0.00	1.16
Na	mg/l	3.3 - 4.0	23 - 81	1.7 - 5.0	13.9
Cl	mg/l	0.75 - 0.97	6.2 - 23	0.3 - 1.2	1.45
Si	mg/l	4.6 - 3.8	5.9 - 10	3.7 - 3.6	17.4
HCO3	mg/l	3.2 - 5.9	37 - 135	1.7 - 9.2	
SO4	mg/l	0.73 - 0.95	6.0 - 22	0.32 - 1.2	0.42
K	mg/l	0.85 - 0.69	1.4 - 1.7	0.60 - 0.80	2.5
Al	mg/l	1.2 - 0.87	0.87 - 0.18	0.92 - 0.60	< 0.06

* calculated from charge balance

Comparisons can be made directly between the compositions of collected waters in borehole 16 and those of fracture waters in the model simulations. These are shown on Tables 4.6.1 and 4.6.2 for three locations within the model, as indicated on Figure 4-36. Zone A and Zone B include grid points along the simulated location of borehole 16, as well as within approximately 0.2 m on either side of this borehole. Zone C corresponds to grid nodes below the heater where the computed pH is the lowest, due to increased drainage of steam condensate at this location. The tabulated data are represented graphically as Shoeller-type diagrams on Figures 4-37 and 4-38, respectively, to facilitate comparing the general character of these waters.

Table 4.6.2 Comparison of water compositions measured in borehole 16 (BH-16) to concentrations computed in model Zones A, B, and C shown on Figure 4-36. Simulation without aluminosilicate minerals (KIN05). Concentrations are listed in order of decreasing temperature within each zone, and correspond to the data shown graphically on Figure 4-38.

		Calculated - 91 days									**Measured 11/25/96**
		Zone A			Zone B			Zone C			BH-16
Temperature	deg.C	88	-	73	68	-	58	80	-	68	
Liquid Saturation		0.66	-	0.49	0.47	-	0.40	0.61	-	0.63	
pH		7.0	-	7.6	7.6	-	7.7	6.6	-	6.6	6.2
Ca	mg/l	0.19	-	4.27	6.02	-	14	0.31	-	0.86	13
Mg	mg/l		-			-			-		1.63
Na	mg/l	1.4	-	38	45	-	73	2.7	-	5.8	16
Cl	mg/l	0.64	-	17	20	-	33	1.2	-	2.6	2.54
Si	mg/l	0.8	-	13.0	14.6	-	23	1.2	-	2.3	16.8
HCO3	mg/l	3.1	-	73	89	-	157	7.7	-	16.3	188 *
SO4	mg/l	0.62	-	17	20	-	32	1.2	-	2.6	1.83
K	mg/l		-			-			-		2.5
Al	mg/l		-			-			-		< 0.06
		Calculated - 161 days									**Measured 2/3/97**
		Zone A			Zone B			Zone C			BH-16
Temperature	deg.C	96	-	90	83	-	72	95	-	83	
Liquid Saturation		0.34	-	0.63	0.57	-	0.46	0.42	-	0.60	
pH		7.7	-	7.2	7.5	-	7.7	7.3	-	6.7	6.9
Ca	mg/l	0.22	-	0.21	0.80	-	4.28	0.11	-	0.27	9.76
Mg	mg/l		-			-			-		1.16
Na	mg/l	1.7	-	2.1	14	-	51	0.7	-	2.7	13.9
Cl	mg/l	0.75	-	0.96	6.2	-	23	0.3	-	1.2	1.45
Si	mg/l	1.3	-	1.3	6.2	-	18	0.6	-	1.6	17.4
HCO3	mg/l	1.8	-	3.9	24	-	92	1.0	-	6.8	
SO4	mg/l	0.73	-	0.94	6.0	-	22	0.33	-	1.2	0.42
K	mg/l		-			-			-		2.5
Al	mg/l		-			-			-		< 0.06

* calculated from charge balance

Computed and observed concentrations generally depict similar trends, with the exception of magnesium and calcium for the simulation with aluminosilicates. In most cases the computed pH is higher than measured values, although reasonably good agreement (lowest values) is obtained with the simulation without aluminosilicates. As mentioned earlier, inclusion of these minerals in the geochemical system results in higher computed pH than in the case of simulations without them.

Rapidly changing hydrochemical conditions in fractures around the heater in space and time make it difficult to exactly match borehole-16 water with simulated results. Refinement of the reaction rates for calcite, calcium zeolites, and magnesium smectite would likely result in closer agreement between measured and calculated calcium and magnesium concentrations. Nevertheless, the simulations appear to correctly represent the processes leading to the formation of waters of the type found in borehole 16, which essentially result from steam condensation followed by mild reaction with surrounding rock. This corroborates the conclusions of Glassley and DeLoach (1997, p. 6) and Glassley (1997, p. 3) regarding the origin of borehole-16 water. It was noted in CRWMS (1997, p. 5-52) that the source of CO_2 leading to the mild acidification of the water was uncertain. From the simulations presented here, it appears that volatilization of dissolved CO_2 from matrix water alone could account for the mild acidification of steam condensate.

The simulated water compositions that best match borehole 16 water are not near the simulated location of borehole 16 but below the heater in the zone of increased drainage. This would indicate that the water in borehole 16 originated from a zone with increased drainage compared to its surroundings. This would be expected in a preferential fluid pathway. The air-injection and gas-tracer data discussed in Chapter 2 of this report suggest a preferential pathway between the heat source and this borehole, which would be consistent with the modeling results.

4.7 Conclusions

Reaction-transport simulations of the SHT were completed to provide insight into THC processes accompanying this test and to further our understanding of these processes. The simulations were also useful for interpreting the chemical composition of water collected in borehole 16, and yield results that are consistent with conclusions reached previously by other authors. The borehole-16 water resulted from steam condensation in fractures, and its mildly acidic character reflects the dissolution of gaseous CO_2 at the time of steam condensation.

The simulations indicate that dissolved carbonate species in matrix water alone provide a sufficient source of CO_2 gas, upon heating, to drive the pH of condensates down to a mildly acidic range (pH 6 to 7). When including the reaction of aluminosilicate minerals, however, the simulations of the SHT overestimate the pH of condensates in fractures (computed pH 7 to 8 as opposed to pH between 6 and 7 in borehole-16 water). This may be related to overestimated mineral reaction rates. An overestimated pH of the initial matrix and fracture water could not be ruled out either.

Calcite, gypsum, and amorphous silica were found in post-test mineralogical analyses and attributed to reactions accompanying the SHT. Calcite and gypsum were predicted by the simulations to precipitate in some areas of the model at elevated temperature upon boiling. However, these three minerals appear to

have formed during the SHT by evaporation at low temperature, most likely sometime after the heater was turned off.

In any case, the THC simulations presented here are encouraging, as they appear to reproduce fairly well the chemical processes affecting the SHT. The results underline the importance of considering a dual-permeability framework (fracture/matrix) when simulating water-gas-rock interactions in the test area, as the water chemistries in fractures and matrix differ significantly from each other and are directly affected by the hydrochemical interaction between these two media. However, the complexity of these processes and their interaction within a dual- permeability context, together with the uncertainty of input data, warrants that some caution be applied when interpreting modeling results. This is particularly true when extrapolating results of the SHT to the larger-scale proposed repository at Yucca Mountain. More work remains ahead to improve the reliability of input data and to enhance computational methods so that mountain-scale models of the repository can be implemented with efficiency and accuracy.

Acknowledgments

TOUGHREACT was developed by Tianfu Xu and Karsten Pruess for another study. We thank these authors for making the program available and allowing us to modify it for simulations of the Yucca Mountain thermal tests. Jens Birkholzer provided input data meshes, data, and assistance with the thermohydrological model. We also thank Steve Chipera for allowing us to use his thermodynamic data on calcium zeolites. Technical reviews by Mark Conrad and Ardyth Simmons are much appreciated in addition to thoughtful discussions with both.

References

Apps, J.A. 1997. "Hydrochemical Analysis." *In:* G.S. Bodvarsson, T.M. Bandurraga, and Y.S. Wu, eds. *The Site-Scale Unsaturated Zone Model of Yucca Mountain, Nevada, for the Viability Assessment,* Chapter 14. Yucca Mountain Project Level 4 Milestone SP24UFM4, LBNL-40376, UC-814. Berkeley, California: Lawrence Berkeley National Laboratory. DTN: LB970601233129.001(Q)

Bear, J. 1972. *Dynamics of Fluid in Porous Media.* New York, New York: Dover Publications. TIC: Copyright Clearance Pending.

Birkholzer, J.T. and Tsang, Y.W. 1996. *Forecast of Thermal-Hydrological Conditions and Air Injection Test Results of the Single Heater Test at Yucca Mountain.* Yucca Mountain Project Level 4 Milestone SP918M4; Report LBNL-39789, UC-814. Berkeley, California: Lawrence Berkeley National Laboratory. MOL.19971124.0089.

Broxton, D.E.; Warren, R.G.; Hagan, R.C.; and Leudemann, G. 1986. *Chemistry Of Diagenetically Altered Tuffs At The Potential Nuclear Waste Repository, Yucca Mountain, Nye County, Nevada.* Report LA-10802-MS, Los Alamos, New Mexico: Los Alamos National Laboratory. MOL.19980618.0425.

Carlos, B.A. 1994. *Preliminary Description of Fracture-Lining Minerals in Drill Core USW UZ-14.* Yucca Mountain Project Milestone 4005. Los Alamos, New Mexico: Los Alamos National Laboratory. TIC: 214888.

Carlos, B.A. 1993. *Preliminary Description of Fracture-Lining Minerals in Drill Core UE25 UZ-16.* Yucca Mountain Project Milestone 4013. Los Alamos, New Mexico: Los Alamos National Laboratory. MOL.19950728.0196.

Carlos, B.A.. 1989. *Fracture-Coating Minerals in the Topopah Spring Member and Upper Tuff of Calico Hills from Drill Hole J-13.* Los Alamos National Laboratory Report LA-11504-MS. Los Alamos, New Mexico: Los Alamos National Laboratory. TIC: 202383.

Carlos, B.A.. 1985. Minerals in Fractures of the Unsaturated Zone from Drill Core USW G-4, Yucca Mountain, Nye County, Nevada. Los Alamos National Laboratory Report LA-10415-MS. Los Alamos, New Mexico: Los Alamos National Laboratory. NNA.19920506.0037.

Carlos, B.A.; Chipera, S.J.; and Bish D.L. 1995. *Distribution and Chemistry of Fracture-Lining Zeolites at Yucca Mountain, Nevada.* Report LA-12977-MS. Los Alamos, New Mexico: Los Alamos National Laboratory. TIC:223000.

Carlos, B.A.; Chipera, S.J.; and Snow, M. 1995. *Multiple Episodes of Zeolite Deposition in Fractured Silicic Tuff.* Report MS4079. LA-UR-95-0871. Los Alamos, New Mexico: Los Alamos National Laboratory. MOL.19960514.0209.

Carlos, B.A.; Bish, D.L.; and Chipera, S.J. 1991. "Fracture-Lining Minerals in the Lower Topopah Spring Tuff at Yucca Mountain." *Proceedings of the Second International High-Level Radioactive Waste Conference, April, 1991.* Las Vegas, Nevada: American Nuclear Society, 1, 486-493. NNA.19910206.0039.

Chipera, S.J. and Apps, J.A. 1998. "Geochemistry of Natural Zeolites." Chapter 4 in *The Z Book.* In preparation. TBV.

Conrad, M.E. 1998. "Carbon Isotope Analyses o Conrad, M. 1998. "Isotope Analyses of Samples from the Drift Scale Test Hydrology Holes." *In: Second Quarter TDIF Submission (Hydrological, Radar and Microseismic),* Chapter 3. Yucca Mountain Project Level 4 Milestone Report SP2790M4. Berkeley, California: Lawrence Berkeley National Laboratory. LB980715123142.003 (Q).

CRC Handbook of Chemistry and Physics, 62nd Edition. 1981. (Weast, R.C. and Astle, J.J. eds). Boca Raton, Florida: CRC Press. TIC: 206666 (65th edition).

CRWMS M&O. 1997. *Single Heater Test Status Report.* BAB000000-01717-5700-00002. Rev. 00. MOL.19880203.0578.

Glassley, W.E. 1998a. "Conceptual Model for Reactive Transport in the Altered Zone." *In:* E.L. Hardin, ed., *Near Field/Altered Zone Models.* Yucca Mountain Project Milestone SP3100M4. Livermore, California: Lawrence Livermore National Laboratory. MOL.19980504.0577. LL980209004242.026 (Q).

Glassley, W.E. 1998b. "Repository-Scale Thermohydrochemical Scoping Calculations Involving Silica." *In:* E.L. Hardin, ed., *Near Field/Altered Zone Models.* Yucca Mountain Project Milestone SP3100M4. Livermore, California: Lawrence Livermore National Laboratory. MOL.19980504.0577. LL980209004242.026 (Q).

Glassley, W.E. 1998c. "Drift-Scale THC Scoping Calculations and Alteration Flow Pathways Above and Below Repository Drifts." *In:* E.L. Hardin, ed., *Near Field/Altered Zone Models.* Yucca Mountain Project Milestone SP3100M4. Livermore, California: Lawrence Livermore National Laboratory. MOL.19980504.0577. LL980209004242.026 (Q).

Glassley, W.E. 1997. *Third Quarter Report, Chemical Analyses of Waters Collected from the Single Heater Test.* Yucca Mountain Project Level 4 Milestone SP9281M4. Livermore, California: Lawrence Livermore National Laboratory. MOL.19980105.0625.

Glassley, W.E. and DeLoach, L. 1997. *Second Quarter Results of Chemical Measurements in the Single Heater Test.* Milestone Report for the CRWMS M&O, U.S. Department of Energy, SP9240M4. Livermore, California: Lawrence Livermore National Laboratory. MOL.19971218.0917.

Helgeson, H.C.; Delany, J.M.; Nesbitt, H.W.; and Bird, D.K. 1978. "Summary and Critique of the Thermodynamic Priorities of Rock Forming Minerals." *American Journal of Science,* 278-A, 229. TIC: 220013.

Johnson, J.W.; Knauss, K.G.; Glassley, W.E.; DeLoach, L.D.; and Thompson, A.F.B. 1998. "Reactive Transport Modeling of Plug-Flow Reactor Experiments: Quartz and Tuff Dissolution at 240 C." Submitted to *Journal of Hydrology.* TIC: Copyright Clearance Pending.

Johnson J.W.; Knauss, K.G.; and Glassley, W.E.; 1997. Reactive Transport Through Topopah Spring Tuff: Summary Of Initial Plug-Flow Reactor Experiments And Associated Computed Simulations. Yucca Mountain Milestone Report, SPL1MB4. Livermore, California: Lawrence Livermore National Laboratory. MOL.19970507.0178.

Johnson, J.W; Oelkers, E.H.; and Helgeson, H.C. 1992. "Equilibrium Constants Calculated with, and Data from, SUPCRT92." *Computers and Geosciences, 18,* 899-947. TIC: Copyright Clearance Pending.

Levy, S.S. and O'Neil, J.R., 1989. "Moderate Temperature Zeolitic Alteration In A Cooling Pyroclastic Deposit." *Chemical Geology,76,* 321-326. NNA.19900531.0051. TIC: 223793.

Levy, S.S; Chipera; S.J.; and Snow, M. 1998. *Mineralogical products of the ESF Single-Heater Test.* Yucca Mountain Project Level 4 Milestone SPY147M4. Los Alamos, New Mexico: Los Alamos National Laboratory, DRAFT. TBV.

Lyman, W.J.; Reehl, W.F.; and Rosenblatt, D.H. 1990. *Handbook of Chemical Property Estimation Methods.* Washington D.C.: American Chemical Society. TIC: Copyright Clearance Pending.

Maier, C,G. and Kelley, K.K., 1932. "An Equation For The Representation Of High Temperature Heat Content Data." *Journal of the American Chemical Society, 54*, 3243-3246. TIC: Copyright Clearance Pending.

Nitao, J.J. 1998. "Thermohydrochemical Alteration of Flow Pathways Above and Below the Repository." *In:* E.L. Hardin, ed., *Near Field/Altered Zone Models.* Yucca Mountain Project Milestone SP3100M4. Livermore, California: Lawrence Livermore National Laboratory. MOL.19980504.0577. LL980209004242.026 (Q).

Paces J.B, Marshall B.D.; Whelan J.F.; Neymark L.A.; and Peterman Z.E. 1998. *Summary of Subsurface Calcite and Opal Deposits and Estimates of the Probable Distribution and Isotopic Composition of Hydrogenic Minerals along the East-West Cross-Drift,* Yucca Mountain, Nevada. U.S. Geol. Surv. Open File Report. Denver, Colorado: U.S. Geological Survey. MOL: TBV.

Pokrovskii, V.A. and Helgeson, H.C. 1995. "Thermodynamic Properties of Aqueous Species and the Solubilities of Minerals at High Pressures and Temperatures: The System Al_2O3-H_2O-NaCl." *American Journal of Science, 295,* 1255-1342. TIC: 236803.

Pruess, K.; Xu, T. 1998. *Coupled Modeling of Non-Isothermal Multi-Phase Flow, Solute Transport and Reactive Chemistry in Porous and Fractured Media: 1. Model Development and Validation.* LBNL Report 42050. Submitted to Journal of Geophysical Research. TIC: On order.

Ragnarsdottir, K.V. 1993. "Dissolution Kinetics of Heulandite at pH 2-12 and 25 C." *Geochim. And Cosmochim. Acta, 57,* 2439-2449. TIC: 222070.

Rimstidt, J.D. and Barnes, H.L. 1980. "The Kinetics of Silica-Water Reactions." *Geochimica et Cosmochimica Acta, 44,* 1683-1699. NNA.19891006.0185. TIC: 219975.

Rimstidt, J.D. 1997. "Quartz Solubility at Low Temperatures." *Geochimica et Cosmochimica Acta, 61*(13), 2553-2558. TIC: Copyright Clearance Pending.

Roberts, S. and Viani, B. 1997. *Mineral Abundances from Six Chemistry (SEAMIST) Holes in the Drift Scale Heater Test Area of the Exploratory Studies Facility.* Yucca Mountain Project Level 4 Milestone, SP9510M4. Livermore, California: Lawrence Livermore National Laboratory. DTN: LL980106404244.050(Q). MOL.19971215.0651.

Sonnenthal, E.; Spycher, N.; Apps, J.; Simmons, A. 1998a. *Thermo-Hydro-Chemical Predictive Analysis for the Drift-Scale Heater Test.* Yucca Mountain Project Level 4 Milestone SPY289M4. Berkeley, California: Lawrence Berkeley National Laboratory. MOL.19980812.0268.

Sonnenthal, E.; Spycher, N; and Apps, J. 1998b. *Interpretative Analysis of the Thermo-Hydro-Chemical Processes of the Drift-Scale Test.* Yucca Mountain Project Level 4 Milestone SP2930M4. Berkeley, California: Lawrence Berkeley National Laboratory. MOL.19980825.0268.

Sonnenthal, E. 1997. "Re: Discussion of Water Chemistry from the Heater Test." Internal memo to G. Bodvarsson, LBNL, January 20. Berkeley, California: Lawrence Berkeley National Laboratory. MOL.19980825.0287.

Steefel, C.I. and Lasaga, A.C. 1994. "A Coupled Model for Transport of Multiple Chemical Species and Kinetic Precipitation/Dissolution Reactions with Application to Reactive Flow in Single Phase Hydrothermal Systems." *American Journal of Science, 294*, 529-592. TIC: 23572.

Tester, J.W.; Worley, G.W.; Robison, B.A.; Grigsby, C.O.; and Feerer, J.L. 1994. "Correlating Quartz Dissolution Kinetics in Pure Water from 25° to 625°C." *Geochimica et Cosmochimica Acta, 58*(11) 2407-2420. TIC: 236776.

Whitbeck, M. and Glassley, W.E. 1998. "Reaction Path Model for Water Chemistry and Mineral Evolution in the Altered Zone." *In:* E.L. Hardin, ed., *Near Field/Altered Zone Models."* Yucca Mountain Project Milestone SP3100M4. Livermore, California: Lawrence Livermore National Laboratory. MOL.19980504.0577. LL980209004242.026 (Q).

Wolery, T.J. 1992. *EQ3NR, a Computer Program for Geochemical Aqueous Speciation-Solubility Calculations: Theoretical Manual, User's Guide and Related Documentation (Version 7.0)* Livermore, California: Lawrence Livermore National Laboratory Report UCRL-MA-110662 PT III, 246 p. NNA.19921218.0010.

Xu, T.; Pruess, K.; and Brimhall, G. 1998. *An Improved Equilibrium-Kinetics Speciation Algorithm for Redox Reactions in Variable Saturated Subsurface Flow Systems.* LBNL-41789. Submitted to Computers and Geosciences. Berkeley, California: Lawrence Berkeley National Laboratory. TIC: On order.

Xu, T.; Gerard, F.; Pruess, K.; and Brimhall, G. 1997. *Modeling Non-Isothermal Multiphase Multi-Species Reactive Chemical Transport in Geologic Media.* Report LBNL-40504, UC-400. Berkeley-California: Lawrence Berkeley National Laboratory. TIC: 238918.

Yang, I.C.; Rattray, G.W.; and Yu, P. 1996a. *Interpretation of Chemical and Isotopic Data from Boreholes in the Unsaturated Zone at Yucca Mountain.* U.S. Geological Survey Water Resources Investigation Report 96-4058. Denver, Colorado: U.S. Geological Survey. DTN: GS970108312271.001 (Q). MOL.19970715.0408.

Yang, I.C.; Yu, P.; Rattray, G.W; and Thorstenson, D.C. 1996b. *Hydrochemical Investigations and Geochemical Modeling in Characterizing the Unsaturated Zone at Yucca Mountain, Nevada.* U.S. Geological Survey Water Resources Investigation Report. Denver, Colorado: U.S. Geological Survey. MOL.19970415.0393.

Figures

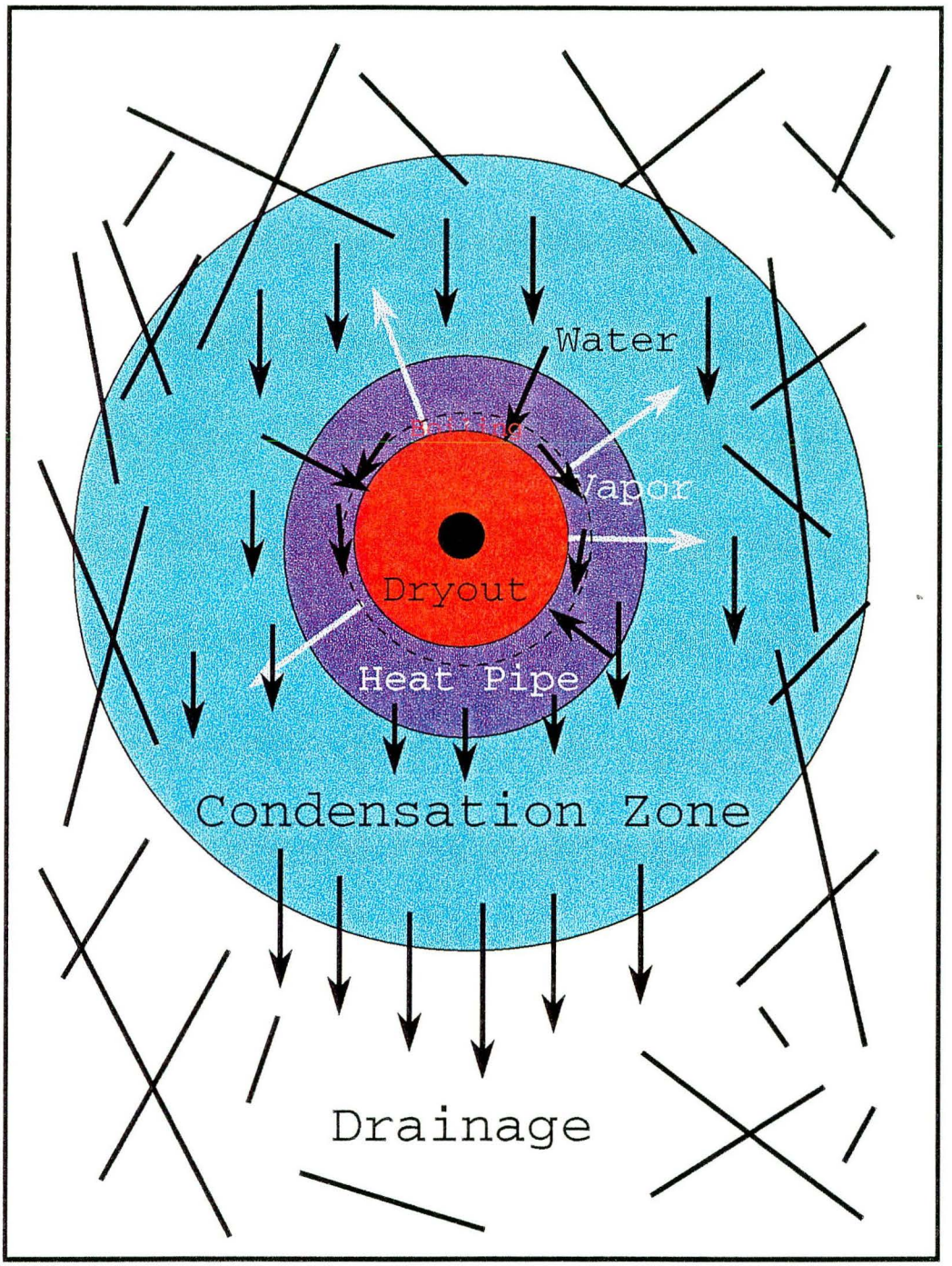

Figure 4-1. Conceptual model of thermohydrological processes for the SHT that are important in the evolution of the geochemistry of waters, gases, and minerals. See text.

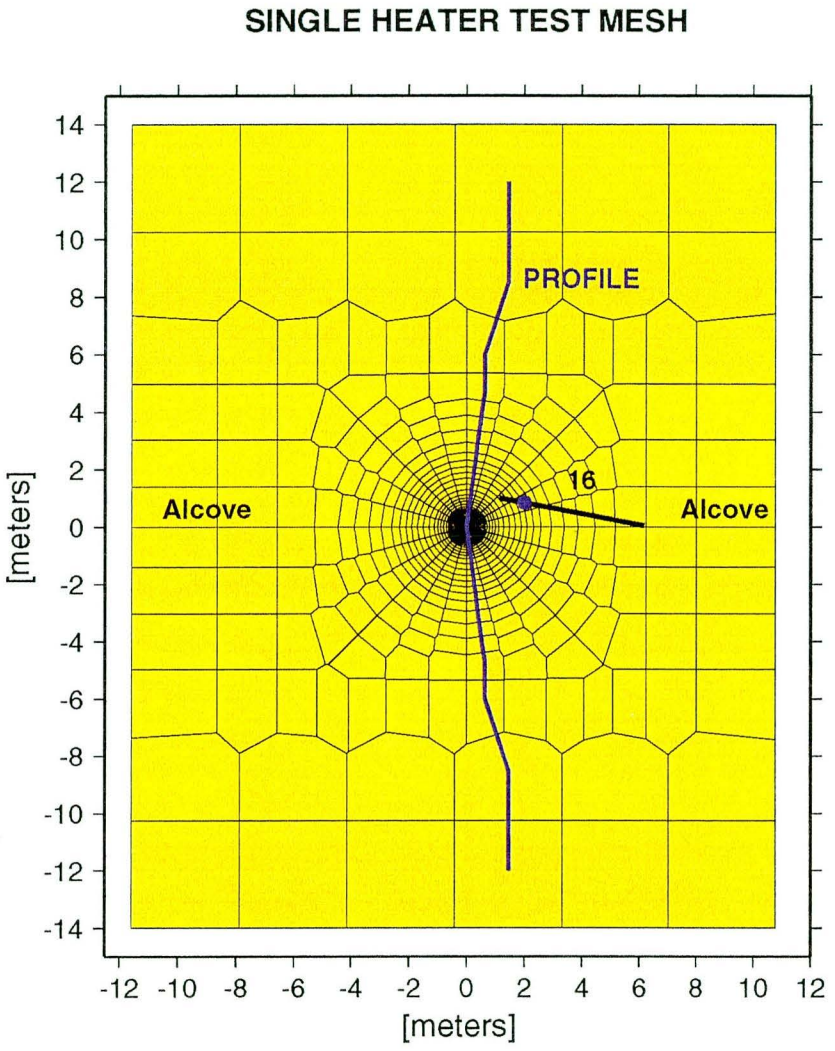

Figure 4-2. Two-dimensional computational mesh for the dual-permeability simulations of the Single Heater Test. Adapted from Birkholzer and Tsang (1996, p. 28). The mesh represents a vertical cross section perpendicular to the axis of the heater borehole. The blue line through the heater coincides with the horizontal axis of profiles shown on Figures 4-28 to 4-30. The blue point plotted on the projection of borehole 16 shows the location of the grid node for which time profiles are displayed on Figures 4-31 to 4-35.

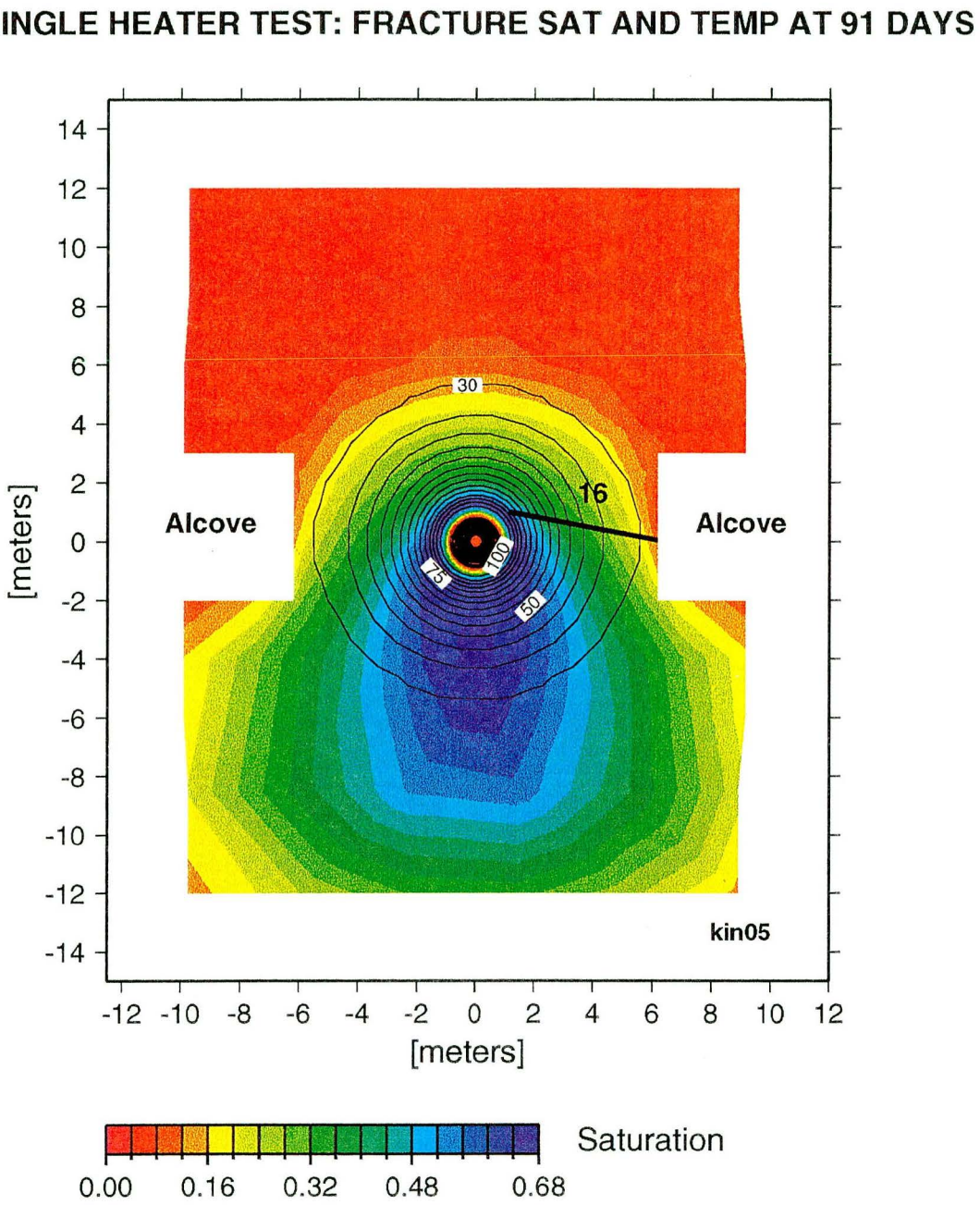

Figure 4-3. Calculated fracture liquid saturation and temperature 91 days after the initiation of heating, corresponding to the sampling time of the first water sample collected from borehole 16 (simulation kin05).

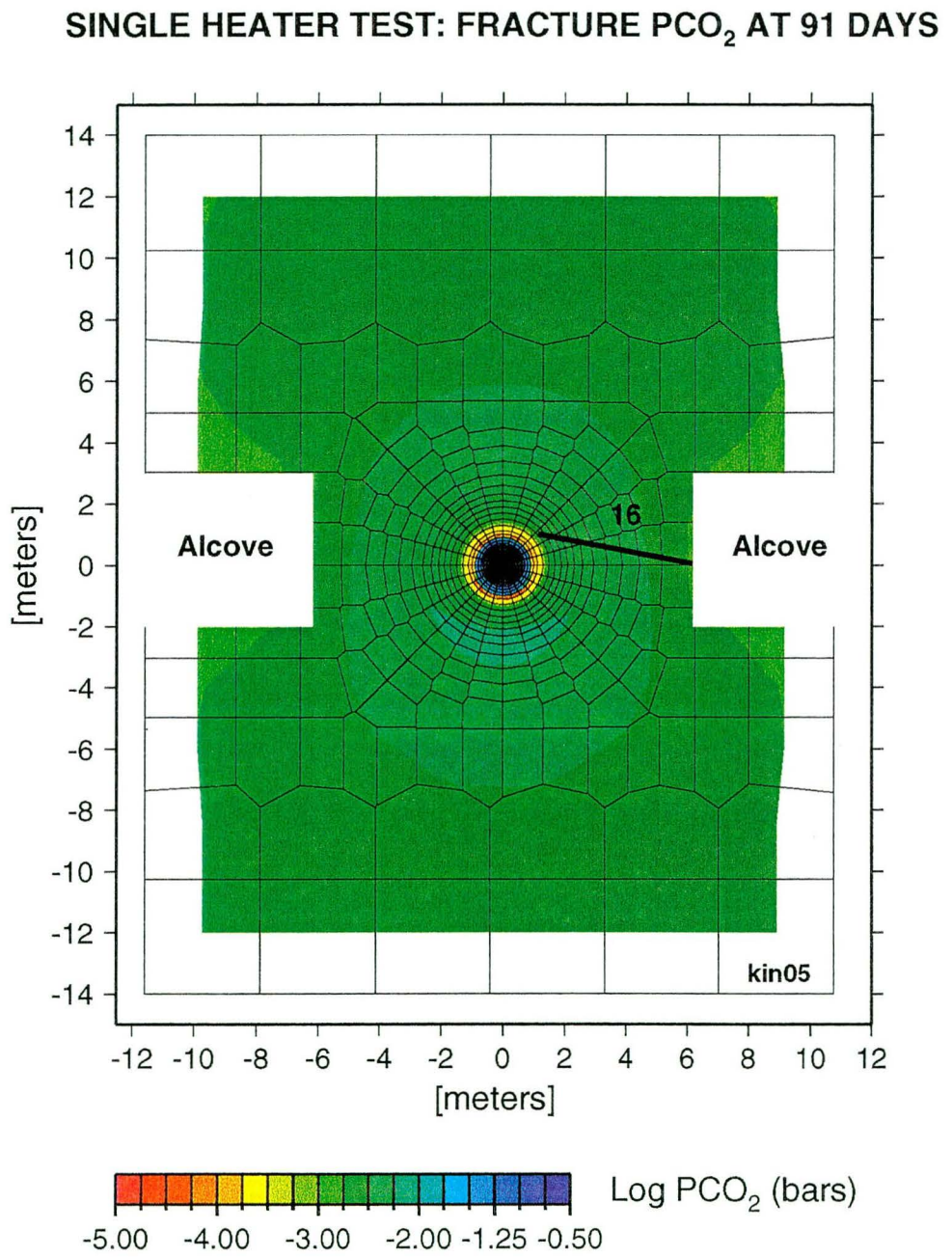

Figure 4-4. Calculated partial pressure of CO_2 in equilibrium with water in fractures after 91 days (simulation kin05).

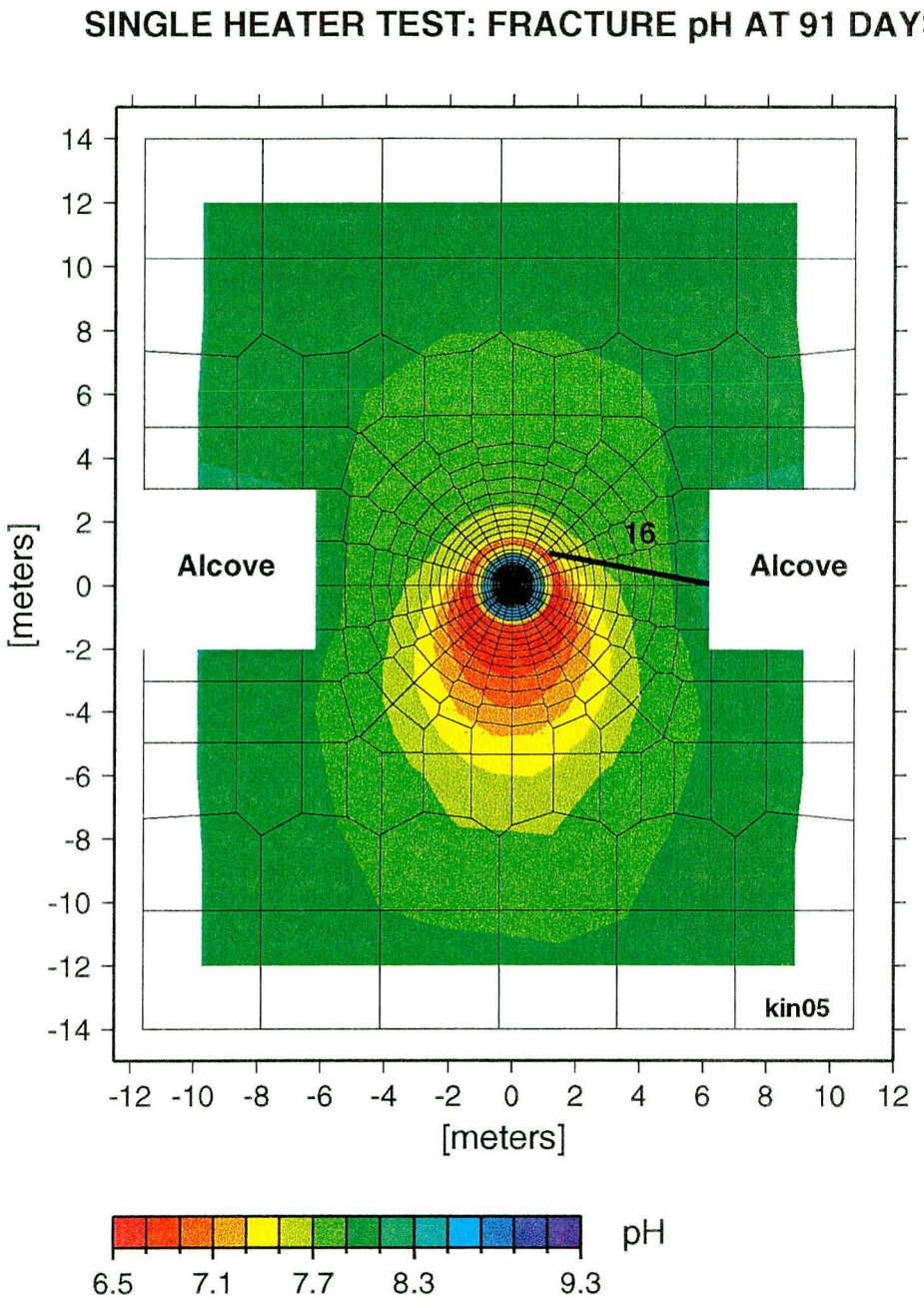

Figure 4-5. Calculated pH in fracture pore waters after 91 days (simulation kin05).

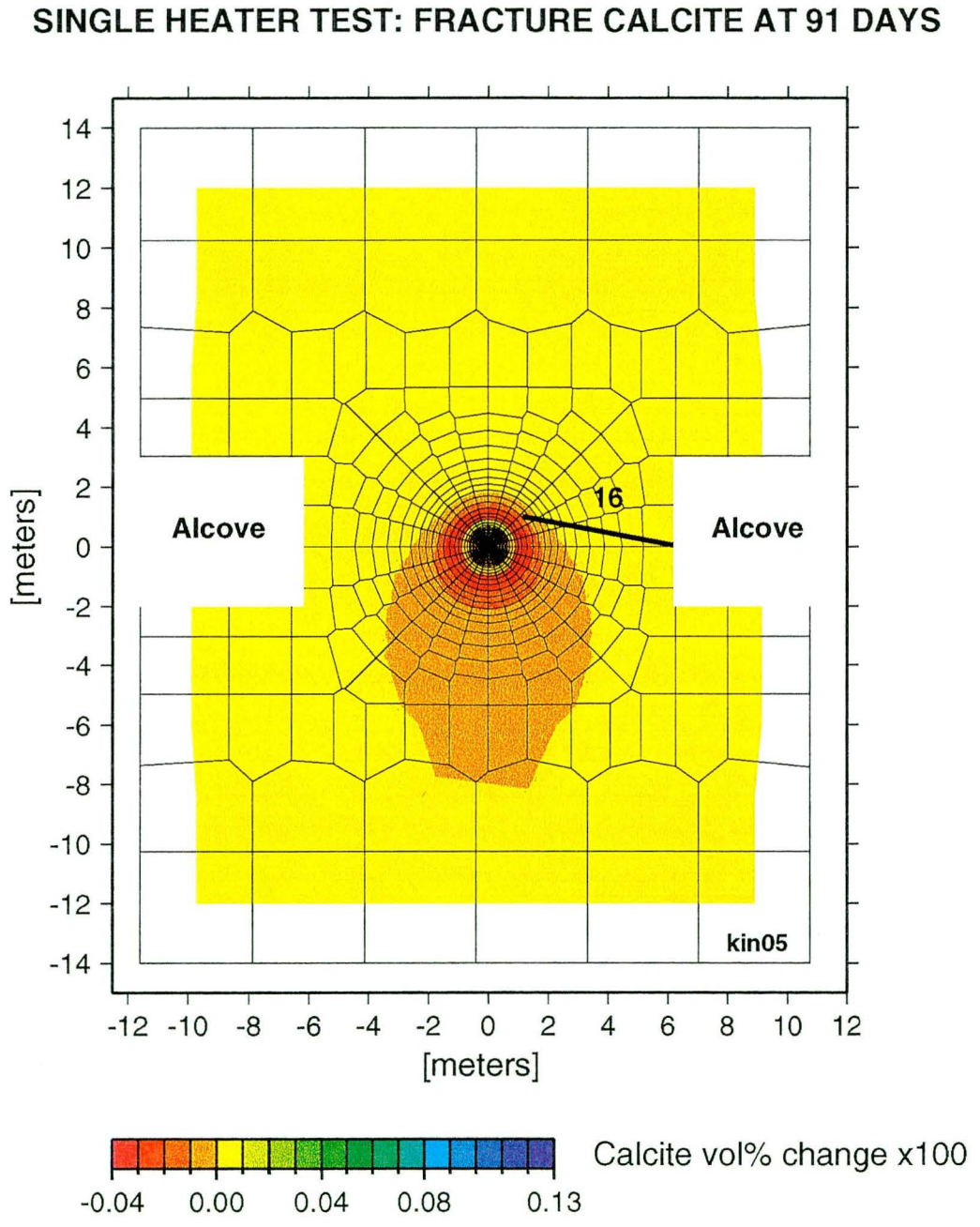

Figure 4-6. Change in calcite volume percent in fractures after 91 days (simulation kin05).

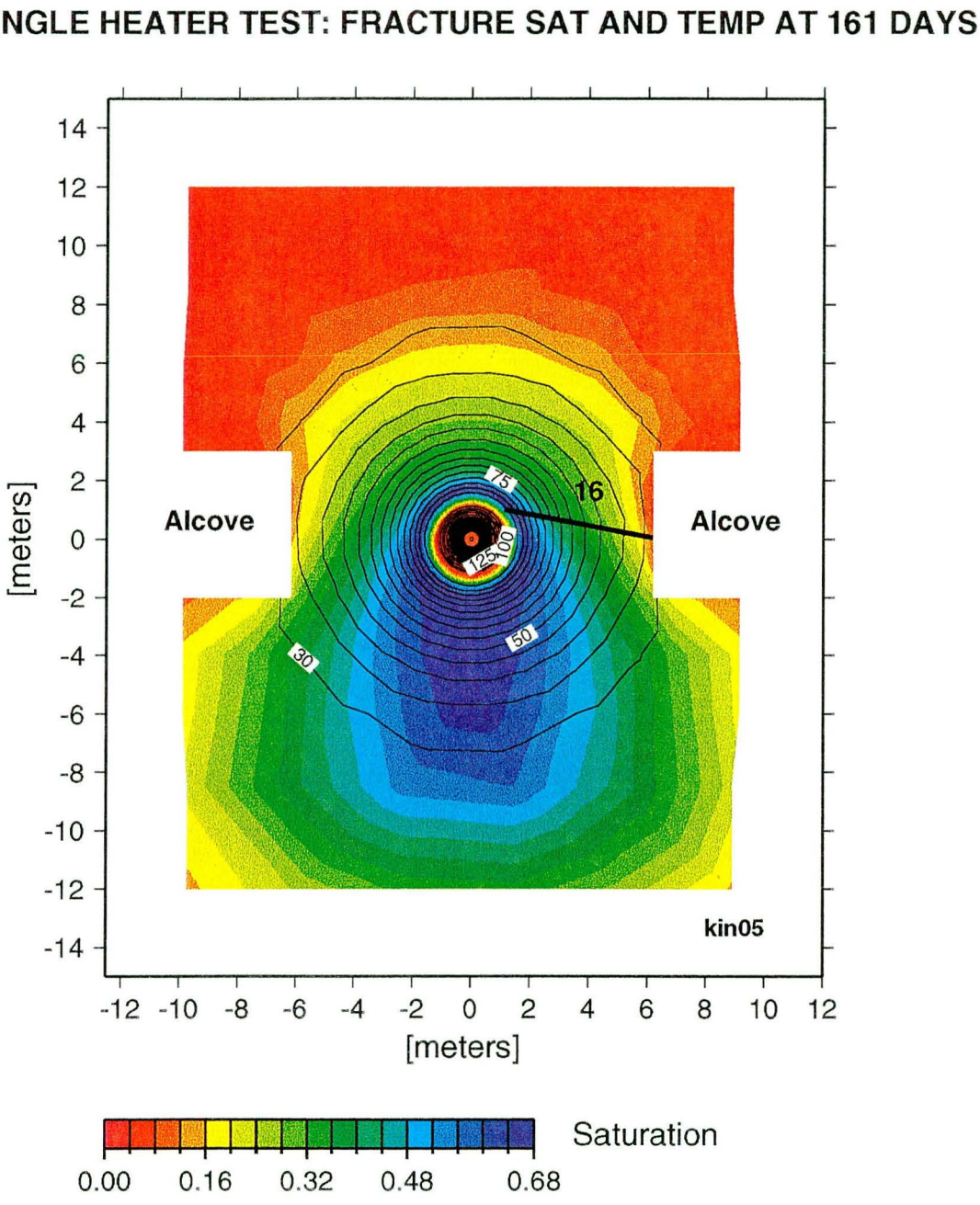

Figure 4-7. Calculated fracture liquid saturation and temperature 161 days after the initiation of heating, corresponding to the sampling time of the second water sample collected from borehole 16 (simulation kin05).

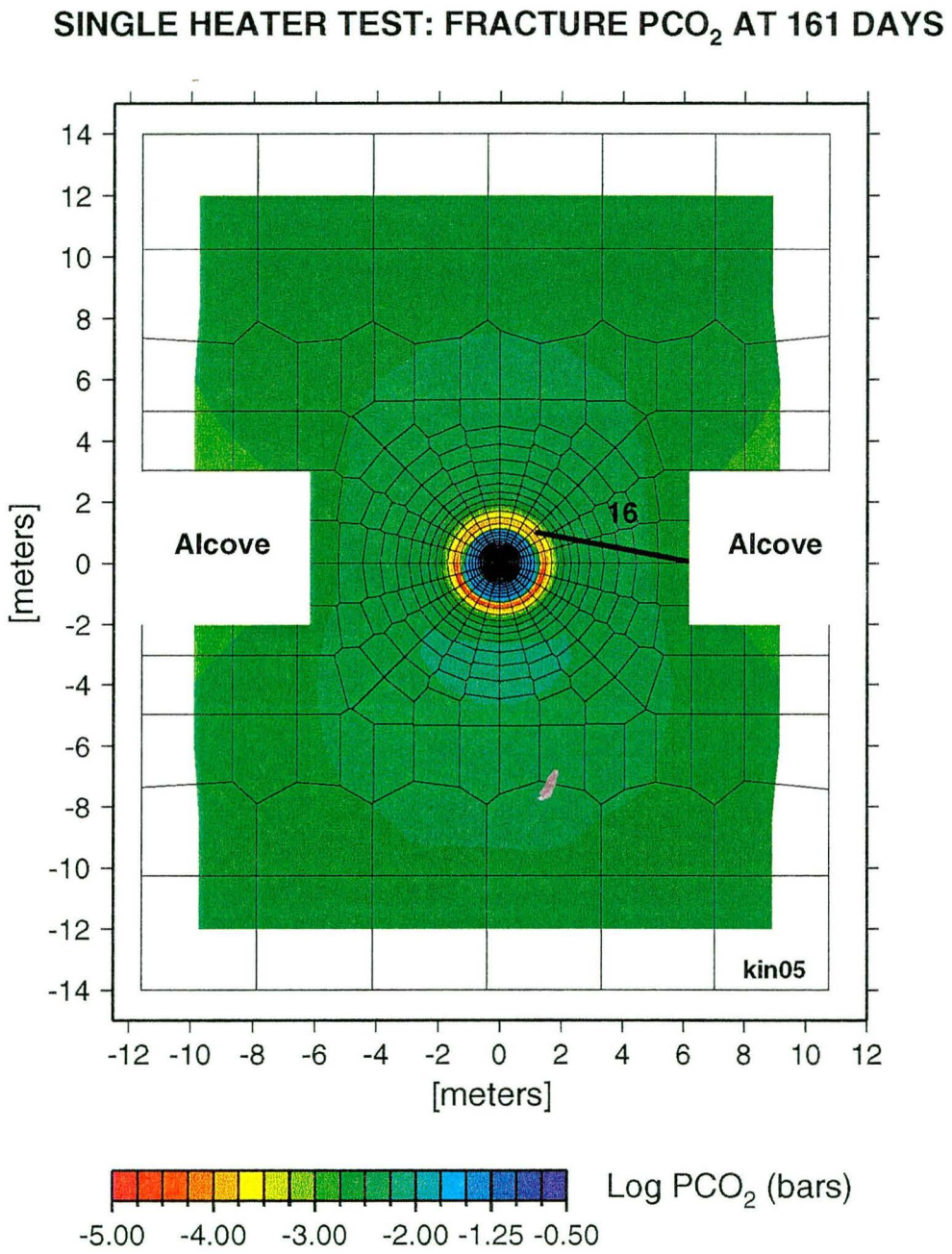

Figure 4-8. Calculated partial pressure of CO_2 in equilibrium with water in fractures after 161 days (simulation kin05).

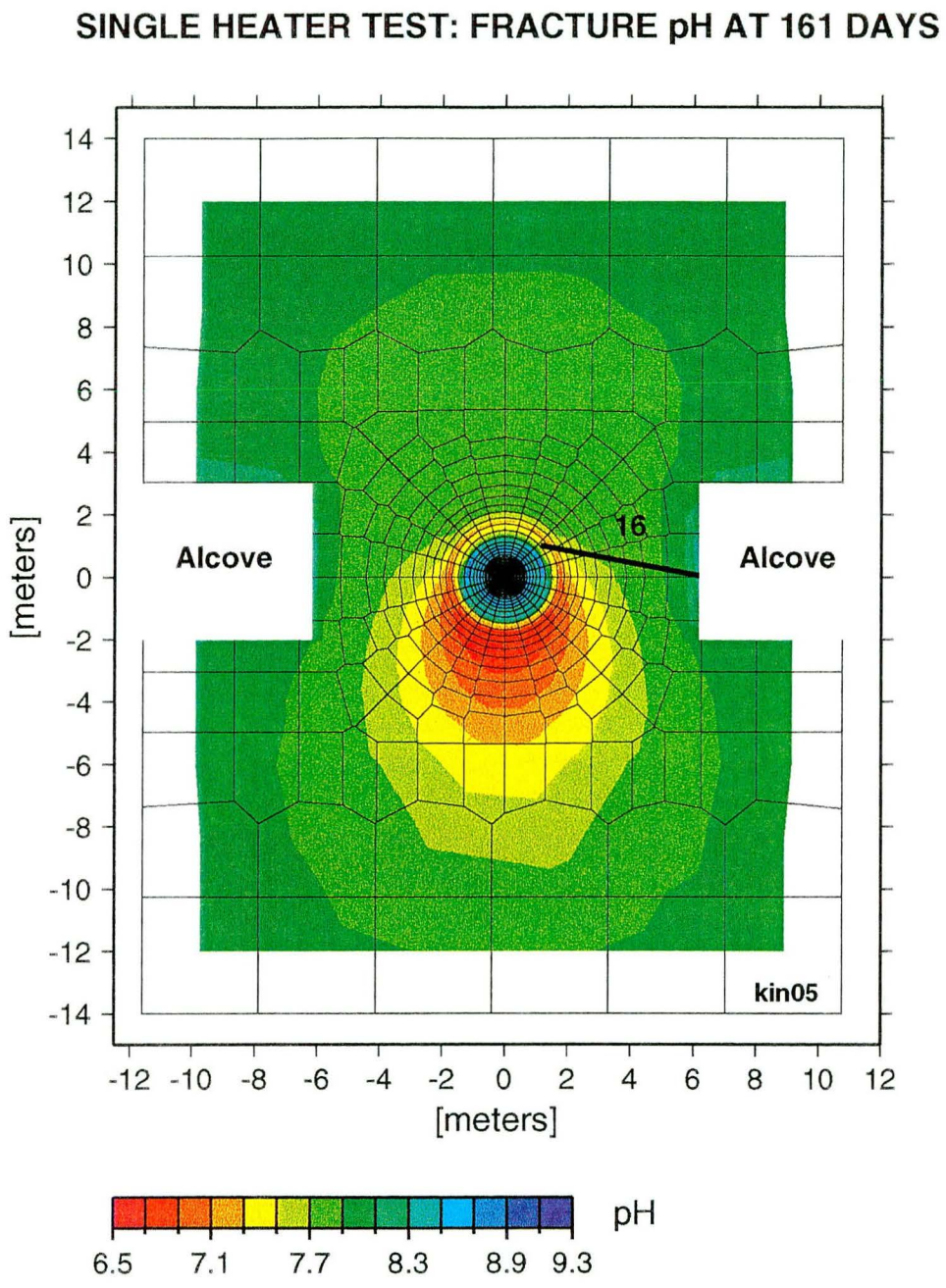

Figure 4-9. Calculated pH in fracture pore waters after 161 days (simulation kin05).

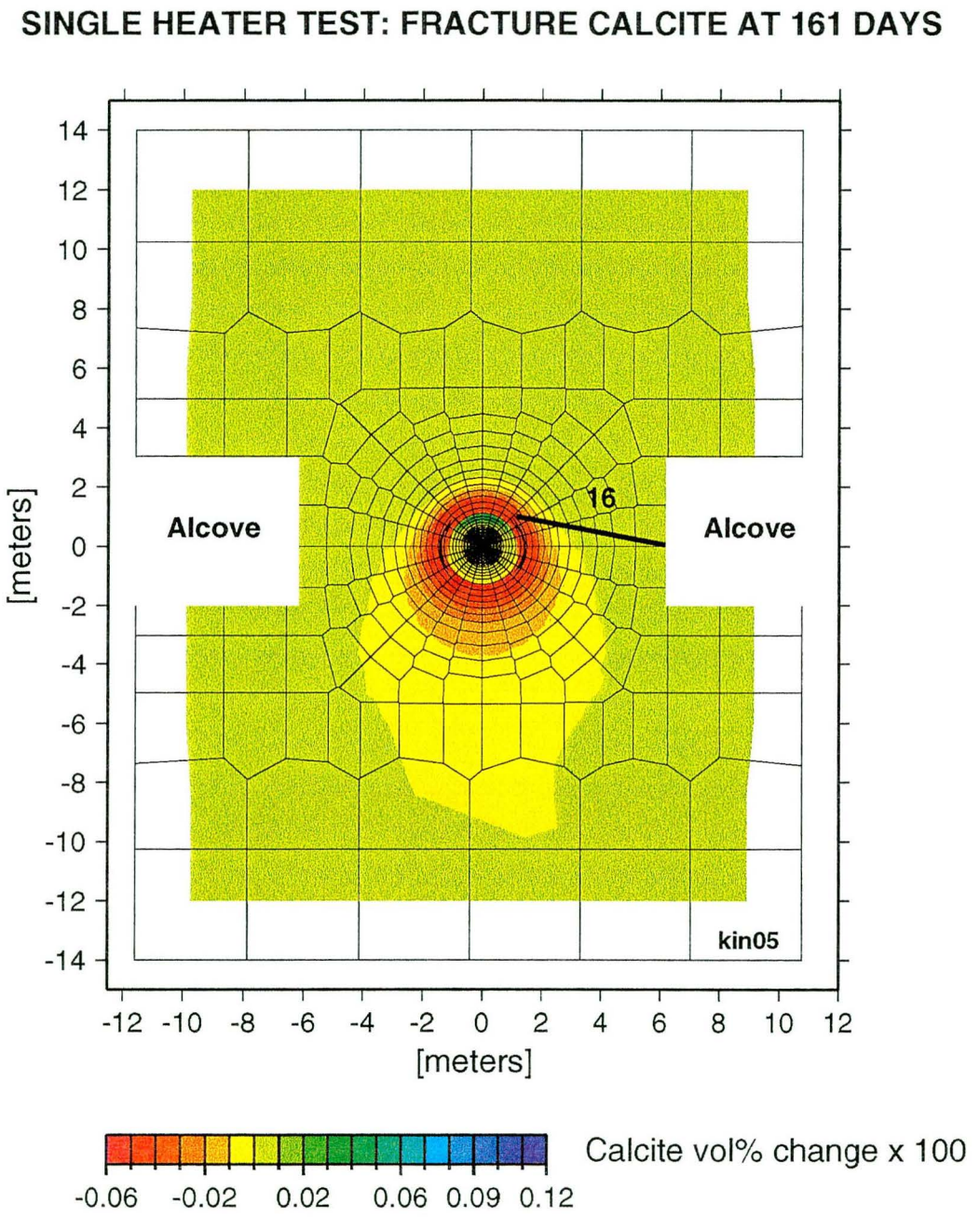

Figure 4-10. Change in calcite volume percent in fractures after 161 days (simulation kin05).

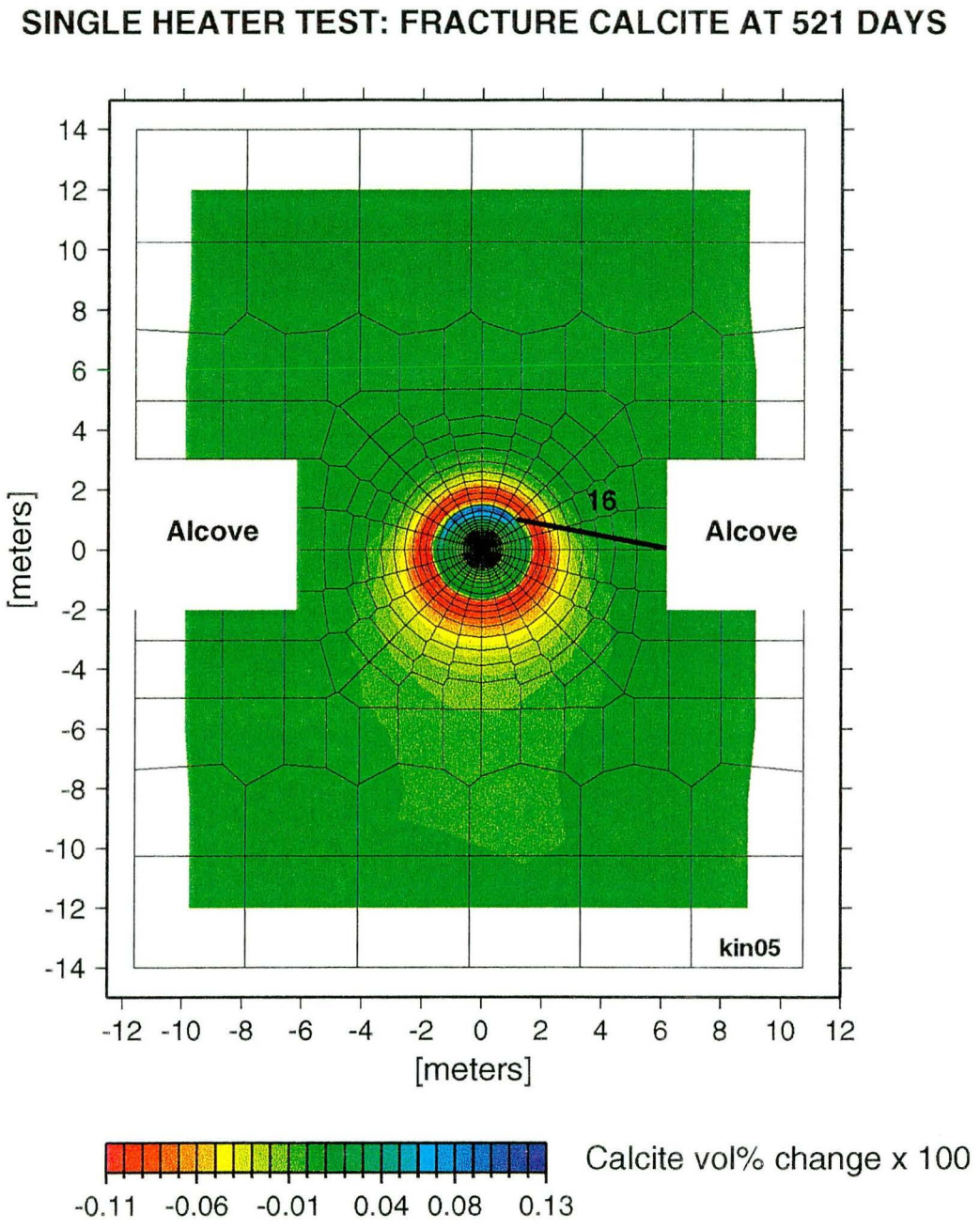

Figure 4-11. Change in calcite volume percent in fractures after 521 days, approximately eight months after the termination of heating (simulation kin05).

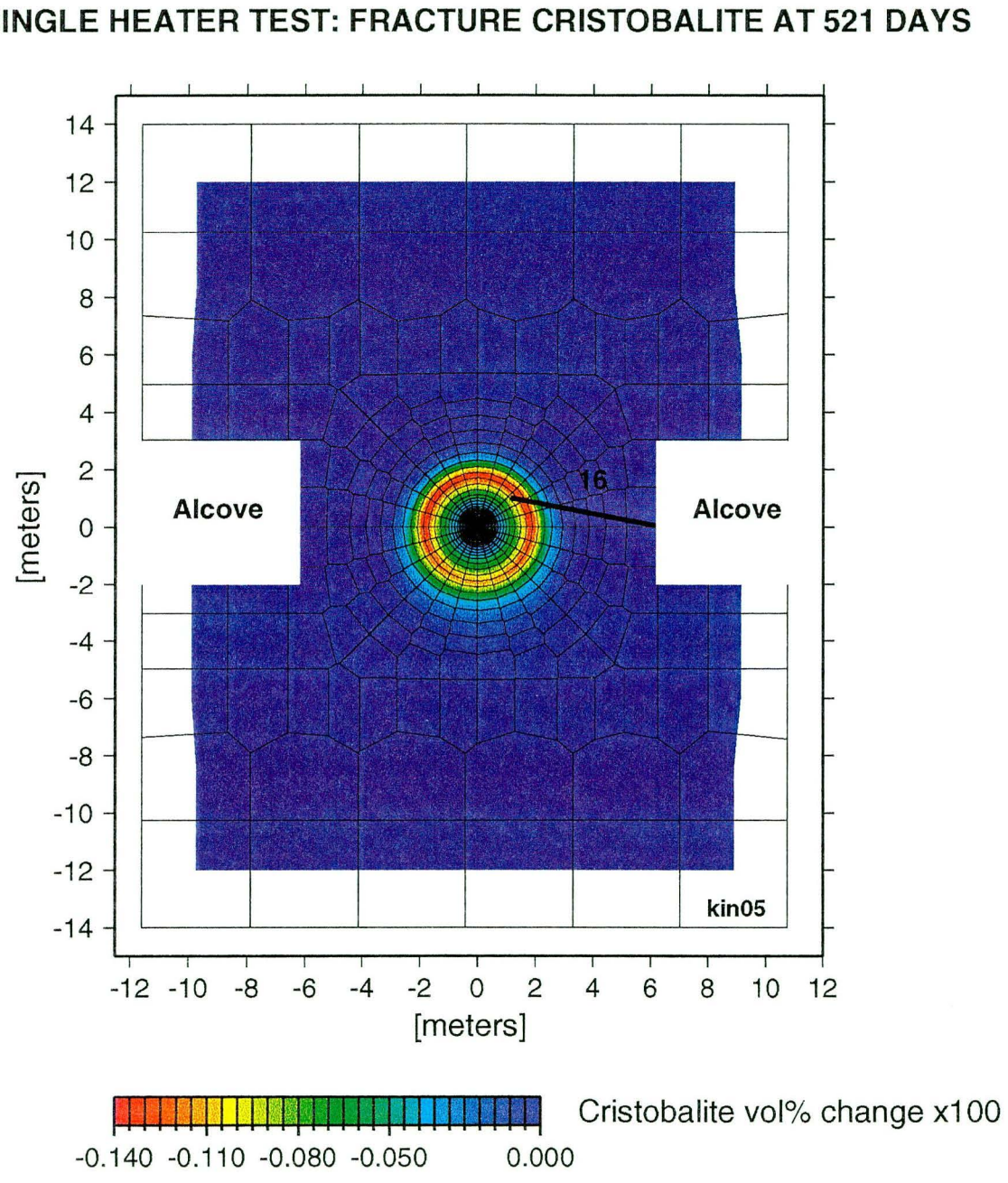

Figure 4-12. Change in cristobalite volume percent in fractures after 521 days (simulation kin05).

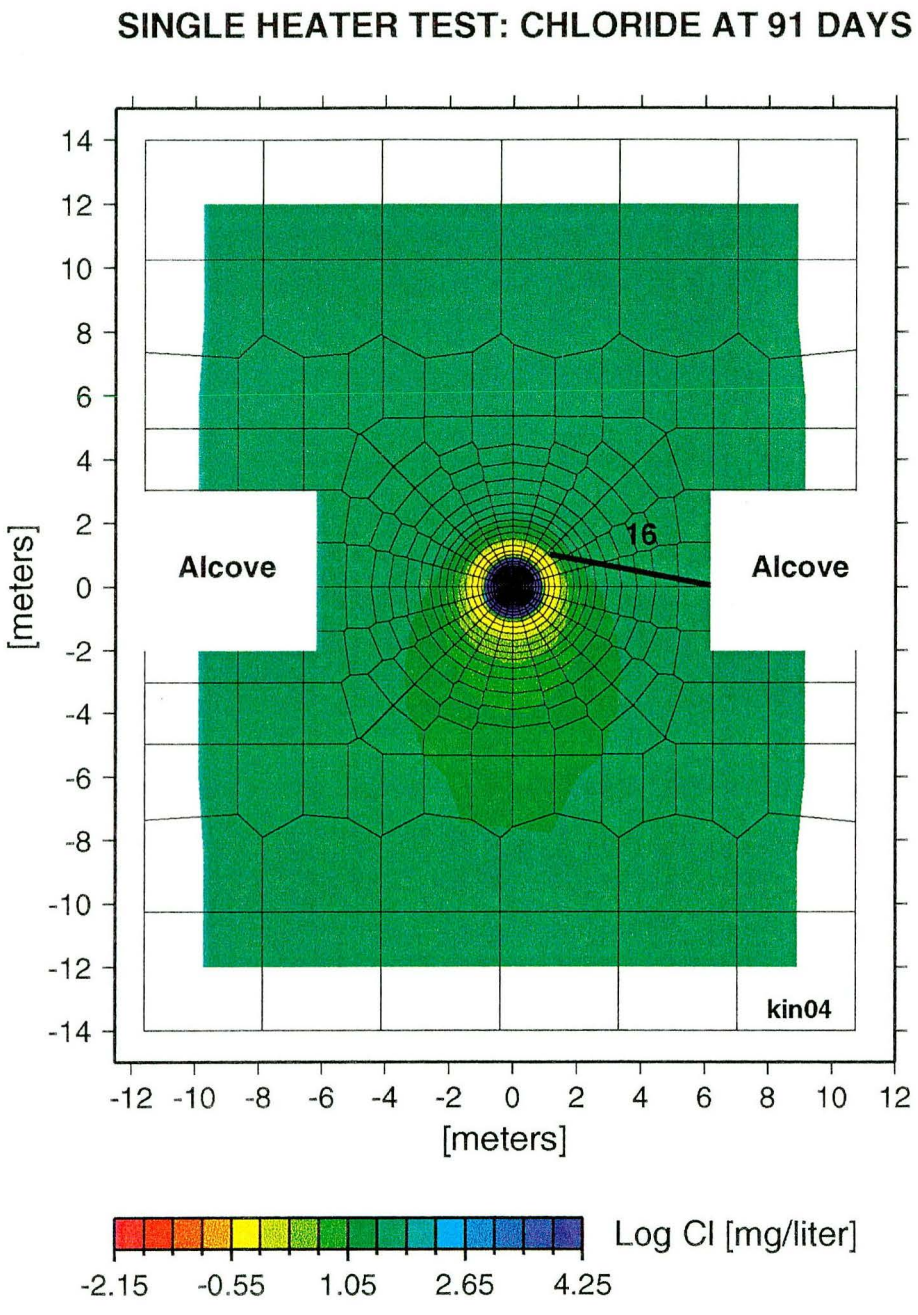

Figure 4-13. Calculated chloride concentration in fracture pore waters after 91 days (simulation kin04).

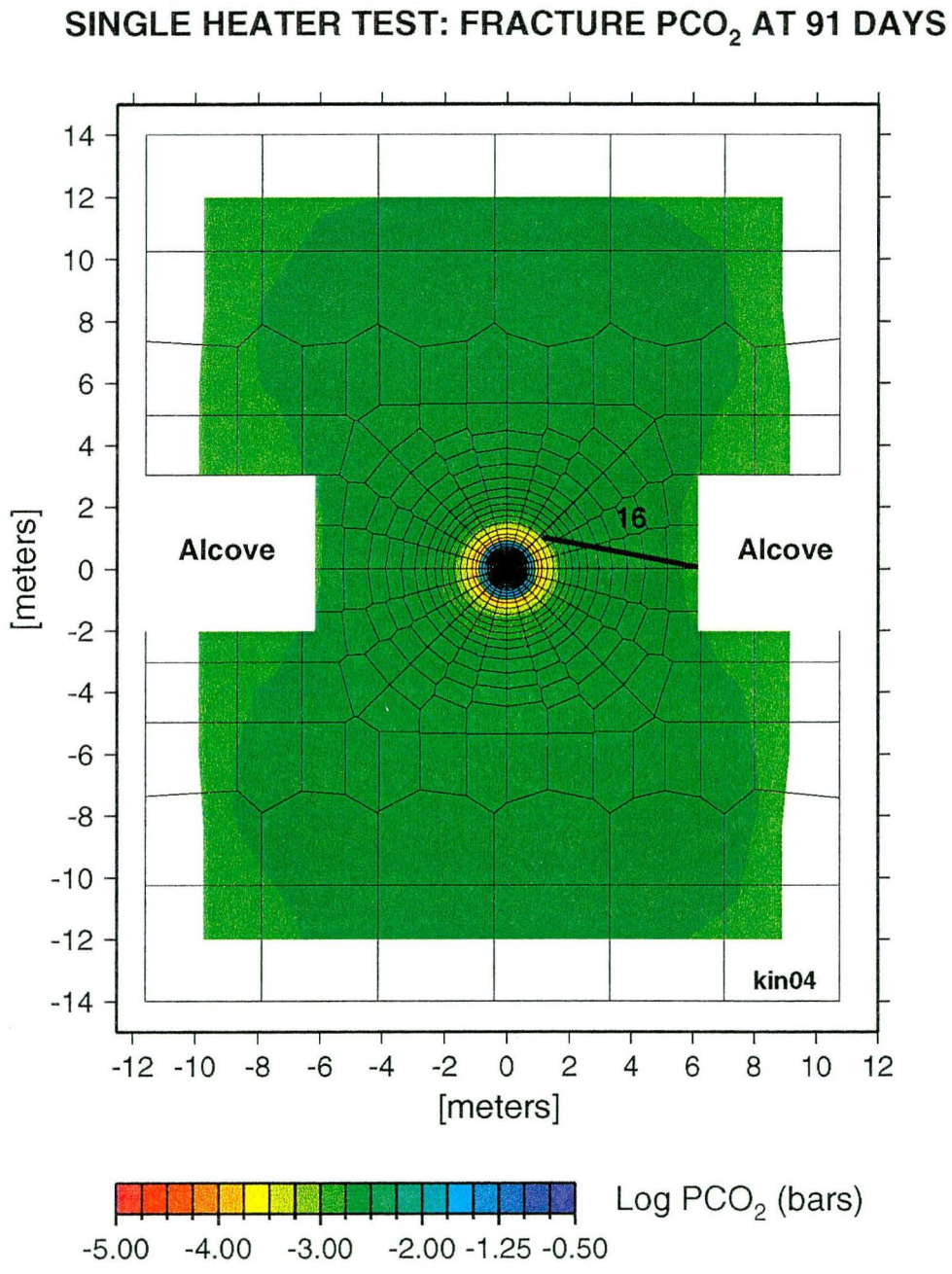

Figure 4-14. Calculated partial pressure of CO_2 in equilibrium with water in fractures after 91 days (simulation kin04).

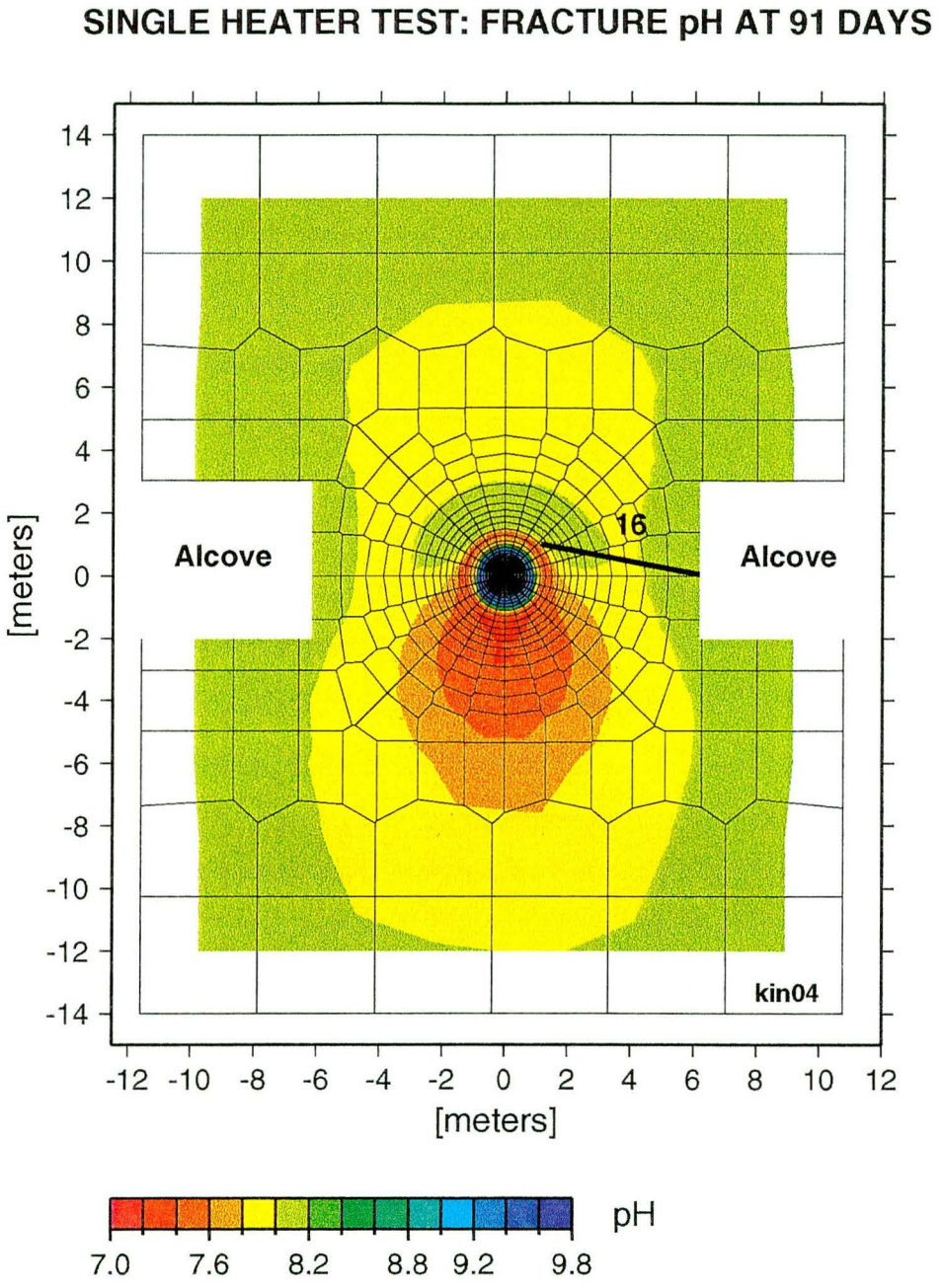

Figure 4-15. Calculated pH in fracture pore waters after 91 days (simulation kin04).

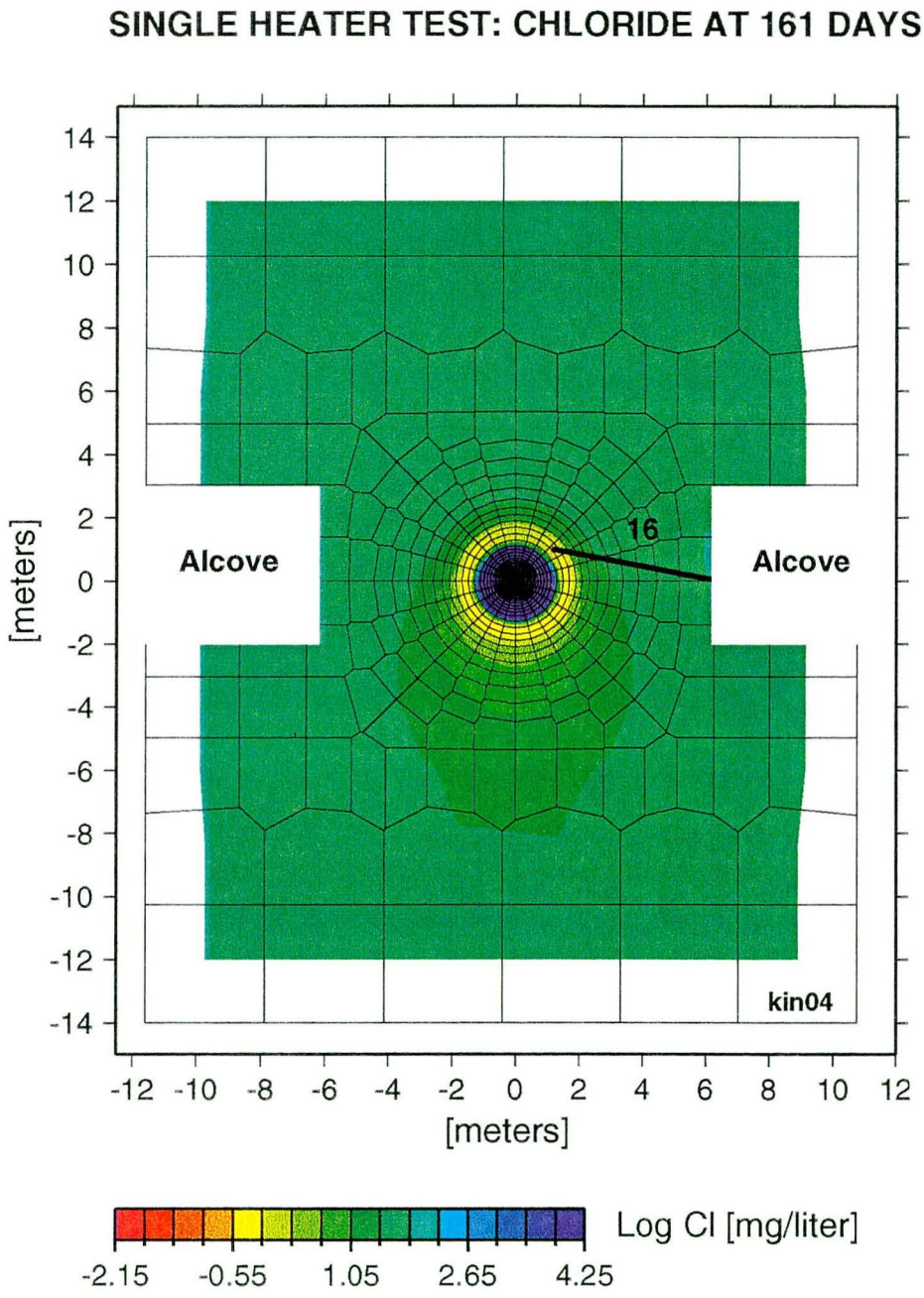

Figure 4-16. Calculated chloride concentration in fracture pore waters after 161 days (simulation kin04).

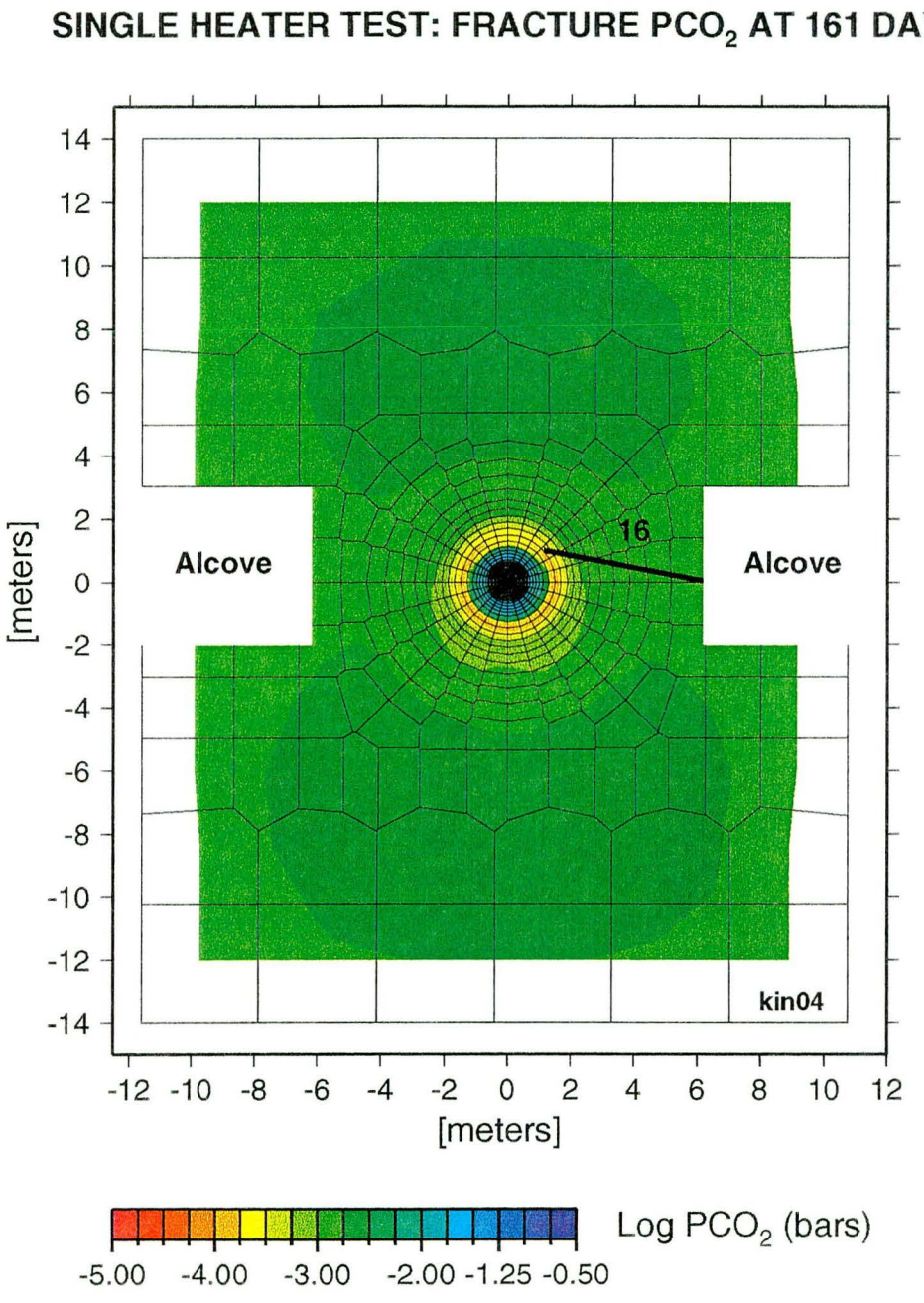

Figure 4-17. Calculated partial pressure of CO_2 in equilibrium with water in fractures after 161 days (simulation kin04).

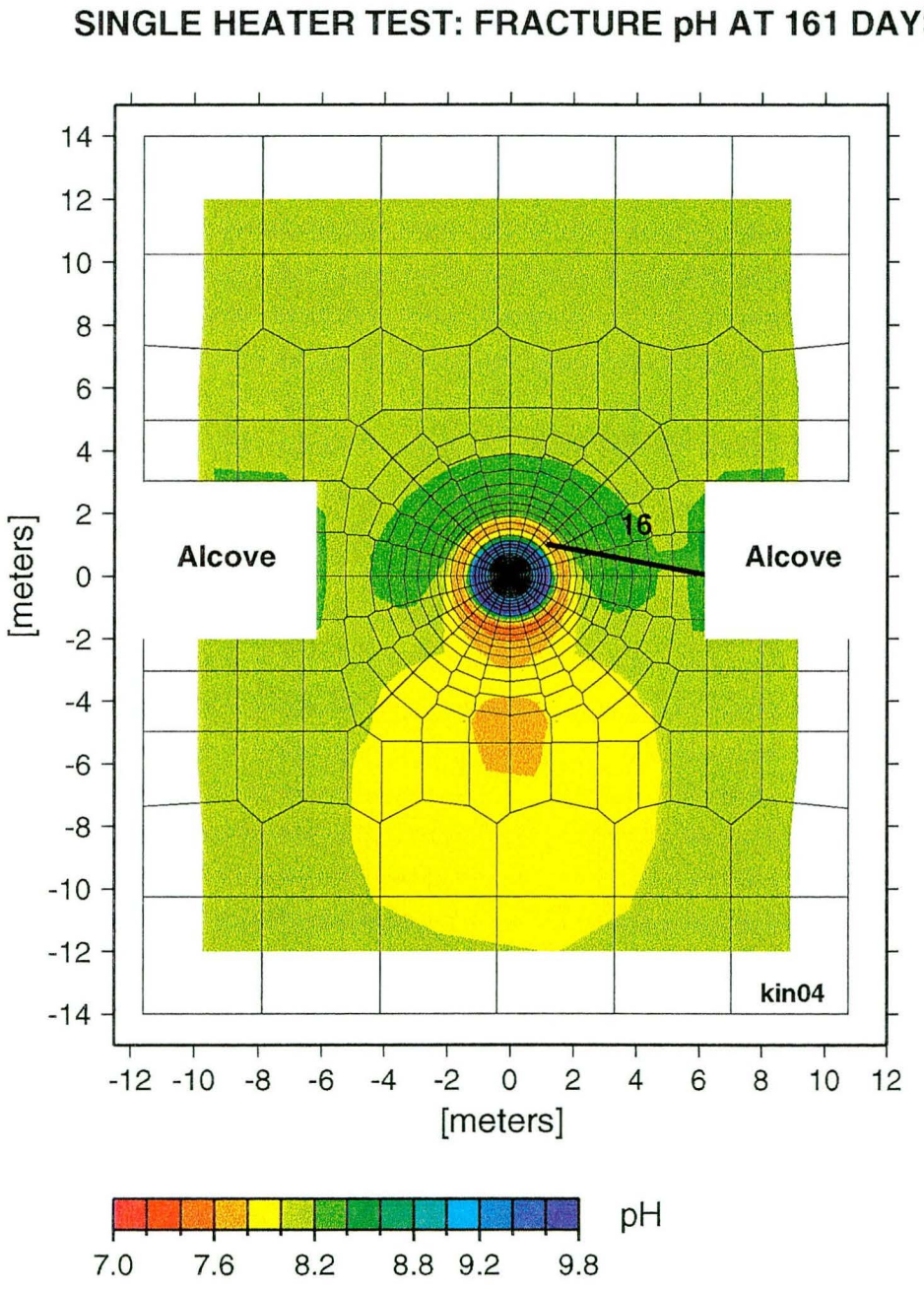

Figure 4-18. Calculated pH in fracture pore waters after 161 days (simulation kin04).

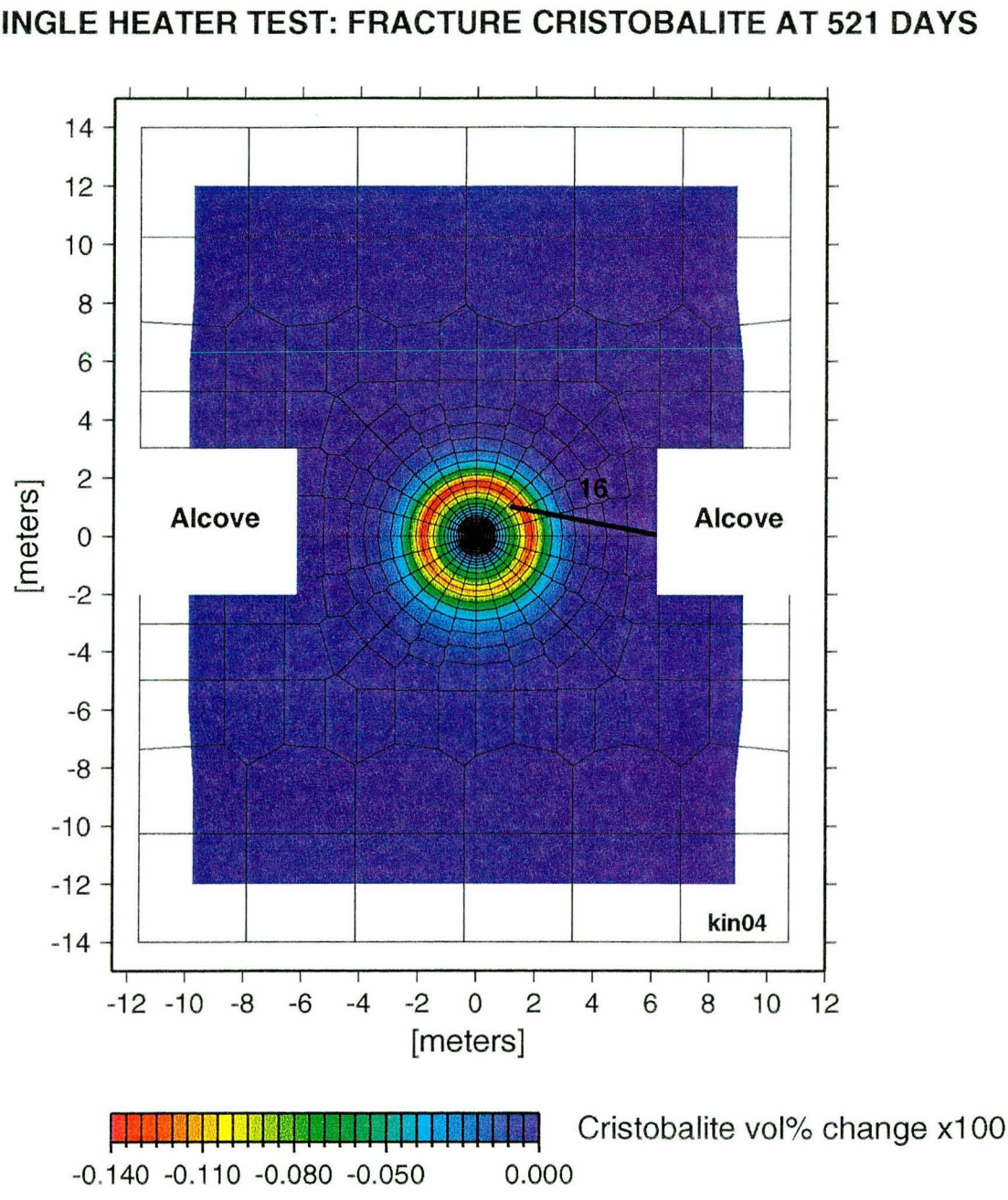

Figure 4-19. Change in cristobalite volume percent in fractures after 521 days, approximately seven months after the termination of heating (simulation kin04).

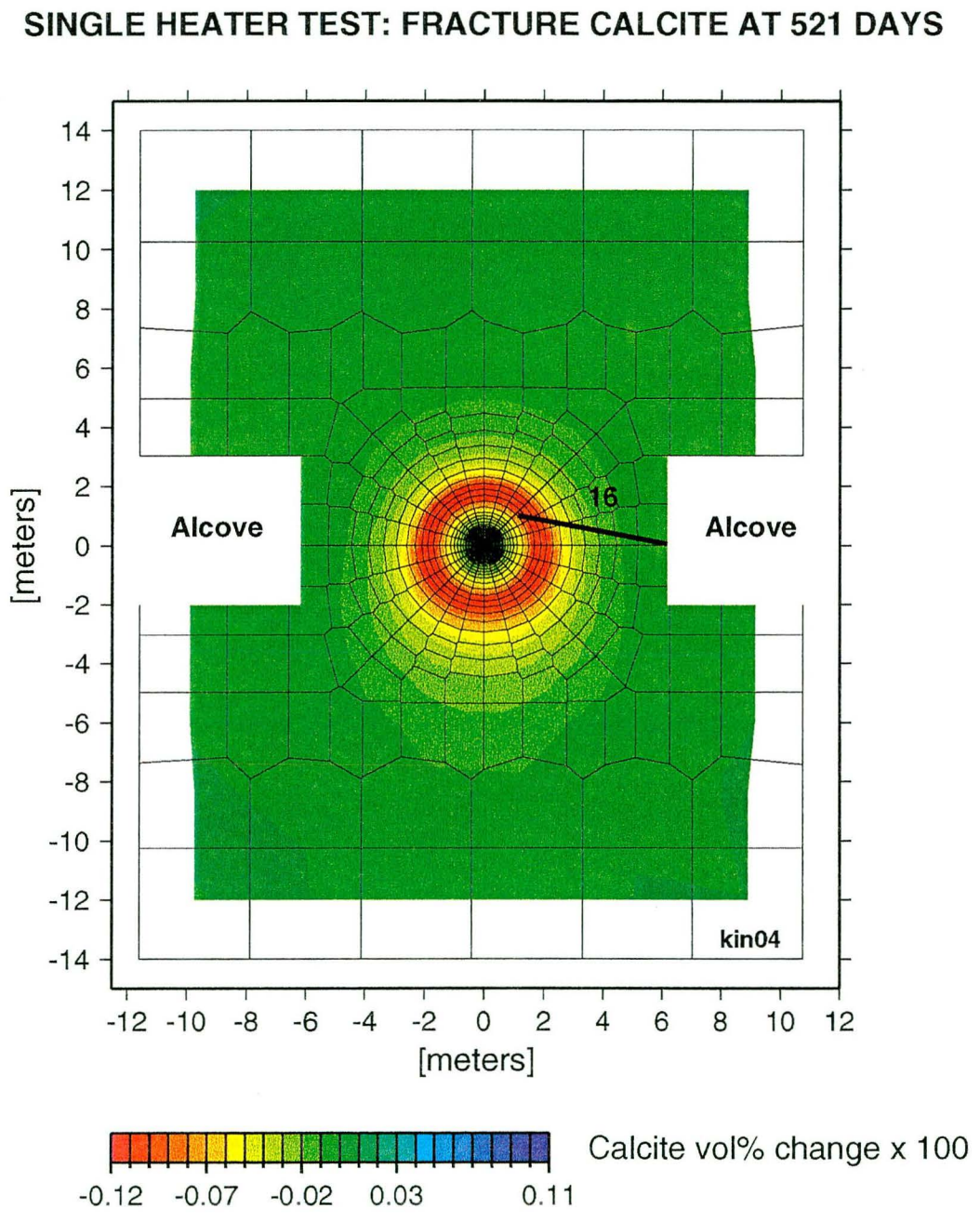

Figure 4-20. Change in calcite volume percent in fractures after 521 days (simulation kin04).

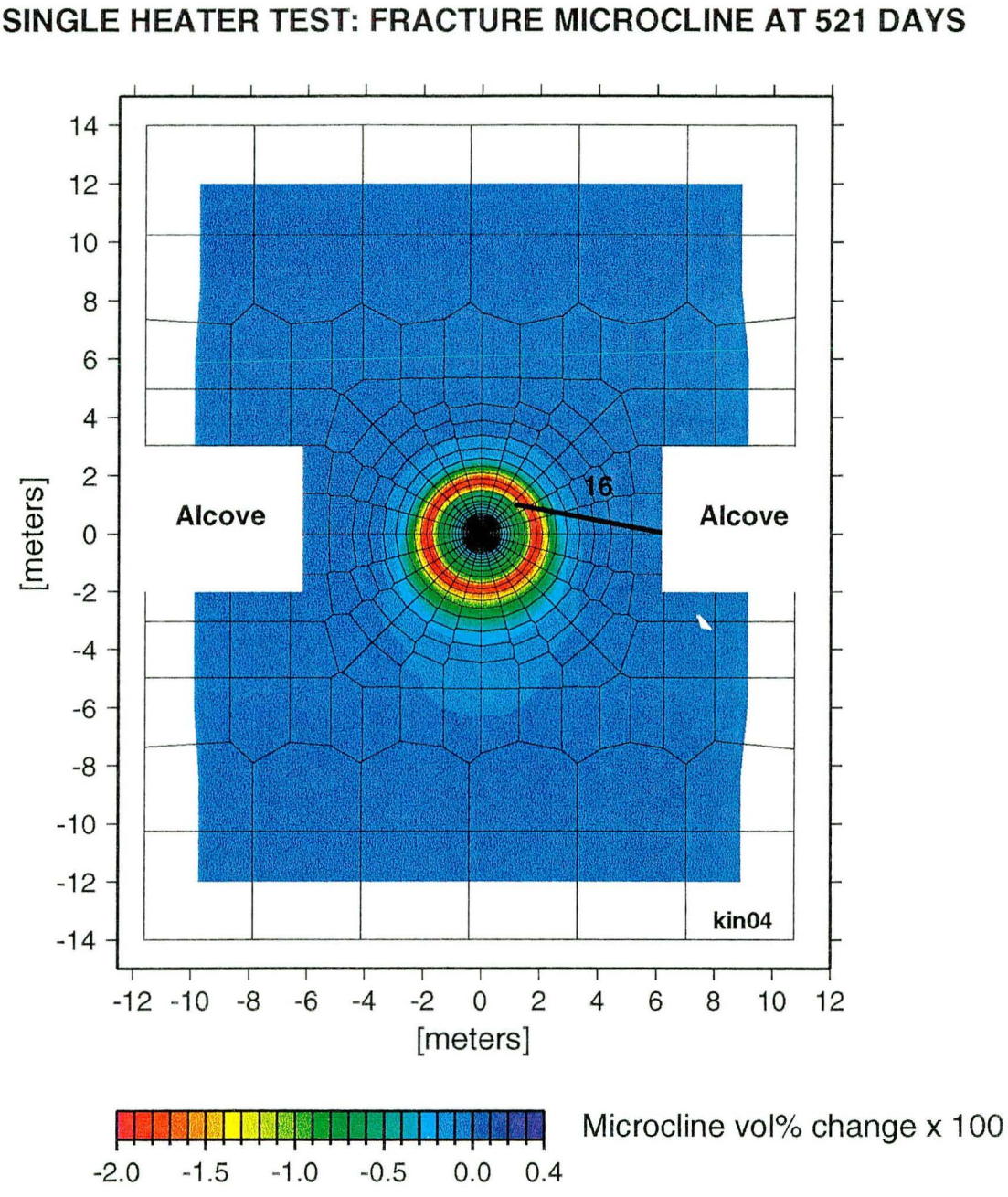

Figure 4-21. Change in microcline (K-feldspar) volume percent in fractures after 521 days (simulation kin04).

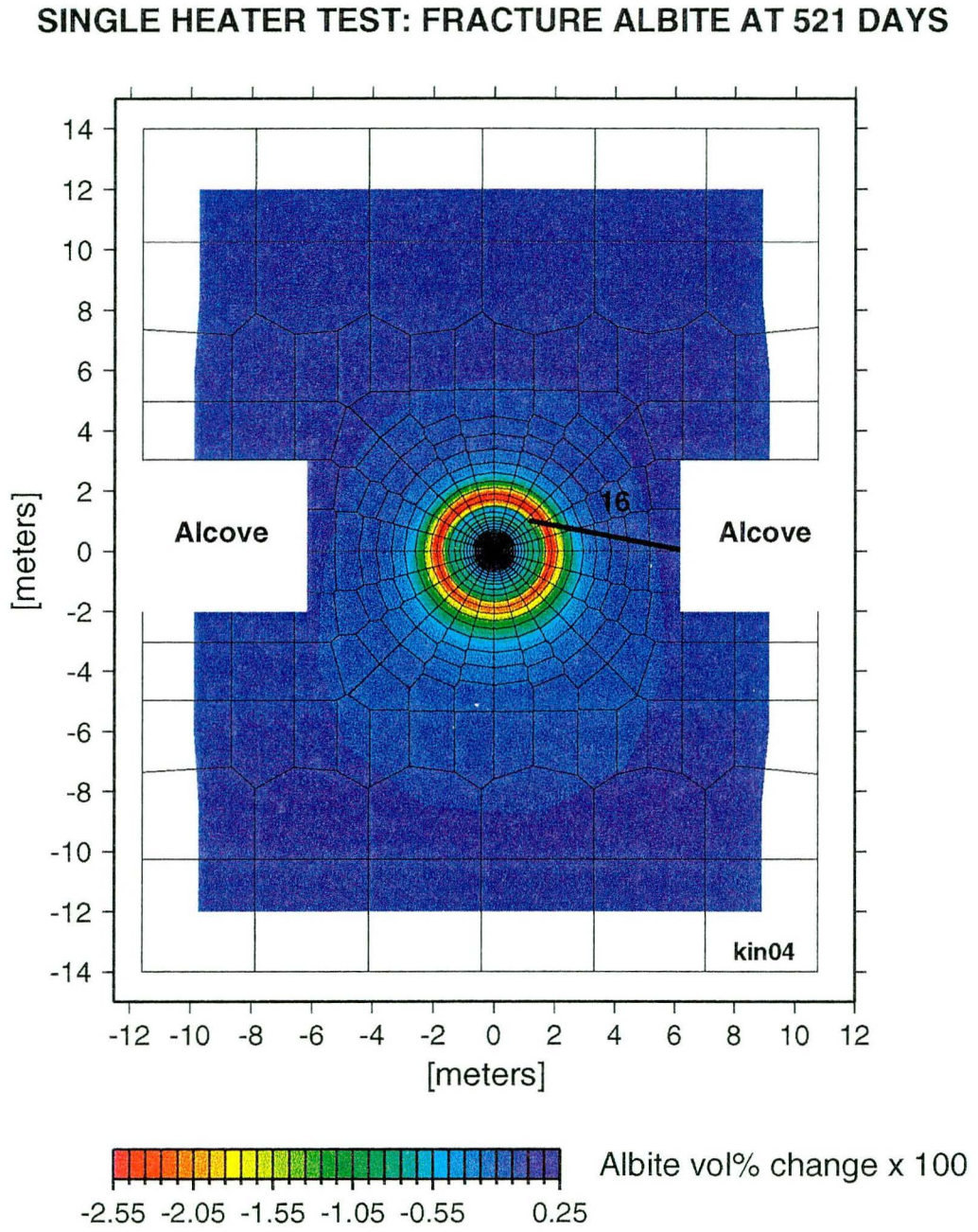

Figure 4-22. Change in albite (Na-feldspar) volume percent in fractures after 521 days (simulation kin04).

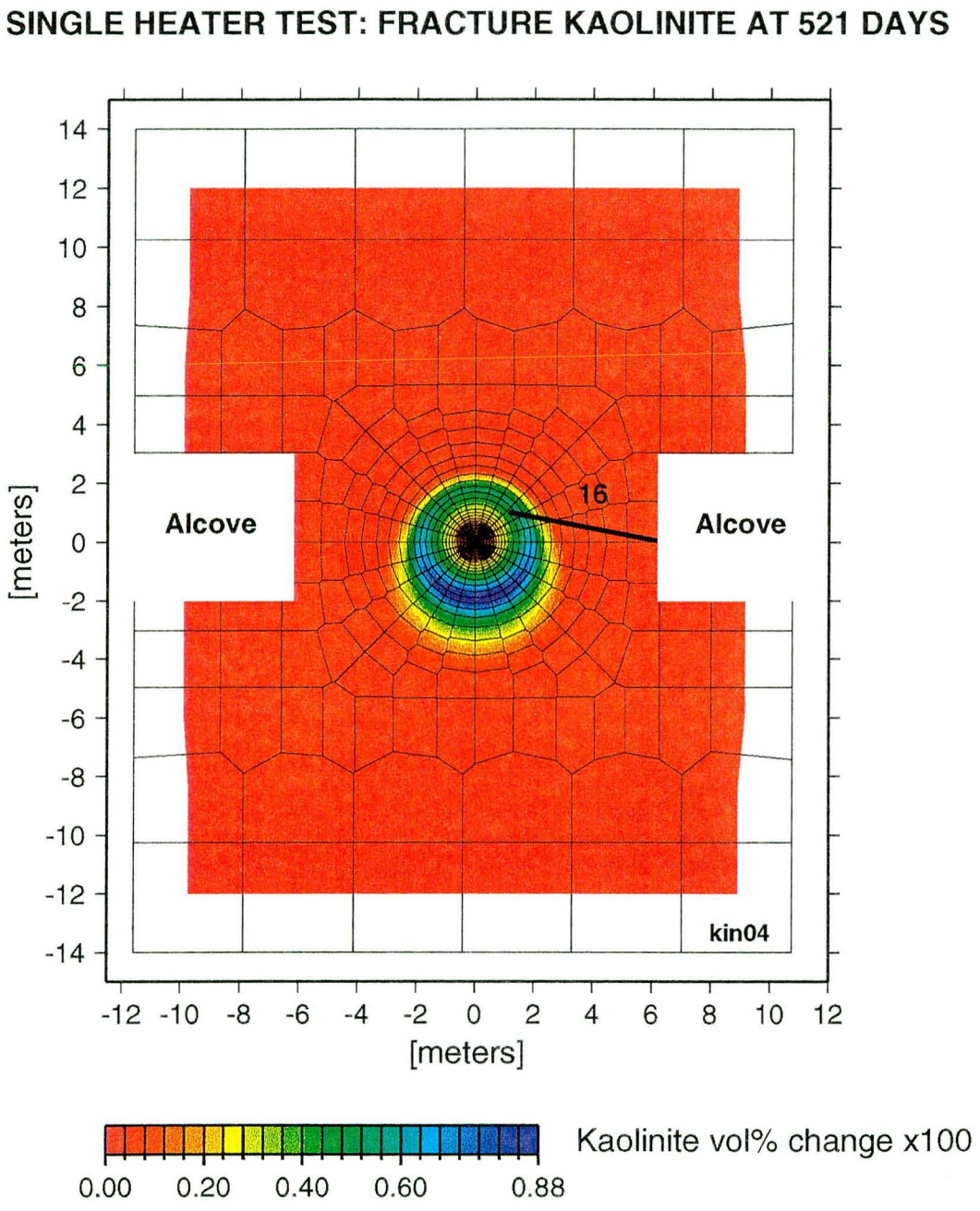

Figure 4-23. Change in kaolinite volume percent in fractures after 521 days (simulation kin04).

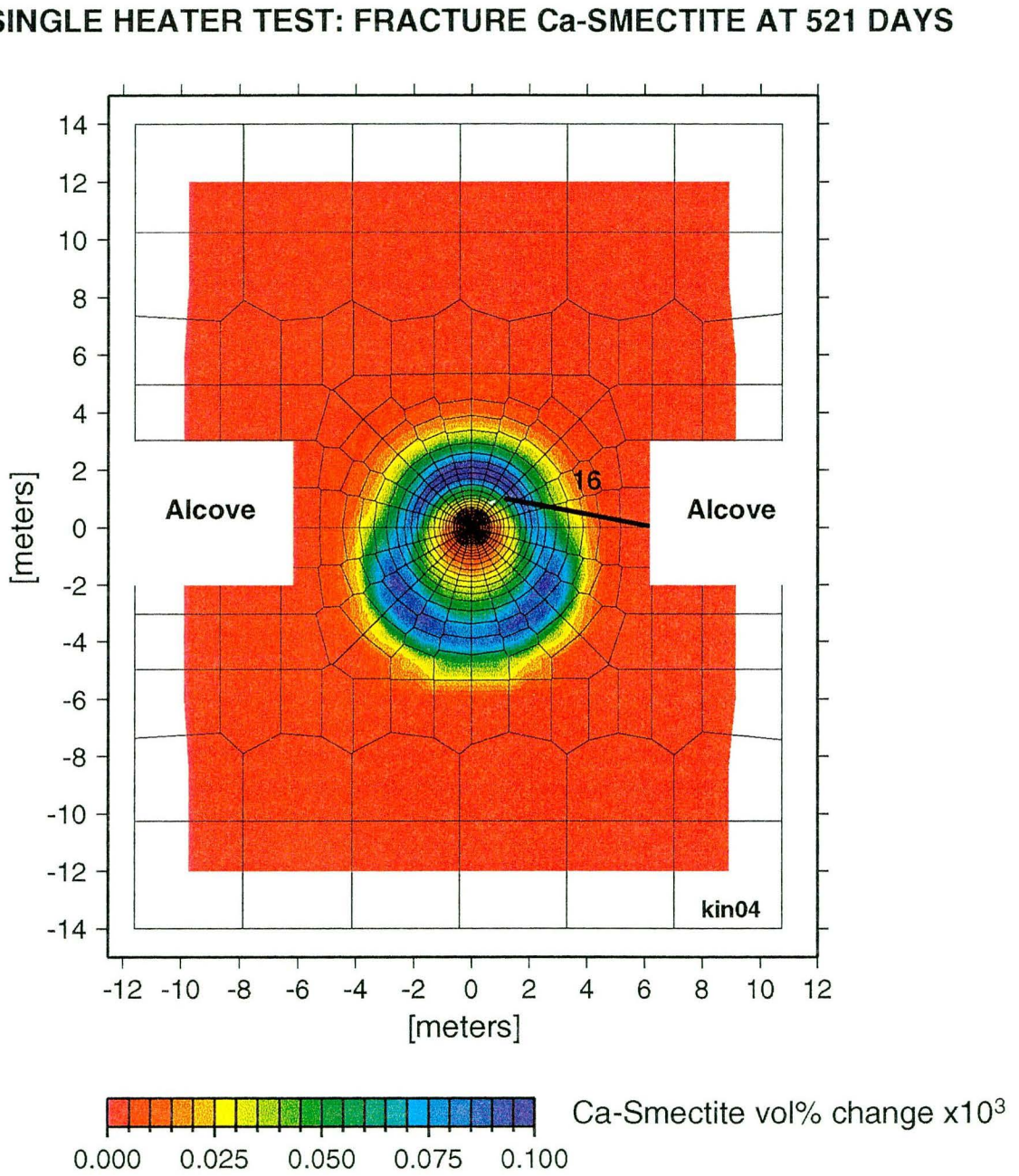

Figure 4-24. Change in Ca-smectite volume percent in fractures after 521 days (simulation kin04).

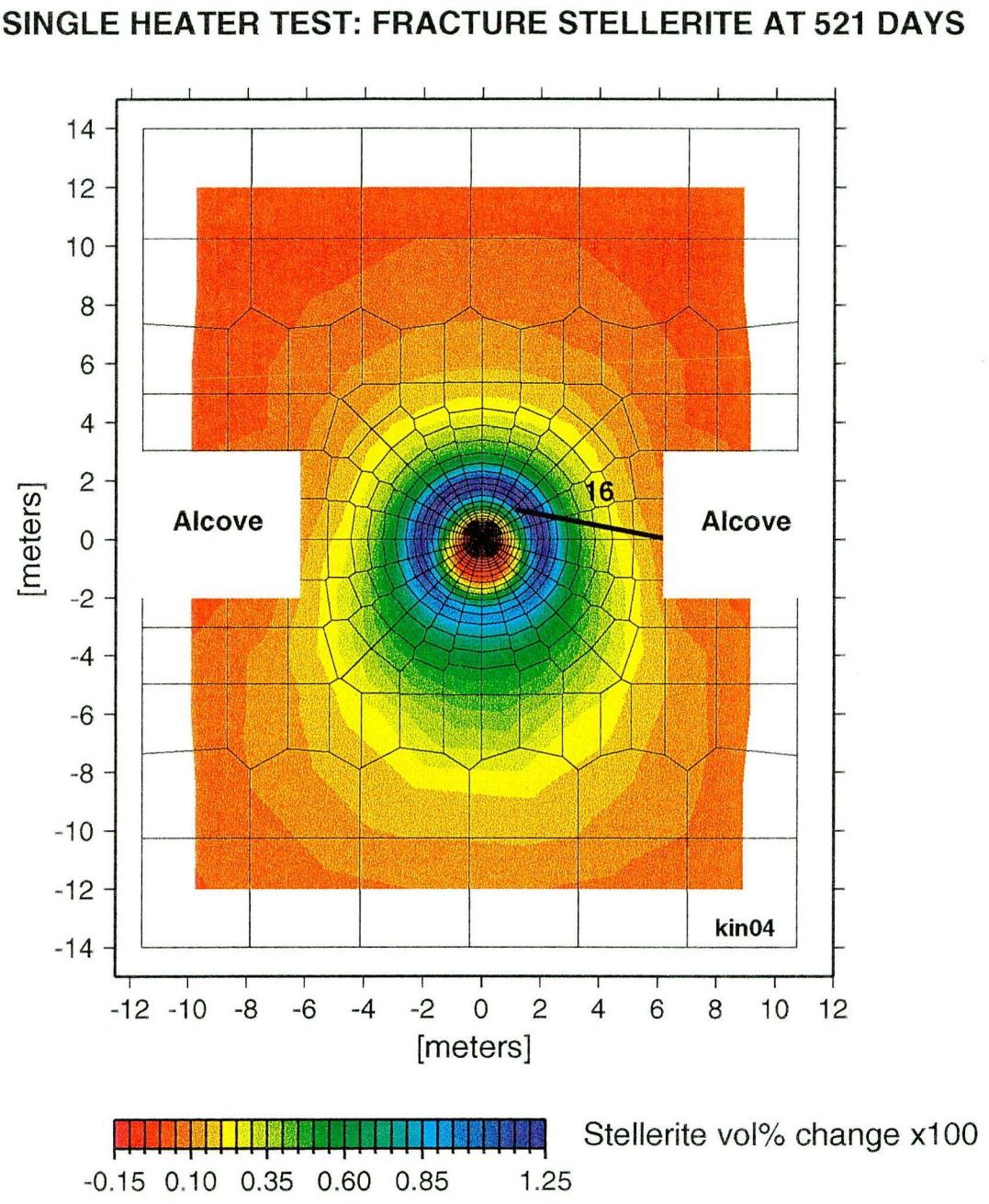

Figure 4-25. Change in stellerite (zeolite) volume percent in fractures after 521 days (simulation kin04).

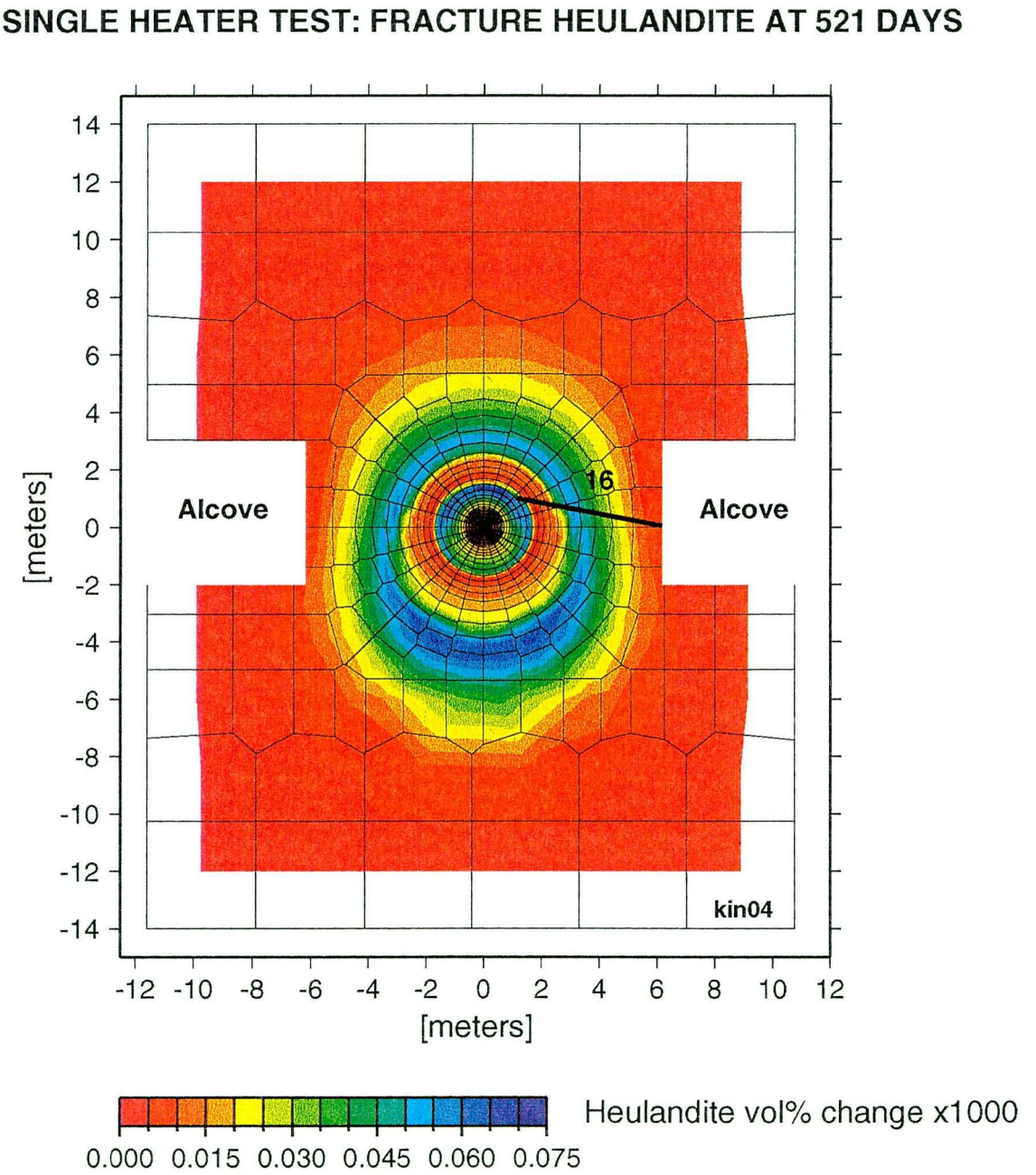

Figure 4-26. Change in heulandite (zeolite) volume percent in fractures after 521 days (simulation kin04).

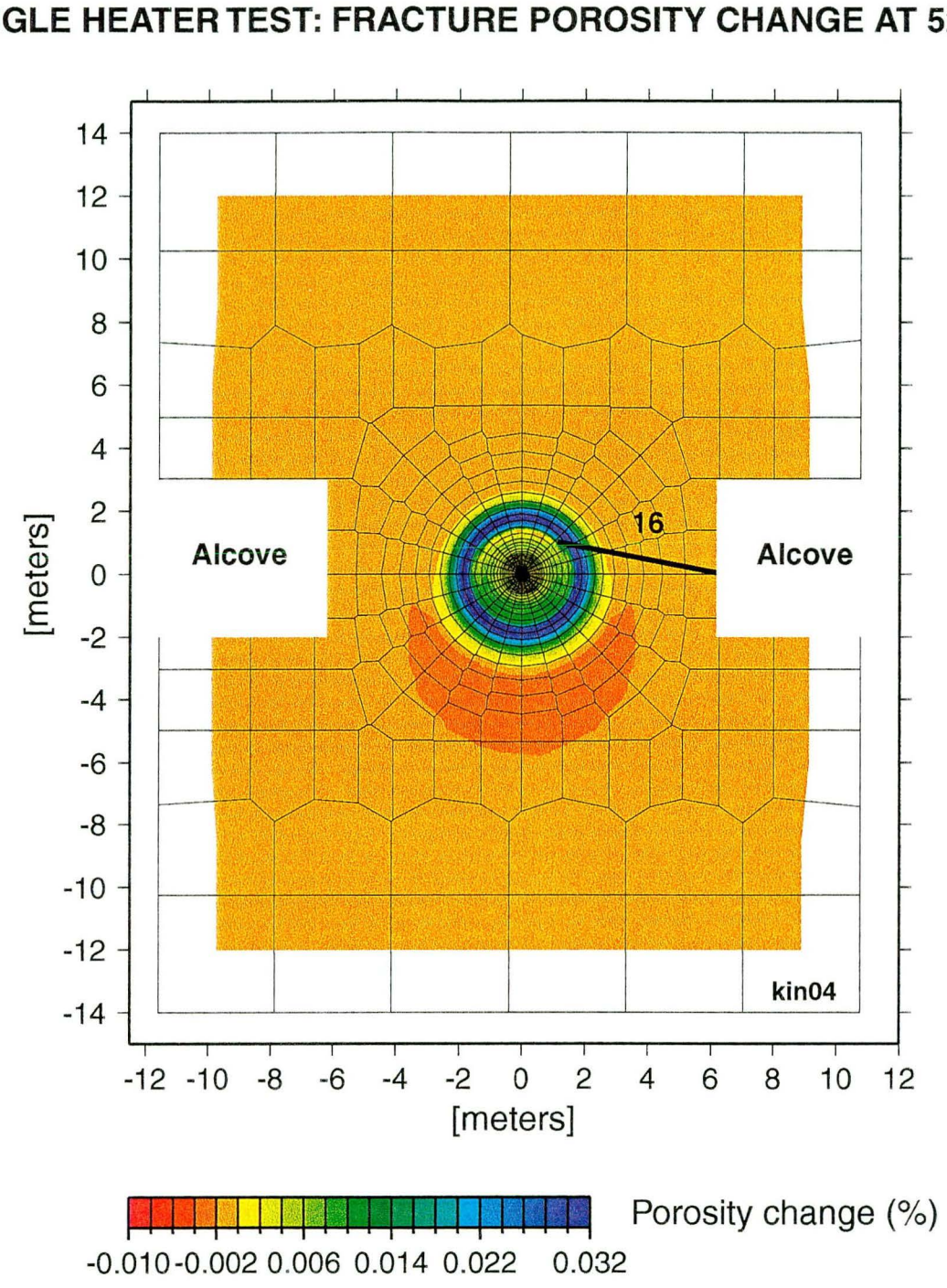

Figure 4-27 Change in fracture porosity (percent) after 521 days (simulation kin04).

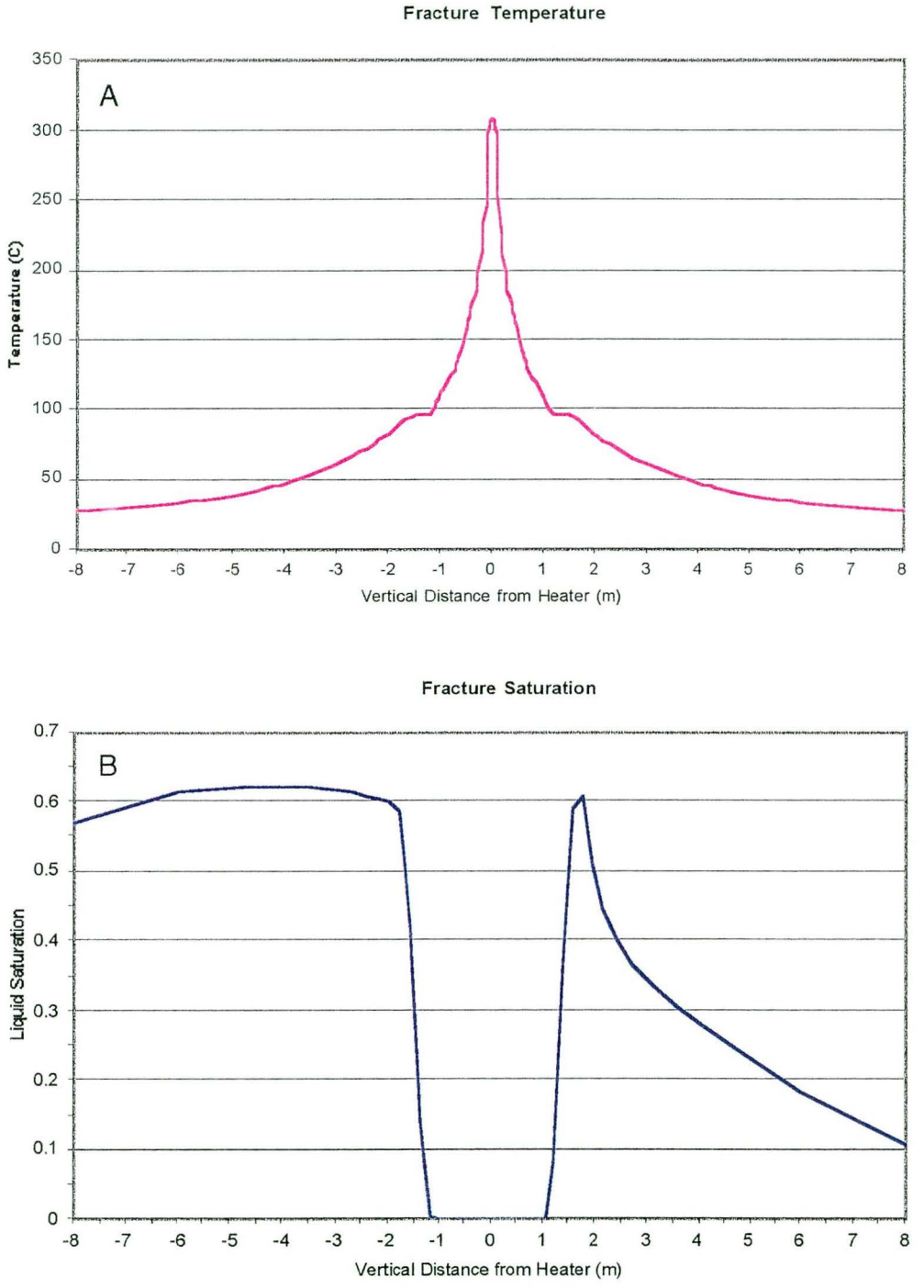

Figure 4-28. (a) Temperature in fractures (b) and liquid saturation in fractures at 161 days. Computed profiles through the heater at the location shown on Figure 4-3. Simulation with aluminosilicates (kin04).

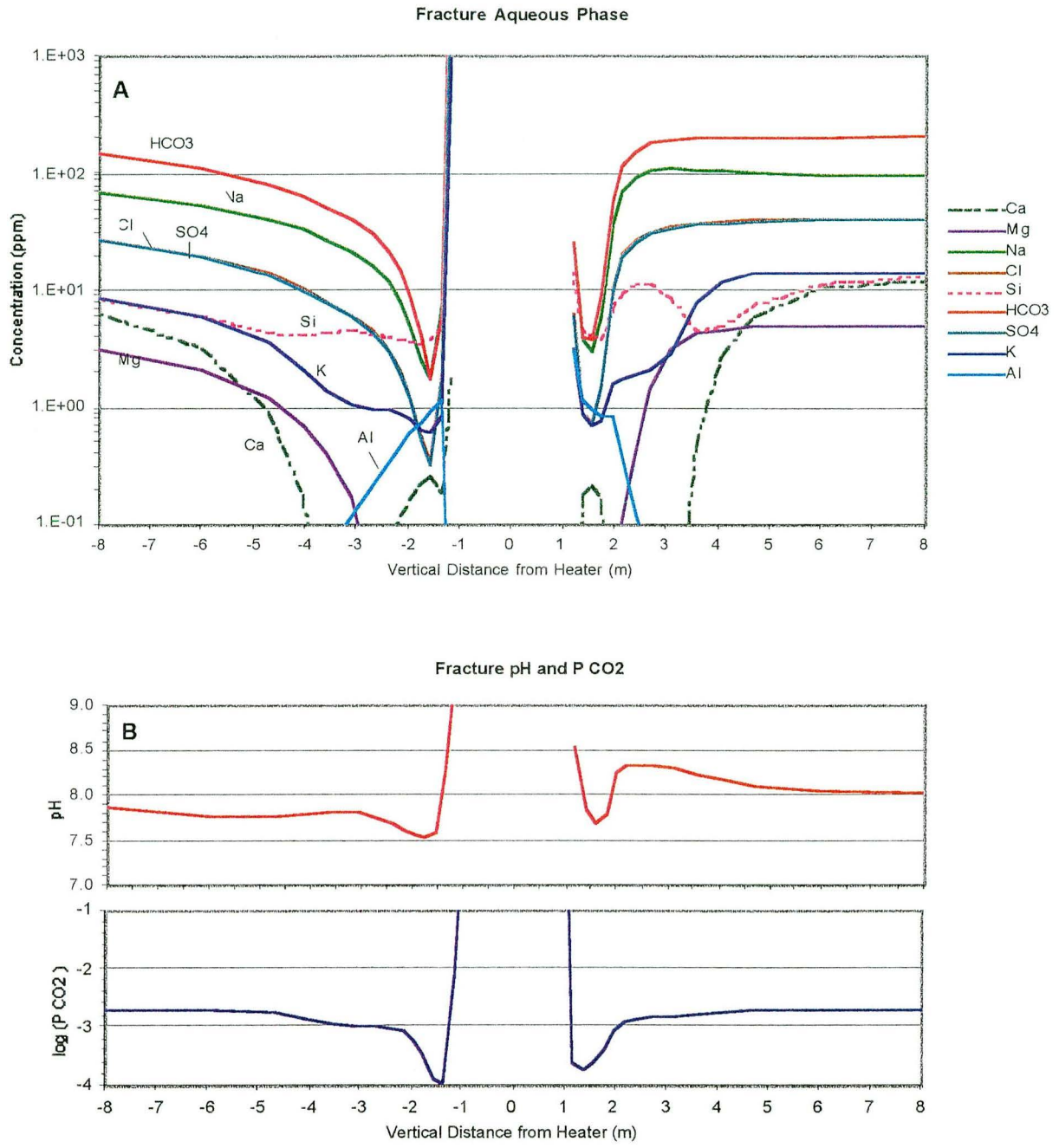

Figure 4-29. (a) Concentrations of aqueous species and (b) pH and CO_2 partial pressure (bars) in fractures at 161 days. Computed profiles through the heater at the location shown on Figure 4-3. Simulation with aluminosilicates (kin04).

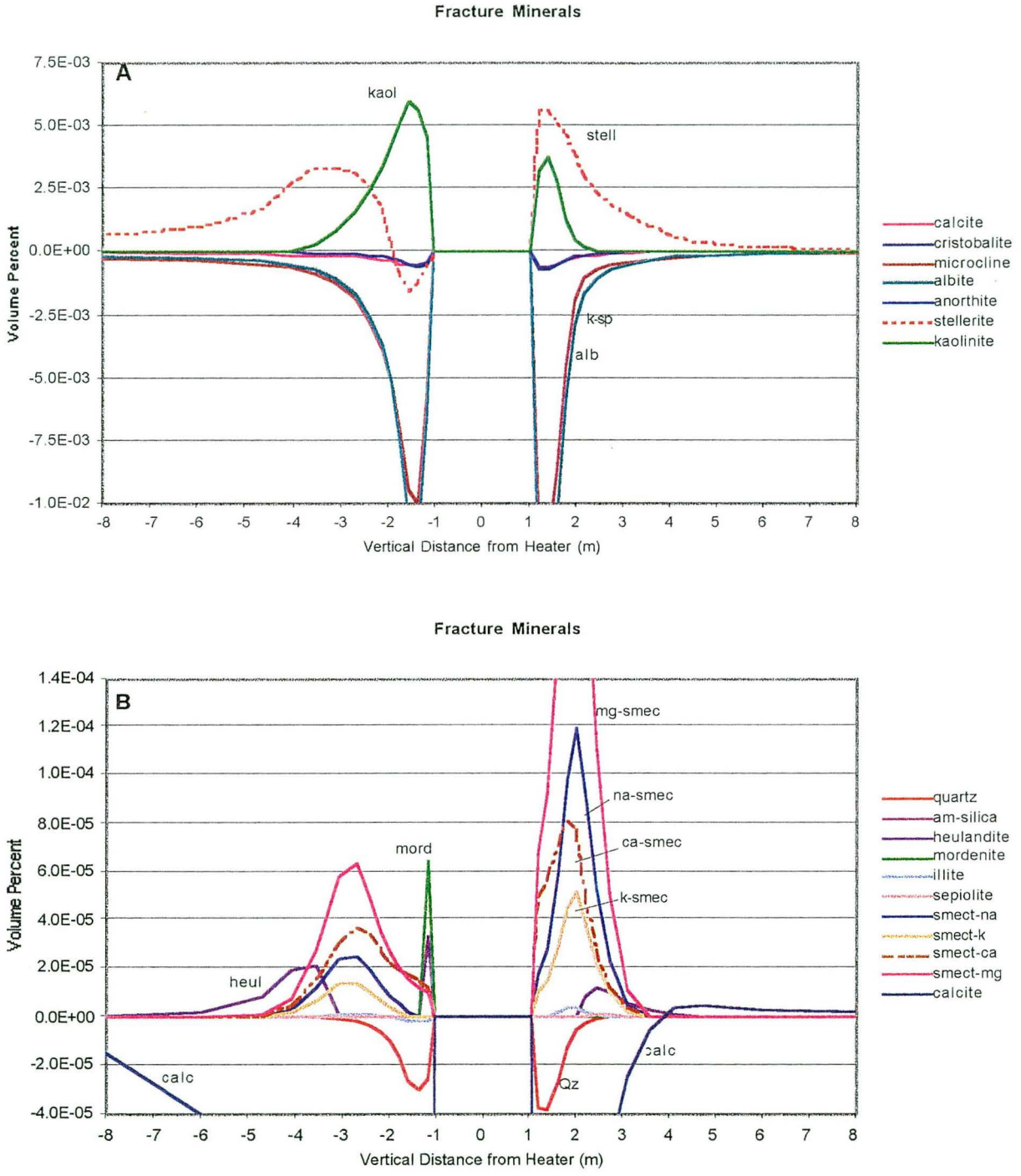

Figure 4-30. Change in mineral volume percent in fractures, at 161 days (a and b). Computed profiles through the heater at the location shown on Figure 4-3. Simulation with aluminosilicates (kin04).

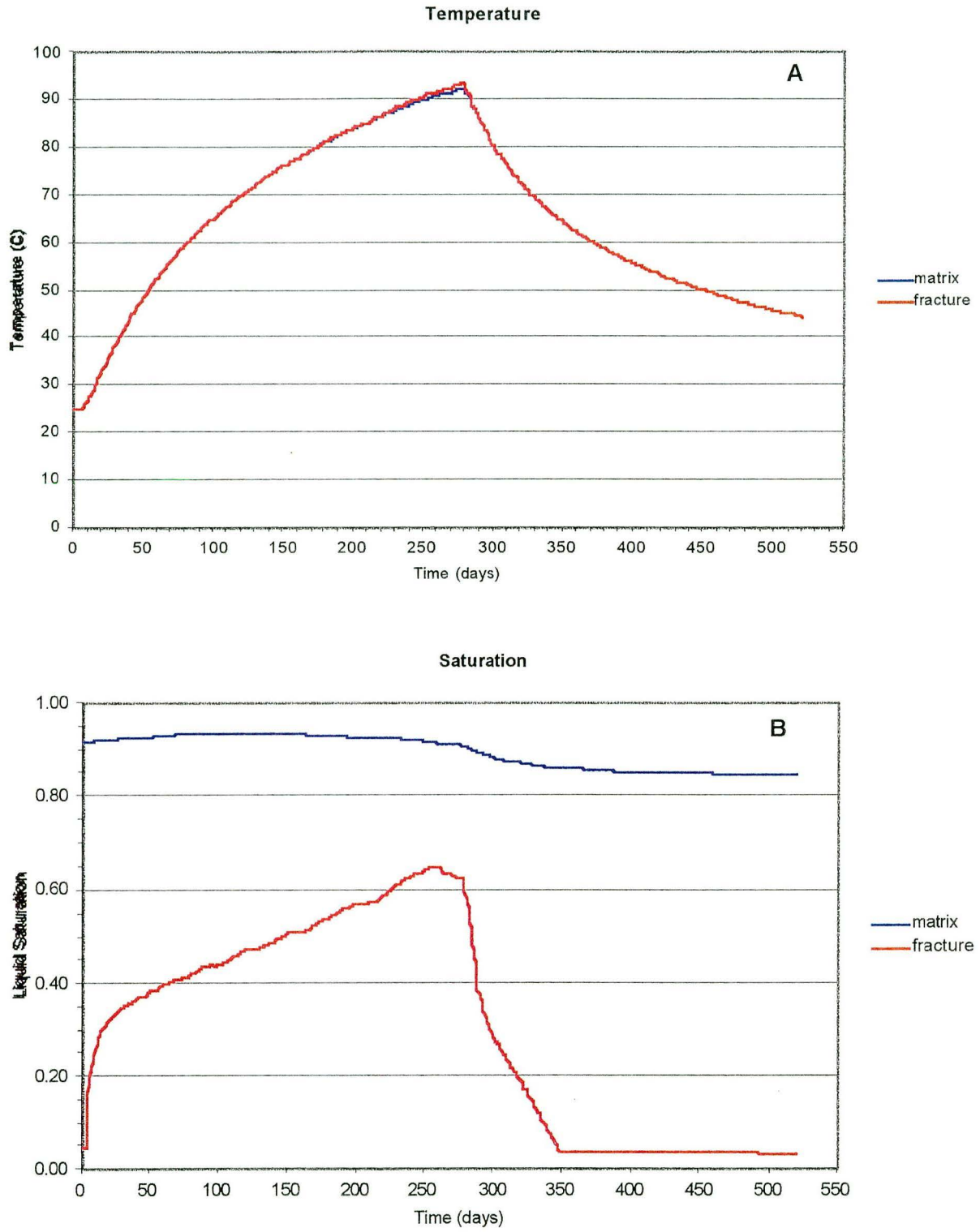

Figure 4-31. Time profiles of (a) temperature and (b) liquid saturation in fractures and matrix, computed at a point shown on Figure 4-3. Simulation with aluminosilicates (kin04).

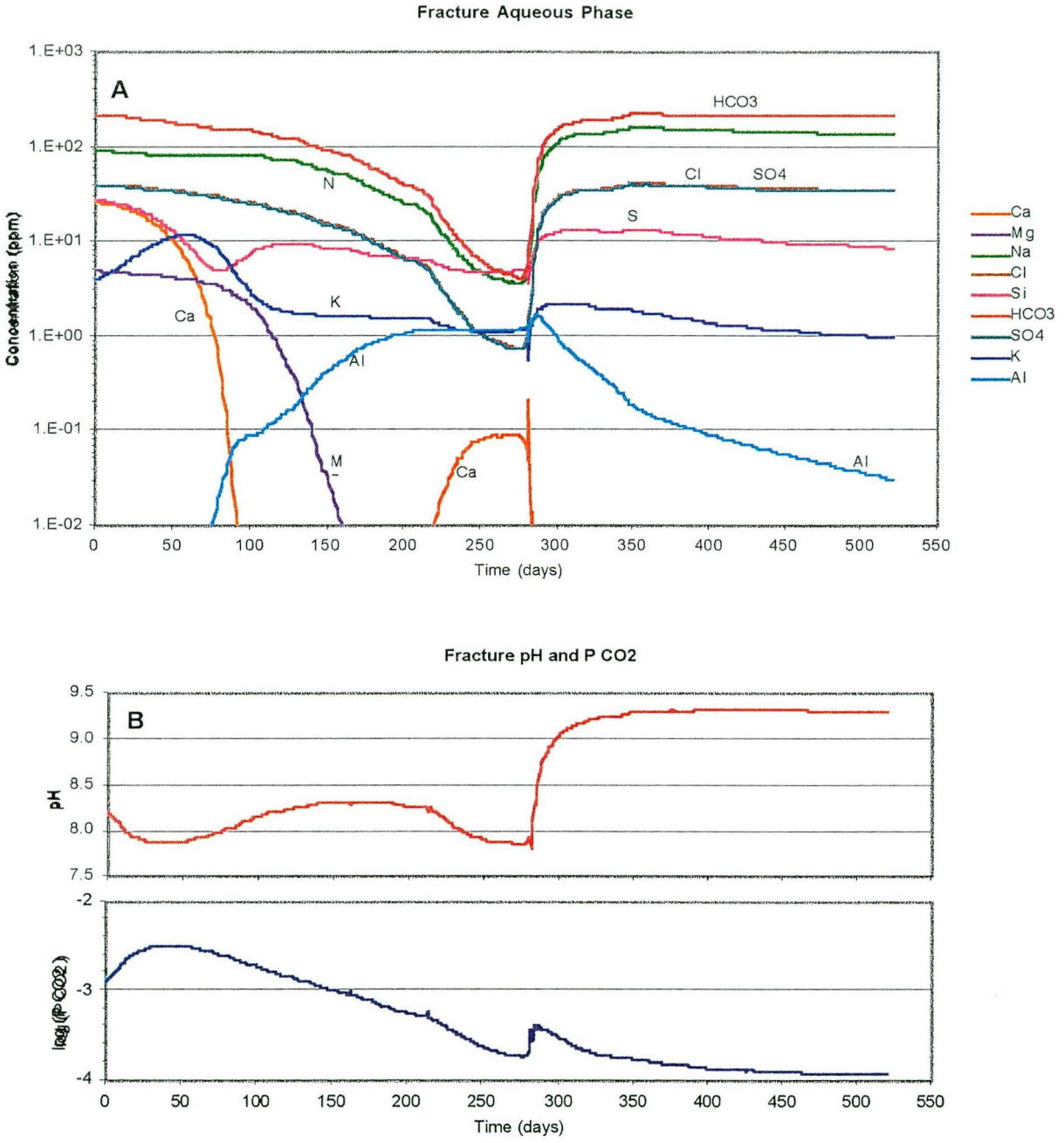

Figure 4-32. Time profiles of (a) aqueous species concentrations and (b) pH and CO_2 partial pressure (bars) in fractures computed at a point shown on Figure 4-3. Simulation with aluminosilicates (kin04).

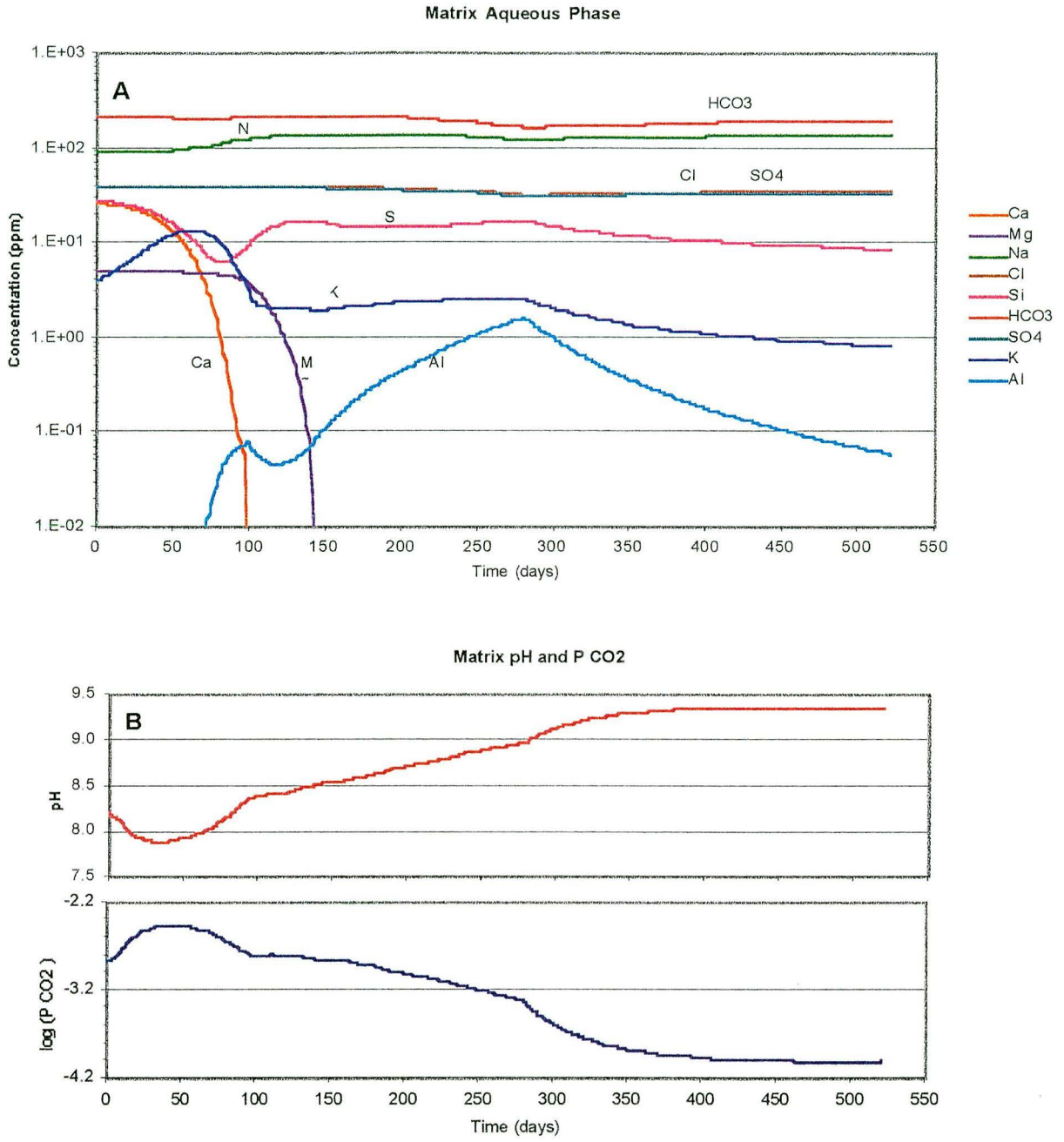

Figure 4-33. Time profiles of (a) aqueous species concentrations and (b) pH and CO_2 partial pressure (bars) in the matrix computed at a grid point shown on Figure 4-3. Simulation with aluminosilicates (kin04).

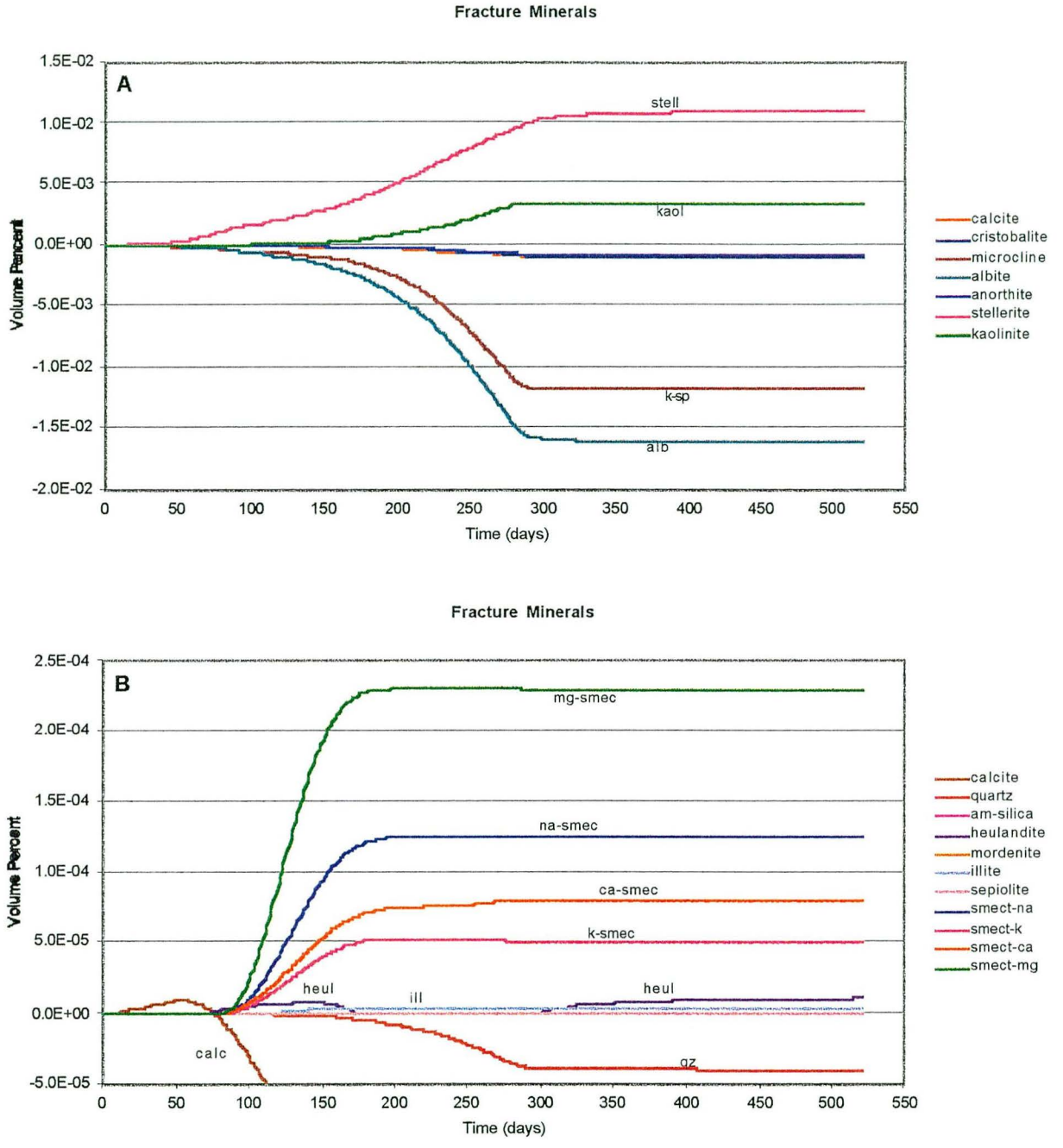

Figure 4-34. Time profiles of mineral volume percent changes in fractures (a and b) computed at a grid point shown on Figure 4-3. Simulation with aluminosilicates (kin04).

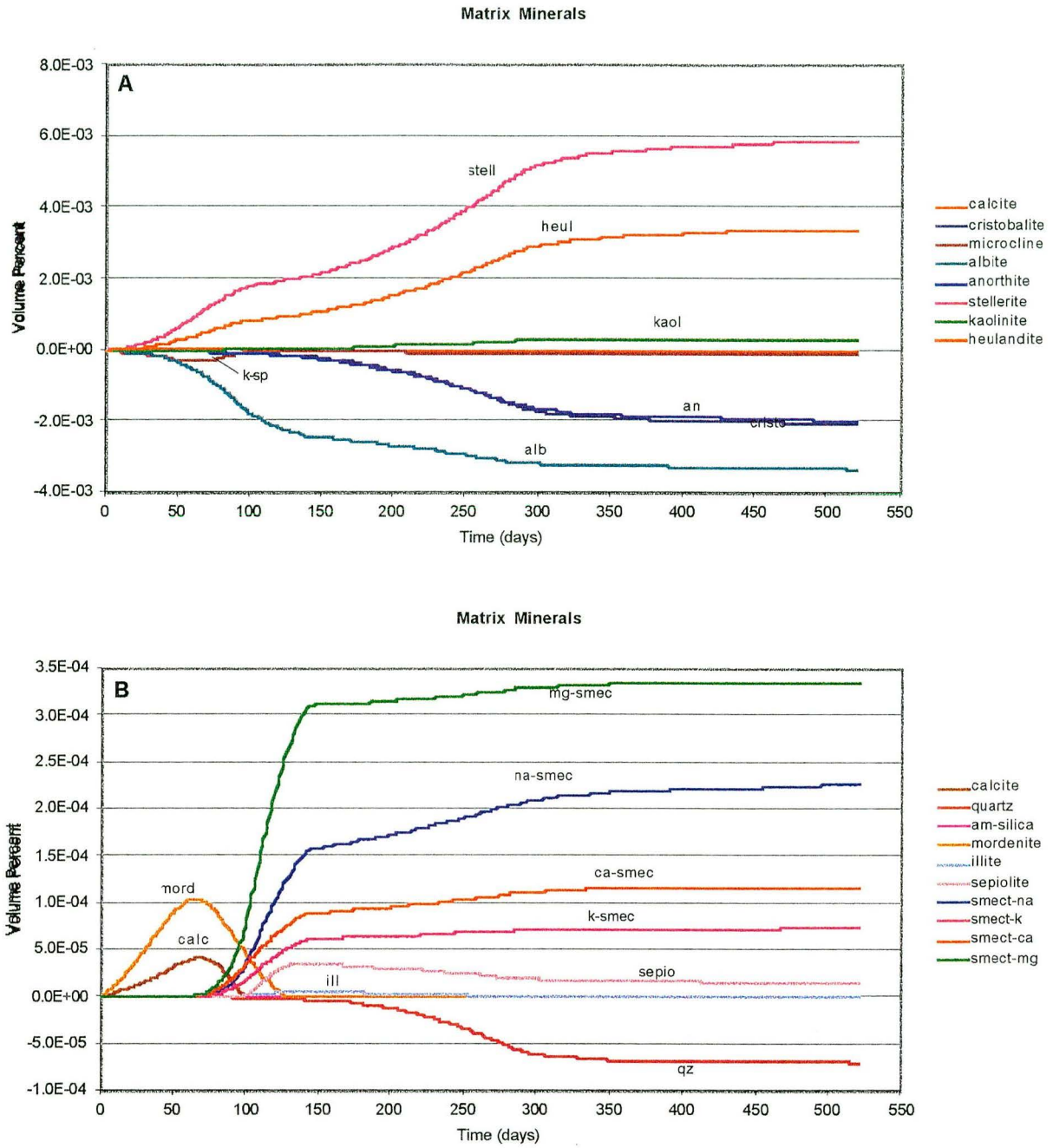

Figure 4-35. Time profiles of mineral volume percent changes in the matrix (a and b) computed at a grid point shown on Figure 4-3. Simulation with aluminosilicates (kin04).

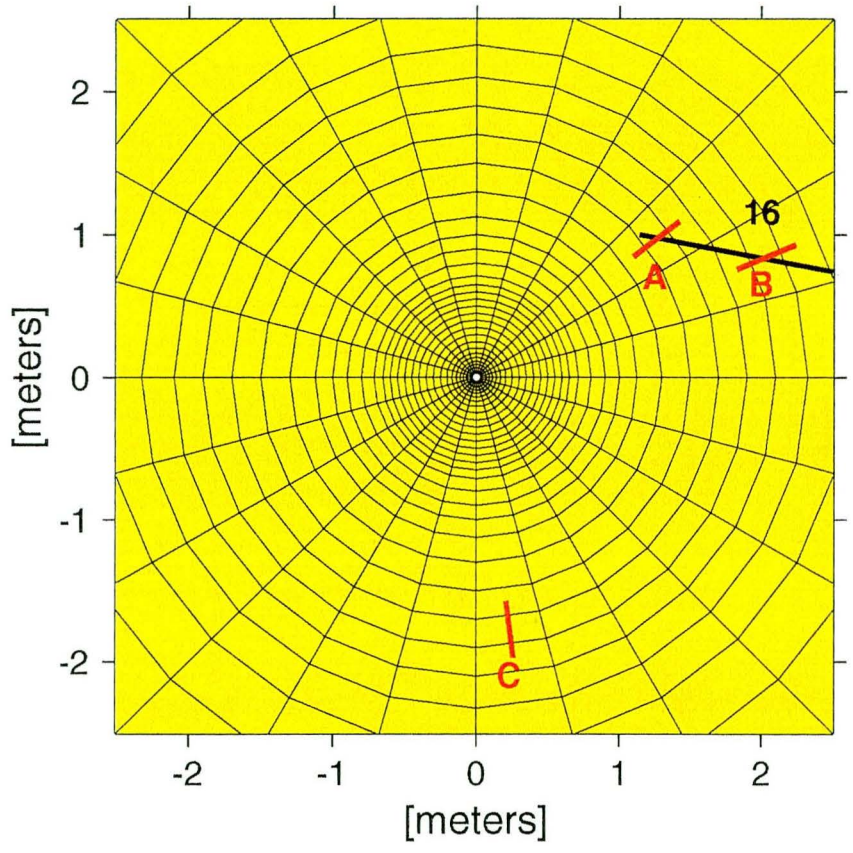

Figure 4-36. Location of Zones A, B, and C used for comparison of measured and calculated data shown on Tables 4.6.1 and 4.6.2 and Figures 4-37 and 4-38.

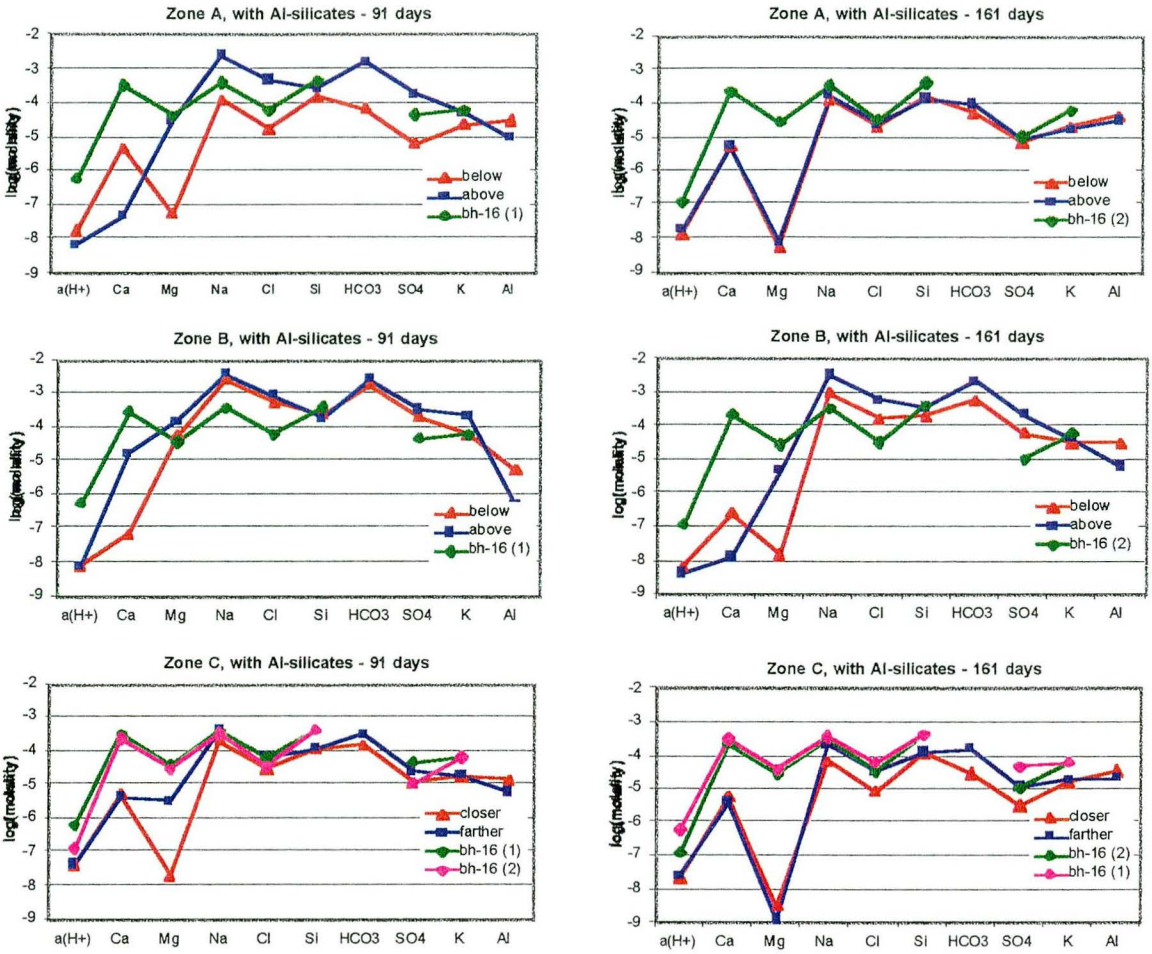

Figure 4-37. Concentrations of aqueous species measured in water collected from borehole 16 on November 25, 1996 [bh-16 (1)] and February 4, 1997 [bh-16 (2)] compared with computed concentrations in Zones A, B, and C shown on Figure 4-36. Simulation with aluminosilicates (kin04). Computed concentrations are for locations either 'below' or 'above' the projected location of borehole 16 (Zone A and B) and 'closer' or 'farther' from the heater (Zone C). Molalities shown correspond to concentrations in mg/l in Table 4.6.1. $a(H^+)$ is the activity of hydrogen ion (10^{-pH}).

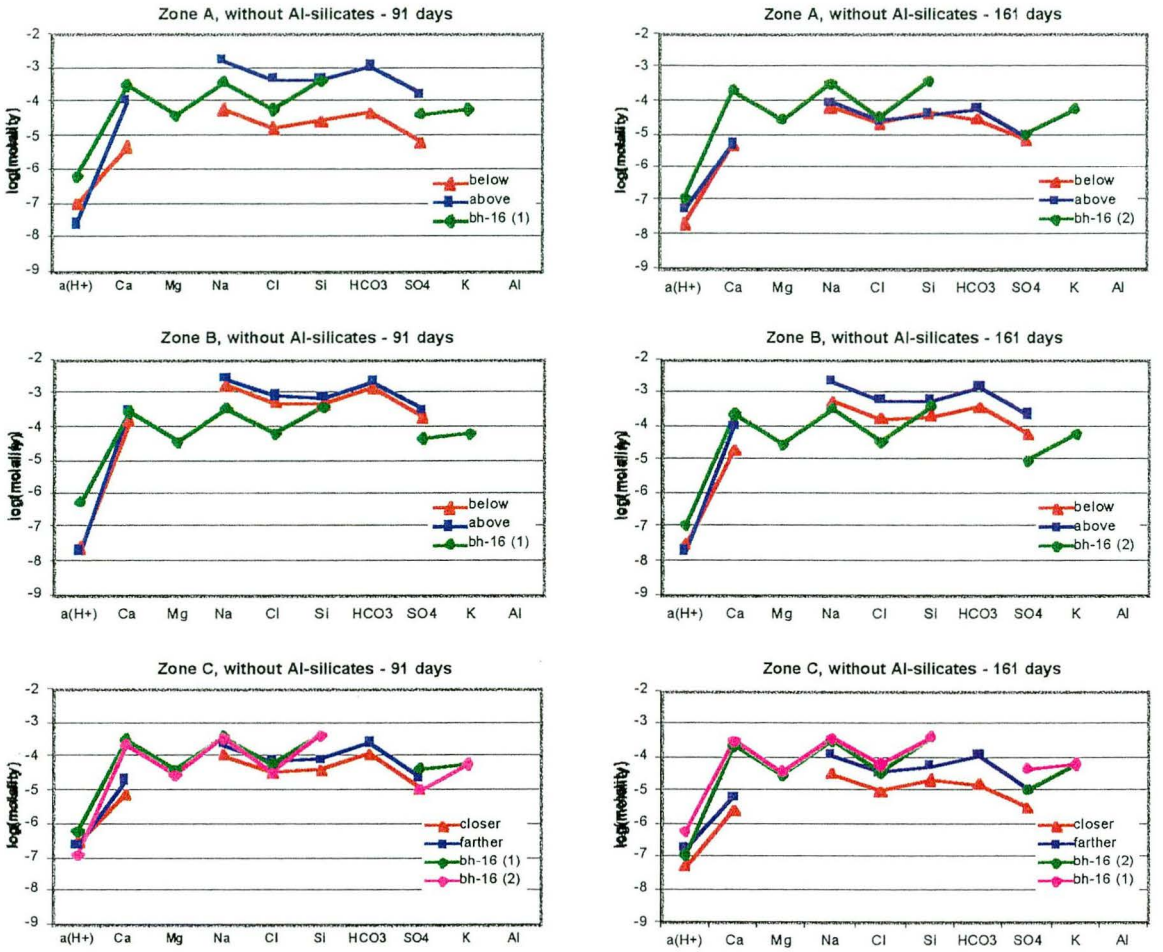

Figure 4-38. Concentrations of aqueous species measured in water collected from borehole 16 on November 25, 1996 [bh-16 (1)] and February 4, 1997 [bh-16 (2)] compared with computed concentrations in Zones A, B, and C shown on Figure 4-36. Simulation without aluminosilicates (kin05). Computed concentrations are for locations either 'below' or 'above' the projected location of borehole 16 (Zone A and B) and 'closer' or 'farther' from the heater (Zone C). Molalities shown correspond to concentrations in mg/l in Table 4.6.2. $a(H^+)$ is the activity of hydrogen ion (10^{-pH}).

Chapter 5 Summary and Conclusions

Y.W. Tsang

Earth Sciences Division, LBNL

The Single Heater Test (SHT) in the Exploratory Studies Facility, Yucca Mountain, Nevada began in FY96. It included extensive instrumentation of a 10-m^3 rock in the fractured welded tuff. All tests and analyses have now been concluded. In the foregoing chapters we have presented a comprehensive analysis of all the test results. All the measurements under the responsibility of LBNL were summarized in Chapter 2. Interpretive analysis of the results by numerical modeling were discussed in Chapters 3 and 4. Chapter 3 focuses on the thermo-hydrological processes, and Chapter 4 emphasizes the thermo-hydrological-chemical aspects of the SHT.

We consider the SHT highly successful for the following reasons:

(1) The SHT was successful in meeting the stated objective of the Yucca Mountain Thermal Test Program, namely; to acquire a more in-depth understanding of the coupled processes – thermal, mechanical, hydrological and chemical – in fractured, partially saturated tuff under the influence of heat.

(2) The good agreement between modeling results and the extensive data set from the SHT indicates that the fundamental basis of our understanding of the coupled processes is sound. Though the fundamental processes are understood, and the general thermally induced behavior in unsaturated fractured rock can be predicted, the detailed behavior in the SHT are impacted by site specific features and local heterogeneities that have a higher degree of uncertainty.

(3) As the first of the two *in situ* thermal tests in the Exploratory Studies Facility, the SHT has also functioned as a testbed for the longer-duration, larger-scale Drift Scale Test (DST). The insights that the Thermal Test Team has gained from conducting the SHT, with regards to overall approach, testing methods, instrumentation, frequency of measurements, and spacing and configuration of boreholes, are presently being applied to the conducting of the DST. Further, numerical modeling and data analysis strategies developed for the SHT have also benefited the DST. Despite the difference in scale and configuration between the two thermal tests (the SHT and the DST), the conceptual model of various coupled processes developed based on the SHT experience has been equally successful in matching the

extensive temperature data set from first six months of heating of the DST (Birkholzer and Tsang, 1998). This is a strong confirmation that the fundamental understanding and formulation of coupled processes obtained in SHT is valid and can be used for Performance Assessment (PA).

(4) The SHT has afforded the Thermal Test Team the opportunity to reduce uncertainty by refining an iterative approach between measurements and modeling. The overall testing approach developed within the SHT is to use the ambient pre-test characterization data as input to predictive modeling; then let the predictive modeling results guide the active testing measurements; and finally iterate between the model and the test data to calibrate and refine the numerical model. This overall testing approach developed in the SHT not only benefits the conducting of the succeeding thermal tests such as the DST currently underway, but could also serve as a blueprint for performance confirmation during the construction phase of the repository.

(5) Because of the SHT experience, we have significantly increased the confidence level in our ability to predict the thermal-hydrological conditions of larger-scale heater tests such as the DST, and perhaps even that of a high-level nuclear waste repository in heterogeneous, partially saturated, fractured tuff.

(6) The success of the SHT is a direct result of the multi-disciplinary and multi-laboratory teamwork of the Thermal Test Team in integrating modeling studies and field and laboratory measurements.

The main technical findings derived from the SHT are as follows:

Heat Conduction is the Dominant Heat Transfer Mechanism in the SHT

In Chapter 3 we presented an interpretive analysis of the thermo-hydrological processes of the SHT by means of numerical simulations. The analysis was applied to extensive passive monitoring and active testing data. Very good quantitative agreement was obtained between the measured and simulated temperatures. Data indicate that heat conduction accounts for most of the temperature rise. Liquid reflux to the heater from the condensed vapor during the heating phase was small.

Complementary Field and Laboratory Techniques Are Important in Tracking the Drying/ Condensation Front; Results Indicate Gravity Drainage of Water through Fractures

The simulated moisture redistribution in the SHT using a dual-permeability 3D model is also well supported by field data, which include those from electrical resistivity tomography, neutron logging, cross-hole radar tomography, air injection tests, and laboratory measurements of liquid saturation for post-cooling cores. The model predicts a drying zone of about 1.2 m around the heater at the end of the heating phase, as well as a condensation zone further away with a large increase in fracture liquid saturation, which gives rise to significant gravity drainage through the fractures. Whether the condensate would mainly drain through the fractures (as predicted by a dual-permeability conceptual model), or whether it would mainly be imbibed and held in the matrix (as predicted by an effective continuum

conceptual model) was a large uncertainly at the start of the SHT, but is not any more at the conclusion of the SHT. That is, the SHT data support the dual-permeability conceptual model. It would be instructive to retrace our steps here to illustrate how the iterative approach as discussed in **(4)** above leads to the reduction of uncertainty.

Both electrical resistivity and cross-hole radar tomograms for the heating phase hint at a larger liquid saturation in the matrix below the heater horizon rather than above it, suggesting water drainage through the fractures. The air permeability values in the condensation zone (Zone 3 of boreholes 16 and 18), while remaining depressed throughout the heating phase because of increased liquid saturation in the fractures, returned to its pre-heat value shortly after the termination of heating, suggesting that water was not held in the fractures once the vaporization and condensation processes ceased at heater turn-off. These observations led the Thermal Test Team to design the placement of the three post-test boreholes 199, 200, 201 (Figure 2.5-1), based on the drying, condensation, and drainage zones as predicted by the model results. The subsequent determination of the liquid saturation of these cores from laboratory measurements confirmed that only a limited amount of water was held in the matrix in the condensation zone. This supports the conceptualization of the matrix and fracture media as a dual continuum in modeling the thermo-hydrological processes.

Water Collected in the SHT Confirmed to Be Condensate

Reaction-transport simulations described in Chapter 4 reproduced fairly well those chemical processes ongoing during the SHT. These simulations confirm that water from borehole 16 resulted from steam condensation in fractures, and that its mildly acidic character reflects the dissolution of gaseous CO_2 at the time of steam condensation.

More insight on the geochemistry of fluids generated by thermal tests can be gained from gas sampling and analysis. In particular, CO_2 measurements can further our understanding of CO_2 volatilization and dissolution processes, which directly affect the pH of pore and fracture waters and, together with temperature, are expected to be important controls of mineral dissolution and precipitation patterns around the repository. CO_2 sampling and analysis are being pursued in the DST.

Small Thermo-Mechanical Changes due to Heating Detected by Air Injection Testing

There is a consistent upward trend in the air-permeability values from pre-heat to post-heat (Table 2.1-5). The increase in the permeability ranged from about 20% to a factor of 3.5. The overall larger post-heat permeability in the SHT may be attributed to microfracturing. Heating may cause some fractures to close and some to open. However, since air -permeability tests are conducted over length scales of meters, and since fluid always seeks the least resistive path, air-permeability tests preferentially register the effect of fracture opening.

An Iterative Approach between Modeling and Observed Data Is Essential for Building Confidence in Models

We reiterate that though the fundamental processes are understood and can be predicted, the detailed behavior in the SHT are impacted by site-specific features and local heterogeneities, and are not likely to be predicted *a priori*. They can only be uncovered by site-specific field measurements with the help of process models. A good example relates to Zone 3 of boreholes 16 and 18. Both boreholes lie in the condensation zone where large increase in the fracture saturation is anticipated, based on model results. A fracture connection between the heat source and borehole 16 would promote water seepage into Zone 3 of borehole 16. This hypothesis remained a speculation through the heating and cooling phases of the SHT. Post-cooling air-injection and gas tracer tests carried out between borehole 1 and boreholes 16 and 18 unequivocally confirm the presence of a direct pneumatic connection for vapor transport to Zone 3 of borehole 16, and not to borehole 18, even though borehole 18 is locally more permeable than borehole 16. Moreover, thermo-hydrologic-chemical modeling of the SHT test as discussed in Chapter 4 indicates that the water collected from borehole 16 has originated from a zone of increased drainage compared to its surroundings, again suggesting the presence of a preferential pathway between the heat source and borehole 16.

The discussion above underlines the value of an iterative approach between model and an extensive set of data such as that from the SHT. Because the SHT has given insight on both how the fundamental processes and site specific heterogeneities impact measured results, confidence in our ability to predict the performance of a waste repository, though considerably greater in spatial and temporal scale, is significantly increased.

Acknowledgment

I thank Jens Birkholzer and Nicolas Spycher for review of this chapter and suggestions for improvement.

References

Birkholzer, J. T. and Tsang, Y. W. 1998. "Interpretive Analysis of the Thermo-Hydrological Processes of the Drift Scale Test." In: Drift Scale Test Progress Report, Lawrence Berkeley National Laboratory, Chapter 2. Yucca Mountain Project Level 4 Milestone SP2930M4. Berkeley, California: Lawrence Berkeley National Laboratory. MOL.19980825.0268.

Ernest Orlando Lawrence Berkeley National Laboratory
One Cyclotron Road | Berkeley, California 94720

Prepared for the U.S. Department of Energy under Contract No. DE-AC03-76SF00098 .